frontiers | Research Topics

Volcanic and tectonic degassing: Fluid origin, transport and implications

Edited by
Maoliang Zhang, Antonio Caracausi, Ying Li and Daniele L. Pinti

Published in
Frontiers in Earth Science

ISSN 1664-8714
ISBN 978-2-8325-3778-7
DOI 10.3389/978-2-8325-3778-7

About Frontiers

Frontiers is more than just an open access publisher of scholarly articles: it is a pioneering approach to the world of academia, radically improving the way scholarly research is managed. The grand vision of Frontiers is a world where all people have an equal opportunity to seek, share and generate knowledge. Frontiers provides immediate and permanent online open access to all its publications, but this alone is not enough to realize our grand goals.

Frontiers journal series

The Frontiers journal series is a multi-tier and interdisciplinary set of open-access, online journals, promising a paradigm shift from the current review, selection and dissemination processes in academic publishing. All Frontiers journals are driven by researchers for researchers; therefore, they constitute a service to the scholarly community. At the same time, the *Frontiers journal series* operates on a revolutionary invention, the tiered publishing system, initially addressing specific communities of scholars, and gradually climbing up to broader public understanding, thus serving the interests of the lay society, too.

Dedication to quality

Each Frontiers article is a landmark of the highest quality, thanks to genuinely collaborative interactions between authors and review editors, who include some of the world's best academicians. Research must be certified by peers before entering a stream of knowledge that may eventually reach the public - and shape society; therefore, Frontiers only applies the most rigorous and unbiased reviews. Frontiers revolutionizes research publishing by freely delivering the most outstanding research, evaluated with no bias from both the academic and social point of view. By applying the most advanced information technologies, Frontiers is catapulting scholarly publishing into a new generation.

What are Frontiers Research Topics?

Frontiers Research Topics are very popular trademarks of the *Frontiers journals series*: they are collections of at least ten articles, all centered on a particular subject. With their unique mix of varied contributions from Original Research to Review Articles, Frontiers Research Topics unify the most influential researchers, the latest key findings and historical advances in a hot research area.

Find out more on how to host your own Frontiers Research Topic or contribute to one as an author by contacting the Frontiers editorial office: frontiersin.org/about/contact

Volcanic and tectonic degassing: Fluid origin, transport and implications

Topic editors

Maoliang Zhang — Tianjin University, China

Antonio Caracausi — National Institute of Geophysics and Volcanology, Section of Palermo, Italy

Ying Li — Institute of Earthquake Forecasting, China Earthquake Administration, China

Daniele L. Pinti — Le Geotop, Canada

Citation

Zhang, M., Caracausi, A., Li, Y., Pinti, D. L., eds. (2023). *Volcanic and tectonic degassing: Fluid origin, transport and implications*. Lausanne: Frontiers Media SA. doi: 10.3389/978-2-8325-3778-7

Table of contents

frontiers | Frontiers in Earth Science

TYPE Editorial
PUBLISHED 10 October 2023
DOI 10.3389/feart.2023.1304789

OPEN ACCESS

EDITED AND REVIEWED BY
Martyn Tranter,
Aarhus University, Denmark

*CORRESPONDENCE
Maoliang Zhang,
mzhang@tju.edu.cn

RECEIVED 30 September 2023
ACCEPTED 03 October 2023
PUBLISHED 10 October 2023

CITATION
Zhang M, Li Y, Caracausi A and Pinti DL (2023), Editorial: Volcanic and tectonic degassing: fluid origin, transport and implications.
Front. Earth Sci. 11:1304789.
doi: 10.3389/feart.2023.1304789

Editorial: Volcanic and tectonic degassing: fluid origin, transport and implications

Maoliang Zhang[1]*, Ying Li[2], Antonio Caracausi[3] and Daniele L. Pinti[4]

[1]School of Earth System Science, Tianjin University, Tianjin, China, [2]Institute of Earthquake Forecasting, Beijing, China, [3]Istituto Nazionale di Geofisica e Vulcanologia, Sezione di Palermo, Palermo, Italy, [4]Geotop and Département des Sciences de la Terre et de l'Atmosphère, Université du Québec à Montréal, Montreal, QC, Canada

KEYWORDS

gas geochemistry, hydrogeochemistry, volcanoes, active faults, Earth degassing

Editorial on the Research Topic
Volcanic and tectonic degassing: fluid origin, transport and implications

Deeply-sourced fluids are released in volcanically and tectonically active regions through conduits such as fumaroles, natural springs, and permeable soils. The origin and transport of the fluids in volcanic and tectonic systems are a key research theme in Earth Sciences, which is of particular importance for geo-hazard mitigation and resource exploration. This Research Topic aims to present recent advances in fluid geochemistry and its application in volcanically and tectonically active regions. Under this context, 10 papers covering a series of research themes in fluid geochemistry were published in this Research Topic, as briefly summarized below.

People living close to active fault zones are threatened by earthquake hazard and therefore monitoring the status of active faults is important to mitigate the damage caused by future earthquakes. Caracausi et al. reported data from a novel infrastructure designed for multidisciplinary and continuous monitoring of the Alto Tiberina fault, Italy. Monitoring results (including seismic, geodetic, and geochemical data) from The Alto Tiberina Near Fault Observatory (TABOO-NFO) would shed new light on earthquake prediction studies in other countries. Fidani et al. conducted a comprehensive statistical analysis of CO_2 time series registered at the Gallicano test site, Italy, and identified the correlations between low-magnitude earthquakes and CO_2 anomalies in spring waters. Li et al. studied the spatial variations in soil Rn and CO_2 emissions in the Wuzhong-Lingwu region, NW China, as well as the possible controlling factors of earthquakes, stress state, and deep-to-shallow crustal structures. Their findings offer new insight into combining geochemical characteristics of soil gas and seismological methods to estimate regional seismic hazards.

Under the context of continuous collision between Indian and Asian continents, the Tibetan Plateau and its surrounding regions have drawn increasing concern from the Earth science community because of intensive and frequent earthquake events. Liu et al. reported the first estimates of diffuse soil CO_2 flux (~1.2 Mt yr^{-1}) for the Anninghe-Zemuhe fault in the Southeast Tibetan Plateau and found close relationships between spatial variations in soil CO_2 fluxes and that of regional seismic activity. Based on the geochemistry of hot spring waters, Liu et al. explored the controls of the Jinshajiang fault zone (SW China) on hydrothermal fluid circulation, water-rock interaction, and earthquakes, which

highlighted the role of hot spring water discharging from fracture zones in receiving the hydrological information on seismic activity. Also published in this Research Topic, Liu et al. presented an example of post-earthquake hydrological changes based on carbon isotope data of spring waters collected after the 2021 M_w 7.4 Maduo earthquake in eastern Tibetan Plateau. They quantitatively identified enhanced mobilization of the shallow soil organic carbon following the 2021 Maduo earthquake and suggested that earthquakes could disturb the circulation of subsurface fluids and their interaction with the country rocks and sediments on short timescales. Wang et al. investigated origin and circulation of geothermal waters in the Karakoram strike-slip fault zone in western Tibet. Their results show that geothermal water is correlated with the epicenter and focal depth of earthquakes, especially for high-temperature spring water with deeper circulation and extremely high Li, B, Fe, and As concentrations.

Three papers in this Research Topic focus on the degassing of historically active volcanoes. Gherardi et al. investigated helium isotopes on gas extracted by crushing from melt and fluid inclusions in minerals from Plinian and inter-Plinian tephra and lavas of Vesuvius, Italy. Their results show that i) $^3He/^4He$ values are buffered within an extended, deep-seated reservoir at about 10 km filled with magma rising from the mantle, and ii) magma ponding at crustal depth could be considered a key mechanism that might have the potential to homogenize the helium isotope signal. Located in the hinterland of Northeast Asia, the active Arxan volcanic field remains less studied for the characteristics of its present-day volcanic degassing. Pan et al. focused on diffuse soil CO_2 fluxes and found that annual CO_2 emission flux from the volcanic field to the atmosphere is ~0.63×10^5 t and is comparable to that of the Iwojima volcano in Japan. This is the first flux estimate for soil CO_2 emissions of the Arxan volcanic field. Cui et al. presented a geochemical study on the hot spring water and gases from the Arxan volcanic field. They identified ~3%–23% mantle helium inputs and thus heat supply in the hydrothermal fluids, suggesting that the residual mantle-derived melts beneath the Arxan volcanic field are still releasing fluids/volatiles and heating the overlying hydrothermal systems.

Author contributions

MZ: Writing–original draft, Writing–review and editing. YL: Writing–review and editing. AC: Writing–review and editing. DP: Writing–review and editing.

Funding

The authors declare that no financial support was received for the research, authorship, and/or publication of this article.

Conflict of interest

The authors declare that the research was conducted in the absence of any commercial or financial relationships that could be construed as a potential conflict of interest.

Publisher's note

frontiers | Frontiers in Earth Science

TYPE Brief Research Report
PUBLISHED 07 November 2022
DOI 10.3389/feart.2022.1011203

OPEN ACCESS

EDITED BY
Ying Li,
Institute of Earthquake Forecasting,
China Earthquake Administration, China

REVIEWED BY
David Graham,
Oregon State University, United States
Ian Ernest Masterman Smith,
The University of Auckland,
New Zealand
Eemu Ranta,
Faculty of Science, University of
Helsinki, Finland

*CORRESPONDENCE
Fabrizio Gherardi,
f.gherardi@igg.cnr.it

SPECIALTY SECTION
This article was submitted
to Geochemistry,
a section of the journal
Frontiers in Earth Science

RECEIVED 03 August 2022
ACCEPTED 21 October 2022
PUBLISHED 07 November 2022

CITATION
Gherardi F, Barsanti M, Principe C and
Magro G (2022), Helium isotopes in
Plinian and inter-Plinian volcanic
products of Vesuvius, Italy.
Front. Earth Sci. 10:1011203.
doi: 10.3389/feart.2022.1011203

Helium isotopes in Plinian and inter-Plinian volcanic products of Vesuvius, Italy

Fabrizio Gherardi[1]*, Mattia Barsanti[2], Claudia Principe[1] and Gabriella Magro[1]

[1]National Research Council of Italy (CNR) - Institute of Geosciences and Georesources (IGG), Pisa, Italy, [2]ENEA Italian National Agency for New Technologies, Italian National Agency for New Technologies (ENEA) - Energy and Sustainable Economic Development, Marine Environment Research Centre S.Teresa, La Spezia, Italy

We investigated helium isotopes on gas extracted by crushing from melt and fluid inclusions in minerals from Plinian and inter-Plinian tephra and lavas of Vesuvius, Italy. Erupted products of different ages were considered, from Avellino eruption (1995 BCE) to the last eruption of 1944, with special focus on the *79 AD* Plinian eruption. $^{3}He/^{4}He$ ratios between 1.5 and 2.7 R_A were measured, with the highest values associated with rocks representative of the roof and the walls of the magma chambers (cumulates). Lowest values occurred in sanidines representative of magma-skarn interfaces. Noteworthy, the highest measured values of the *79 AD* pumices were comparable with both lavas and tephra emitted from flank vents and under open-conduit conditions during the *Medieval Period* and *Present Period* of Vesuvius activity, and present-day fumarolic discharges. $^{3}He/^{4}He$ values are buffered within an extended, deep-seated reservoir at about 10 *km* filled with magma rising from the mantle. A fact that might potentially limit the accuracy of future eruption forecasting through monitoring of $^{3}He/^{4}He$ changes in Vesuvius fumaroles. Ageing and interaction with crustal rocks emerged as possible mechanisms that lowered the $^{3}He/^{4}He$ ratio of the melt during its intra-crustal magma chambers stay, with highest values associated with more dynamic conditions.

KEYWORDS

Helium isotopes, Carbon isotopes, melt and fluid inclusions, Plinian eruptions, Sub-Plinian eruptions, Violent Strombolian eruptions, flank eruptions, Vesuvius

Introduction

The volcanoes of Monte Somma, Vesuvius, and Phlegraean Fields occupy the southern part of the Campania Plain, southern Italy, and border a densely populated region currently inhabited by more than two million people that also includes the metropolitan city of Naples. Starting in the 1980s', the high volcanic risk related with the possible renewal of activity of one of these volcanoes fostered an intense scientific effort to increase knowledge on the eruptive history and mechanisms of these volcanoes (e.g., Barberi et al., 1984; De Vivo et al., 1993). Present volcanic activity mostly consists of active

seismicity, ground deformation with alternation of deflation/inflation episodes (mostly in the Phlegraean Fields area), moderate fumarolic emissions, and hot spring discharges.

At Vesuvius, over the last decades, a large number of rock and fluid samples have been collected, and an extended database of mineralogical and geochemical analyses of various deposits is now available (De Vivo et al., 2010; Peccerillo, 2020). The historic activity of the Vesuvius volcanic system is characterized by occasional Plinian eruptions (Avellino, *79 AD*, *472 AD*, 1631) separated by periods of inactivity or semi-persistent activity (Arnò et al., 1987). During semi-persistent phases of activity, the volcano experienced an open-conduit behavior, and produced effusive, often from flank vents (Principe et al., 2004), and mixed (effusive and explosive) eruptions, from Strombolian, to Violent Strombolian and Sub-Plinian type (Arrighi et al., 2001).

As the last eruption occurred in 1944, most of the current scientific interest is in the possible correlation between ongoing observed dynamics and past geological record. In particular, the link between present-day fluid composition and magma degassing at depth is considered a key element in understanding the mechanisms that could control any possible future volcanic activity.

Due to its well-defined isotopic signature for different geological settings (e.g., Kurz et al., 1982; Ozima and Podosek, 1983; Mamyrin and Tolstikhin, 1984; Burnard, 2013), the helium isotope composition (expressed as the $^3He/^4He$ ratio measured in the sample, R, normalized to same isotope ratio measured in air, $R_A = 1.39 \times 10^{-6}$) has the potential to be usefully employed to investigate eruptive mechanisms and magma dynamics. As a general statement, under closed conduit conditions, a number of information on the primary magma source could be lost due to the long residence time of a magma into shallow intra-crustal magmatic chambers. Despite this uncertainty, the R/R_A signature of gases extracted from fluid inclusions can disclose important information on the evolution of melts inside the magmatic chambers, and on the interactions between magma and wall rocks. Further to this, the comparison of $^3He/^4He$ ratios measured on fluid inclusions of phenocrysts with values from present-day fluids (fumaroles, hot springs, gas dissolved in water, mofettes, etc.) provide additional insights on the time evolution of the magmatic-hydrothermal system, because variations in the chemical and isotopic composition of fluids may reveal the onset of a new phase of volcanic activity (e.g., Ozima and Podosek, 1983; Mamyrin and Tolstikhin, 1984; Porcelli et al., 2002; Burnard, 2013).

At Vesuvius, $^3He/^4He$ ratios have been mostly determined on olivine and pyroxene phenocrysts separated from lavas emitted under open conduit conditions during the last 400 years (from 1,631 to 1,944; Graham et al., 1993; Graham and Lupton, 1999; Martelli et al., 2004). Until today, no He isotope were available for products—such as Plinian pumices—emitted after long periods of permanence in a magmatic chamber under closed conduit condition—or from Violent Strombolian and Sub-Plinian products—deriving from the refilling of the open conduit with gas-rich magma from a deep-seated reservoir. This paper aims at filling this gap, by integrating the existing He isotope composition data with new data on minerals from tephra and lavas belonging to all these types of eruptions. Special emphasis is on volcanic products emitted during the *79 AD* Plinian eruption.

Geological-volcanological setting

Monte Somma is a complex volcanic structure affected by several calderas and structural collapses (e.g., Principe et al., 2021). In the middle of the resulting morphological depression, the volcanic cone of Vesuvius has grown. Along with the Phlegraean Fields volcanic area and the Roccamonfina stratovolcano, Monte Somma-Vesuvius volcano is hosted in a large graben within the Campania plain (Figure 1) that originated during the Upper Pliocene-Lower Pleistocene. This graben is part of a macro-regional extensional system that stretches along the Tyrrhenian margin of the Apennine mountainous chain, from southern Toscana to northern Calabria. This belt experienced widespread volcanism in Pleistocene (e.g., Scandone, 1979; Turco et al., 2006).

The volcanic activity in the area now occupied by Monte Somma and Vesuvius started about 400 ka BP (Brocchini et al., 2001). The outcropping deposits all belong to the volcanic activity following the Campanian Ignimbrite eruption (about 39 ka ago; Rosi and Sbrana, 1987). Dated to about 22 ka BP (Cioni et al., 2008), the *Pomici di Base* eruption—the oldest eruption considered in the present work—is the first one and the major Plinian eruption occurred in Vesuvius area (Bertagnini et al., 1998). Other major explosive eruptions followed, such as the *Greenish Pumices* Sub-Plinian eruption (about 20 ka BP; Cioni et al., 2003), and the *Pomici di Mercato* Plinian eruption (about 8,900 years BP; Mele et al., 2011). The activity occurred at Vesuvius during the last 4 ka BP has been subdivided into four synthematic units, on the basis of major geological events, marked by depositional unconformities (Paolillo et al., 2016): 1) *Proto -Vesuvius*, between the Plinian eruptions of *Pomici di Avellino* (about 4 ka ago) and *79 AD*; 2) *Ancient Vesuvius*, between *79 AD* Plinian eruption and *472 AD* Sub-Plinian eruption; 3) *Medieval Vesuvius*, from the *472 AD* Sub-Plinian eruption and the 1631 small-scale Plinian eruption; 4) *Present Vesuvius*, between 1631 and 1944 eruptions.

The *Medieval Vesuvius* activity is characterized by the emission of lava flows from flank vents opened on the slopes of the Vesuvius cone, and of Strombolian and Violent Strombolian scoriae fallout (Principe et al., 2004; Paolillo et al., 2016). During the *Present Vesuvius* period, the volcano passed from effusive and markedly Strombolian activity to episodes of violent Strombolian and Sub-Plinian eruptions

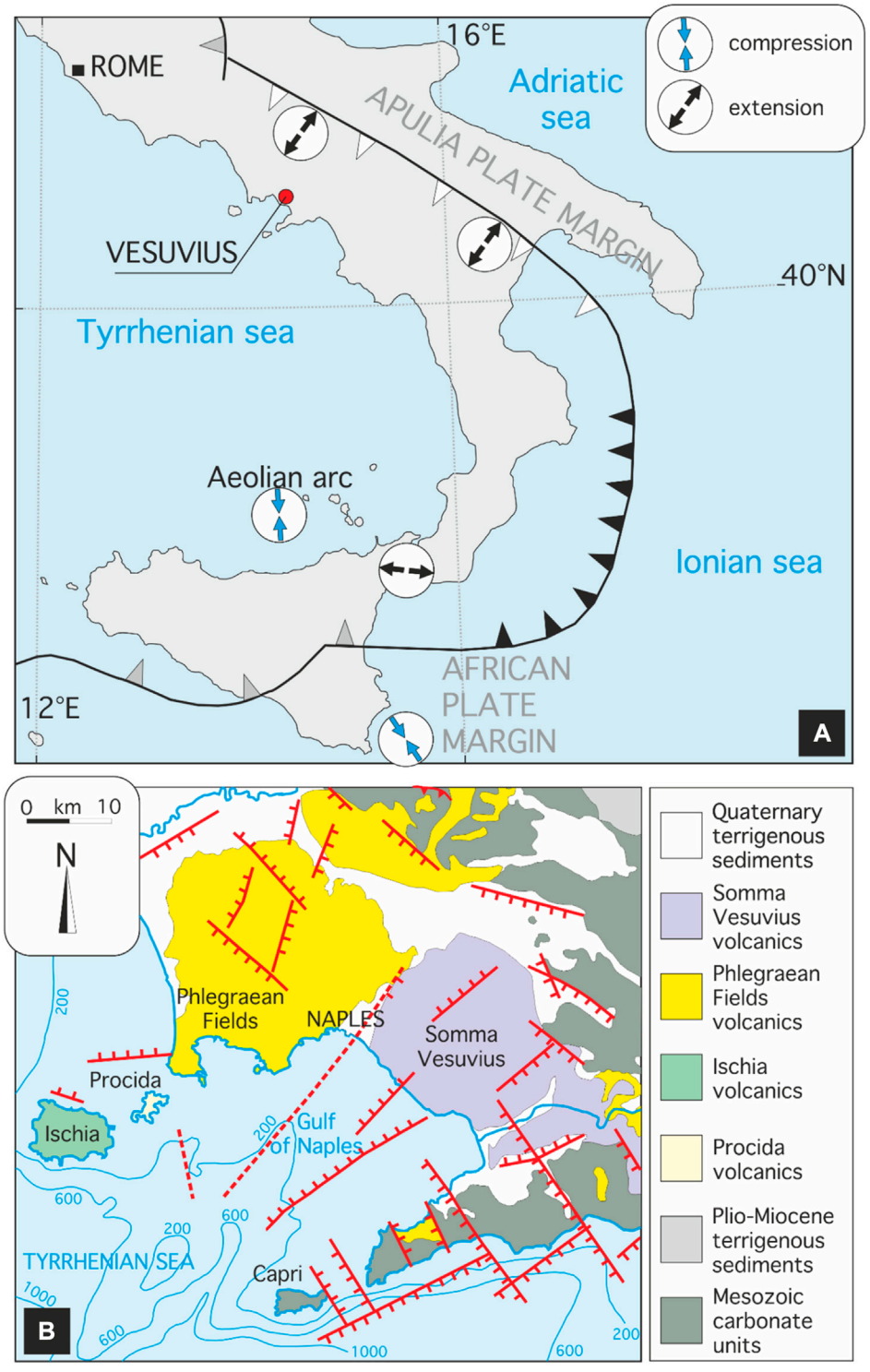

FIGURE 1
(A) Geodynamical sketch map of Southern Italy, with location of the Monte Somma and Vesuvius (modified after Montone et al., 1999). Bold lines = structural arcs; shaded triangles = active compressional fronts; solid triangles = active oceanic subduction; open triangles = front of the Plio-Pleistocene thrust, now prevalently affected by extension. **(B)** Simplified geological map of the Campania plain and volcanic districts.

with mixed effusive and explosive character (Arrighi et al., 2001).

Since the last eruption of 1944, Vesuvius entered a period of eruptive rest. In the crater area, temperatures between 600 and 800°C were recorded in the fumaroles during the period 1944–1960 (Chiodini et al., 2001), before starting to gently decrease close to the boiling point of water at the crater altitude (around 95°C) during the 1990s, down to present-day sub-boiling temperatures (about 72°C). The residual activity consists of fumaroles, diffuse degassing (e.g., Baubroun et al., 1991; Chiodini et al., 2001; Federico et al., 2002; Frondini et al., 2004), general subsidence and low-magnitude seismicity (e.g., Ricco et al., 2021; and references therein). The present-day, mildly fumarolic activity is concentrated near the crater only, whereas diffuse soil emissions widely occur around the flanks of the volcano, in correspondence of structural and volcano-tectonic elements (Paolillo et al., 2016). In this area, the extensive interaction between rising magmatic fluids and groundwater has been revealed by C-He systematics of dissolved species (Federico et al., 2002).

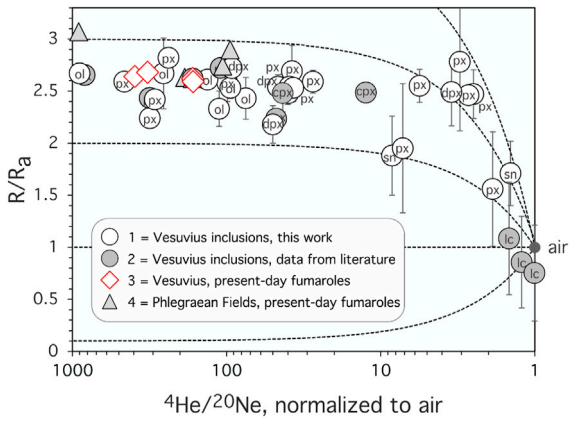

FIGURE 2
R/R_a vs. $^4He/^{20}Ne$ ratio (normalized to air) diagram for Monte Somma and Vesuvius samples. 1 = Monte Somma and Vesuvius fluid inclusions (this work); 2 = Monte Somma and Vesuvius fluid inclusions (data from literature); 3 = Vesuvius present-day fumaroles (this work); 4 = Phlegraean Fields present-day fumaroles (this work). Labels are as follows: cpx, clinopyroxene; dpx, diopside; lc, leucite; ol, olivine; px, pyroxene; sn, sanidine. The black dashed lines represent binary mixing trends between the atmospheric end-member (air) and a number of deep components with different $^3He/^4He$ signature and fixed $^4He/^{20}Ne$ ratio ($^4He/^{20}Ne$ = 10,000).

Methods

Bulk rocks samples were disaggregated and the mineral phases of interest separated with a magnet separator. Then, olivine and pyroxene crystals were carefully collected from the enriched fraction by handpicking under binocular microscope, and cleaned ultrasonically. Mineral samples successively underwent several hours under-vacuum degassing at 100–150°C to minimize air contamination on crystal surfaces. Fluid inclusions gases were then extracted by under-vacuum crushing of 1–2 g of the selected mineral fragments (grain size from 0.5 to 1 mm). The crushing efficiency was checked by verifying that the granulometric size of the powder was below 20 μm for all samples.

Both fumarolic gases and minerals were processed on a stainless-steel vacuum line equipped with cold and hot Ti getters to separate noble gases from the gaseous mixture. The extraction line was connected to both a magnetic mass spectrometer (MAP 215-50) equipped with ion counting detector, and a quadrupole mass spectrometer (Spectralab 200, VG-Micromass; Magro et al., 2003).

The $^3He/^4He$ resolution was close to 600 AMU for HD_^{3}He at 5% of the peak. Typical blanks, during the measurement period, were on the order of 0.6–1 × 10^{-9} cc STP for ^4He, with R close to air. No blank corrections were applied to R values of fumarolic gases, as the He concentration of these samples was several orders of magnitude higher than the blank (a few hundred ppm in the samples vs. ppb level concentrations in the blank). Minerals samples with He concentrations below the arbitrary threshold of five times the concentration of the blank, or with $^4He/^{20}Ne$ ratios lower than five times the air ratio were marked as "low-gas samples" in Supplementary Table S1A.

A standard volume of air at different pressures (from 1,013 to 10.13 mbar) was introduced into the extraction line and processed like the samples. The reproducibility of $^3He/^4He$ and 4/(20 + 22) mass ratios measurements on air samples was better than 10% and 5%, respectively, over the analysis period. To check He isotopes results, we performed duplicate analyses on: 1) the gas extracted from an olivine crystal from the 1983 Mt. Etna eruption ($^3He/^4He$ between 6.0 and 6.7 R_A; Marty et al., 1994); 2) the gas extracted from a pyroxene crystal of the 1906 lava flow of Vesuvius ($^3He/^4He$ = 2.61 ± 0.08 R_A; Graham et al., 1993); 3) the gas extracted from an olivine and a pyroxene crystal of the 1944 lava flow of Vesuvius ($^3He/^4He$ = 2.42 ± 0.14 R_A; Graham et al., 1993). These results are summarized in Supplementary Table S1C.

The CO_2 fraction extracted from three sanidine samples was first entrapped in a stainless-steel finger equipped with high-vacuum valves, and then analyzed in a stable isotope mass spectrometer (Europe lab) for the determination of $\delta^{13}C$ values.

Cross controls were performed to exclude C isotopic fractionation during crushing, and in particular, we verified that CO_2 could be not released by the crushing device by comparing the analytical results of "standard" samples with a quartz sample without inclusions.

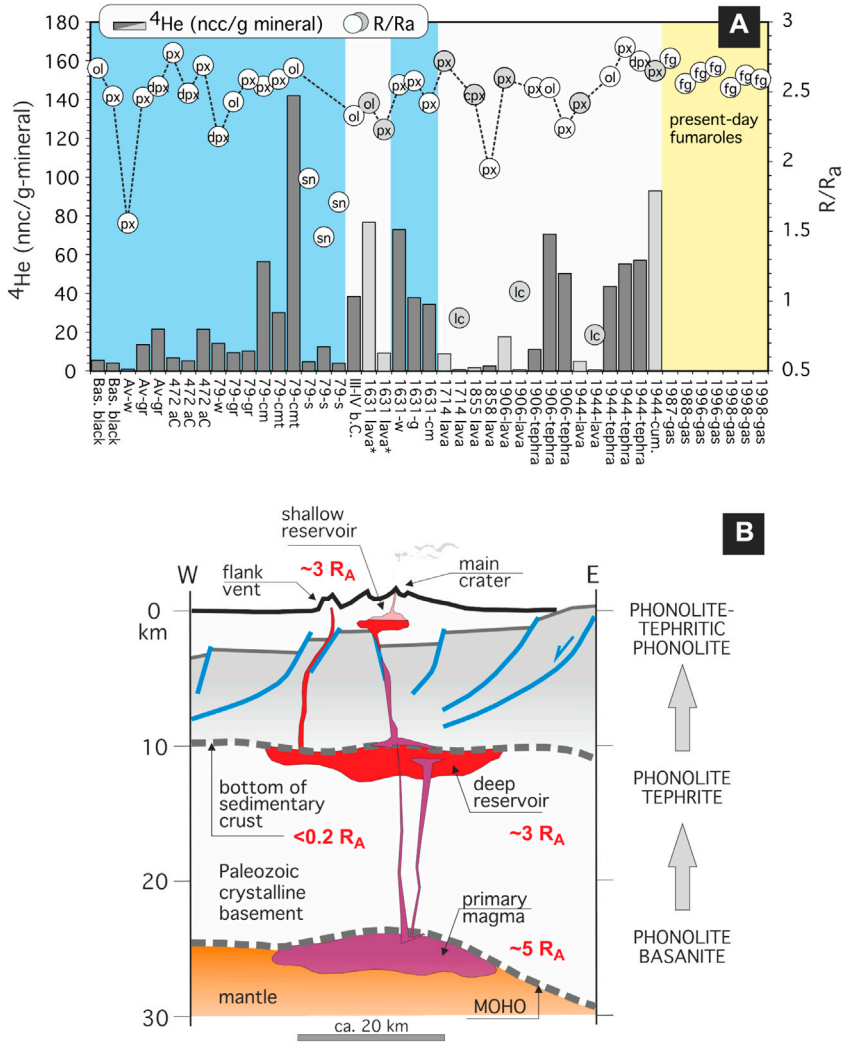

FIGURE 3
(A) R/R_A ratios (dots) and ^4He contents (bars) for different, individual eruptions (abundances are in ncc/grams of crushed mineral). Empty dots/grey bars: data from this work. Pale grey dots/pale grey bars: data after Graham et al. (1993). Leucites after Graham et al. (1993) were likely compromised by air contamination (low He concentrations, and air-like $^4He/^{20}Ne$ and $^3He/^4He$ ratios). The dashed line connects olivine and pyroxene samples. (*) 1,631 lava samples should be attributed to Medieval age activity Principe et al. (2004). Pale blue background: closed conduit activity; white background: open conduit activity; pale yellow background: present-day fumarolic activity. **(B)** Simplified conceptual model of Vesuvius, with indication of various hypothetical levels of magma accumulation and differentiation (modified after Stoppa et al., 2017). Volcanic activity is driven by the recurrent arrival of primitive mafic magma batches from the mantle into an extended deep-seated reservoir ("deep reservoir"), where homogenization occurs with resident, pre-existing magmas. From this reservoir, magmas can be directly emitted at the surface, or stored into shallow magma chambers ("shallow reservoir"), giving origin to the different eruptive styles and types of volcanic deposits of Vesuvius. Numbers in red are approximate $^3He/^4He$ signatures of different domains/reservoirs.

Results and discussion

The concentration and the isotopic composition of He, and the $^4He/^{20}Ne$ ratios of fluid and melt inclusions, and fumarolic gases analyzed for this study are reported in Supplementary Table S1A (data from this work) and Supplementary Table S1B (data from the literature).

The $^3He/^4He$ ratio (normalized to air) of olivine and cogenetic pyroxenes range between 2.25 and 2.84 R_A, in close agreement with literature values (2.2–2.7 R_A; Graham et al., 1993; Graham and Lupton, 1999). The lowest $^3He/^4He$ values measured in olivine and clinopyroxene correspond to an olivine phenocryst from white pumices of the *79 AD* Plinian eruption, the highest ones to a pyroxene of the 1944 tephra fallout. Sialic minerals, leucites from 1631 to 1944 period (*Present Vesuvius*), and sanidines from magma-skarn interface of *79 AD* eruption, show the lowest $^3He/^4He$ values, in the range 0.7–1.8 R_A. The $^3He/^4He$ values for fumarolic gases range

from 2.64 to 2.78 R_A, that are of the same range of the highest values measured in pyroclastic products of 1944 eruption. For comparison, present-day fluids discharged in the neighboring volcanic area of Phlegraean Fields (mostly in the range 2.4–3.2 R_A, up to about 3.53 R_A; Tedesco et al., 1990; Chiodini et al., 1996; Tedesco and Scarsi, 1999) partially overlap with the upper values of Vesuvius range.

The R/R_A vs. $^4He/^{20}Ne$ correlation plot (Figure 2) shows that most of samples from this work plot along mixing lines connecting the atmospheric end-member with a possible deep-seated component having a $^3He/^4He$ signature of 2–3 R_A. Samples with lowest $^4He/^{20}Ne$ values possibly suggest the mixing with a correspondingly ^3He- enriched component (up to about 3.5 R_A), but the R/R_A ratios of these samples are affected by a relatively large error due to the low amount of He extracted from minerals, and should be treated with caution. Only sialic minerals from leucites (data from literature) do not follow this trend, plotting at comparatively lower $^3He/^4He$ values (~1 R_A). Overall, all plotted values are markedly lower than most ^3He- enriched values measured in most volcanic arcs (7–9 R_A; Poreda and Craig, 1989), and the average range of subduction zones worldwide (5.4 ± 1.9 R_A; Hilton et al., 2002). The compositional resemblance between mineral separates from the considered eruptive units, and present-day fluids indicates a common magmatic source that has remained almost unchanged over time.

$^3He/^4He$ time patterns over the course of different phases of activity of the volcano (Figure 3) indicate that: 1) coexisting olivines and pyroxenes are characterized by similar R/R_A values; 2) the two generations of dark (i.e., ferrosalitic) and light (i.e., diopsidic) green pyroxenes of 1944 tephra have by similar R/R_A values; 3) grey and white pumices of the *79 AD* eruption have a significantly lower He content (one order of magnitude less) compared to cumulates of the same eruption. Vesuvius cumulates are typically dunites, wherlites, and biotite-bearing pyroxenites (e.g., Joron et al., 1987; Belkin and De Vivo, 1993), with clinopyroxene, phlogopite, biotite, apatite, plagioclase, and fosteritic olivine ($Fo_{80–90}$) as main phases; 4) the He content of olivine and pyroxene from lavas of the 1631–1944 Vesuvius phase of activity is generally lower than cogenetic tephra, despite similar $^3He/^4He$ values, whereas the products of 1944 and 1906 eruptions do not show the same differences in helium abundance; 5) R/R_A values systematically decrease from femic to sialic minerals, and sanidines are characterized by the lowest He contents, despite the presence of volatile-rich fluid inclusions (mostly CO_2-enriched).

Data from literature suggest low $^3He/^4He$ ratios and He total content typically associated with leucites can be tentatively attributed to a relatively minor efficiency in volatile trapping of this mineral during magma transport and cooling. Structural reasons (i.e., a less compact structure of sanidine crystals compared to more retentive minerals like pyroxene and olivine) can be invoked to explain gas loss phenomena affecting sanidines (Graham et al., 1993).

Data from this work point to a negligible effect (at least on He isotope distribution) of processes such as later crystallization and/or wall rock assimilation in magma chambers, because pyroxenes are not characterized by a ^4He-richer signature than coexisting olivine, as found elsewhere, where these processes are active (e.g., Hilton et al., 1995; Marty et al., 1994; Shaw et al., 2006). Overall, highest $^3He/^4He$ ratios were observed in *79 AD* cumulates, representative of the roof and the walls of the magma chambers (e.g., Cioni et al., 1995). Lowest values occur in sanidines representative of the magma-skarn interface (e.g., Fulignati et al., 1998, 2005). Noteworthy, the highest measured values of the *79 AD* paleo-fluids are comparable with both lavas and tephra emitted under open-conduit conditions during the 1631–1944 period, and present-day fumarolic discharges. *Medieval Period* lavas are phonolitic basanites, with primitive magmatic composition (i.e., the Vesuvius parental melts). These lavas have modal olivine ~10%, MgO content >7 wt%, high Mg# (83–86) and high Cr + Ni (usually in the 200–270 ppm range), which are reasonable figures for primitive, mantle-derived melts (Stoppa et al., 2017). Lavas and tephra of the *Present Period* are phono-tephrites (Figure 3B).

A tendency of $^3He/^4He$ ratios to decrease from South to North in Central-Southern Italy has been recognized long ago, based on data from present-days fluids and from fluid/melt inclusions (e.g., Sano et al., 1989; Graham et al., 1993; Marty et al., 1994; Tedesco, 1997; Martelli et al., 2004; Martelli et al., 2008). This trend has been put in relation with the geodynamic context of this part of the Mediterranean area, dominated during the last 30 Ma by the subduction of the Ionian-Adriatic plate. As a result of this subduction process, a large spatial and temporal heterogeneity of the volcanic products has been identified in the Tyrrhenian Sea region, associated with a variety of tectonic regimes (subduction-related, intraplate, rifting, e.g., among many others, Peccerillo, 2020). The noble gas signature of present-day fluids and products of Plio-Quaternary volcanism has been used to constrain the deep sources of the regional volcanism, and a 6.7–7.1 R_A range has been identified as representative of the mantle component in Southern Italy (Marty et al., 1994; Martelli et al., 2008). Crustal contamination acts in the direction of lowering the $^3He/^4He$ value of this component, and a northward increase in ^4He is generally observed in association with an increase in radiogenic Sr and Pb, and unradiogenic Nd (Martelli et al., 2008, and references therein). Based on data from Procida Island (Martelli et al., 2004), we can assume a value of 5.2 R_A for this modified mantle component in the Neapolitan area.

Low R/R_A ratios in fumarolic gases and basalt phenocrysts have been explained in many arc-related environments either by degassing of subducted sediments or continental crust, or by the assimilation of crustal material by magma stored in an intra-crustal condition (Hilton et al., 1993a; Hilton et al., 1993b). A metasomatized mantle with a He isotope signature of 2.4 ± 0.4 R_A

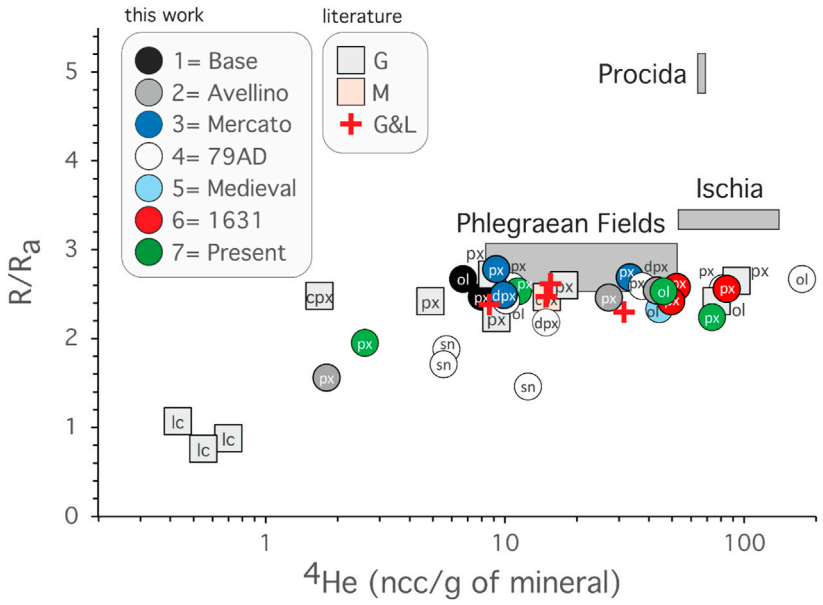

FIGURE 4
R/R_A vs. ^4He correlation diagram. Data from this work: 1 = *Pomici di Base* Plinian eruption black pumice; 2 = *Pomici di Avellino* Plinian eruption; 3 = *Pomici di Mercato* Plinian eruption; 4 = *79 AD* Plinian eruption; 5 = *Medieval Vesuvius*, Calastro lava; 6 = 1,631 small-scale Plinian eruption; 7 = *Present Vesuvius* activity. Data from literature: G = Graham et al. (1993); M = Martelli et al. (2004); G&L = Graham and Lupton (1999). The compositional fields for Phlegraean Fields, Procida and Ischia islands are also shown for comparison (data from Martelli et al., 2004). Labels as in Figure 2.

was suggested by Graham et al. (1993) for the area under study. Geochemical features of Monte Somma, Vesuvius, Phlegraean Fields, and Ischia-Procida rocks have been linked by some authors to a dominant fertile OIB-type (Ocean Island Basalts) source, probably contaminated by subducted terrigenous (Ayuso et al., 1998), or pelagic sediments (Gasperini et al., 2002). Some authors more recently claimed that the release of metasomatic fluids from the subducting Ionian-Adriatic plate could be realistically invoked to explain the low-^3He signature and the He-Sr isotope trends of Plio-Quaternary volcanism over all Central-Southern Italy (Martelli et al., 2008).

Irrespective of these hypotheses, the correlation between He amounts and R/R_A (Figure 4) highlights a relatively uniform and lower R/R_A compositional range for Vesuvius fluid/melt inclusions, compared to other volcanoes of the Campania magmatic province. In particular, a partial overlapping with R/R_A values from Phlegraean Fields is recognizable, along with a clear separation from values from Ischia (about −1 R_A) and Procida (about −2 R_A) islands. Noteworthy, all these volcanoes are only a few kilometers from each other (up to a maximum of about 40 *km* between Vesuvius and Ischia Island; Figure 1), and the observed differences cannot be easily ascribed to short-scale compositional heterogeneities of the mantle wedge.

Numerical models and laboratory experiments on site-specific rocks have emphasized the importance of crustal contamination/assimilation processes at mid-crustal depth (e.g., Iacono-Marziano et al., 2008; Iacono-Marziano et al., 2009; Pichavant et al., 2014), in agreement with the geology of the Vesuvius substratum, that comprises: 1) about 10 km of Mesozoic carbonates above the Paleozoic crystalline basement (e.g., Berrino et al., 1998; Brocchini et al., 2001; Improta and Corciulo, 2006; Di Renzo et al., 2007); 2) a possibly large (400 km^2), deep reservoir zone identified by tomography imaging at a depth of 8–10 km, well above the supposed depth of the Moho discontinuity (about 30 *km* depth; De Natale et al., 2006).

Supporting observations to this conjecture include the following points. 1) The occurrence of effective interactions between magma and rocks hosting the magma chamber, as testified by the mineralogical and geochemical characterization of cognate xenoliths and skarn fragments ejected during the different eruptions of the volcano (e.g., Barberi and Leoni, 1980; Belkin et al., 1985; Cioni et al., 1995; Fulignati et al., 1998; Gilg et al., 2001; Pascal et al., 2009; Stoppa et al., 2017). 2) The possibility that magma contamination by carbonate rocks widely occurs in the plumbing system of the volcano, as corroborated by Sr systematics (e.g., Civetta et al., 1991; Piochi et al., 2006), and quantitatively modelled by several authors (e.g., Pappalardo et al., 2004; Pappalardo and Mastrolorenzo, 2010). 3) The emission of large amounts of CO_2 generated by sidewall assimilation processes after the intrusion of alkali-basaltic magma into the sedimentary carbonate basement (Iacono-Marziano et al., 2008,

2009). In addition, the presence of a mantle source affected by the incorporation of U-rich carbonated melts has been recently advanced on the basis of data on U-Th disequilibria and Sr-Nd-Pb-U isotope systematics (Avanzinelli et al., 2018), supporting the hypothesis that interactions between carbonate-rich lithologies and magma may also occur below the local crystalline basement (Figure 3B).

However, other studies questioned the thermodynamic and geochemical grounds of conceptual models that consider extensive (i.e., >10%) country-rock assimilation processes active in the roots of Vesuvius (e.g., Bailey, 2005; Woolley et al., 2005; Bell and Kjarsgaard, 2006; Stoppa et al., 2017). Overall, despite the large amount of geoscientific data now available, there is no agreement on the actual effectiveness of carbonate assimilation, and whether the crustal component was involved at the time of melting of the source, or subsequently during the ascent of magma, or in what proportions the two processes can possibly overlap at Vesuvius.

In this complex picture, the main result of our work is to highlight the striking constancy of the He isotope signal of fluid/melt inclusions, and its close similarity to the composition of present-day gaseous emanations. This temporal stability points to a common deep source beneath the volcano, and to a mechanism of compositional homogenization that has the potential to smooth variations possibly related to the ascent of new magma batches. In the frame of the currently accepted multi-depth magma chamber (MDMC) model, this entails that magma ageing and interaction with crustal rocks could be effective in lowering the $^3He/^4He$ ratio of the primitive melt during its intra-crustal storage, most likely during the stay inside the "deep reservoir" of Figure 3B. The MDMC model foresees the presence of a shallow reservoir, possibly migrating up and down over time within the upper 8 *km* under Vesuvius (Auger et al., 2001; Scaillet et al., 2008; Pappalardo and Mastrolorenzo, 2010; and references therein), and of a large, deep-seated reservoir at about 10 *km* (De Natale et al., 2006). The longer is the storage time, the more effective is the expected re-equilibration of fluid inclusions in femic minerals like olivine and pyroxene. Even though, the efficiency of this process may also depend on additional, ill-defined parameters, such the volume ratio of the reservoir and of the recharge, the feeding frequency of the new batches of magma and their possible channeling, or any other structural element which may locally enhance or prevent magma-rock interactions. Conditions of homogenization are expected to be easily achieved for helium, due to its high diffusivity in melts. Based on data from literature (Trull and Kurz, 1993), we speculate that this homogenization can occur over a spatial scale of about 1 mm over less than about 1,060 and 2.5 years for olivine and pyroxene, respectively, at temperatures of about 965°C, with these numbers decreasing to less than 32 years and 10 days at about 1,100°C. These features are compatible with the hypothesized large range of temperatures (possibly betweeen 850 and more than 1,150°C) and residence times (from few months up to thousands of years) experienced during the magmatic history of Somma-Vesuvius (e.g., among many others, Macdonald et al., 2016; Scheibner et al., 2008; Di Renzo et al., 2007; Morgan et al., 2004).

The carbon-isotope composition of CO_2 extracted from fluid inclusions in sanidines of *79 AD* plinian syenites further supports this scenario. The $\delta^{13}C$ values of these samples ranges in fact from +1.3‰ to +2.1‰ (vs. V-PDB; Supplementary Table S2), higher than present-day crater fumarolic emissions (~0‰; Federico et al., 2002), and significantly different from both the typical mantle range ($\delta^{13}C$ = −4‰ to −7‰; Pineau et al., 2004), and the regional mantle end-member of Pantelleria Island, southern Italy ($\delta^{13}C$ = −4.2‰ to −5.8‰; Parello et al., 2000).

The positive $\delta^{13}C(CO_2)$ values of sanidines are compatible with both a decarbonation process at near magmatic temperature (>500°C; Valley, 1986) of local unmetamorphosed carbonates ($\delta^{13}C$ = −0.5‰ to +1.3‰; Fulignati et al., 2005) and/or metalimestones and metadolostones ($\delta^{13}C$ = −2‰ to +2‰; Gilg et al., 2001), and the degassing (by decompression during its ascent towards the surface) of a magma that underwent increasing carbonate assimilation at depth (e.g., Iacono-Marziano et al., 2008). Independent on the predominant mechanism between these two, in a more general sense, also the C-isotope signature of fluid inclusions supports an important involvement of crustal materials in the mechanisms of magma generation, transport and physical-chemical evolution at Vesuvius.

Conclusion

With the aim of shedding light on the precursory path of a possible future reactivation of Vesuvius, we investigated helium isotope abundances in gases extracted by crushing from melt and fluid inclusions of volcanic products of different type and age, and we compared them with present-day fumarolic discharges.

For the first time, we analyzed pyroxene, olivine and sanidine crystals from both lavas and tephra coming from Plinian and inter-Plinian eruptions. In particular, we focused on volcanic products emitted after long periods of permanence in a magmatic chamber under closed conduit condition, by paying special attention to *79 AD* Plinian eruption.

We measured $^3He/^4He$ ratios between 1.5 and 2.7 R_A, with the highest values for the deposits emitted from the *79 AD* magma chamber. This striking constancy of the $^3He/^4He$ signal, regardless of the occurrence of open vs. closed conduit conditions, and its similarity with values obtained on present-day fumarolic discharges, suggests that helium isotope patterns are consistent with an efficient mechanism of homogenization at depth, under Vesuvius.

We related this homogenization mechanism to the existence of a deep-seated (about 10 *km* b.g.l.), extended magma reservoir filled with magma rising from the mantle. This reservoir directly

fed lava flows emitted from flank vents during the *Medieval Period*, and the overlying magma chambers that produced mixed and explosive eruptions during other phases of Vesuvius history, through the ascent of pulses of mafic magma. Our data indicate that, independently of the effectiveness of carbonate assimilation processes, minor variations in $^3He/^4He$ are associated either with the ascent of magma along the upward path above the main, deep storage region, or with the formation of shallow magma chambers, as in the case of *79 AD* Plinian eruption. The hypothesis that crustal contamination/assimilation processes at mid-crustal depth played a role at Vesuvius, is corroborated by the occurrence of positive $\delta^{13}C$ values of the CO_2 extracted from fluid inclusions in sanidines of the *79 AD* event.

Overall, our data emphasize the fundamental role of the multiple-chamber structure in the magma dynamics of the Vesuvius volcanic system, and suggest that magma ponding at crustal depth could be considered a key mechanism that might have the potential to homogenize the helium isotope signal. Should this hypothesis be confirmed, the accuracy of future eruption forecasting through monitoring of $^3He/^4He$ changes in Vesuvius fumaroles would be questioned.

Data availability statement

The original contributions presented in the study are included in the article/Supplementary Material, further inquiries can be directed to the corresponding author.

Author contributions

FG: Noble gas analysis, data interpretation, writing of the original draft, review and editing; MB: Mineral separation, noble gas analysis, data interpretation, review and editing; CP: Field work, data interpretation, review and editing; GM: Conceptualization, methodology, noble gas analysis, data interpretation, writing the original draft, review and editing.

Acknowledgments

We warmly acknowledge the three reviewers for their constructive criticisms.

Conflict of interest

The authors declare that the research was conducted in the absence of any commercial or financial relationships that could be construed as a potential conflict of interest.

Publisher's note

All claims expressed in this article are solely those of the authors and do not necessarily represent those of their affiliated organizations, or those of the publisher, the editors and the reviewers. Any product that may be evaluated in this article, or claim that may be made by its manufacturer, is not guaranteed or endorsed by the publisher.

Supplementary material

The Supplementary Material for this article can be found online at: https://www.frontiersin.org/articles/10.3389/feart.2022.1011203/full#supplementary-material

References

Arnò, V., Principe, C., Rosi, M., Santacroce, R., Sbrana, A., and Sheridan, M. F. (1987). "Eruptive history," in *Somma-vesuvius*. Editor R. Santacroce (Roma: CNR Edizioni), Vol. 114, 53–104.8

Arrighi, S., Principe, C., and Rosi, M. (2001). Violent strombolian and subplinian eruption at Vesuvius during the post-1631 activity. *Bull. Volcanol.* 63, 126–150.

Auger, E., Gasparini, P., Virieux, J., and Zollo, A. (2001). Seismic evidence of an extended magmatic sill under Mt. Vesuvius. *Science* 294, 1510–1512. doi:10.1126/science.1064893

Avanzinelli, R., Casalini, M., Elliott, T., and Conticelli, S. (2018). Carbon fluxes from subducted carbonates revealed by uranium excess at Mount Vesuvius, Italy. *Geology* 46, 259–262. doi:10.1130/g39766.1

Ayuso, R. A., De Vivo, B., Rolandi, G., and Seal, R. R. (1998). Seal II R., Paone AGeochemical and isotopic (Nd-Pb-Sr-O) variations bearing on the Genesis of volcanic rocks from Vesuvius, Italy. *J. Volcanol. Geotherm. Res.* 82, 53–78. doi:10.1016/s0377-0273(97)00057-7

Bailey, D. K. (2005). Carbonate volcanics in Italy: Numerical tests for the hypothesis of lava-sedimentary limestone mixing. *Period. Mineral.* 74 (3), 205–208.

Barberi, F., Corrado, G., Innocenti, F., and Luongo, G. (1984). Phlegraean fields 1982–1984: Brief chronicle of a volcano emergency in a densely populated area. *Bull. Volcanol.* 47, 175–185. doi:10.1007/bf01961547

Barberi, F., and Leoni, L. (1980). Metamorphic carbonate ejecta from vesuvius plinian eruptions: Evidence of the occurrence of shallow magma chambers. *Bull. Volcanol.* 43, 107–120. doi:10.1007/bf02597615

Baubron, J.-C., Allard, P., Sabroux, J.-C., Tedesco, D., and Toutain, J.-P. (1991). Soil gas emanations as precursory indicators of volcanic eruptions. *J. Geol. Soc. Lond.* 148, 571–576. doi:10.1144/gsjgs.148.3.0571

Belkin, H. E., and De Vivo, B. (1993). Fluid inclusion studies of ejected nodules from plinian eruptions of Mt. Somma-Vesuvius. *J. Volcanol. Geotherm. Res.* 58, 89–100. doi:10.1016/0377-0273(93)90103-x

Belkin, H. E., De Vivo, B., Roedder, E., and Cortini, M. (1985). Fluid inclusion geobarometry from ejected Mt. Somma-vesuvius nodules. *Am. Mineral.* 70, 288–303.

Bell, K., and Kjarsgaard, B. (2006). Discussion of Peccerillo (2004) "carbonate-rich pyroclastic rocks from central apennines: Carbonatites or carbonate-rich rocks?" *Period. Mineral.* 75 (1), 85–92.

Berrino, G., Corrado, G., and Riccardi, U. (1998). Sea gravity data in the gulf of naples: A contribution to delineating the structural pattern of the vesuvian area. *J. Volcanol. Geotherm. Res.* 82, 139–150. doi:10.1016/s0377-0273(97)00061-9

Bertagnini, A., Landi, P., Rosi, M., and Vigliargio, A. (1998). The Pomici di Base plinian eruption of Somma-Vesuvius. *J. Volcanol. Geotherm. Res.* 83, 219–239. doi:10.1016/s0377-0273(98)00025-0

Brocchini, D., Principe, C., Castradori, D., Laurenzi, M., and Gorla, L. (2001). Quaternary evolution of the southern sector of the campanian plain and early somma–vesuvius activity: Insights from the trecase 1 well. *Mineral. Pet.* 73, 67–91. doi:10.1007/s007100170011

Burnard, P. (2013). *The noble gases as geochemical tracers*. Berlin Heidelberg: Springer-Verlag.

Chiodini, G., Cioni, R., Magro, G., Marini, L., Panichi, C., Raco, B., et al. (1996). Chemical and isotopic variations of bocca grande fumarole (solfatara volcano, phlegrean fields). *Acta Vulcanol.* 8, 228–232.

Chiodini, G., Marini, L., and Russo, M. (2001). Geochemical evidence for the existence of high-temperature hydrothermal brines at Vesuvio volcano, Italy. *Geochim. Cosmochim. Acta* 65, 2129–2147. doi:10.1016/s0016-7037(01)00583-x

Cioni, R., Civetta, L., Marianelli, P., Metrich, N., Santacroce, R., and Sbrana, A. (1995). Compositional layering and syn-eruptive mixing of a periodically refilled shallow magma chamber: The AD 79 plinian eruption of vesuvius. *J. Petrology* 36, 739–776. doi:10.1093/petrology/36.3.739

Cioni, R., D'Oriano, C., and Bertagnini, A. (2008). Fingerprinting ash deposits of small scale eruptions by their physical and textural features. *J. Volcanol. Geotherm. Res.* 177, 277–287. doi:10.1016/j.jvolgeores.2008.06.003

Cioni, R., Sulpizio, R., and Garruccio, N. (2003). Variability of the eruption dynamics during a subplinian event: The greenish pumice eruption of somma-vesuvius (Italy). *J. Volcanol. Geotherm. Res.* 124, 89–114. doi:10.1016/s0377-0273(03)00070-2

Civetta, L., Galati, R., and Santacroce, R. (1991). Magma mixing and convective compositional layering within the Vesuvius magma chamber. *Bull. Volcanol.* 53, 287–300. doi:10.1007/bf00414525

De Natale, G., Troise, C., Pingue, F., Mastrolorenzo, G., and Pappalardo, L. (2006). The Somma–Vesuvius volcano (southern Italy): Structure, dynamics and hazard evaluation. *Earth. Sci. Rev.* 74, 73–111. doi:10.1016/j.earscirev.2005.08.001

De Vivo, B., Petrosino, P., Lima, A., Rolandi, G., and Belkin, H. E. (2010). Research progress in volcanology in the neapolitan area, southern Italy: A review and some alternative views. *Mineral. Pet.* 99, 1–28. doi:10.1007/s00710-009-0098-6

B. De Vivo, R. Scandone, and R. R. Trigila (Editors) (1993). *Mount Vesuvius: Special issue of J. Volcanol. Geotherm. Res.*, Vol. 58, 1–381.

Di Renzo, V., Di Vito, M. A., Arienzo, I., Carandente, A., Civetta, L., D'Antonio, M., et al. (2007). Magmatic history of Somma–Vesuvius on the basis of new geochemical and isotopic data from a deep borehole (Camaldoli della Torre). *J. Petrology* 48 (4), 753–784. doi:10.1093/petrology/egl081

Federico, C., Aiuppa, A., Allard, P., Bellomo, S., Jean-Baptiste, P., Parello, F., et al. (2002). Magma-derived gas influx and water-rock interactions in the volcanic aquifer of Mt. Vesuvius, Italy. *Geochim. Cosmochim. Acta* 66, 963–981. doi:10.1016/s0016-7037(01)00813-4

Frondini, F., Chiodini, G., Caliro, S., Cardellini, S., Granieri, D., and Ventura, G. (2004). Diffuse CO_2 soil degassing at Vesuvio, Italy. *Bull. Volcanol.* 66, 642–651. doi:10.1007/s00445-004-0346-x

Fulignati, P., Gioncada, A., and Sbrana, A. (1998). The 79AD vesuvius magma chamber: A SEM-EDS study of doughter minerals in hypersaline fluid inclusions from cognate syenites. *N. Jb. Mineral. Abh.* 9, 403–416.

Fulignati, P., Panichi, C., Sbrana, A., Caliro, S., Gioncada, A., and Del Moro, A. (2005). Skarn formation at the walls of the 79AD magma chamber of Vesuvius (Italy): Mineralogical and isotopic constraints. *njma.* 181, 53–66. doi:10.1127/0077-7757/2005/0181-0007

Gasperini, D., Blichert-Toft, J., Bosch, D., Del Moro, A., Macera, P., and Albarède, F. (2002). Upwelling of deep mantle material through a plate window: Evidence from the geochemistry of Italian basaltic volcanics. *J. Geophys. Res.* 107 (B12), ECV 7-1–ECV 7-19. doi:10.1029/2001jb000418

Gilg, H. A., Lima, A., Somma, R., Belkin, H. E., De Vivo, B., and Ayuso, R. A. (2001). Isotope geochemistry and fluid inclusion study of skarns from Vesuvius. *Mineral. Pet.* 73, 145–176. doi:10.1007/s007100170015

Graham, D. W., Allard, P., Kilburn, C. R. J., Spera, F. J., and Lupton, J. E. (1993). Helium isotopes in some historical lavas from Mount Vesuvius. *J. Volcanol. Geotherm. Res.* 58, 359–366. doi:10.1016/0377-0273(93)90117-a

Graham, D. W., and Lupton, J. E. (1999). Helium isotopes in historical lavas from Mount Vesuvius. *Earth Planet. Sci. Lett.* 174, 241–244. doi:10.1016/s0012-821x(99)00268-x

Hilton, D. R., Barling, J., and Wheller, G. E. (1995). Effect of shallow-level contamination on the helium isotope systematics of ocean-island lavas. *Nature* 373, 330–333.

Hilton, D. R., Fischer, T. P., and Marty, B. (2002). "Noble gases and volatile recycling at subduction zones," in *Noble gases in geochemistry and cosmochemistry*. Editors D. P. Porcelli, C. J. Ballentine, and R. Wieler (Washington, DC: Reviews in Mineralogy and Geochemistry), Vol. 47, 319–370.

Hilton, D. R., Hammerschmidt, K., Loock, G., and Friedrichsen, H. (1993a). Helium and argon isotope systematics of the central Lau Basin and Valu Fa Ridge: Evidence of crust/mantle interactions in a back-arc basin. *Geochim. Cosmochim. Acta* 57, 2819–2841. doi:10.1016/0016-7037(93)90392-a

Hilton, D. R., Hammerschmidt, K., Teufel, S., and Friedrichsen, H. (1993b). Helium isotope characteristics of Andean geothermal fluids and lavas. *Earth Planet. Sci. Lett.* 120, 265–282. doi:10.1016/0012-821x(93)90244-4

Iacono-Marziano, G., Gaillard, F., and Pichavant, M. (2008). Limestone assimilation by basaltic magmas: An experimental re-assessment and application to Italian volcanoes. *Contrib. Mineral. Pet.* 155, 719–738. doi:10.1007/s00410-007-0267-8

Iacono-Marziano, G., Gaillard, F., Scaillet, B., Pichavant, M., and Chiodini, G. (2009). Role of non-mantle CO_2 in the dynamics of volcano degassing: The Mount Vesuvius example. *Geology* 37, 319–322. doi:10.1130/g25446a.1

Improta, L., and Corciulo, M. (2006). Controlled source nonlinear tomography: A powerful tool to constrain tectonic models of the southern apennines orogenic wedge, Italy. *Geol.* 34, 941–944. doi:10.1130/g22676a.1

Joron, J. L., Metrich, N., Rosi, M., Santocroce, R., and Sbrana, A. (1987). "Chemistry and petrography," in *Somma-vesuvius*. Editor R. Santacroce (Rome, Italy: CNR, Quaderni De La Ricerca Scientifica), Vol. 114, 105–174.

Kurz, M. D., JenkinsSchilling, W. J, J. G., and Hart, S. R. (1982). Helium isotopic variations in the mantle beneath the central North Atlantic Ocean. *Earth Planet. Sci. Lett.* 58, 1–14. doi:10.1016/0012-821x(82)90099-1

Macdonald, R., Baginski, B., Rolandi, G., De Vivo, B., and Kopczynska, A. (2016). Petrology of parasitic and eccentric cones on the flanks and base of Somma-Vesuvius. *Min. Pet.* 110, 65–85. doi:10.1007/s00710-015-0410-6

Magro, G., Ruggieri, G., Gianelli, G., Bellani, S., and Scandiffio, G. (2003). Helium isotopes in paleofluids and present-day fluids of the Larderello geothermal field: Constraints on the heat source. *J. Geophys. Res.* 108, ECV 3-1–ECV 3-12. doi:10.1029/2001jb001590

Mamyrin, B. A., and Tolstikhin, I. N. (1984). *Helium isotopes in nature*. Amsterdam, Netherlands: Elsevier, 273.

Martelli, M., Nuccio, P. M., Stuart, F. M., Burgess, R., Ellam, R. M., and Italiano, F. (2004). Helium–strontium isotope constraints on mantle evolution beneath the Roman Comagmatic Province, Italy. *Earth Planet. Sci. Lett.* 224, 295–308. doi:10.1016/j.epsl.2004.05.025

Martelli, M., Nuccio, P. M., Stuart, F. M., Di Liberto, V., and Ellam, R. M. (2008). Constraints on mantle source and interactions from He-Sr isotope variation in Italian Plio-Quaternary volcanism. *Geochem. Geophys. Geosyst.* 9, Q02001. doi:10.1029/2007GC001730

Marty, B., Trull, T., Lussiez, P., Basile, I., and Tanguy, J. C. (1994). He, Ar, O, Sr and Nd isotope constraints on the origin and evolution of Mount Etna magmatism. *Earth Planet. Sci. Lett.* 126, 23–39. doi:10.1016/0012-821x(94)90240-2

Mele, D., Sulpizio, R., Dellino, P. F., and La Volpe, L. (2011). Stratigraphy and eruptive dynamics of a pulsating plinian eruption of somma-vesuvius: The Pomici di Mercato (8900 years B.P.). *Bull. Volcanol.* 73, 257–278. doi:10.1007/s00445-010-0407-2

Montone, P., Amato, A., and Pondrelli, S. (1999). Active stress map of Italy. *J. Geophys. Res.* 104, 25595–25610. doi:10.1029/1999jb900181

Morgan, D. J., Blake, S., Rogers, N. W., DeVivo, B., Rolandi, G., Macdonald, R., et al. (2004). Time scales of crystal residence and magma chamber volume from modelling of diffusion profiles in phenocrysts: Vesuvius 1944. *Earth Planet. Sci. Lett.* 222, 933–946. doi:10.1016/j.epsl.2004.03.030

Ozima, M., and Podosek, F. A. (1983). *Noble gas geochemistry*. Cambridge: Cambridge University Press.

Paolillo, A., Principe, C., Bisson, M., Gianardi, R., Giordano, D., and La Felice, S. (2016). Volcanology of the southwestern sector of Vesuvius volcano, Italy. *J. Maps* 12, 425–440. doi:10.1080/17445647.2016.1234982

Pappalardo, L., and Mastrolorenzo, G. (2010). Short residence times for alkaline Vesuvius magmas in a multi-depth supply system: Evidence from geochemical and textural studies. *Earth Planet. Sci. Lett.* 296, 133–143. doi:10.1016/j.epsl.2010.05.010

Pappalardo, L., Piochi, M., and Mastrolorenzo, G. (2004). The 3800 yr BP–1944 AD magma plumbing system of somma-vesuvius: Constraints on its behaviour and present satte through a review of isotope data. *Ann. Geophys.* 47, 1363–1375.

Parello, F., Allard, P., D'Alessandro, W., Federico, C., Jean-Baptiste, P., and Catani, O. (2000). Isotope geochemistry of Pantelleria volcanic fluids, sicily channel rift: A mantle volatile end-member for volcanism in southern europe. *Earth Planet. Sci. Lett.* 180, 325–339. doi:10.1016/s0012-821x(00)00183-7

Pascal, M. L., Di Muro, A., Fonteilles, M., and Principe, C. (2009). Zirconolite and calzirtite in banded fosterite-spinel-calcite skarn ejecta from vesuvius 1631 eruption: Inferences for the magma-wallrock interactions. *Mineral. Mag.* 73 (1), 149–172.

Peccerillo, A. (2020). "Campania volcanoes: Petrology, geochemistry, and geodynamic significance." in *Vesuvius, campi flegrei, and campanian volcanism*. Editor B. De Vivo, H. E. Belkin, and G. Rolandi (Amsterdam, Netherlands: Elsevier), 79–120.

Pichavant, M., Scaillet, B., Pommier, A., Iacono-Marziano, G., and Cioni, R. (2014). Nature and evolution of primitive vesuvius magmas: An experimental study. *J. Petrology* 55, 2281–2310. doi:10.1093/petrology/egu057

Pineau, F., Shilobreeva, S., Hekinian, R., Bideau, D., and Javoy, M. (2004). deep-sea explosive activity on the mid-atlantic ridge near 34°50′N: A stable isotope (C, H, O) study. *Chem. Geol.* 211, 159–175. doi:10.1016/j.chemgeo.2004.06.029

Piochi, M., Ayuso, R. A., De Vivo, B., and Somma, R. (2006). Crustal contamination and crystal entrapment during polybaric magma evolution at Mt. Somma–Vesuvius volcano, Italy: Geochemical and Sr isotope evidence. *Lithos* 86, 303–329. doi:10.1016/j.lithos.2005.05.009

Porcelli, D., Ballentine, C. J., and Wieler, R. (2002). An overview of noble gas geochemistry and cosmochemistry. *Rev. Mineralogy Geochem.* 47, 1–19. doi:10.2138/rmg.2002.47.1

Poreda, R., and Craig, H. (1989). Helium isotope ratios in circum-Pacific volcanic arcs. *Nature* 338, 473–478. doi:10.1038/338473a0

Principe, C., Paolillo, A., La Felice, S., and Arrighi, S. (2021). "Forma vesuvii-2 volcanic morphology at the time of the 79AD plinian eruption," in *Physis*. Editor L. Olschki, 289–303. Firenze. 2021/1-2 (LVI).

Principe, C., Tanguy, J. C., Arrighi, S., Paiotti, A., Le Goff, M., and Zoppi, U. (2004). Chronology of Vesuvius' activity from AD 79 to 1631 based on archeomagnetism of lavas and historical sources. *Bull. Volcanol.* 66, 703–724. doi:10.1007/s00445-004-0348-8

Ricco, C., Petrosino, S., Aquino, I., Cusano, P., and Madonia, P. (2021). Tracking the recent dynamics of Mt. Vesuvius from joint investigations of ground deformation, seismicity and geofluid circulation. *Sci. Rep.* 11, 965. doi:10.1038/s41598-020-79636-w

M. Rosi and A. Sbrana (Editors) (1987). *Phlegraean fields* (Roma: Collana Quaderni della Ricerca Scientifica, Consiglio Nazionale delle Ricerche), 175.

Sano, Y., Wakita, H., Italiano, F., and Nuccio, M. P. (1989). Helium isotopes and tectonics in southern Italy. *Geophys. Res. Lett.* 16, 511–514. doi:10.1029/gl016i006p00511

Scaillet, B., Pichavant, M., and Cioni, R. (2008). Upward migration of Vesuvius magma chamber over the past 20, 000 years. *Nature* 455, 216–219. doi:10.1038/nature07232

Scandone, P. (1979). Origin of the Tyrrhenian Sea and calabrian arc. *Boll. Soc. Geol. It.* 98, 27–34.

Scheibner, B., Heumann, A., and Wörner, C. L. (2008). Crustal residence times of explosive phonolite magmas: U–Th ages of magmatic Ca-garnets of Mt. Somma-vesuvius (Italy). *Earth Planet. Sci. Lett.* 276, 293–301. doi:10.1016/j.epsl.2008.09.028

Shaw, A. M., Hilton, D. R., Fisher, T. P., Walker, J. A., and de Leew, G. A. M. (2006). Helium isotope variations in mineral separates from Costa Rica and Nicaragua: Assessing crustal contributions, timescale variations and diffusion-related mechanisms. *Chem. Geol.* 230, 124–139. doi:10.1016/j.chemgeo.2005.12.003

Stoppa, F., Principe, C., Schiazza, M., Liu, Y., Giosa, P., and Crocetti, S. (2017). Magma evolution inside the 1631 Vesuvius magma chamber and eruption triggering. *Open Geosci.* 9, 24–52. doi:10.1515/geo-2017-0003

Tedesco, D., Allard, P., Sano, Y., Wakita, H., and Pece, R. (1990). Helium-3 in subaerial and submarine fumaroles of Campi Flegrei caldera, Italy. *Geochim. Cosmochim. Acta* 54, 1105–1116. doi:10.1016/0016-7037(90)90442-n

Tedesco, D. (1997). Systematic variations in the 3He/4He ratio and carbon fumarolic fluids from active volcanic areas in Italy: Evidence for radiogenic 4He and crustal carbon addition by the subducting African plate? *Earth and Planetary Science Letters* 151, 255–269.

Tedesco, D., and Scarsi, P. (1999). Chemical (He, H_2, CH_4, Ne, Ar, N_2) and isotopic (He, Ne, Ar, C) variations at the solfatara crater (southern Italy): Mixing of different sources in relation to seismic activity. *Earth Planet. Sci. Lett.* 171, 465–480. doi:10.1016/s0012-821x(99)00137-5

Trull, T. W., and Kurz, M. D. (1993). Diffusivity of ^{3}He and ^{4}He in olivine and clinopyroxene at magmatic and mantle temperatures. *Geochim. Cosmochim. Acta* 57, 1313–1324. doi:10.1016/0016-7037(93)90068-8

Turco, E., Schettino, A., Pierantoni, P. P., and Santarelli, G. (2006). "The Pleistocene extension of the Campania plain in the framework of the southern tyrrhenian tectonic evolution: Morphotectonic analysis, kinematic model and implications for volcanism," in *Developments in volcanology*. *Developments in volcanology*. Editor B. De Vivo, Vol. 9, 27–51.

Valley, J. W. (1986). "Stable isotope geochemistry of metamorphic rocks," in *Stable isotopes in high temperature geological processes*. *Reviews in mineralogy*. Editors J. W. Valley, H. P. TaylorJr., and J. R. O'Neil, Vol. 16, 445–489.

Woolley, R. A., Bailey, D. K., Castorina, F., Rosatelli, G., Stoppa, F., and Wall, F. (2005). Reply to: "Carbonate-rich pyroclastic rocks from central apennines: Carbonatites or carbonated rocks? A commentary". A. Peccerillo. *Period. Mineral.* 74 (3), 183–194.

frontiers | Frontiers in Earth Science

TYPE Original Research
PUBLISHED 21 December 2022
DOI 10.3389/feart.2022.1021550

OPEN ACCESS

EDITED BY
Maoliang Zhang,
Tianjin University, China

REVIEWED BY
Peiyue Li,
Chang'an University, China
Yong Xiao,
Southwest Jiaotong University, China

*CORRESPONDENCE
Xiaocheng Zhou,
zhouxiaocheng188@163.com
Yang Li,
liyangxbdx@163.com

SPECIALTY SECTION
This article was submitted to Geochemistry, a section of the journal Frontiers in Earth Science

RECEIVED 17 August 2022
ACCEPTED 07 November 2022
PUBLISHED 21 December 2022

CITATION
Wang J, Zhou X, He M, Li J, Dong J, Tian J, Yan Y, Li Y, Liu K and Li Y (2022), Hydrogeochemical origin and circulation of spring waters along the Karakorum fault, Western Tibetan Plateau: Implications for interaction between hydrosphere and lithosphere. *Front. Earth Sci.* 10:1021550. doi: 10.3389/feart.2022.1021550

Hydrogeochemical origin and circulation of spring waters along the Karakorum fault, Western Tibetan Plateau: Implications for interaction between hydrosphere and lithosphere

Jingli Wang[1,2], Xiaocheng Zhou[3]*, Miao He[3], Jingchao Li[3], Jinyuan Dong[3], Jiao Tian[3], Yucong Yan[3], Ying Li[3], Kaiyi Liu[4] and Yang Li[1]*

[1]State Key Laboratory of Continental Dynamics, Department of Geology, Northwest University, Xi'an, China, [2]School of Petroleum Engineering and Environmental Engineering, Yan'an University, Yan'an, China, [3]United Laboratory of High-Pressure Physics and Earthquake Science, Institute of Earthquake Forecasting, CEA, Beijing, China, [4]The University of Sydney Business School, University of Sydney, Sydney, NSW, Australia

Geochemical investigation on the origin and circulation of geothermal water is crucial for better understanding the interaction between hydrosphere and lithosphere. Previous studies on the Himalayan geothermal belt mainly distributed in the central and eastern Tibetan Plateau. In this study, water samples (8 hot springs and 1 cold spring) from the Karakorum fault (KKF) zone of western Tibetan Plateau were analyzed for the hydrogeochemical characteristics and isotopic compositions. Three types of spring water along the KKF were classified on basis of ionic concentration and Sr isotopic composition: type A water (HCO_3–Mg or Ca), type B water (HCO_3–Na) and type C water (Cl–Na). Type A water is originated from the infiltration of meteoric water and the dissolution of silicate/evaporite. Type B water is mainly leached from the metamorphic and granitoid rocks. Type C water is formed by the dissolution of chlorides and sulphates. δD and $\delta^{18}O$ isotopes indicate that geothermal fluid along the fault zone was mainly recharged by local precipitation. Moreover, reservoir temperatures of 144.2–208.6°C were estimated by the silica–enthalpy mixing model, and the thermal waters have a relatively deep circulation depth (≥ 7.0 km). Meanwhile, the thermal waters are characterized by extremely high Li, B, Fe and As concentrations and earthquakes frequently happened in the vicinity, suggesting that the KKF is a deep and active fault, which also indicates that the thermal fluids are strongly associated with seismicity. Therefore, thermal fluid can potentially be used as continuous monitoring sites for earthquake forecasting.

KEYWORDS

hydrogeochemistry, water-rock interaction, circulation model, spring along Karakorum fault, western Tibetan Plateau

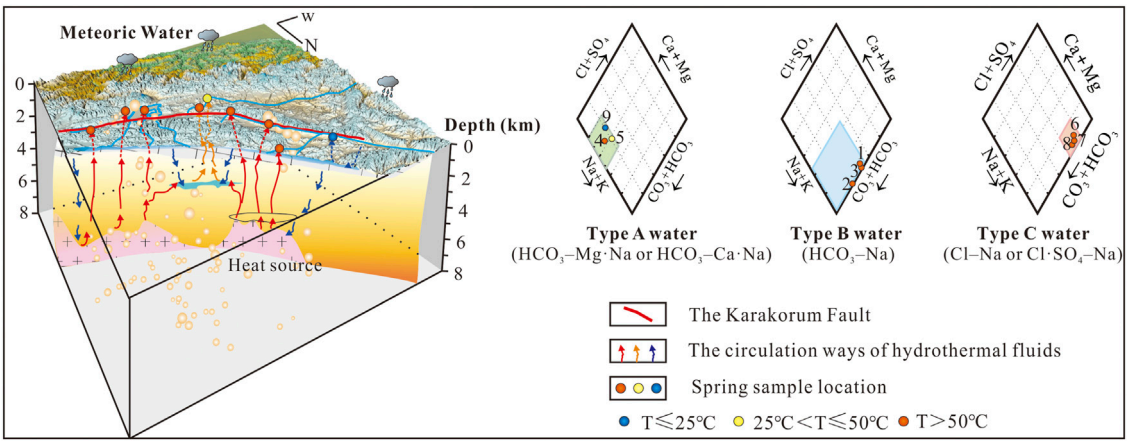

GRAPHICAL ABSTRACT

1 Introduction

Geothermal energy is one of the most competitive resources with the potential to substitute fossil fuels in the future (Wang, 2009; Vakulchuk et al., 2020). Hot spring water, a geothermal resource that develops mostly along faults, acts as a window of deeper and shallower crusts, and is closely related to deep thermal systems (Bianchi et al., 2010; Guo, 2012). The geochemical characterisation of geothermal water not only contributes to the exploration and development of geothermal resources but also provides information about the geothermal reservoirs (Guo et al., 2014a, b; Brahim et al., 2020), the tectonic setting, activity and penetration depth of related faults (Du et al., 2005; Zhao et al., 2014; Daniele et al., 2020). New findings have been made in understanding the genesis type, recharge source, reservoir temperature, circulation depth and formation mechanisms of geothermal water and even some earthquake precursor signals (Skelton et al., 2019; Barberio et al., 2020; Franchini et al., 2021; Yan et al., 2022). In addition, geothermal water is one of the important windows to study the interaction between the lithosphere and hydrosphere.

The India-Eurasia continental collision, ongoing since ca. 60–50 Ma (Molnar and Tapponnier, 1975; Hu et al., 2015; Zhu et al., 2021), has created the Tibetan Plateau. Many medium- to high-temperature geothermal resources have developed in the Tibetan Plateau (Figure 1A) located in the Himalayas geothermal belt, which is an important part of the Mediterranean–Himalayas geothermal belt (Guo, 2012) and provides ideal systems for studying the deep-time interaction between the lithosphere and hydrosphere. Systematic geological works, including geochemical investigations and quantitative assessment of the geothermal reservoirs, have been conducted in the central and eastern Tibetan Plateau, such as the Yangyi geothermal system (The Geothermal Geological Team of Tibet, 1990; Guo et al., 2009; Yuan et al., 2014), the Rehai geothermal system (Shangguan and Huo, 2002; Guo et al., 2014a, b), the Yangbajing geothermal system (Guo et al., 2008, 2010; Yuan et al., 2014) and the Kangding–Litang–Batang geothermal belt (Tang et al., 2017). Moreover, it has been verified that the magma chamber or molten granite is the heat source for most of these high-temperature (> 150°C) hydrothermal systems (Nelson et al., 1996; Guo and Wang, 2012). However, due to location approaching the disputed international boundaries at a high elevation, relatively few systematic studies have been conducted on the high-temperature geothermal fields with non-volcanogenic heat sources in the western Tibetan Plateau (Wu et al., 2011; He et al., 2016; Wang et al., 2016).

In this contribution, the interaction of deep lithosphere and hydrosphere was discussed by the study of thermal and cold springs along the Karakorum fault (KKF) in the western Tibetan Plateau. Systematical analyses, including physicochemical characteristics (including pH and electrical conductivity), hydrochemical characteristics (anion, cation and trace element concentrations), stable hydrogen and oxygen isotopic compositions and Sr isotopic compositions, were conducted to construct a model of the origin and circulation for the geothermal water. The petrological characteristics and penetration depth of the KKF were also analyzed to identify whether high-temperature geothermal fluids in the study area were heated by magma or other heat source. About the geochemical study of spring waters along the KKF, it can be used to estimate the circulation depth of geothermal fluids that have closed relationships to earthquake distribution. So we speculate that geothermal fluids can be considered as potential continuous monitoring sites for forecasting shallow-focus earthquakes and compensating for the shortcomings of conventional fluid seismic observations in the future.

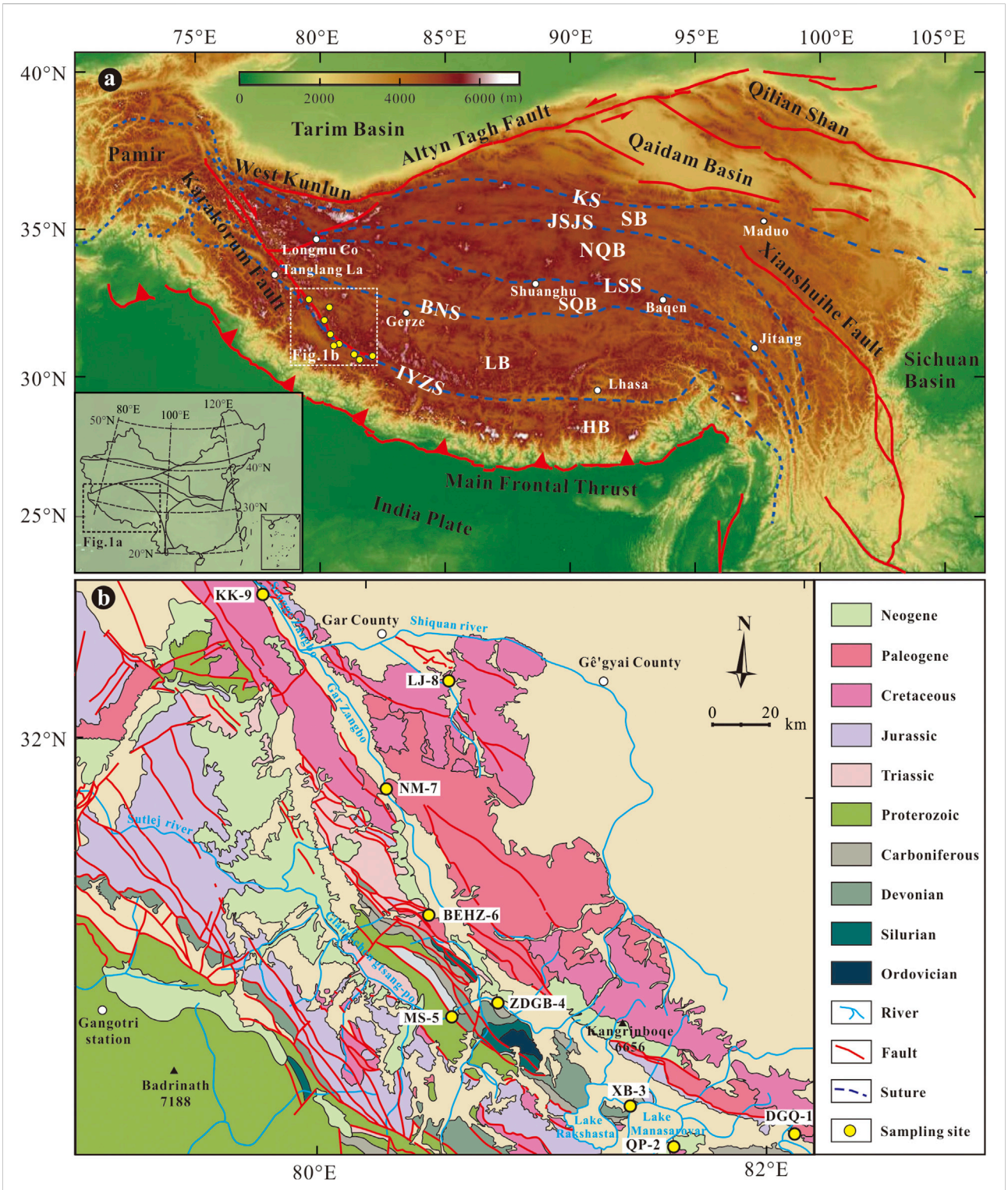

FIGURE 1
(A) Tectonic framework of the Tibet and surrounding regions (modified after Lu et al., 2022); **(B)** Geological map with sampling sites of the study area. Abbreviations: HB- Himalayan block; LB- Lhasa block; SQB- South Qiangtang block; NQB- North Qiangtang block; SB- Songpan-Ganze block; KS- Kunlun suture; JSJS- Jinshajiang suture; LSS- Longmu Co-Shuanghu suture; BNS- Bangong Co-Nujiang suture; IYZS- India-Yarlung Zangbo suture.

2 Hydrogeologic and geological setting

The KKF is characterised by a highland monsoon climate, with an elevation range of 4,200–4,900 m, average annual temperature of 0.4°C and average annual precipitation of 74.8 mm/yr (Wu et al., 2011). The annual solar radiation in the town of Shiquanhe is as high as 8.16×10^{15} J/m^2, which is the highest value in Tibet. Geologically, the KKF is a dextral strike–slip active fault that trends NW–SE, stretching for more than 1,000 km from the Pamir to the Indus–Tsangpo suture zone. South of Shiquanhe, the southeastern segment of the KKF extends along the Indus–Tsangpo suture zone eastward of the Kailas range for at least 150 km and becomes parallel to the Indus suture (Lacassin et al., 2004). Its contemporary and late Pleistocene slip rates are in dispute [InSAR: 1 ± 3 mm/yr (Wright et al., 2004); GPS: ≈3–5 mm/yr (Kundu et al., 2014; Z. Tian et al., 2019); ≈11 mm/yr (Banerjee and Bürgmann, 2002)]. Although investigations on the penetration depth of the KKF have been carried out (Rai et al., 2006; Priestley et al., 2008; Nábělek et al., 2009; Zhao et al., 2010; Klemperer et al., 2013; He et al., 2016), whether the KKF access to the mantle depth remain unclear.

Strata that outcrop in the KKF area are mainly covered by sediments, including Holocene (Qh^{alp}), Pleistocene (Qp), Paleogene (N_2w), Oligocene to early Miocene (E_3N_1r) and Middle Cretaceous (K_2s) that consist of carbonate breccia, calcareous sinter, gravels, sandstones, mudstones and shales. In addition, Magmatic rocks in the study area mainly contain Upper Cretaceous granodiorite ($K_2\gamma\delta$), the Lower Cretaceous (K_1d and K_1l), the Upper Triassic mafic rocks ($T_3M\sum$) and complex rocks ($T_3M\sum m$), the Lower Neocene monzogranite ($\eta\gamma N_1$). Overall, the most widespread strata in the KKF are Cretaceous. Lower Cretaceous shallow marine and terrestrial deposits intruded by Gangdese granitoids with predominantly Cretaceous and rarely Cenozoic ages (Schwab et al., 2004), unconformably overlie ophiolitic mélange and locally Permian metasediments (Kapp et al., 2003). Strong Cretaceous and Cenozoic magmatism and metamorphism of the KKF, which are related to an Andean-type margin along the southern margin of Asia (Schwab et al., 2004), offer the required conditions for the development of abundant large-scale geothermal resources along the KKF. The fault provides channels for the circulation of geothermal fluids (Sachan et al., 2016), facilitating water–rock interaction and convection of heat (Wang et al., 2016).

Some previous studies have depended on geological and geophysical data to examine geothermal water along the KKF. However, a few geochemical investigations on the hydrothermal waters of the KKF field have been conducted and examined the ion origin and phase equilibrium of minerals, the mixing of thermal and cold waters, and the geothermal reservoir temperature (e.g., Wu et al., 2011; Wang et al., 2016). No works have been reported about the circulation depth and circulation models of the geothermal water along the KKF.

3 Methodology

3.1 Sampling and analytical procedures

A total of nine samples were obtained from eight thermal springs (DGQ-1, QP-2, XB-3, ZDGB-4, MS-5, BEHZ-6, NM-7, LJ-8) and the Kalakoram cold spring (KK-9), distributing along the KKF of the western Tibetan Plateau Figure 1B. The samples were collected for chemical and isotope analyses on August 2–4, 2019, except for the sample from the Kalakunlun Mountain spring, which was collected on 8 October 2020, and the sample from sample ZDGB-4, which was collected on 28 September 2021. The longitude, latitude, elevation, lithology, and aquifer type of each sampling site were recorded during the sampling. The physicochemical parameters of the thermal water samples, including pH and electrical conductivity (EC), were measured on site using a Thermo Orion 4-Star Meter, which was calibrated before sampling. The water temperature was determined using a YF-160 thermometer, and the measurement error was estimated to be within 0.1°C. The water samples were collected by underwater sampling and were stored in 50-mL polyethene (PE) bottles that had been pre-cleaned by immersion in ultrapure water for 3 days, oscillation in an ultrasonic oscillator for 15 min, rinsing in ultrapure water and drying in an oven. One vial was an unacidified sample used for anion analyses, and another vial was acidified with analytical reagent (AR) for cation and trace element analyses.

Chemical analysis of the spring water samples was performed in the Key Laboratory of the Earthquake Forecasting Institute of the China Earthquake Administration. The concentrations of cations (K^+, Na^+, Mg^{2+}, Ca^{2+}, Li^+) and anions (F^-, Cl^-, NO_3^- and SO_4^{2-}) in the water samples were determined using an ion chromatography system (Dionex ICS-900) and an autosampler (AS40) with a detection limit of 0.01 mg/L (Chen et al., 2015). The HCO_3^- and CO_3^{2-} concentrations of the samples were measured with a ZDJ-3D titrator with 0.05 mol/L HCl, using methyl orange and phenolphthalein indicators. For the purpose of calibration of the chromatography, the standard samples were measured before and after measurement of each batch of water samples. The deviation of the measurements was within ± 1%.

The concentrations of trace elements were detected by inductively coupled plasma mass spectrometry (ICP-MS, Element XR) in the Analytical Laboratory of the Beijing Research Institute of Uranium Geology (Knappett et al., 2018). Sr isotope compositions were determined using a thermoionisation mass spectrometer (TIMS, IsotopX Phenix), largely according to the experimental procedures described by Wang et al. (2014). Silica (SiO_2) concentrations were analysed using an inductively coupled plasma optical emission spectrometer (ICP-OES) (Perkin-Elmer Optima 5300DV, United States). The O and H isotopic compositions of the water samples were

determined using a Thermo-Finnigan MAT253 mass spectrometer. The O–H isotopic results are reported in delta (δ) notation *versus* the international Vienna Standard Mean Ocean Water (VSMOW) and expressed in per-mile percentages. The precisions were better than ± 0.2‰ and ± 1‰ for $\delta^{18}O$ and δD, respectively (Liu et al., 2013).

3.2 Hydrochemistry and isotopes

The spring waters were classified according to the Schukarev classification system. The total equivalents of cations and anions were taken to be 100%, and ions greater than 25% of the milligram equivalents were considered in the classification. Piper (1944) proposed an effective tool (Piper diagram) based on a multiple-trilinear diagram with respect to sources of hydrochemical constituents and water–rock interaction processe. A $Cl–SO_4–HCO_3$ ternary diagram was used to determine whether there is a volatile magmatic influence on the high-temperature geothermal fluid (Giggenbach, 1988). The triangular Na–K–Mg diagram can be used to evaluate the equilibrium between hot water and rocks, which can further distinguish three states of water: fully equilibrated water, partially equilibrated (mixed) water and immature water.

Stable oxygen and hydrogen isotopes can be used to calculate the recharge elevation of meteoric waters because of their relationship with altitude (Craig, 1961), and to trace the origin of hydrothermal waters (Giggenbach et al., 1983). Studies of the δD and $\delta^{18}O$ values of precipitation related to altitude (Craig, 1961) suggest that the isotopes of meteoric water become progressively lighter with increasing altitude. Thus, the recharge elevation of groundwater can be estimated by using the following formula:

$$H = \frac{\delta^{18}O_{gw} - \delta^{18}O_{lw}}{\mathrm{grad}^{18}O} + h$$

where H (m) is the recharge elevation; $\delta^{18}O_{gw}$ and $\delta^{18}O_{lw}$ (‰) are the oxygen isotope ratios of the groundwater sample and local meteoric water, respectively; $\mathrm{grad}^{18}O$ (‰/km) is the isotope elevation gradient of meteoric water; and h (m) is the elevation of the local meteoric water sampling point.

The mixing ratio of magmatic water in geothermal fluid can be calculated using the following isotopic bivariate mixture model (Pang, 2006):

$$\delta_G = \lambda\delta_M + (1-\lambda)\delta_P$$

where δ_G, δ_M, and δ_P represent the $\delta^{18}O$ or δD of geothermal fluid, magmatic water and precipitated meteoric water, respectively. λ is the percentage of magmatic water mixed in the geothermal fluid.

Strontium isotope ratios are originally used as a geochronologic tool and a petrogenetic tracer to determine the age or source of rock formations (Faure, 1977), since rocks or minerals have different ages and Rb/Sr ratios, resulting in variable strontium isotopes in different geological terranes (Hajj et al., 2017). Later, strontium isotopes have been used to investigate Earth surface processes, such as quantifying the weathering and erosion rates of rocks and calculating the contributions of different mixing sources to water bodies (Gaillardet et al., 1999; Wang and Tang, 2020) Strontium in rocks is released into water and soil as Sr primarily through weathering and dissolution. The $^{87}Sr/^{86}Sr$ values of surface and ground water are a function of bedrock weathering (Frei and Frei, 2011). Previous studies have concluded that the dominant source of Sr (water, plants, soils, snail shells and animal and human tooth enamel and bones) is largely determined by the underlying geology (Hajj et al., 2017).

3.3 Statistical analysis and geochemical modeling

As the Lower Cretaceous shallow marine and terrestrial deposits were intruded by the Gangdese granitoid (Schwab et al., 2004), the geothermal water in the KKF area likely interacted with the intruding granite. So, the corresponding trace element compositions of granodiorite from Jiangba pluton in the Shiquanhe area (Yan, 2019) were used as the reference. Ti was selected as the reference element because of its widespread presence in the crust, low susceptibility to contamination, stable chemical properties and lower volatility than other trace elements. In this study, the enrichment factor (EF), a qualitative indicator used to assess the water–rock interaction of thermal waters, was calculated by normalizing the concentrations of trace elements (Li, Be, Al, Ti, V, Cr, Fe, Co, Ni, Cu, Zn, Sr, Sn, Ba, Tl, Pb, Th and U) using the following formula:

$$EF_i = \frac{(C_i/T_i)_\omega}{(C_i/T_i)_r}$$

where T_i is the selected reference element, C_i is an element in the spring sample, ω is the element concentration of the spring sample, and r is the element concentration of the reference rocks.

The AquaChem–PHREEQC software (Parkhurst and Appelo, 1999) developed by Waterloo Hydrogeologic Inc. was used to evaluate the geochemical properties and saturation index of each mineral.

The silica–enthalpy mixing model is another available method for determining reservoir temperatures of spring water. The silica–enthalpy mixing model (Fournier and Truesdell, 1974) assumes that 1) there is no precipitation of silicon and SiO_2 controlled by quartz in thermal water before mixing with cold water; 2) and no conduction cooling occurs after mixing. These factors eliminate the effects of the mixing process and represent the maximum reservoir temperatures of thermal water before mixing. In this study, sample KK-9 is selected as the end-member of cold water, while the other

TABLE 1 Hydrochemical properties and major chemical constituents of the spring waters along the Karakorum Fault. The values were expressed in mg/L.

Sample	Type of sample	T (°C)	pH	EC (μs/cm)	Na	K	Mg	Ca	Cl	SO_4	CO_3	HCO_3	Li	F	SiO_2	TDS	Hydrochemical type	δD (‰)	$\delta^{18}O$ (‰)
DGQ-1	Geothermal spring	75.00	7.75	45600	770.67	78.90	10.80	20.90	742.48	57.76	87.94	1299.28	16.16	11.19	81.11	1230.04	HCO_3·Cl–Na	−142.7	−16.4
QP-2	Geothermal spring	83.40	8.28	1697	367.97	32.44	0.87	4.05	112.63	86.43	98.58	498.22	2.41	11.87	214.00	679.49	HCO_3–Na	−136.3	−16.8
XB-3	Geothermal spring	70.00	8.11	47000	1005.71	97.48	3.00	14.34	676.75	257.83	160.28	1360.56	9.50	6.81	149.59	1694.18	HCO_3·Cl–Na	−121.8	−15.3
ZDGB-4	Geothermal spring	69.60	7.29	144.7	118.09	38.42	38.94	148.78	15.05	85.49	0.00	852.78	0.34	3.19	46.87	60.28	HCO_3–Ca·Na	−128.4	−15.5
MS-5	Geothermal spring	48.50	6.72	2412	225.44	98.57	177.65	50.25	67.21	181.75	0.00	1307.21	0.68	1.44	32.96	176.00	HCO_3–Mg·Na	−130.4	−16.5
BEHZ-6	Geothermal spring	74.00	7.87	62900	1082.17	135.49	21.65	59.11	1822.34	137.11	145.39	845.04	36.88	8.14	153.44	3196.92	Cl–Na	−115.8	−13.3
NM-7	Geothermal spring	77.88	8.10	1245	250.92	8.84	0.21	11.51	179.87	145.00	28.37	135.55	0.96	15.08	77.25	649.49	Cl·SO_4–Na	−131.4	−14.3
LJ-8	Geothermal spring	81.17	8.20	2813	573.14	43.65	1.93	24.80	444.78	374.87	73.76	440.54	5.56	10.01	147.45	1478.20	Cl·SO_4–Na	−119.9	−13.3
KK-9	Cold spring	6.00	7.43	155.10	11.33	0.88	3.81	18.00	1.40	14.54	0.00	79.52	0.00	0.77	8.65	20.66	HCO_3–Ca·Na	−124.7	−15.5

Note: δD and $\delta^{18}O$ were expressed in ‰ vs. V-SMOW, standard.

10.3389/feart.2022.1021550

TABLE 2 Chemical composition of trace elements of the spring waters along the Karakorum Fault. The values were expressed in μg/L.

Sample	DGQ-1	QP-2	XB-3	ZDGB-4	MS-5	BEHZ-6	NM-7	LJ-8	KK-9
Li	16935.00	2251.00	9235.00	320.00	627.00	35553.00	923.00	5091.00	12.80
Be	26.90	5.91	2.10	0.27	0.09	14.10	1.48	4.35	0.08
B	315473.00	40509.00	84849.00	3004.00	10351.00	497014.00	19451.00	52286.00	326.00
Al	70.60	486.00	168.00	8.46	9.10	69.00	96.20	33.40	265.00
Ti	20.50	31.70	29.90	5.14	8.27	32.70	9.38	22.00	23.80
V	3.72	1.16	3.18	2.15	0.96	6.64	1.28	2.25	2.12
Cr	2.07	2.77	2.68	2.52	1.58	1.72	1.56	1.69	2.60
Fe	344.00	259.00	331.00	85.30	12.80	411.00	90.50	97.00	568.00
Co	0.06	0.10	0.16	0.47	0.31	0.09	0.06	0.05	0.31
Ni	0.92	1.20	1.35	7.39	3.65	1.51	0.75	0.65	1.62
Cu	1.42	1.35	2.35	1.82	1.84	1.72	1.19	2.64	31.70
Zn	4.80	3.99	5.02	12.10	5.11	5.58	3.14	4.69	17.00
Sr	1465.00	216.00	2612.00	1825.00	5142.00	1147.00	280.00	1895.00	103.00
Mo	0.26	0.07	1.69	0.14	0.10	0.11	57.30	5.76	1.23
As	29224.00	329.00	3814.00	69.200	30.00	5339.00	4478.00	4324.00	110.00
Ag	0.01	0.03	0.01	0.01	0.02	<0.002	0.01	<0.002	0.01
Cd	0.02	0.05	<0.002	0.00	0.02	0.03	0.10	0.03	0.01
Sn	0.15	0.13	0.09	0.09	0.08	0.16	0.07	0.11	0.61
Sb	31.00	262.00	296.00	16.00	0.19	26.10	4.37	58.90	2.37
Ba	294.00	101.00	137.00	187.00	112.00	4307.00	6.39	90.00	12.90
Tl	0.50	0.71	1.16	0.07	0.01	1.01	0.23	2.16	0.01
Pb	0.12	0.36	0.39	0.14	0.06	0.05	0.10	0.04	0.73
Th	0.08	0.12	0.10	<0.002	0.02	0.05	0.07	0.03	0.03
U	0.04	0.04	0.03	0.04	0.13	0.02	0.01	0.02	1.93
$^{87}Sr/^{86}Sr$ (‰)	0.711531	0.742322	0.724661	0.714484	0.715482	0.711505	0.708902	0.712194	0.710253

medium-to high-temperature spring waters of the KKF are the another end-member of thermal water.

In addition, we plot the quartz solubility curve under the conditions of steam separation occurring (maximum steam loss) or not (no steam loss). In addition, the silica–enthalpy diagram can quantify the mixing ratio of cold water when thermal springs ascend. Based on a sequence of enthalpies and quartz solubilities in various temperatures, the fraction of cold water (X_t) can be calculated by the follow formula (Fournier and Truesdell, 1974):

$$X_t = \frac{(H_R - H_S)}{(H_R - H_C)}$$

where H_S is the enthalpy of hydrothermal spring water, H_C is the enthalpy of cold water, and H_R is the enthalpy of reservoir waters.

3.4 Circulation depth

The circulation depth of the geothermal fluids can be calculated as the following formula (Lu et al., 2017):

$$D = \frac{T - T_0}{G} + Z_0$$

where D is the circulation depth (km), T is the estimated reservoir temperature (°C), T_0 is the local annual average temperature (°C), G is the geothermal gradient (°C/km), and Z_0 is the thickness of the constant-temperature zone (km). For the samples of spring water collected along the Karakorum fault, the circulation depth was estimated by applying a local annual average temperature of 0.4°C (Wu et al., 2011), a constant-temperature zone at 30 m, and a regional geothermal gradient of 30°C/km (Chen et al., 2013).

4 Results

4.1 Physicochemical properties of the geothermal system

The geochemical compositions of the spring water samples collected along the KKF are presented in Table 1. Except for sample KK-9, a cold spring with a temperature of

6°C, all the spring water samples were from thermal springs with temperatures in the range of 48.5–83.4°C at the spring vent. The pH values of the spring water samples were 6.72–8.28 (neutral to alkaline), and the electrical conductivity (EC) and total dissolved solids (TDS) values varied widely, from 144.7 to 62,900 μS/cm and from 20.66 to 3,196.92 mg/L, respectively.

Based on the concentrations (Table 1) in milligram equivalents from high to low, the main cations of most of the spring water samples (excluding samples ZDGB-4, MS-5 and KK-9) were Na^+ (250.92–1,082.17 mg/L), K^+ (8.84–135.49 mg/L), Ca^{2+} (4.05–59.11 mg/L) and Mg^{2+} (0.21–21.65 mg/L). The major cationic concentrations in the sample collected from sample MS-5 were Mg^{2+} (177.65 mg/L) and Na^+ (225.44 mg/L). The major cationic concentrations in the samples collected from samples ZDGB-4 and KK-9 were Ca^{2+} (148.783 and 18 mg/L, respectively) and Na^+ (118.091 and 11.33 mg/L, respectively). The main anion in samples BEHZ-6, NM-7 and LJ-8 was Cl^- (179.87–1822.34 mg/L), while that in the rest of the samples was HCO_3^- (79.52–1,360.56 mg/L). The dissolved SiO_2 contents were 32.96–214.00 mg/L in the thermal springs and as low as 8.65 mg/L in the cold spring.

Trace elements were present in a wide range of concentrations (see Table 2), ranging from fractions to hundreds of thousands of μg/L. Boron (B), arsenic (As), lithium (Li), strontium (Sr), barium (Ba), iron (Fe) and antimony (Sb) were the most abundant elements, present at concentrations from 326.00 to 497,014.00 μg/L, 30.00–29,224.00 μg/L, 12.8–35,553.00 μg/L, 103.00–5,142.00 μg/L, 6.39–4,307.00 μg/L, 12.80–568.00 μg/L, and 0.19 μg/L to 293.00 μg/L, respectively. The Li, B, Sr and As concentrations were higher in the higher-temperature thermal springs than in the lower-temperature springs (samples ZDGB-4, MS-5 and KK-9) along the KKF, while the Fe, Cu, Zn, Sn, Pb and U concentrations in the thermal springs were lower than in the low-temperature springs. Compared to the concentrations of B, F, As and Li in typical high-temperature geothermal systems, such as the Kangding (Tang et al., 2017), Yangbajing (Guo et al., 2008, 2010), Yangyi (The Geothermal Geological Team of Tibet, 1990; Guo et al., 2009; Yuan et al., 2014), Rehai (Shangguan and Huo, 2002; Guo et al., 2014a, b) and Cuopu (J. Tian et al., 2019) systems in the Himalayan geothermal belt, those of the medium- to high-temperature geothermal springs along the KKF ranged from 3 to 497.01 mg/L, 1.44–15.08 mg/L, 0.03–29.22 mg/L, and 0.32–35.55 mg/L, respectively, which were consistent with the typical 'geothermal suite' (Kaasalainen et al., 2015).

4.2 Isotopic characteristics of the geothermal system

The stable oxygen and hydrogen isotopic compositions of the spring water samples from the KKF ranged from -16.8 to -13.3‰ and from -142.7 to -115.8‰, respectively, *versus* V-SMOW. The results are shown in Table 1. A plot of δD-$\delta^{18}O$ is shown in Table 1.

The Sr isotopic compositions of the spring water samples from the KKF region are shown in Table 2. The ratios varied from 0.7089 to 0.7423. Extremely radiogenic ratios (> 0.724) were detected for samples QP-2 and XB-3, which are adjacent to Lake Manasarovar.

5 Discussion

5.1 Origin of thermal springs

5.1.1 Hydrochemical features

Physicochemical parameters (such as temperature, EC and TDS) can be used to determine the water chemistry and circulation characteristics of groundwater. Our results demonstrate that geothermal spring water samples with higher temperatures exhibit higher EC (>1,000 μs/cm) and TDS (>650 mg/L) values than type A water (Table 1). In general, high EC values can be caused by high concentrations of dissolved minerals in water (Zainal et al., 2016). Higher TDS values reflect a longer circulation path and residence time (Belhai et al., 2016). Assuming that the springs belong to the same water source, geological context and thermal source, temperatures at the spring vent indicate the circulation depth, time of circulation and regional geothermal gradients (Zainal et al., 2016).

5.1.1.1 Major elements

The hydrochemical characteristics of most of the geothermal water samples analysed in this study were those of bicarbonate types besides samples BEHZ-6, NM-7 and LJ-8. The concentrations of major cations and anions of springs in the KKF (Table 2) are shown on a Piper diagram (Piper, 1944) (Figure 2) with three types of faces: (A) HCO_3–Mg·Na (sample MS-5) or HCO_3–Ca·Na (samples ZDGB-4 and KK-9); (B) HCO_3–Na (sample QP-2) or HCO_3·Cl–Na (samples DGQ-1 and XB-3); and (C) Cl–Na (sample BEHZ-6) or Cl·SO_4–Na (samples NM-7 and LJ-8). Type A water, especially the cold spring water (sample KK-9), is characteristic of shallow or subsurface water in the unsaturated zone and has high concentrations of Ca^{2+}, Mg^{2+} and HCO_3^-, which may be caused by the dissolution of Ca^{2+} and Mg^{2+} ions in a rock field of limestone and Marl+$CaSO_4$ origin (Appelo and Postma, 2004) or in the soil by meteoric water action (Hiscock, 2005). Therefore, considering the temperature measured at the spring vent, sample KK-9 (as a cold spring, 6°C), with type A water, can be classified as shallow and as having closed stable oxygen isotope characteristics with the local meteoric water (e.g., Shiquanhe station, $\delta^{18}O$: -14.4‰; altitude: 4,278 m) (Yao et al., 2013). Whereas the relatively high temperatures of samples ZDGB-4 and MS-5 (69.6°C and 48.5°C, respectively) may be influenced by mixing with thermal

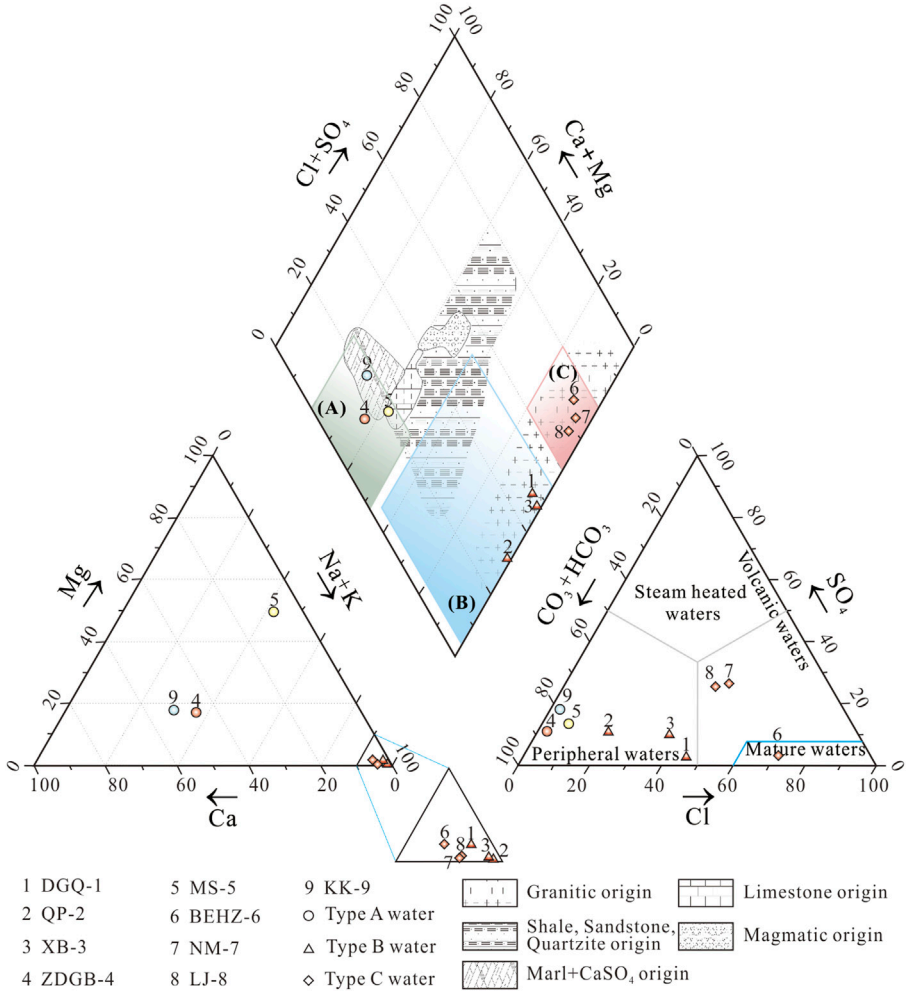

FIGURE 2
Piper diagram to recognise the hydrogeochemical facies in spring water samples from the KKF. Cl–SO_4–HCO_3 triangular diagram in the lower right corner of Piper diagram (based on Nicholson, 1993). The rock field in the Piper diagram was adopted from Zuurdeeg and Van der Weiden (1985) and Appelo and Postma (2004). The legend filled blue, yellow, and red color represent the temperatures at the spring vent below 25°C, between 25°C and 50°C, and above 50°C of spring water samples, respectively.

water. The A and B water types are bicarbonate-type spring waters formed by chemical reactions between infiltrated meteoric water and dissolved carbon dioxide, the distinction being that type B water may be formed by a reservoir rock field of granitic origin, according to the Piper diagram, that contains albite and microcline as the major minerals (J. Tian et al., 2019). In comparison to type A water, type B water is richer in Na^+ and deficient in Ca^{2+} and Mg^{2+} as a result of deep infiltration and water–rock interaction processes. The flow pattern of this type of water is characteristic of the evolution of groundwater (Stuyfzand, 1999). Unlike the two types mentioned above, type C water may represent thermal water that probably are at most the groundwater flow system with a long flow distance and long residence time in the aquifer. The Cl–Na-type spring shows that dissolution of chlorides prevails in sample BEHZ-6. In addition, samples NM-7 and LJ-8 are of the Cl·SO_4–Na type, indicating that the dissolution of chlorides and sulphates prevails in sample LJ-8.

Three groups of geothermal waters are shown in the lower right corner of Figure 2: steam-heated waters, mature waters and peripheral waters. Type A water and type B water are bicarbonate types. Both were plotted in the peripheral zone and are considered to be peripheral water with a relatively shallow heating hydrological circuit in the crust and no obvious material contribution from a magmatic fluid. Type C water samples are plotted in the chloride field. Among the type C water samples, sample BEHZ-6 plot in the chloride mature field is similar to typical high-temperature geothermal waters from

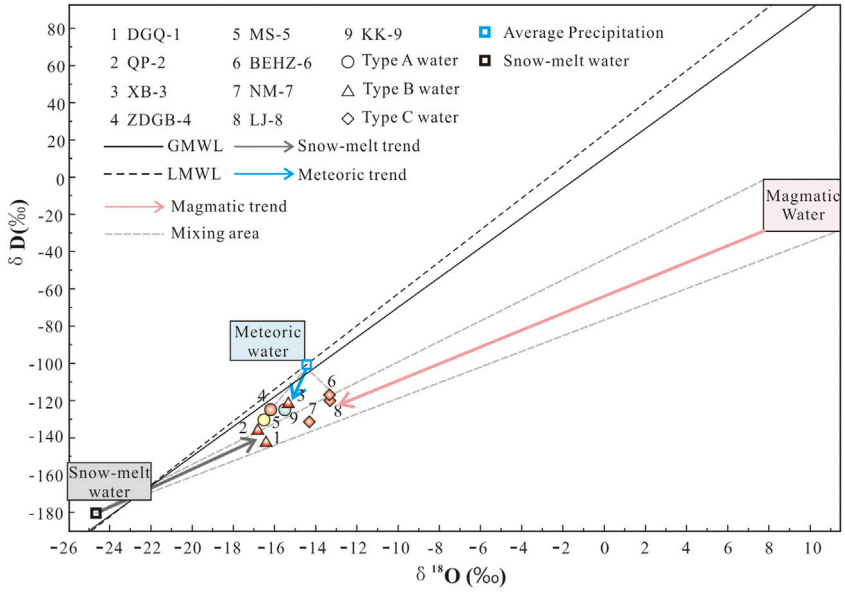

FIGURE 3
Plot of stable oxygen and hydrogen isotopes of spring water samples from the KKF. The straight line ($\delta D = 8.0\delta^{18}O + 10.0$; Craig, 1961) represents the global meteoric water line (GMWL), and the dashed line ($\delta D = 7.93\delta^{18}O + 11.59$) represents the local meteoric water line (LMWL) at the Gangotri station, India. V-SMOW = Vienna Standard Mean Ocean Water. The legend is the same as in Figure 2.

Yangbajing and the Yellowstone National Park, which are generally considered to be heated by underlying magma, and the water is affected by magmatic fluid (water and volatile) to various degrees. This conclusion is confirmed by the results of the analysis of oxygen and hydrogen isotopes (Figure 3), presented in section 5.1.2. It is widely recognized in the geothermal community that Cl^- in high concentrations in high–temperature geothermal fluids originates mainly from mixing with magmatic water (Guo et al., 2014a, b; Tian et al., 2018). Samples NM-7 and LJ-8 have lower HCO_3/Cl ratios than sample BEHZ-6 and fall in the chloride field away from the chloride mature field, suggesting these thermal water samples underwent fast-ascending partial mixing with near-surface water.

5.1.1.2 Trace elements

The enrichment factors (EF_i) of trace elements in spring waters along the Karakorum fault are shown in Figure 4. According to the concentrations of trace elements, the hot spring water is similar to granodiorite from the Jiangba pluton in the Shiquanhe area, with high concentrations of Li, Al, Fe, Sr, Ba and Pb, compared to other elements (Be, Ti, Cr, Co, Ni, Cu, Sn, Tl, and U), indicating that these elements in the hot spring water mainly originate from water–rock interactions. For instance, thermal water has high concentrations of Sr and Ba, 103–5,142 μg/L and 6.39–4,307 μg/L, respectively. It is assumed that the geothermal water in the study area has water–rock interaction with volcanic and magmatic rocks at the depth of the KKF. During this process, Sr and Ba in potassium feldspar and hornblende minerals in volcanic and magmatic rocks are often replaced with Ca and K in geothermal water, thus contributing Sr and Ba elements to the spring water. In addition, Sr is more easily migrated and occurs at a higher concentration than Ba in bicarbonate-type spring water. However, differences in the chemical properties and migration capacities of various trace elements lead to Be, Ni, Cu, Tl and U enrichment in addition to that of Li Sr, and Ba in some springs, compared to the granodiorite from the Jiangba pluton in the Shiquanhe area (Figure 4). Li is more enriched than other elements in the spring water samples, except for sample DGQ-1 (C_{Li} = 0.0128 mg/L), where its concentration was up to 16.935 mg/L. The enrichment factors for Al, V, Co, Pb, Sn and Th were less than 1, indicating sources of geothermal water other than the interaction of Jiangba pluton.

Previous studies on high-temperature geothermal systems have recognized Li, B, Fe and As being a typical 'geothermal suite' (Kaasalainen et al., 2015). The Li, B, Fe and As concentrations of type A water are 1–3 orders lower than those of type B and type C waters along the KKF (Table 2; Figure 5) and other typical high-temperature geothermal systems in the Tibetan Plateau (Guo et al., 2008, 2009, 2014a, b). This phenomenon is probably due to a shallow circulation depth of type A water, where there is no mantle-derived magmatic intrusion in the shallow crust supplying both heat and volatiles (J. Tian et al., 2019). The type B and C thermal waters along the KKF have high Li concentrations (> 0.96 mg/L), a signature of deep fluid upwelling. Hydrolysis of lithium silicate minerals (such as

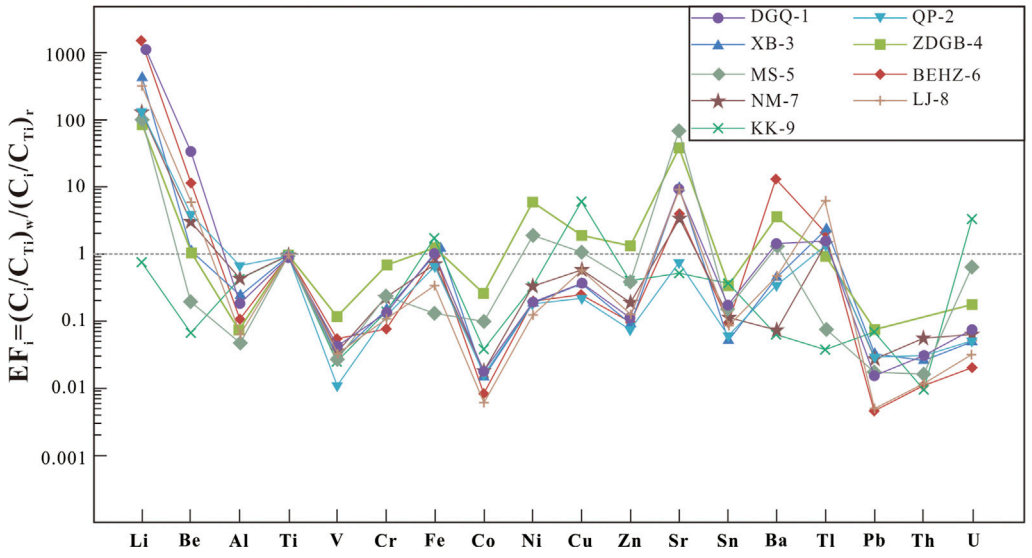

FIGURE 4
Trace element distribution for geothermal water samples along the KKF.

lepidolite and hydroxyapatite) in granites and granodiorite during deep circulation processes are speculated to result in the dissolution of Li entering thermal water (Zhang et al., 2003). As the solubility of boron (B) in geothermal water increases with depth, pressure and temperature (Zhang et al., 2003), a higher boron content in a water sample indicates a greater depth at which geothermal water is circulating. The relatively high boron contents of the type B and type C waters, shown in Figure 5, suggest deep circulation.

Arsenic (As), a toxic trace element, plays an important role in the study of geothermal resources. The arsenic concentrations of sample KK-9 vary widely (Figure 5; Table 2). The type B and type C waters have higher arsenic contents (0.33–29.22 mg/L) than the type A waters (0.03–0.11 mg/L), especially sample DGQ-1 having an extremely high arsenic concentration (as high as 29.22 mg/L), compared to those in typical high-temperature geothermal systems that are recognized as being influenced by underlying magma or hot thickened crust to different degrees (Guo et al., 2008, 2009, 2014a, b; Wang, 2021). The high arsenic concentrations in type B and type C waters may be related to Gangdese granitoids, deeper circulation and water–rock interaction. This is because arsenic in geothermal fluids mainly derives from the dissolution of arsenic from As-rich minerals in upper crustal rocks during water–rock interaction when deep circulation of geofluids occurs. Arsenic then migrates to the surface as geothermal fluids rise (Wang, 2021).

5.1.2 Hydrogen and oxygen stable isotopes

As shown in Figure 3, all the spring water samples fall near the global meteoric water line (GMWL) and the local meteoric water line (LMWL), providing significant information about the origin of geothermal water (Craig, 1961; Pang et al., 2017; Duan et al., 2022), i.e. that the springs are mainly recharged by infiltrated precipitation.

In this study, the local precipitation isotope data were selected for the Shiquanhe station ($\delta^{18}O$: -14.4‰; altitude: 4,278 m) of the Tibetan Network for Isotopes in Precipitation (TNIP) (Yao et al., 2013), which is the closest to the sampling sites. The $\delta^{18}O$ vertical gradient in the Tibetan Plateau was assumed to be -3.1‰/km (Yu et al., 1984). Consequently, the recharge elevation range (calculated as 4,568–5,052 m) for the KKF spring water samples was slightly higher than the elevation of the local meteoric water sampling point (4,278 m), excluding type C water (samples BEHZ-6, NM-7 and LJ-8). The recharge elevation is lower than the snow-capped mountain elevation around the locations of the spring water samples from the KKF area (5,500–6,000 m for the Gangdise mountains, 6,000 m for the Himalayan mountains, 5,500–6,000 m for the Kunlun mountains and 5,500–6,000 m for the Nyenchen Tanglha and Tanglha mountains). This suggests that the recharge source of all type A and B waters (excluding type C waters) is presumably not only meteoric water but also snowmelt water. Nevertheless, the recharge elevation of type C water was calculated to be 3,923–4,245 m, and type C water was more enriched in $\delta^{18}O$ (> -14‰) than type A and type B waters, which means that there should be other recharge sources. We speculate that magmatic waters enriched in D and ^{18}O may contribute to these geothermal fluids.

The $\delta^{18}O$ and δD values were plotted for the thermal springs and cold springs, as well as three end members

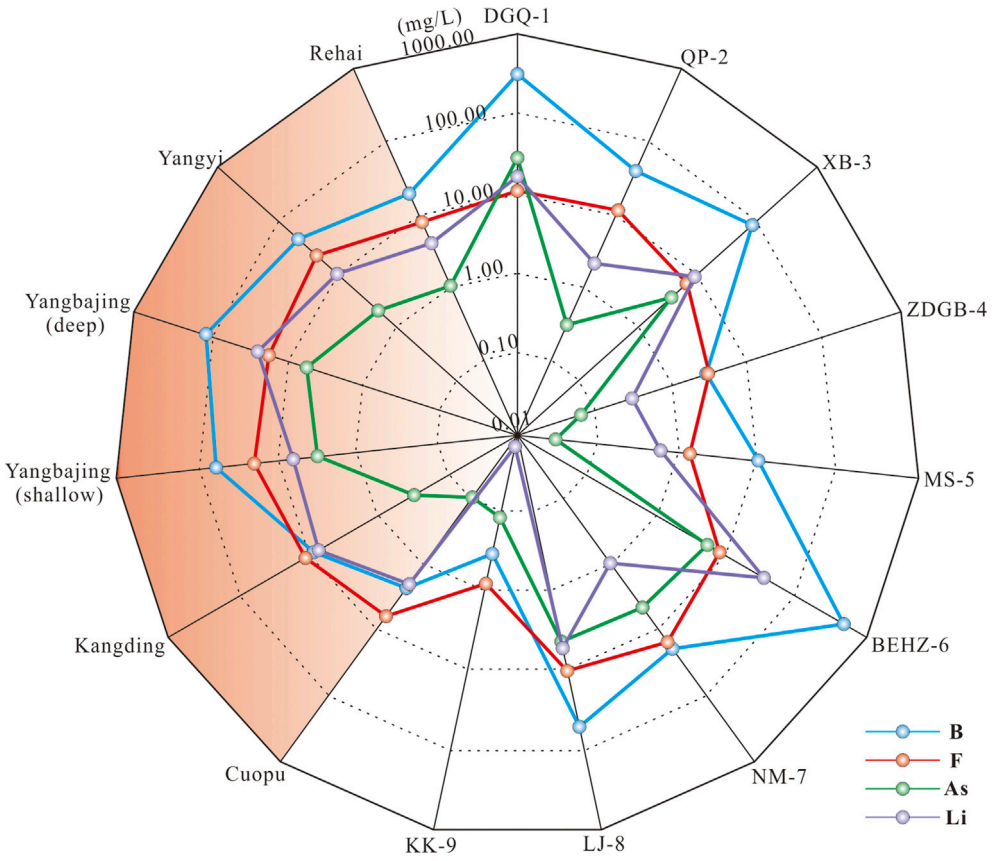

FIGURE 5
Concentrations of Li, B, F and As in geothermal waters along the KKF compared with those from typical high-temperature geothermal systems in the Himalayan geothermal belt (Guo et al., 2008, 2009; 2014; Wang, 2021).

(meteoric water, snowmelt water and magmatic water) (Figure 3). The snowmelt isotopes are referenced from glacier data (the Tanglang La in India, elevation 5,210 m) reported by Pande et al. (2000). The precipitation isotopes and the local meteoric water line are referenced from the Gangotri station, India, in GNIP (http://www-naweb.iaea.org/napc/ih/IHS_resources_gnip.html). The snowmelt water with δD of -180‰ and $\delta^{18}O$ of -24.7‰ falls to the lower left of the global meteoric water line (GMWL) and the local meteoric water line (LMWL), which can be explained by an isotopic fraction during the snow melting process and isotope altitude effect (Clark and Frintz, 1997). The weighted mean precipitation isotopes of the Gangotri station ($\delta^{18}O$: -14.5‰; δD: -103.7‰) plot on the LMWL or close to the GMWL. The magma water is enriched in δD and $\delta^{18}O$ within ranges of -20 ± 10‰ and 10 ± 2‰, respectively (Giggenbach, 1992).

Almost all the spring water samples fall into the mixing area among the three end members (Figure 3). At the mixing area, the type C water samples exhibit strong $\delta^{18}O$ enrichment and plot in the mixing zone between snowmelt water and magmatic water, suggesting that it is a mixture of snowmelt water and magmatic water. The mixing ratio of magmatic water in the spring waters was estimated to be 13%–17%. Type A and B waters in KKF are more likely to be influenced by evaporation or other factors than only by the magma water, so the actual mixing ratios are influenced by evaporation and other factors below 6%–13%.

An obvious oxygen isotope shift in geothermal waters is usually observed as a result of strong water–rock interaction when the rock is richer in $\delta^{18}O$ (Giggenbach, 1992). The positive $\delta^{18}O$ shift is generally ascribed to water–rock interactions affected by three factors: 1) the high temperature of reservoirs; 2) a long circulation time; 3) high ratios of rock to water (Tian et al., 2018). Nevertheless, no remarkable oxygen isotope shift ($\delta^{18}O$: -21.51‰ to -15.25‰; δD: -166.8‰ to -127.4‰) in the geothermal waters along the KKF was observed, which is consistent with numerous high-temperature geothermal systems in the Tibetan Plateau (Guo et al., 2010; Tan et al., 2014). This is probably because that the geothermal water circulates too quickly and stays too short a time within the reservoir to allow the water to attain full equilibrium between

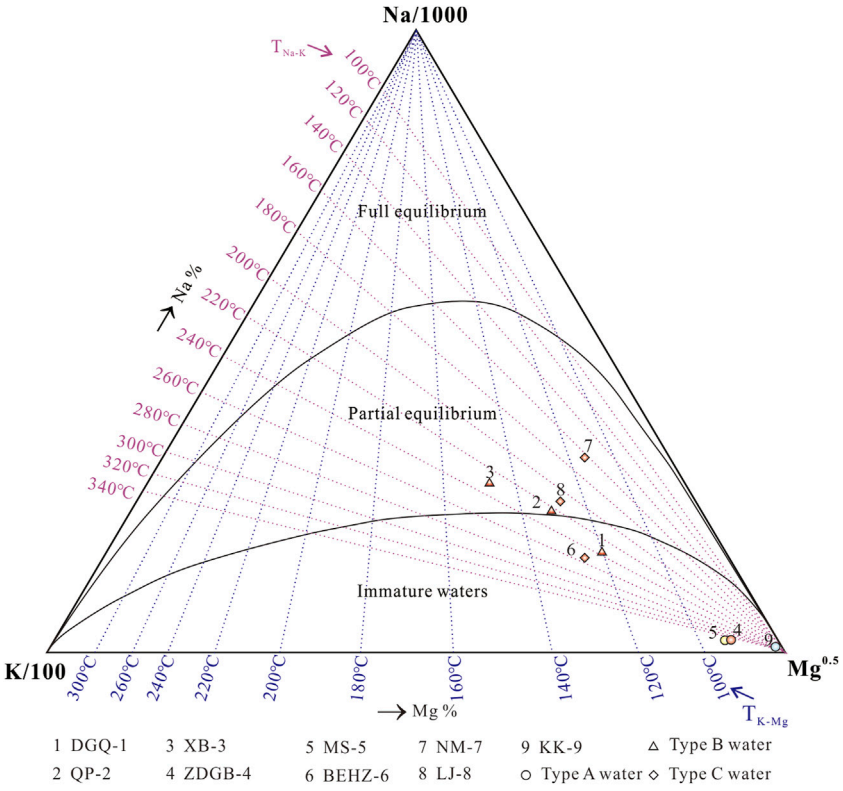

FIGURE 6
Giggenbach Na–K–Mg ternary diagram of spring water samples from the KKF. The legend is the same as in Figure 2.

water and rocks. This explanation is supported by the finding that none of the waters in the KKF region attain full equilibrium between water and rocks. As shown in Figure 3, the higher-temperature springs in the KKF area are slightly deficient in δD, with values ranging from -142.7 to -136.3‰ (type B water except for sample XB-3) or are more enriched in $\delta^{18}O$, with values ranging from -14.3 to -13.3‰ (type C water) than the lower-temperature springs (type A spring water). Therefore, the isotopic compositions with minimal oxygen isotopic shift of the type A water along the KKF could imply relatively shallower circulation or lower geothermal gradient than that of the type B and type C waters.

5.1.3 Water–rock interaction

Samples of DGQ-1, ZDGB-4, MS-5, BEHZ-6 and KK-9 is distributed in the immature water field (shallow or mixed waters), while samples QP-2, XB-3, NM-7 and LJ-8 is located in the partial equilibrium zone or mature field (Figure 6). The equilibrium temperatures of samples QP-2, XB-3, NM-7 and LJ-8 range from 160 to 240°C, indicating that these thermal waters came from deep and hot reservoirs. Therefore, they underwent water–rock interaction during the deep circulation process, and then were cooled with shallow cold water mixing during ascent. However, all the samples from the KKF are distributed in the immature water zone or partial equilibrium zone and away from the full equilibrium zone, indicating that none of these waters had attained full equilibrium between water and rocks. Type A water (samples ZDGB-4, MS-5 and KK-9) falls closer to the $Mg^{1/2}$ corner than the other water samples, indicating that mixed thermal waters are far from equilibrium and at low temperatures (Giggenbach, 1988). Therefore, the application of cation geothermometers such as Na–K and K–Mg thermometers to type A water would be problematic (Giggenbach, 1988). In contrast, types B and C waters are closer to the line of full equilibrium, indicating a slightly higher degree of water–rock interaction than type A water in the study area. This suggests a deeper or longer circulation which is less affected by the mixing process for type B and C waters. Thus, these springs can be used to estimate the reservoir temperature with cation geothermometers. An interesting point is that the type B waters (samples DGQ-1, QP-2 and XB-3) fall along the same isotherm of the reservoir temperature of ~ 220–240 °C (194.9–207.2 °C as calculated by the Na/K geothermometer), which suggests that they share a parent

TABLE 3 SI values of minerals in the spring waters along the Karakorum Fault.

Sample	DGQ-1	QP-2	XB-3	ZDGB-4	MS-5	BEHZ-6	NM-7	LJ-8	KK-9
Barite	−0.18	−0.30	0.06	−0.20	−0.11	1.21	−1.00	0.09	−0.86
Anhydrite	−2.51	−2.85	−2.28	−1.47	−2.03	−1.78	−2.01	−1.52	−3.05
Celestite	−1.94	−2.37	−1.18	−1.78	−1.23	−1.81	−1.96	−0.96	−3.34
Gypsum	−2.68	−3.11	−2.40	−1.58	−1.95	−1.95	−2.21	−1.76	−2.79
Alunite	−21.48	−21.42	−27.04	−2.27	−3.92	−15.22	−19.84	−22.84	0.86
Jarosite-K	−14.77	−17.44	−21.50	2.17	−6.32	−8.78	−15.30	−16.69	−4.43
Melanterite	−18.25	−19.84	−23.00	−8.16	−8.90	−14.39	−17.62	−19.14	−6.67
Calcite	1.11	0.73	1.26	1.30	0.20	1.10	0.54	1.22	−1.00
Aragonite	0.99	0.62	1.14	1.18	0.07	0.98	0.43	1.11	−1.16
Dolomite	2.36	1.11	1.86	2.49	1.46	2.21	−0.34	1.59	−2.64
Rhodochrosite	−0.47	−0.81	−0.96	2.29	−1.53	0.32	−0.32	0.24	−1.62
Siderite	−9.29	−10.80	−14.19	−0.13	−1.73	−6.17	−9.69	−10.97	−0.38
Strontianite	0.34	−0.08	0.98	−0.38	−0.49	−0.28	−0.73	0.48	−2.69
Witherite	−1.36	−1.39	−1.27	−2.30	−3.08	−0.71	−3.20	−1.87	−4.53
K-feldspar	−0.86	−0.22	−2.99	1.66	−0.11	1.16	−1.50	−1.43	0.82
Albite	−1.69	−0.93	−3.85	0.27	−1.83	0.24	−1.84	−2.08	−0.65
Anorthite	−3.08	−1.93	−4.48	2.47	−3.89	−1.46	−2.75	−3.60	−1.02
K-mica	0.23	1.54	−3.77	11.33	6.09	4.07	0.19	−1.69	12.38
Illite	−4.72	−4.36	−5.67	−0.44	−2.27	−3.81	−4.41	−5.37	0.15
Kaolinite	−3.70	−2.70	−7.68	4.57	0.49	−0.29	−3.99	−5.24	5.14
Ca-Montmorillonite	−3.62	−2.76	−7.27	5.37	2.17	−0.59	−2.92	−4.90	7.66
Sepiolite(d)	−5.49	−4.34	−10.57	4.69	0.63	−1.39	−4.67	−6.82	6.55
Sepiolite	1.23	0.55	1.82	−5.12	−6.63	0.02	−2.68	0.45	−8.29
Chrysotile	5.25	4.73	5.75	−1.20	−3.16	4.03	1.40	4.60	−5.92
Talc	11.07	10.32	13.89	0.71	−3.31	7.70	5.25	10.19	−9.54
Chlorite(14A)	14.93	14.50	15.88	4.88	0.75	12.75	9.26	14.22	−6.23
SiO_2(a)	18.46	18.06	21.46	9.56	−1.32	14.43	9.40	15.78	−8.17
Quartz	−0.88	−0.74	−1.81	−0.72	−0.72	−0.29	−0.81	−0.81	−0.96
Chalcedony	0.11	0.22	−0.80	0.30	0.40	0.71	0.17	0.15	0.44
Halite	−0.19	−0.06	−1.10	−0.01	0.04	0.41	−0.12	−0.13	−0.06
Fluorite	−5.02	−6.13	−4.96	−7.47	−6.53	−4.51	−6.06	−5.37	−9.29

geothermal fluid at depth but mix with cold water near the surface. This phenomenon further confirms that geothermal water rises along the same conduit underground until it is dispersed in the anisotropic porous Quaternary sediment (J. Tian et al., 2019).

5.1.4 Mineral saturation states (SI)

The mineral saturation index (SI) of geothermal springs reflects mineral thermodynamic behaviours and water–rock equilibrium processes (Wang et al., 2016). By the PHREEQC program, we calculated mineral saturation index values for the spring water samples collected along the KKF at the outflow temperature. The saturation index values obtained are shown in Table 3; Figure 7. Almost all the spring water samples were unsaturated (SI < 0) with respect to sulphates (anhydrite, celestite, gypsum, alunite, jarosite-K, melanterite), carbonates (siderite and witherite), feldspars (K-feldspar, albite, anorthite) and halite. Most carbonates (calcite, aragonite, dolomite, rhodochrosite, strontianite), barite, silica and fluorite were in equilibrium (SI ≈I) with spring water in the KKF at the outflow temperature. The calculated results for the slightly saturated calcite and aragonite at the outflow temperature were consistent with field observations of the calcareous sinter at the spring vent. All of the hot spring water samples were saturated (SI > 0) with respect to quartz except sample XB-3, possibly because of a mixture of cold or snowmelt water during the thermal water ascent, resulting in a reduction in the quartz solubility with decreasing temperature. Consequently, the temperature calculated using the quartz thermometer was lower than the true temperature.

Interestingly, SI with respect to some minerals vary greatly for the different spring water types. SI values with respect to

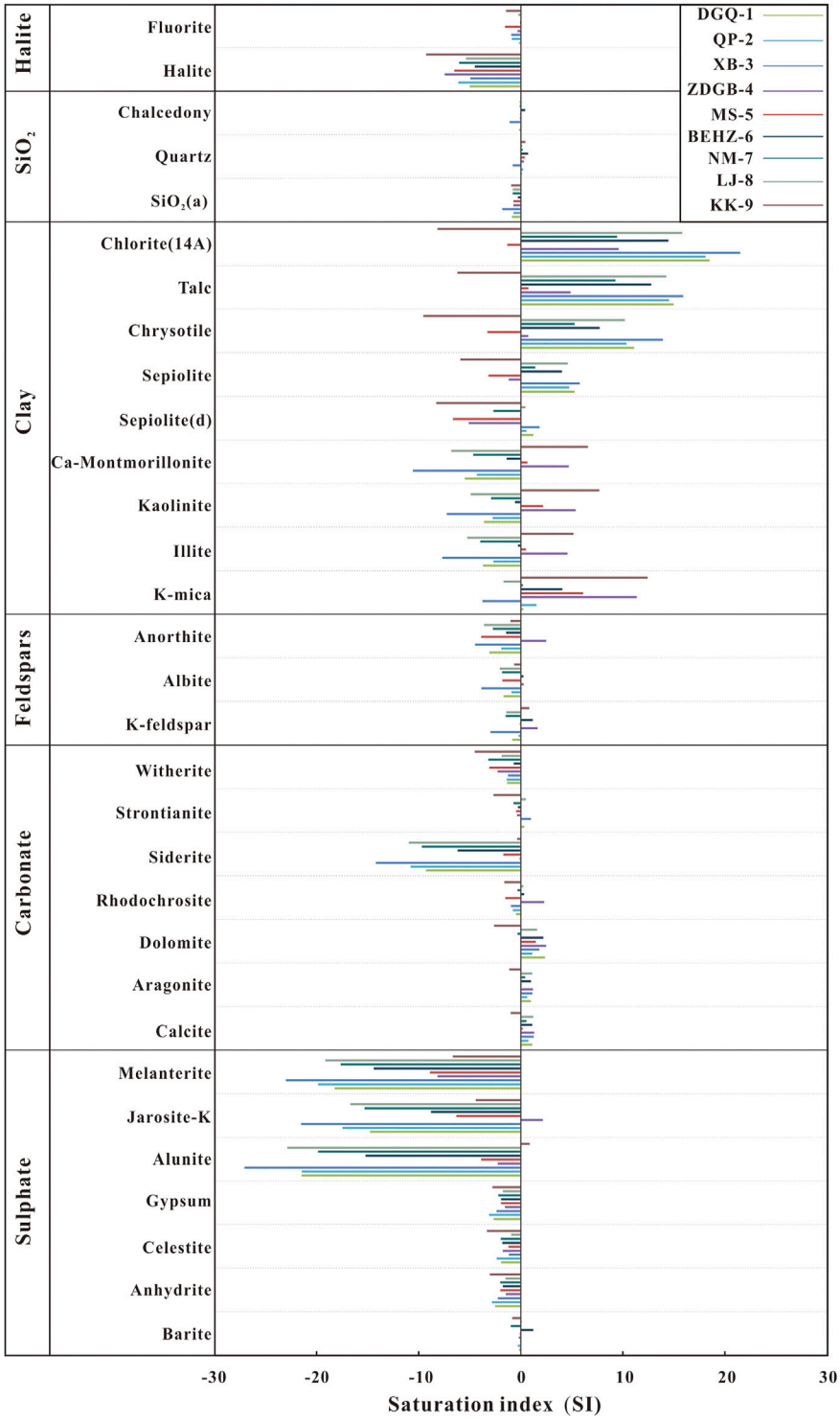

FIGURE 7
Saturation indexes of geothermal springs along the KKF zone at the outflow temperature.

siderite, Ca-montmorillonite, K-mica, illite and kaolinite (SI values from -1.73 to -0.13, -0.63 to 6.55, 6.09 to 12.38, 0.49 to 5.14 and 2.17 to 7.66, respectively) of Type A water is higher than that of type B and C waters (SI values from -14.19 to -6.17, -10.57 to -1.39, -3.77 to 4.07, -7.68 to -0.29 and -7.27 to -0.59, respectively). However, SI values with respect to

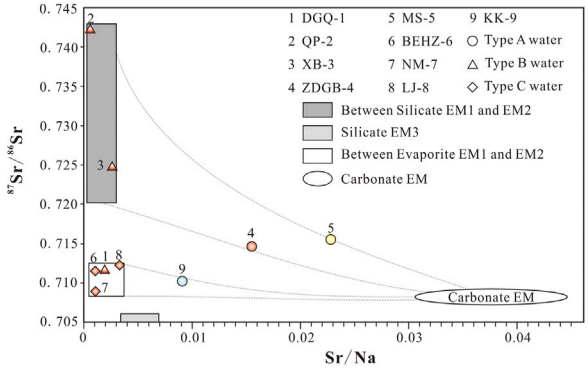

FIGURE 8
Plots of $^{87}Sr/^{86}Sr$ *versus* the corresponding Sr/Na for different spring waters from the KKF. The data for six end-members—silicate–EM1 (Gaillardet et al., 1999; Noh et al., 2009), silicate–EM2 (Xu and Liu, 2010), silicate–EM3 (Gaillardet et al., 1999; Noh et al., 2009), evaporite–EM1 (Liu et al., 2016), evaporite–EM2 (Moon et al., 2007; Xu and Liu, 2010), and carbonate–EM (Xu and Liu, 2010)—are based on lithological characteristics observed in China. The legend is the same as in Figure 2.

sepiolite, chrysotile, talc, and chlorite (SI values from -5.92 to -1.20, -9.54 to 0.71, -6.23 to 4.88 and -8.17 to 9.56, respectively) of type A water is lower than that of type B and type C waters (SI values from 1.40 to 5.75, 5.25–13.89, 9.26–15.88, 9.40–21.46, respectively). Relatively high SI values indicate high contents of these minerals and long residence times in the aquifer system. This phenomenon may reflect differences in the thermal reservoirs and the surrounding rock characteristics. For instance, oversaturation of typical hydrothermally altered minerals (sepiolite, chrysotile, talc and chlorite) in type B and type C waters indicates that Mg-rich carbonates are widely distributed due to hydrothermal alteration.

5.1.5 Strontium isotopic compositions

The results show a large range (0.708902–0.742322) for the $^{87}Sr/^{86}Sr$ ratios of the spring water samples from the KKF, which is consistent with the significantly variable $^{87}Sr/^{86}Sr$ ratios found in the terranes of the southern Tibetan Plateau (e.g., the Lhasa terrane, Qiangtang terrane and Himalaya Block) (Wang and Tang, 2020). The southern Tibetan Plateau, one of the most tectonically active regions, has an extremely complex geological setting, with a large amount of exposed Palaeozoic–Mesozoic sedimentary rock, low–high metamorphic rock and granitoids, contributing to the highly heterogeneous Sr isotope range. This suggests that differences in the Sr isotopic compositions of spring waters in the KKF region are largely dependent on the divergent geological conditions of the fracture zone.

The $^{87}Sr/^{86}Sr$ ratios against the corresponding Sr/Na values were plotted for different spring water samples (Figure 8) to examine the genesis of the Sr isotopic compositions. Samples QP-2 and XB-3, which are much more radiogenic (> 0.724) than the other springs (0.708–0.716), exhibit a mixing between silicate EM1 and silicate EM2, which is probably due to the influence of metamorphic rocks and granitoid sources (Gaillardet et al., 1999; Noh et al., 2009). Samples DGQ-1, BEHZ-6, NM-7 and LJ-8, which are less radiogenic (0.708–0.712) and exhibit low Sr/Na ratios (0.001–0.003), are distributed in the mixing range between evaporite EM1 and evaporite EM2, indicating that the evaporate dissolution plays an important role in these spring waters. The water samples from samples ZDGB-4, MS-5 and KK-9, with higher milligram equivalent percentages of Ca, Mg and HCO_3^- as well as Sr/Na ratios, are located closer to the carbonate EM than other samples, reflecting the strong influence of carbonate weathering on Sr isotopes. Samples ZDGB-4 and MS-5 are distributed along the mixing line of silicate and carbonate end-members, suggesting that the water from samples ZDGB-4 and MS-5 is more likely to be derived from silicate/carbonate weathering. The $^{87}Sr/^{86}Sr$–Sr/Na of sample KK-9 is located between the mixing lines of evaporite and carbonate end-members, which suggests that both of the carbonate rock weathering and evaporite dissolution contribute significantly to the $^{87}Sr/^{86}Sr$ ratios of sample KK-9.

5.2 Estimates of geothermal reservoir temperature

All the studied water samples from the KKF are ploted in the non-equilibrium field (partially equilibrated or immature) (Figure 9), indicating that none of these waters attained full equilibrium between water and rocks. Therefore, different multi-element geothermometers, such as Na–K and Na–K–Ca, may not reflect the true thermal reservoir temperature. In addition, meteoric water or snowmelt water mixing with ascending thermal water from the KKF leads to a

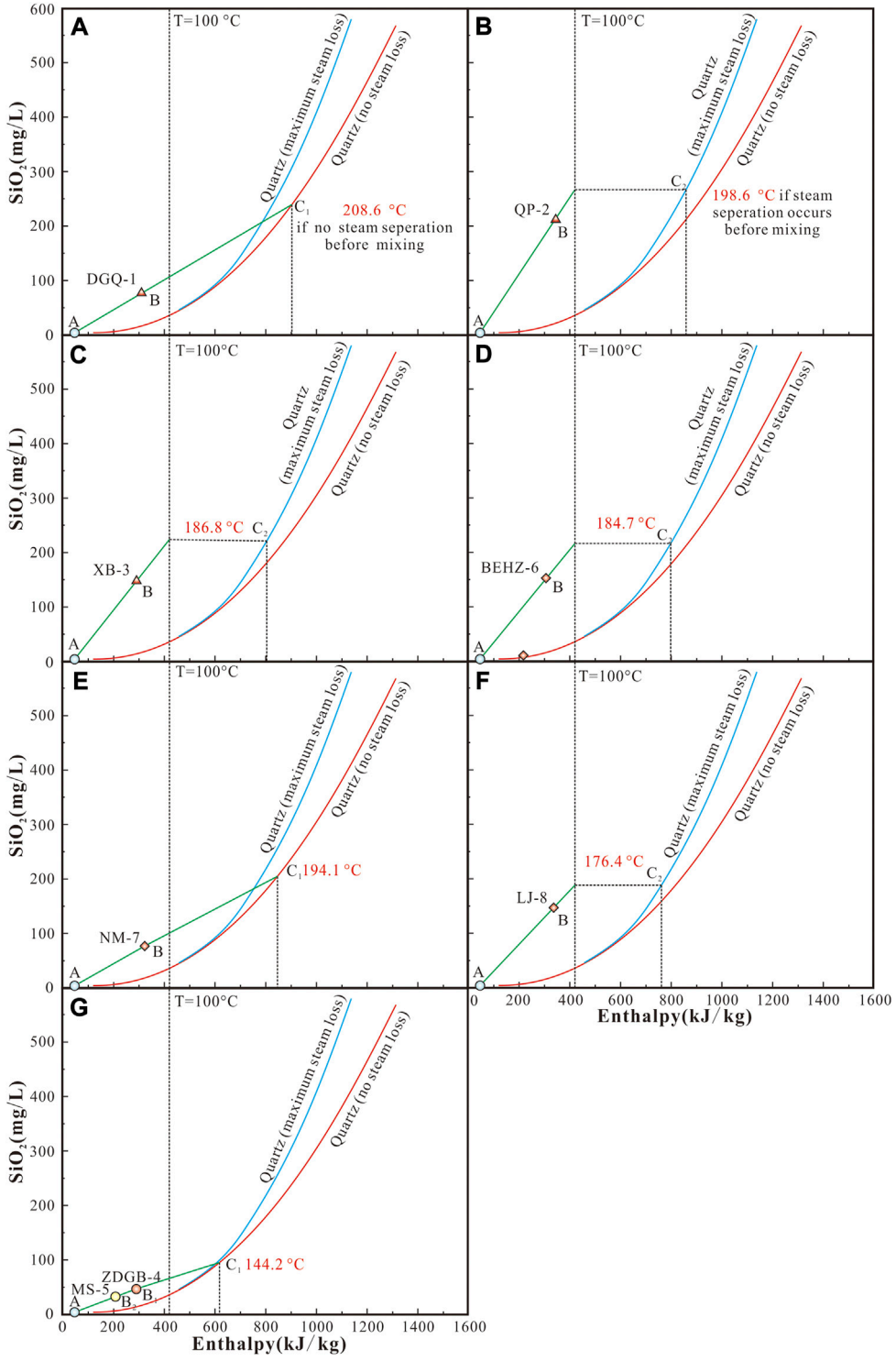

FIGURE 9
Plots of enthalpy *versus* silica for geothermal spring waters along the KKF. The legend is the same as in Figure 2.

decrease in SiO_2 concentration. Additionally, classical geothermometers (e.g., quartz geothermometers) mainly reflect the reservoir temperatures after the mixing of thermal water and cold water, the temperature calculated by quartz geothermometers is lower than the true thermal reservoir temperature before the mixing. The silica–enthalpy

TABLE 4 Calculated geothermometers of the geothermal fluids along the Karakorum Fault(°C).

Sample	Measured temperature	Silica geothermometers①				Cation geothermometers			Silica-enthalpy mixing model				Circulation depth (km)
		Quartz	Quartz (steam loss)	Chalcedony	Chalcedony (steam loss)	K/Mg②	Na/K③	Na-K-Ca④	Maximum steam loss		No steam loss		
									Enthalpy (kJ/kg)	Temperature	Enthalpy (kJ/kg)=	Temperature	
DGQ-1	75.0	125.8	123.1	97.9	98.5	121.0	207.2	235.6	–	–	903.6	208.6	7.0
QP-2	83.4	184.6	171.9	164.2	151.1	132.7	194.9	232.8	858.8	198.6	–	–	6.6
XB-3	70.0	161.0	152.6	137.2	130.0	148.9	202.6	276.2	806.1	186.8	–	–	6.2
ZDGB-4	69.6	98.8	99.97	68.67	74.18	83.3	341.1	102.0	–	–	616.9	144.2	4.8
MS-5	48.5	83.3	86.5	52.2	60.2	88.0	387.1	187.8	–	–	616.9	144.2	4.8
BEHZ-6	74.0	162.6	153.9	139.0	131.5	127.0	225.4	232.9	796.9	184.7	–	–	6.2
NM-7	77.9	123.3	120.9	95.1	96.2	114.3	139.6	121.1	–	–	839.0	194.1	6.5
LJ-8	81.2	160.1	151.8	136.2	129.2	129.4	183.9	186.0	759.9	176.4	–	–	5.9
KK-9	6.0	34.6	43.1	1.8	15.9	27.9	185.0	12.8	–	–	–	–	–

Note: Geothermometers are from ① Quartz geothermometer: If no loss of steam, $t(℃) = 1522/5.19 - \log SiO_2 - 273.15$; If maximum steam loss, $t(℃) = \frac{1522}{5.75-\log SiO_2} - 273.15$; Chalcedony geothermometer: If no loss of steam, $t(℃) = 1032/4.69 - \log SiO_2 - 273.15$; If maximum steam loss, $t(℃) = 1264/5.31 - \log SiO_2 - 273.15$ (Fournier, 1977); ② $T_{K/Mg} = 4410/13.95 - \log\ (K^2/Mg) - 273.15$ (Giggenbach, 1988); ③ $T_{Na/K} = 1052/1 + e^{(1.714\times\log(Na/K)+0.252)} + 76$ (Can, 2002); ④ $T_{Na-K-Ca} = 1647/\log(Na/K) + \beta(\log(\sqrt{Ca}/Na) + 2.06) + 2.47 - 273.15$ (Fournier, 1981).

10.3389/feart.2022.1021550

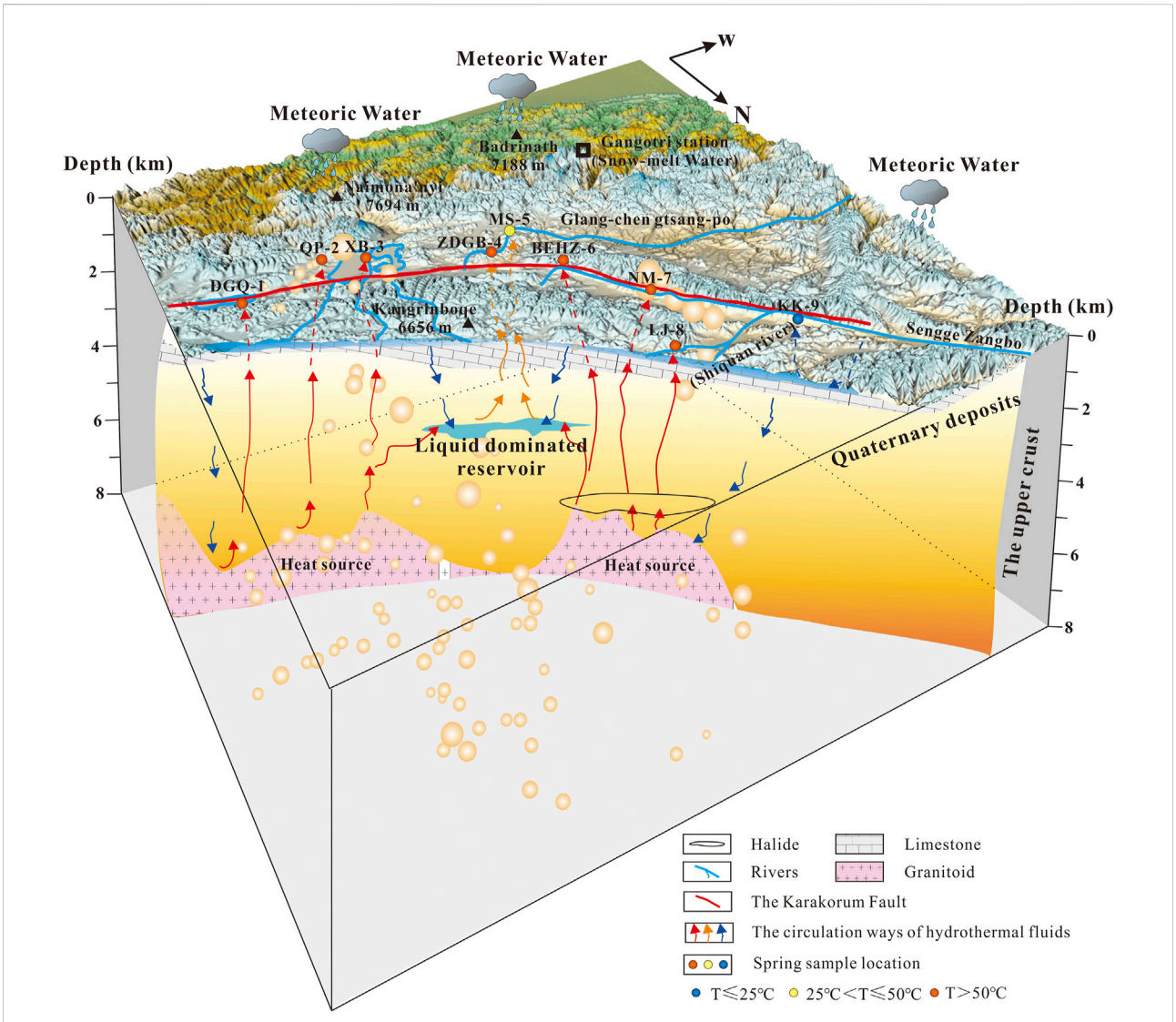

FIGURE 10
Conceptual hydrothermal model of the hydrogeochemical cycling process in high-temperature geothermal systems along the KKF. The red line and blue lines represent the main fault and rivers of the KKF, respectively. The blue, yellow, and red arrows represent the circulation pathways of hydrothermal fluids with low, intermediate, and high temperatures, respectively. The orange sphere shows the earthquakes that have occurred along the KKF within 200 km since 1970, and its dimensions (0.8–4.4 mm) correspond to the magnitude of the earthquake (M_L 1.0–5.9).

mixing model (Figure 9), as an available method for determining reservoir temperatures of spring water, was applied. For the samples of DGQ-1 (Figure 9A), NM-7 (Figure 9E), ZDGB-4 and MS-5 (Figure 9G), the extrapolations of the mixing lines from cold water (point A) to thermal water in the KKF have an intersection point C_1 with the quartz solubility curve (no steam loss). The intersection point C_1 suggests the enthalpy and SiO_2 concentration of the initial thermal fluid if there is no steam separation before mixing with cold water (largely meteoric water). It is noteworthy that samples ZDGB-4 and MS-5 are plotted on one mixing line (Figure 9G), suggesting that they have the same reservoir temperature. Nevertheless, for samples QP-2, XB-3, BEHZ-6 and LJ-8 with high SiO_2 concentrations (Figures 9B–D,F), no intersection point has been found between the extended mixing lines (from cold water to these thermal water) and the quartz solubility curve, indicating the presence of steam loss of thermal fluid before mixing with cold water during ascent. The mixing line from cold water to these thermal water has an intersection with a assumed vertical boiling line (100°C). Then, a horizontal line paralleling to the enthalpy axis was drawn from this intersection to intersect with the quartz solubility curve (maximum steam loss) at point C_2. The intersection point C_2 indicates the enthalpy and SiO_2 concentration when the thermal fluid begins to boil. In summary, the reservoir

temperatures of the deep geothermal reservoir were estimated by the silica–enthalpy mixing model, (Figure 9; Table 4), varying from 144.2°C to 208.6°C.

Moreover, the thermal water samples exhibit a wide range of mixing fractions with cold water quantified by the silica–enthalpy diagram, varying from 19% (sample QP-2) to 72% (sample MS-5). Varying mixing proportions of cold water indicate a remarkable decrease in temperatures (enthalpies) and dissolved silica concentrations. For instance, due to the different mixing proportions (57% and 72%, respectively) of cold water, different temperatures (69.6°C and 48.5°C, respectively) of spring vent were measured for samples ZDGB-4 and MS-5 in spite of the same reservoir temperatures (144.2°C) (Figure 9G).

5.3 Circulation model of geothermal fluid in the KKF

5.3.1 Estimates of geothermal circulation depth

Geothermal genesis can be categorised into three types: 1) magmatic genesis associated with active magma in the shallow crust; 2) radiogenic genesis related to the decay of radioactive elements in S-type granites; 3) tectonic deep circulation genesis related to regional tectonic movements, high background values of heat flow and deep circulation of geothermal water (Korhonen and Johnson, 2015; Wang, 2021). The KKF, a ~1,000-km-long strike–slip fault, has developed a series of extensional and transtensional fractures, which act as channels not only for groundwater infiltration but also for deep-derived geothermal fluid rising fluently. Many geothermal resources are widely distributed along the KKF. Previous geophysical studies of the geothermal system (He et al., 2016) described a low-resistivity anomaly characterized by resistivity in the range of 1–8 Ω m at a depth greater than 7 km, and suggested that the low-resistivity anomaly may be indicative of potentially partially melted magma in the upper crust, representing the heat source of the Qupu geothermal system. Furthermore, sample BEHZ-6 is located in the chloride mature field of the Cl–SO_4–HCO_3 diagram, similar to typical high-temperature geothermal waters from Yangbajing and Yellowstone National Park. According to previous studies, this high-temperature geothermal waters were heated by underlying magma since the Middle Palaeocene, and the water was affected by the magmatic fluid (water and volatile) to various degrees (Guo et al., 2014a, b; Tian et al., 2018). Nevertheless, there is insufficient evidence for volcanic activity in the KFF. Thus, we inferred that the high-temperature springs in the study area are primarily due to deep syntectonic hydrothermal circulation, and the dependence of the reservoir temperature on the heat source (the crustal rocks, e.g., granites) is largely controlled by the fault depth.

Based on the Na-K-$Mg^{1/2}$ diagram, the reasonable cation geothermometry and the silica–enthalpy mixing model, the reservoir temperature range of 144.6°C–208.6°C was determined for thermal water before mixing. The result for the circulation depth of geothermal fluids shows a wide range, from 4.8 km to 7.0 km (Table 4). As a result, the measured temperature at the spring vent is defined by the factor combining the mixing ratio of meteoric water or snowmelt water in the spring waters, the reservoir temperature and the circulation depth. Specifically, type A water with low temperature at the spring vent has a comparatively shallow circulation depth (4.8 km for samples ZDGB-4 and MS-5). In contrast, type B water (with circulation depths of 7.0 km, 6.6 km and 6.2 km for samples DGQ-1, QP-2 and XB-3, respectively) and type C water (with circulation depths of 6.2 km, 6.5 km and 5.9 km for samples BEHZ-6, NM-7 and LJ-8, respectively) have relatively large circulation depths.

5.3.2 Conceptual model

Combining the hydrochemistry characteristic, the recharge elevation, the reservoir temperature and the circulation depth of the spring water, we propose a conceptual model for the origin and evolution of geothermal fluid along the KKF (Figure 10). The geothermal water of the KKF is primarily recharged by local precipitation and melting ice water, which infiltrate to a depth of 4.8–7.0 km, and then are heated to 144.2–208.6°C during water–rock interaction with the Gangdese granitoids instead of underlying magmas. In the reservoir, the chemical reactions between water and the surrounding rocks (widely distributed granites and carbonate rockscontaining Na-rich minerals and carbonate minerals) result in the formation of geothermal water. The differences between type A water (HCO_3–Mg·Na or HCO_3–Ca·Na), type B water (HCO_3–Na) and type C water (Cl–Na or Cl·SO_4–Na) mainly depend on the type of surrounding rock, the circulation depth of the thermal fluid and the mixing ratio with cold water.

The circulation depth represents the lower limit of the fault depth. Therefore, the circulation depth estimated from the thermal reservoir temperature suggests a penetration depth of at least 7 km for the KKF. As shown in Figure 7, the location of medium-to high-temperature springs along the KKF is also an area of frequent occurrence of shallow earthquakes with minor magnitude. In addition, the epicentre depth was found to coincide with the circulation depth of the corresponding thermal water. This water participated in deep circulation and has been overpressured during water–rock interaction in an active fault system, which may drive the fluid flow and cause the fault weakening and seismicity. The important role of overpressured fluids palyedin the earthquake generation has been acknowledged by many researchers (e.g., Chiodini et al., 2011; Curzi et al., 2021). The frequent occurrence of earthquakes in turn weakens the crustal rocks and produces abundant fissures. These fissures are good for leaching out of the toxic

elements (e.g., As) from the surrounding rocks, and for migration of these elements to the surface by deep fluid ascent. The deeper the circulation happened, the more arsenic was leached from the crust during water–rock interaction, which can be evidenced by the arsenic concentrations in samples DGQ-1, QP-2, XB-3, BEHZ-6, NM-7 and LJ-8 are 1–3 orders of magnitude higher than that in samples ZDGB-4, MS-5 and KK-9 (Table 2; Figure 5). Overall, the geothermal water is significantly correlated with the epicentre and focal depth of earthquakes along the KKF, specifically in terms of the typical 'geothermal suite' (Li, B, F and As) and circulation depth of the thermal water.

In addition, the seismic catalogue shows that earthquakes along the KKF occur mostly at depths > 5 km, yet the traditional groundwater observation is dominated by shallow sources (< 5 km), so the traditional shallow groundwater are not involved in the inception process of deeper-source earthquakes but rather only as a passive post-earthquake response. Compared to shallow groundwater, geothermal fluids are less disturbed by the surface environment and human activities, which makes its utility in capturing realistic earthquake precursor information. Therefore, in addition to traditional groundwater observation stations, geothermal fluids is an effective supplement in forecasting earthquake, especially for short-term seismic prediction.

6 Conclusion

(1) Three types of the spring waters along the KKF were classified: type A water (HCO_3–Mg or HCO_3–Ca), type B water (HCO_3–Na) and type C water (Cl–Na or Cl·SO_4–Na). Type A and B waters are bicarbonate-type spring waters which were formed by chemical reactions among infiltrated meteoric water and dissolved carbon dioxide. Type A water was formed by the dissolution of Ca^{2+} and Mg^{2+} ions in rock fields of limestone and Marl+$CaSO_4$ origin, whereas type B water was formed by a reservoir rock field of granitic origin which contains albite and microcline as major minerals. Type C water was resulted from the dissolution of chlorides and sulphates.

(2) The Sr isotopic composition of type B water, except for sample DGQ-1, exhibits much more radiogenesis, which is resulted from the influence of metamorphic rocks and a granitoid source. Type C water and sample DGQ-1 are characterized by less radiogenesis and low Sr/Na ratios, indicating evaporate dissolution. The genesis of type A water is derived from the combined process of the dissolution of silicate/evaporite and infiltration of widespread carbonate rocks by meteoric water.

(3) Almost all of the spring waters were recharged mainly by infiltrated precipitation, with the recharge elevation range of 3.9–5.1 km. Type A and B waters were recharged not only by meteoric water but also by snowmelt water. Moreover, slightly anomalous ^{18}O enrichment occurs in type C water, indicating a water–rock interaction.

(4) Reservoir temperatures of 144.2–208.6°C and mixing ratios of 19%–72% were estimated. A conceptual model for geothermal fluid along the KKF was proposed, in which type A water with a low temperature at the spring vent has a comparatively shallow circulation depth, while type B and type C waters have relatively deep circulation depths (up to 7 km). The heat source of the geothermal system is resulted from the heating of crustal rocks rather than from the active magmas. The penetration depth of KKF is larger than 7 km.

(5) The geothermal water is significantly correlated with the epicentre and focal depth of earthquakes, especially for high-temperature spring water with deeper circulation and extremely high Li, B, Fe and As concentrations. Geothermal fluids can be used as a supplementary indicator in forecasting earthquake.

Data availability statement

The original contributions presented in the study are included in the article/Supplementary Material, further inquiries can be directed to the corresponding authors.

Author contributions

JW: data curation, validation, and writing—original draft. XZ: conceptualization, supervision, funding acquisition, and writing—review and editing. MH: investigation. JL: data curation. JD: formal analysis. JT: investigation. YY: data curation. YL: conceptualization. KL: data curation. YL: supervision, methodology, and writing—review and editing.

Funding

This research was financially supported by Central Public-interest Scientific Institution Basal Research Fund (CEAIEF2022030205, CEAIEF20220507, CEAIEF20220213), Special Fund of the Institute of Earthquake Forecasting (2021IEF0101, 2021IEF1201), Open Fund of Earthquake Forecasting, China Earthquake Administration (XH22034D), National Key Research and Development Project (2017YFC1500501-05, 2019YFC1509203), National Natural Science Foundation of China (41803035, 41802212, 41673106, 42073063, 4193000170), International Geoscience Program (724).

Acknowledgments

The authors are grateful to the editor and reviewers for constructive comments and suggestions. The authors benefitted a lot from the assistance of Yihai Yang, Yurong Qiu and Xinyan Li and Wei Tao.

Conflict of interest

The authors declare that the research was conducted in the absence of any commercial or financial relationships that could be construed as a potential conflict of interest.

The handling editor MZ declared a past co-authorship with the author XZ.

Publisher's note

References

Appelo, C. A. J., and Postma, D. (2004). *Geochemistry, groundwater and pollution*. Florida, FL, USA: CRC Press. doi:10.1201/9781439833544

Banerjee, P., and Bürgmann, R. (2002). Convergence across the northwest Himalaya from GPS measurements. *Geophys. Res. Lett.* 29 (13), 16521–17304. doi:10.1029/2002gl015184

Barberio, M. D., Gori, F., Barbieri, M., Billi, A., Caracausi, A., De Luca, G., et al. (2020). New observations in Central Italy of groundwater responses to the worldwide seismicity. *Sci. Rep.* 10, 17850. doi:10.1038/s41598-020-74991-0

Belhai, M., Fujimitsu, Y., Bouchareb Haouchine, F. Z., Iwanaga, T., Noto, M., and Nishijima, J. (2016). Hydrogeochemical and isotope geochemical study of northwestern Algerian thermal waters. *Arab. J. Geosci.* 9 (3), 169–217. doi:10.1007/s12517-015-2252-2

Bianchi, A., Bovini, L., Botti, F., Doveri, M., Lelli, M., Manzella, A., et al. "Multidisciplinary approach to the study of the relationships between shallow and deep circulation of geofluids," in Proceedings of the World geothermal congress, Bali, Indonesia, April 2010, 25–29.

Brahim, F. B., Boughariou, E., Makni, J., and Bouri, S. (2020). Evaluation of groundwater hydrogeochemical characteristics and delineation of geothermal potentialities using multi criteria decision analysis: Case of Tozeur region, Tunisia. *Appl. Geochem.* 113, 104504.

Can, I. (2002). A new improved Na/K geothermometer by artificial neural networks. *Geothermics* 31 (6), 751–760. doi:10.1016/s0375-6505(02)00044-5

Chen, H. H., Wu, Y., and Xiao, Q. G. (2013). Thermal regime and Paleogeothermal gradient evolution of Mesozoic Cenozoic sedimentary basins in the Tibetan Plateau, China. *Earth Sci. J. China Univ. Geosciences* 38 (3), 541–552. doi:10.1016/S0264-3707(00)00002-8

Chen, Z., Zhou, X. C., Du, J. G., Xie, C. Y., Liu, L., Li, Y., et al. (2015). Hydrochemical characteristics of the hot spring waters in the Kangding district related to the Lushan MS 7.0 earthquake in Sichuan, China. *Nat. Hazards Earth Syst. Sci.* 2, 7293–7308. doi:10.5194/nhess-15-1149-2015

Chiodini, G., Caliro, S., Cardellini, C., Frondini, F., Inguaggiato, S., and Matteucci, F. (2011). Geochemical evidence for and characterization of CO_2 rich gas sources in the epicentral area of the Abruzzo 2009 earthquakes. *Earth Planet. Sci. Lett.* 304 (3–4), 389–398. doi:10.1016/j.epsl.2011.02.016

Clark, I. D., and Frintz, P. (1997). *Environmental isotopes in hydrogeology*. Boca Raton: Lewis & Co. doi:10.1201/9781482242911

Craig, H. (1961). Isotopic variations in meteoric waters. *Science* 133, 1702–1703. doi:10.1126/science.133.3465.1702

Curzi, M., Bernasconi, S. M., Billi, A., Boschi, C., Aldega, L., Franchini, S., et al. (2021). U–Pb age of the 2016 Amatrice earthquake causative fault (Mt. Gorzano, Italy) and paleo fluid circulation during seismic cycles inferred from inter and co-seismic calcite. *Tectonophysics* 819, 229076. doi:10.1016/j.tecto.2021.229076

Daniele, L., Taucare, M., Viguier, B., Arancibia, G., Aravena, D., Roquer, T., et al. (2020). Exploring the shallow geothermal resources in the Chilean southern volcanic zone: Insight from the liquine thermal springs. *J. Geochem. Explor.* 218, 106611. doi:10.1016/j.gexplo.2020.106611

Du, J. G., Liu, C. Q., Fu, B. H., Ninomiya, Y., Zhang, Y. L., Wang, C. Y., et al. (2005). Variations of geothermometry and chemical isotopic compositions of hot spring fluids in the Rehai geothermal field, southwestern China. *J. Volcanol. Geotherm. Res.* 142 (3–4), 243–261. doi:10.1016/j.jvolgeores.2004.11.009

Duan, R., Li, P. Y., Wang, L., He, X. D., and Zhang, L. (2022). Hydrochemical characteristics, hydrochemical processes and recharge sources of the geothermal systems in Lanzhou City, northwestern China. *Urban Clim.* 43, 101152. doi:10.1016/j.uclim.2022.101152

Faure, G. (1977). *Principles of isotope geology*. New York, NY, USA: John Wiley & Sons.

Fournier, R. O. (1981). "Application of water geochemistry to geothermal exploration and reservoir engineering," in *Geothermal systems: Principles and case histories*. Editors L. Rybach and L. J. P. Muffler (New York, NY, USA: John Wiley & Sons), 109–143.

Fournier, R. O. (1977). Chemical geothermometers and mixing models for geothermal systems. *Geothermics* 5 (1–4), 41–50. doi:10.1016/0375-6505(77)90007-4

Fournier, R. O., and Truesdell, A. H. (1974). Geochemical indicators of subsurface temperature—Part 2, estimation of temperature and fraction of hot water mixed with cold water. *J. Res. U. S. Geol. Surv.* 2, 263–270. doi:10.3133/ofr741032

Franchini, S., Agostini, S., Barberio, M. D., Barbieri, M., Billi, A., Boschetti, T., et al. (2021). HydroQuakes, central Apennines, Italy: Towards a hydrogeochemical monitoring network for seismic precursors and the hydro-seismo-sensitivity of boron. *J. Hydrology* 598, 125754. doi:10.1016/j.jhydrol.2020.125754

Frei, K. M., and Frei, R. (2011). The geographic distribution of strontium isotopes in Danish surface waters–a base for provenance studies in archaeology, hydrology and agriculture. *Appl. Geochem.* 26, 326–340. doi:10.1016/j.apgeochem.2010.12.006

Gaillardet, J., Dupré, B., Louvat, P., and Allègre, C. J. (1999). Global silicate weathering and CO_2 consumption rates deduced from the chemistry of large rivers. *Chem. Geol.* 159, 3–30. doi:10.1016/s0009-2541(99)00031-5

Giggenbach, W. F. (1988). Geothermal solute equilibria. derivation of Na–K–Mg–Ca geoindicators. *Geochimica Cosmochimica Acta* 52 (12), 2749–2765. doi:10.1016/0016-7037(88)90143-3

Giggenbach, W. F., Gonfiantini, R., Jangi, B. L., and Truesdell, A. H. (1983). Isotopic and chemical composition of parbati valley geothermal discharges, North-West Himalaya, India. *Geothermics* 12, 199–222. doi:10.1016/0375-6505(83)90030-5

Giggenbach, W. F. (1992). Isotopic shifts in waters from geothermal and volcanic systems along convergent plate boundaries and their origin. *Earth Planet. Sci. Lett.* 113 (4), 495–510. doi:10.1016/0012-821x(92)90127-h

Guo, Q. (2012). Hydrogeochemistry of high-temperature geothermal systems in China: A review. *Appl. Geochem.* 27 (10), 1887–1898. doi:10.1016/j.apgeochem.2012.07.006

Guo, Q., Liu, M., Li, J., Zhang, X., and Wang, Y. (2014a). Acid hot springs discharged from the Rehai hydrothermal system of the tengchong volcanic area (China): Formed via magmatic fluid absorption or geothermal steam heating? *Bull. Volcanol.* 76 (10), 868–912. doi:10.1007/s00445-014-0868-9

Guo, Q., Nordstrom, D. K., and McCleskey, R. B. (2014b). Towards understanding the puzzling lack of acid geothermal springs in Tibet (China): Insight from a comparison with Yellowstone (USA) and some active volcanic hydrothermal systems. *J. Volcanol. Geotherm. Res.* 288, 94–104. doi:10.1016/j.jvolgeores.2014.10.005

Guo, Q., and Wang, Y. (2012). Geochemistry of hot springs in the Tengchong hydrothermal areas, Southwestern China. *J. Volcanol. Geotherm. Res.* 215, 61–73. doi:10.1016/j.jvolgeores.2011.12.003

Guo, Q., Wang, Y., and Liu, W. (2008). B, As, and F contamination of river water due to wastewater discharge of the Yangbajing geothermal power plant, Tibet, China. *Environ. Geol.* 56 (1), 197–205. doi:10.1007/s00254-007-1155-2

Guo, Q., Wang, Y., and Liu, W. (2009). Hydrogeochemistry and environmental impact of geothermal waters from Yangyi of Tibet, China. *J. Volcanol. Geotherm. Res.* 180 (1), 9–20. doi:10.1016/j.jvolgeores.2008.11.034

Guo, Q., Wang, Y., and Liu, W. (2010). O, H, and Sr isotope evidences of mixing processes in two geothermal fluid reservoirs at Yangbajing, Tibet, China. *Environ. Earth Sci.* 59 (7), 1589–1597. doi:10.1007/s12665-009-0145-y

Hajj, F., Poszwa, A., Bouchez, J., and Guérold, F. (2017). Radiogenic and "stable" strontium isotopes in provenance studies: A review and first results on archaeological wood from shipwrecks. *J. Archaeol. Sci.* 86, 24–49. doi:10.1016/j.jas.2017.09.005

He, L. F., Chen, L., Xi, X. L., Zhao, X. F., Chen, R. J., Yao, H. C., et al. (2016). Mapping the geothermal system using AMT and MT in the mapamyum (QP) field, Lake Manasarovar, southwestern Tibet. *Energies* 9 (10), 855. doi:10.3390/en9100855

Hiscock, K. M. (2005). "Hydrogeology. Principles and practice," in *Chemical hydrogeology*. Editor M. A. Malden (New york, NY, USA: Wiley Blackwell). doi:10.1111/j.1468-8123.2005.00118.x

Hu, X. M., Garzanti, E., Moore, T., and Raffi, I. (2015). Direct stratigraphic dating of India Asia collision onset at the Selandian (middle Paleocene, 59 ± 1 Ma). *Geology* 43, 859–862. doi:10.1130/g36872.1

Kaasalainen, H., Stefánsson, A., Giroud, N., and Arnórsson, S. (2015). The geochemistry of trace elements in geothermal fluids, Iceland. *Appl. Geochem.* 62, 207–223. doi:10.1016/j.apgeochem.2015.02.003

Kapp, P., Murphy, M. A., Yin, A., Harrison, T. M., Ding, L., and Guo, J. (2003). Mesozoic and cenozoic tectonic evolution of the Shiquanhe area of Western Tibet. *Tectonics* 22 (4), 1029. doi:10.1029/2001tc001332

Klemperer, S. L., Kennedy, B. M., Sastry, S. R., Makovsky, Y., Harinarayana, T., and Leech, M. L. (2013). Mantle fluids in the karakoram fault: Helium isotope evidence. *Earth Planet. Sci. Lett.* 366, 59–70. doi:10.1016/j.epsl.2013.01.013

Knappett, P. S. K., Li, Y. M., Hernandez, H., Rodriguez, R., Aviles, M., Deng, C., et al. (2018). Changing recharge pathways within an intensively pumped aquifer with high fluoride concentrations in Central Mexico. *Sci. Total Environ.* 622–623, 1029–1045. doi:10.1016/j.scitotenv.2017.12.031

Korhonen, F. J., and Johnson, S. P. (2015). The role of radiogenic heat in prolonged intraplate reworking: The Capricorn Orogen explained? *Earth Planet. Sci. Lett.* 428, 22–32. doi:10.1016/j.epsl.2015.06.039

Kundu, B., Yadav, R. K., Bali, B. S., Chowdhury, S., and Gahalaut, V. K. (2014). Oblique convergence and slip partitioning in the NW Himalaya: Implications from GPS measurements. *Tectonics* 33, 2013–2024. doi:10.1002/2014tc003633

Lacassin, R., Valli, F., Arnaud, N., Leloup, P. H., Paquette, J. L., Haibing, L., et al. (2004). Large-scale geometry, offset and kinematic evolution of the Karakorum fault, Tibet. *Earth Planet. Sci. Lett.* 219 (3–4), 255–269. doi:10.1016/s0012-821x(04)00006-8

Liu, H. B., Jin, G. S., Li, J. J., Han, J., Zhang, J. F., Zhang, J., et al. (2013). Determination of stable isotope composition in uranium geological samples. *World Nucl. Geosci.* 30 (3), 174–179. doi:10.1016/j.clay.2020.105736

Liu, W. J., Jiang, H., Shi, C., Zhao, T., Liang, C. S., Hu, J., et al. (2016). Chemical and strontium isotopic characteristics of the rivers around the badain jaran desert, northwest China: Implication of river solute origin and chemical weathering. *Environ. Earth Sci.* 75, 1119. doi:10.1007/s12665-016-5910-0

Lu, G. P., Wang, X., Li, F. S., Xu, F., Wang, Y. X., Qi, S. H., et al. (2017). Deep geothermal processes acting on faults and solid tides in coastal Xinzhou geothermal field, Guangdong, China. *Phys. Earth Planet. Interiors* 264, 76–88. doi:10.1016/j.pepi.2016.12.004

Lu, R. K., Li, Y., Sun, S. L., Liu, Y. M., Nan, G. W., Cui, H. F., et al. (2022). Middle triassic remnant of the palaeo tethys ocean, central Tibet: Constraints from the pianshishan retrograded eclogite type rocks. *Geol. J.* 57 (8), 3033–3047. doi:10.1002/gj.4453

Molnar, P., and Tapponnier, P. (1975). Cenozoic Tectonics of Asia: Effects of a Continental Collision: Features of recent continental tectonics in Asia can be interpreted as results of the India-Eurasia collision. *Science* 189, 419–426. doi:10.1126/science.189.4201.419

Moon, S., Huh, Y., Qin, J., and van Pho, N. (2007). Chemical weathering in the hong (red) river basin: Rates of silicate weathering and their controlling factors. *Geochimica Cosmochimica Acta* 71, 1411–1430. doi:10.1016/j.gca.2006.12.004

Nábělek, J., Hetényi, G., Vergne, J., Sapkota, S., Kafle, B., Jiang, M., et al. (2009). The hi-climb teamUnderplating in the himalaya-tibet collision zone revealed by the hi-CLIMB experiment. *Science* 325, 1371–1374. doi:10.1126/science.1167719

Nelson, K. D., Zhao, W. J., Brown, L. D., Kuo, J., Che, J. K., Liu, X. W., et al. (1996). Partially molten middle crust beneath southern Tibet: Synthesis of project INDEPTH results. *Science* 274, 1684–1688. doi:10.1126/science.274.5293.1684

Nicholson, K. (1993). *Geothermal fluids: Chemistry and exploration techniques*. New York NY, USA: Springer Verlag Berlin Heidelberg.

Noh, H., Huh, Y., Qin, J., and Ellis, A. (2009). Chemical weathering in the three rivers region of eastern Tibet. *Geochimica Cosmochimica Acta* 73, 1857–1877. doi:10.1016/j.gca.2009.01.005

Pande, K., Padia, J. T., Ramesh, R., and Sharma, K. K. (2000). Stable isotope systematics of surface water bodies in the Himalayan and Trans Himalayan (Kashmir) region. *J. Earth Syst. Sci.* 109 (1), 109–115. doi:10.1007/bf02719154

Pang, Z. H., Kong, Y. L., Li, J., and Tian, J. (2017). An isotopic geoindicator in the hydrological cycle. *Procedia Earth Planet. Sci.* 17, 534–537. doi:10.1016/j.proeps.2016.12.135

Pang, Z. H. (2006). pH dependant isotope variations in arc type geothermal waters: New insights into their origins. *J. Geochem. Explor.* 89 (1–3), 306–308. doi:10.1016/j.gexplo.2005.12.006

Parkhurst, D. L., and Appelo, C. A. J. (1999). *User's guide to PHREEQC (version 2): A computer program for speciation, batch reaction, one dimensional transport and inverse geochemical calculations*. Washington, DC, USA: United States Geological Survey (USGS), Water Resources Investigations Report, 312. doi:10.3133/wri994259

Piper, A. M. (1944). A graphic procedure in the geochemical interpretation of water analyses. *Trans. AGU.* 25 (6), 914–928. doi:10.1029/tr025i006p00914

Priestley, K., Jackson, J., and McKenzie, D. (2008). Lithospheric structure and deep earthquakes beneath India, the Himalaya and southern Tibet. *Geophys. J. Int.* 172, 345–362. doi:10.1111/j.1365-246X.2007.03636.x

Rai, S. S., Priestley, K., Gaur, V. K., Mitra, S., Singh, M. P., and Searle, M. (2006). Configuration of the Indian moho beneath the NW Himalaya and ladakh. *Geophys. Res. Lett.* 33, L15308. doi:10.1029/2006GL026076

Sachan, H. K., Santosh, M., Prakash, D., Kharya, A., Singh, P. C., and Rai, S. K. (2016). Metamorphic P–T conditions and CO_2 influx history of medium grade metapelites from Karakorum, Trans Himalaya, India. *J. Asian Earth Sci.* 124, 126–138. doi:10.1016/j.jseaes.2016.04.019

Schwab, M., Ratschbacher, L., Siebel, W., McWilliams, M., Minaev, V., Lutkov, V., et al. (2004). Assembly of the Pamirs: Age and origin of magmatic belts from the southern Tien Shan to the southern Pamirs and their relation to Tibet. *Tectonics* 23, TC4002. doi:10.1029/2003TC001583

Shangguan, Z., and Huo, W. (2002). δD values of escaped H_2 from hot springs at the Tengchong Rehai geothermal area and its origin. *Chin. Sci. Bull.* 47, 146–149. doi:10.1360/02tb9034

Skelton, A., Liljedahl-Claesson, L., Wästeby, N., Andrén, M., Stockmann, G., Sturkell, E., et al. (2019). Hydrochemical changes before and after earthquakes based on long-term measurements of multiple parameters at two sites in northern Iceland-a review. *J. Geophys. Res. Solid Earth* 124, 2702–2720. doi:10.1029/2018jb016757

Stuyfzand, P. J. (1999). Patterns in groundwater chemistry resulting from groundwater flow. *Hydrogeology J.* 7 (1), 15–27. doi:10.1007/s100400050177

Tan, H., Zhang, Y., Zhang, W., Kong, N., Zhang, Q., and Huang, J. (2014). Understanding the circulation of geothermal waters in the Tibetan Plateau using oxygen and hydrogen stable isotopes. *Appl. Geochem.* 51, 23–32. doi:10.1016/j.apgeochem.2014.09.006

Tang, X. C., Zhang, J., Pang, Z. H., Hu, S. B., Wu, Y., and Bao, S. J. (2017). Distribution and Genesis of the eastern Tibetan Plateau geothermal belt, Western China. *Environ. Earth Sci.* 76 (1), 31–15. doi:10.1007/s12665-016-6342-6

The Geothermal Geological Team of Tibet (1990). *Exploration report for the Yangyi geothermal field of the Tibet autonomous region*.

Tian, J., Pang, Z. H., Guo, Q., Wang, Y. C., Li, J., Huang, T. M., et al. (2018). Geochemistry of geothermal fluids with implications on the sources of water and heat recharge to the Rekeng high-temperature geothermal system in the Eastern Himalayan Syntax. *Geothermics* 74, 92–105. doi:10.1016/j.geothermics.2018.02.006

Tian, J., Pang, Z. H., Wang, Y. C., and Guo, Q. (2019). Fluid geochemistry of the Cuopu high temperature geothermal system in the eastern Himalayan syntaxis with implication on its Genesis. *Appl. Geochem.* 110, 104422. doi:10.1016/j.apgeochem.2019.104422

Tian, Z., Yang, Z. Q., Bendick, R., Zhao, J. L., Wang, S. D., Wu, X. L., et al. (2019). Present day distribution of deformation around the southern Tibetan plateau revealed by geodetic and seismic observations. *J. Asian earth Sci.* 171, 321–333. doi:10.1016/j.jseaes.2018.12.018

Vakulchuk, R., Overland, I., and Scholten, D. (2020). Renewable energy and geopolitics: A review. *Renew. Sustain. Energy Rev.* 122, 109547. doi:10.1016/j.rser.2019.109547

Wang, J. Y. "Discussions on geothermal energy exploration and utilization of China, from the point of world geothermal energy," in Proceedings of the Workshop on Chinese Geothermal Energy Exploration Scientifically, Beijing, China, 2009 (Beijing: Geology Press), 3–6.

Wang, P., Chen, X. H., Shen, L. C., Wu, K. Y., Huang, M. Z., and Xiao, Q. (2016). Geochemical features of the geothermal fluids from the Mapamyum non volcanic geothermal system (Western Tibet, China). *J. Volcanol. Geotherm. Res.* 320, 29–39. doi:10.1016/j.jvolgeores.2016.04.002

Wang, X. M., Cui, J. Y., Liu, Y. A., and Pei, L. Y. (2014). Discussion of correction method for mass fractionation effect of strontium spike isotopic ratios. *World Nucl. Geosci.* 31 (1), 48–52. doi:10.2343/geochemj.2.0448

Wang, X., and Tang, Z. (2020). The first large scale bioavailable Sr isotope map of China and its implication for provenance studies. *Earth. Sci. Rev.* 210, 103353. doi:10.1016/j.earscirev.2020.103353

Wang, Y. (2021). PhD dissertation. Yunnan, China: Institute of Geophysics China Earthquake Administration, P152.A research on geochemical characteristics of geothermal fluids in southeast yunnan province.

Wright, T. J., Parsons, B., England, P. C., and Fielding, E. J. (2004). InSAR observations of low slip rates on the major faults of Western Tibet. *Science* 305, 236–239. doi:10.1126/science.1096388

Wu, K. Y., Shen, L. C., Wang, X. G., Xiao, Q., and Wang, P. (2011). Study on hydrochemical features of hot springs in Langjiu geothermal field, Tibet, China. *Carsologica Sin.* 30 (1), 1–8.

Xu, Z. F., and Liu, C. Q. (2010). Water geochemistry of the Xijiang basin rivers, South China: Chemical weathering and CO_2 consumption. *Appl. Geochem.* 25, 1603–1614. doi:10.1016/j.apgeochem.2010.08.012

Yan, J. J. (2019). *Geochronology, Geochemistry and petrogenesis of mesozoic magmatic rocks in Shiquanhe area, Tibetan plateau* (Beijing, China: China University of Geosciences), 1–160.

Yan, Y., Zhou, X. C., Liao, L. X., Tian, J., Li, Y., Shi, Z. M., et al. (2022). *Hydrogeochemical characteristic of geothermal water and precursory anomalies along the Xianshuihe fault zone, Southwestern China. water* 14, 550.

Yao, T. D., Masson Delmotte, V., Gao, J., Yu, W. S., Yang, X. X., Risi, C., et al. (2013). A review of climatic controls on $\delta^{18}O$ in precipitation over the Tibetan Plateau: Observations and simulations. *Rev. Geophys.* 51 (4), 525–548. doi:10.1002/rog.20023

Yu, J., Zhang, H., Yu, F., and Liu, D. (1984). Oxygen and hydrogen isotopic compositions of meteoric waters in the eastern part of Xizang. *Geochemistry* 3 (2), 93–101. doi:10.1007/bf03179285

Yuan, J., Guo, Q., and Wang, Y. (2014). Geochemical behaviors of boron and its isotopes in aqueous environment of the Yangbajing and Yangyi geothermal fields, Tibet, China. *J. Geochem. Explor.* 140, 11–22. doi:10.1016/j.gexplo.2014.01.006

Zainal, S., Ismail, M. A. M., Mostafa, R., Narita, N., Mahmood, N., and Ng, S. M. (2016). Hydrogeochemistry of tunnel seepage water along the contact of zone of metasedimentary and granitic rock within the Pahang Selangor Raw Water Transfer Tunnel Project. *Arabian J. Geosciences* 9 (4), 1–11. doi:10.1007/s12517-015-2260-

Zhang, C. S., Zhang, Y. C., and Wu, M. L. (2003). Study on relationship between earthquake and hydro geochemistry of groundwater in southern part of North South Earthquake Belt in China. *J. Geomechanics* 9 (3), 21–30. (in Chinese with English abstract).

Zhao, C. P., Chen, Y. L., Wang, Y., and Zhou, Z. (2014). Geothermal field in the uppermost crust in the Ning'er Tongguan volcanic zone, Southwest China: Implications for tectonics and magmatism. *Acta Petrol. Sin.* 30 (12), 3645–3656. (in Chinese with English abstract).

Zhao, J., Yuan, X., Liu, H., Kumar, P., Pei, S., Kind, R., et al. (2010). The boundary between the Indian and Asian tectonic plates below Tibet. *Proc. Natl. Acad. Sci. U. S. A.* 107, 11229–11233. doi:10.1073/pnas.1001921107

Zhu, C. Y., Wang, G. C., Leloup, P. H., Cao, K., Mahéo, G., Chen, Y., et al. (2021). Role of the early Miocene jinhe-qinghe thrust belt in the building of the southeastern Tibetan plateau topography. *Tectonophysics* 811, 228871. doi:10.1016/j.tecto.2021.228871

Zuurdeeg, B. W., and Van der Weiden, M. J. J. (1985). "Geochemical aspects of European bottled waters, geochemical aspects of European bottled waters," in *Geothermics, thermal-mineral waters and hydrogeology*. Greece: Theophrastus, 235–264.

frontiers | Frontiers in Earth Science

TYPE Original Research
PUBLISHED 13 January 2023
DOI 10.3389/feart.2022.996583

OPEN ACCESS

EDITED BY
Maoliang Zhang,
Tianjin University, China

REVIEWED BY
Jun Zhong,
Tianjin University, China
Zhihui Cheng,
Lingnan Normal University, China

*CORRESPONDENCE
Ying Li,
subduction6@hotmail.com
Jianguo Du,
jianguodu@hotmail.com

SPECIALTY SECTION
This article was submitted to Geochemistry, a section of the journal Frontiers in Earth Science

RECEIVED 17 July 2022
ACCEPTED 14 November 2022
PUBLISHED 13 January 2023

CITATION
Cui Y, Sun F, Liu L, Xie C, Li J, Chen Z, Li Y and Du J (2023), Contribution of deep-earth fluids to the geothermal system: A case study in the Arxan volcanic region, northeastern China.
Front. Earth Sci. 10:996583.
doi: 10.3389/feart.2022.996583

Contribution of deep-earth fluids to the geothermal system: A case study in the Arxan volcanic region, northeastern China

Yueju Cui[1], Fengxia Sun[1], Lei Liu[1], Chao Xie[2], Jing Li[3], Zhi Chen[1], Ying Li[1]* and Jianguo Du[1]*

[1]United Laboratory of High-Pressure Physics and Earthquake Science, Key Laboratory of Earthquake Prediction, Institute of Earthquake Forecasting, CEA, Beijing, China, [2]The Second Monitoring and Application Center, CEA, Xi'an, China, [3]Institute of Disaster Prevention, Langfang, China

Investigations of the hot spring water and gas in the volcanic region are involved in assessing geothermal resources and understanding groundwater circulation, volcano, and earthquake activities. The origins of water and gas of the hot springs, lakes, rivers, and rain in the Arxan volcanic region (AVR), northeastern (NE) China, were investigated by conducting a field survey and geochemical analysis. The low electrical conductivity (40–835 μS/cm) and low total dissolved solids (TDS, 23.83–540.00 mg/L) of the water samples indicate that they are fresh water. $\delta^{18}O$ and δD values of the water samples range from −4.1% to −16.0% and from −61.3% to −119.9%, respectively. Enrichment of heavy isotopes in the rainwater and the crater lake waters was caused by evaporation. The component H_2O of the water samples predominantly originated from the meteoric water, with less than 1 vol% contributed by deep-earth fluids. Ions in the rain sample were predominantly derived from sea salt and continental aerosol. Ions in the surface water samples had multiple origins (mineral dissolution, atmospheric, and anthropogenic sources). While the ions in the hot spring water were predominantly derived from both the dissolution of rocks and deep-earth fluids, the latter contributed 73%–87% of Cl^- and 86%–99% of Na^+ to the hot spring waters. Gases from the hot springs were composed of more than 95% N_2 and less than 5% O_2 and Ar, with $^3He/^4He$ ratios of 0.14–1.17 R_A (R_A=1.4×10^{-6}). Excess N_2, Ar, He, and CO_2 of the hot springs were mainly derived from both the crust and upper mantle. About 3%–23% of the total He in the bubbling gases from the crater lake waters and hot springs is derived from the mantle, implying a supplement of heat energy from the mantle to the geothermal systems. Significantly, about 12% of the He dissolved in the Budonghe water is derived from the mantle, indicating that plenty of mantle-derived heat transported by deep-earth fluids keeps the river water from freezing. Our results indicate that Cl and Na ions and $^3He/^4He$ ratio are the feasible geochemical indicators for source partitioning of geothermal fluids.

KEYWORDS

geothermal system, Arxan volcanic region, hot spring water, $^3He/^4He$ ratio, fluids

1 Introduction

The origins of geothermal fluids in the volcanic areas are involved in investigations of natural resources, environment, and hydrological cycle. Ion concentrations and isotope ratios of groundwater are the efficient indicators of water origin, circulation process of groundwater, geothermal potential, and volcanic activity (Giggenbach et al., 1993; Shaw et al., 2003; Taran, 2009, 2011; Benavente et al., 2016; Tardani et al., 2016; Rizzo et al., 2019). Therefore, geochemical observations of fluids can reveal the fluid origins, magmatic and seismic processes, and dynamic processes in the deep earth.

It is a major challenge in geoscience to decipher the complexity of fluids and minerals in the earth's interior. Sources of dissolved solids in groundwater can be divided into three categories: dissolution of minerals in circulation, deep-earth fluids, and atmospheric and anthropogenic sources. The deep-earth fluids, meaning waters, gases, and supercritical fluids that are derived from the deep crust and mantle, may be composited with different genetic types of fluids such as initial, magmatic, metamorphic, deep hydrothermal, and diagenetic fluids that usually mix into geothermal fluids. The origins of ions and gases can be traced by using concentrations and isotopic ratios of the chemical species and techniques of statistical analysis (Han et al., 2019; Li, 2020; Chen et al., 2021). A variable non-sea-salt contribution usually causes the slope to differ from the seawater ratio and the intercept to differ from zero (Keene et al., 1986). Cl^- and Na^+ are the most reliable indicators for discriminating and partitioning sources of ions in the spring waters because they tend to exist in aqueous solution during water circulation, while other ions are partially fixed in secondary minerals.

Ion concentrations, $\delta^{18}O$ and δD, of water have been widely used for investigating the origins of geothermal fluids. For instance, the high values of $\delta^{18}O$, δD, $\delta^{13}C$, and Cl^- concentrations of spring waters in Oita Plain, Japan, implied an origin of andesitic-magmatic steam or metamorphic water, while the low values of δD and Li and B concentrations of groundwater indicated meteoric water (Amita et al., 2005). Li et al. (2012) investigated the water vapor sources of meteoric water in NE China using $\delta^{18}O$ and δD data. The hydrochemical data indicated that the main stream water of the Kherlen River in eastern Mongolia, neighboring to the west of the Arxan volcanic region (AVR), were recharged by meteoric water from the headwater region of more than 1,650 m altitude (Tsujimura et al., 2007). $\delta^{18}O$ and δD values of the lake, river, and well waters in the Lake Hulun Basin neighboring to the north of the AVR indicated that the waters originated from meteoric water and suffered evident evaporation (Gao et al., 2018).

The concentrations of gaseous components, He/Ne, $^4He/^{20}Ne$, N_2/Ar, $^3He/^4He$, $CO_2/^3He$, and $\delta^{13}C$, provide insight on the sources of the gaseous species in the geothermal and volcanic systems (Giggenbach et al., 1993; Shaw et al., 2003; Du et al., 2005; Taran, 2009; 2011; Xu et al., 2013; Benavente et al., 2016; Rizzo et al., 2019; Bini et al., 2022), secondary processes of geothermal fluids (Zhang et al., 2016; Barry et al., 2020), volcanic and seismic activities (Chen et al., 2014; Zhou et al., 2015; Tardani et al., 2016), and contribution of volcanic gas to environment (Sun et al., 2020; Zhao et al., 2021). The regional variations in $^3He/^4He$, $\delta^{13}C$ of CO_2, $\delta^{15}N$, and $^{87}Sr/^{86}Sr$ values of hydrothermal fluids along an intra-arc fault system in the southern Volcanic Zone of the Chilean Andes indicated the geothermal gas was a mixture of mantle-derived gas and radiogenic gas in the crust (Tardani et al., 2016). The molecular and isotopic data of hot spring fluids and fumarolic gases in the Tateyama volcanic hydrothermal system in Japan (Seki et al., 2019), the Tengchong volcanic area (Du et al., 2005) and western Sichuan Province (Du et al., 2006) in southwestern China, and the Wudalianchi volcanic field (Du et al., 1999; Xu et al., 2013), Changbaishan volcano (CBV) (Wei et al., 2016), and the Songliao continental rift system (Zhao et al., 2019) in NE China indicated the gases were predominantly derived from the mantle and crustal sources.

The mantle worldwide and regionally appears heterogeneous. The crust and upper mantle in NE China are characterized by fluctuation of Moho depth, mantle uplift in the rift valley and geophysical and geochemical heterogeneities (Jia and Zhang, 2020). The crust thickness in the Greater Khingan Range orogenic belt ranges from 34.5 to 43.5 km, while it becomes 32.4–36.2 km in the Songliao Basin in the east (Li et al., 2014; Jia and Zhang, 2020). The statistic histogram of 279 $^3He/^4He$ ratios of mantle xenoliths in eastern China shows multiple peaks with a wider range from 0.1 to 12 R_A (excluding eight individual data from 12.1 to 33 R_A; R_A is atmospheric $^3He/^4He = 1.4\times10^{-6}$) (Cui et al., 2022). Isotopic ratios of noble gases in mantle xenoliths in the orogenic belt and rift valley indicate that the mantle in NE China is heterogeneous. Obviously, the geochemical characteristics of the mantle in NE China differ from those in the middle ocean ridge and volcanic arc (Sano and Marty, 1995; Shaw et al., 2003; Roulleau et al., 2015).

The previous investigations in AVR mainly involved geology, volcanology, geothermics and hydrology (Tang, 1984; Sun, 1999; Zhang, 2017; Gu et al., 2017; Chen et al., 2021). The hydrogeochemical investigations for 36 hot springs (defined as their temperatures being 5°C higher than the local annual atmospheric temperature) around the Hot Spring Museum, a natural museum established for tourism and spa in the Arxan city, suggested that the hot spring waters were chemically classified into $Ca{\cdot}Na\text{-}HCO_3{\cdot}SO_4$, $Na{\cdot}Ca\text{-}HCO_3$, and $Na\text{-}HCO_3$ (Gu et al., 2017; Zhang, 2017), and the residence time of high-temperature hot spring waters ranges from 70 a to 90 a, and that of low-temperature hot springs/shallow groundwater is about 10 a (Gu et al., 2017). Recently, the groundwater in the basalts of Arxan was considered exogenous water from the Tibetan Plateau based on the data of the water balance relationship and $\delta^{18}O$ and δD values (Chen et al., 2021). Zhao et al. (2021) reported that

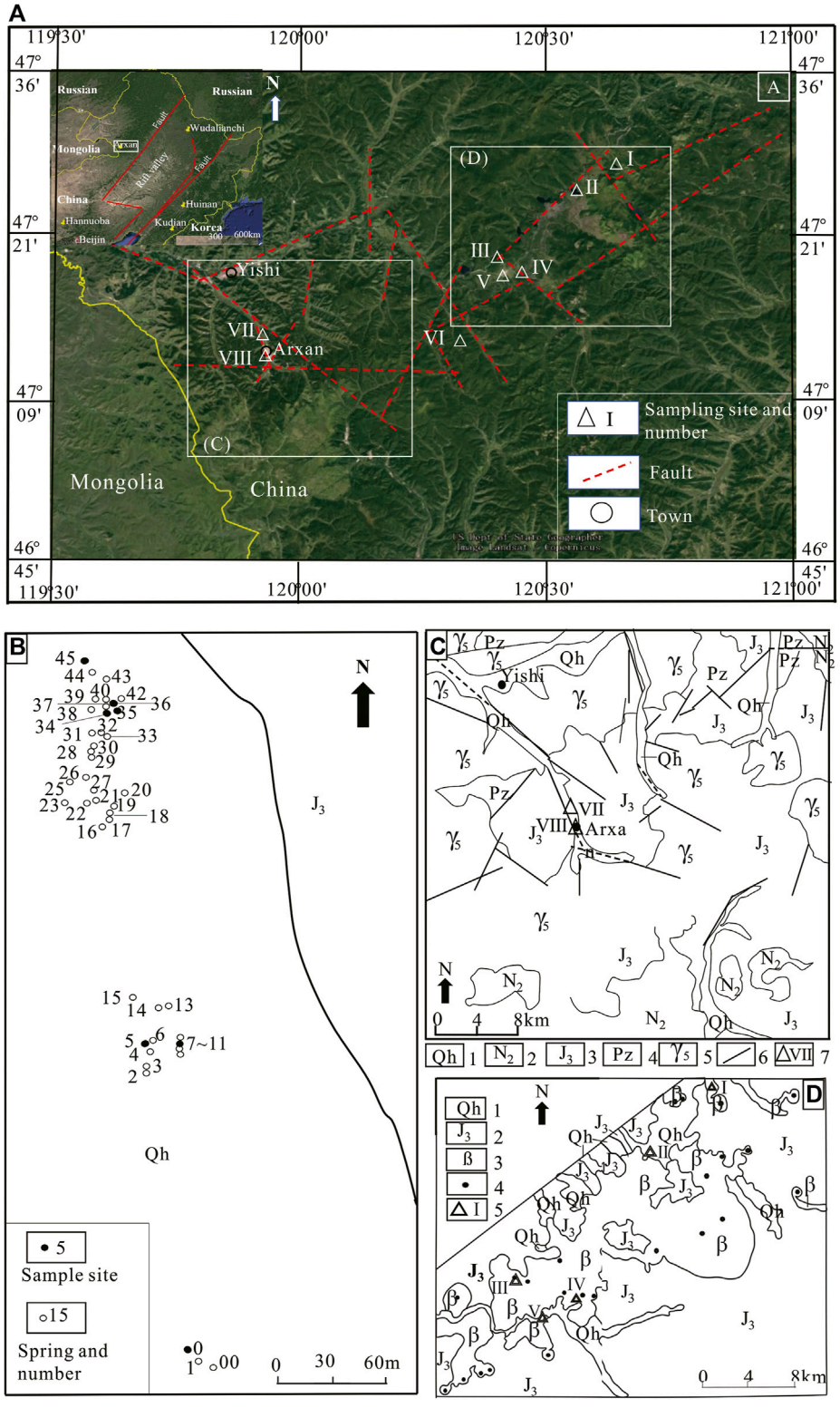

FIGURE 1
(A) Topography of the study area and vicinity, showing main faults and the sampling sites (the image from Google Earth); the inset of the DEM image shows the location of the study area; sampling sites: I- Tuofengling; II- Dujuanhu; III- Tianchi; IV- Dichi; V- Budonghe; VI- Jinjianggou; VII- Wuliquan; VIII- the Hot Spring Museum. **(B)** Hot spring locations at the sampling site no. VIII, 45 springs occur in an area of 700 m long from north to south and 70 m wide from east to west (modified after Zhang (2017)). **(C)** Geological map of the Arxan volcanic region (square C in A); 1 -
(*Continued*)

FIGURE 1 (Continued)
Holocene fluvial sediments; 2 - Neogene basalts, andesitic basalt, and andesite; 3 - Late Jurassic rhyolite and rhyolitic pyroclastic rocks; 4 - Paleozoic clastic rocks intercalated limestone; 5 - moyite; 6 - fault; 7 - sampling site and number (modified after Xie et al. (2011)). **(D)** Distribution of Holocene volcanism and sampling sites (square D in A), 1 - Holocene fluvial sediments; 2 - Late Jurassic rhyolite and rhyolitic pyroclastic rocks; 3 - Holocene alkali olivine basalts; 4 - Holocene crater; 5 - sampling site and number (modified after Fan et al. (2011)).

gases from two hot springs in the AVR were mainly composed of N_2 with low $^3He/^4He$ ratios (c. 0.1 R_A), high $^4He/^{20}Ne$ ratios (150–380), and $\delta^{13}C$ values of CO_2 (-6.2% to -13.6%). They concluded that the spring gases were mainly derived from the crust. So far, the origins of hot spring fluids in the AVR remain debated. This paper aims at revealing the contribution of deep-earth fluids to the geothermal system in the AVR based on the molecular and ion concentrations and isotope compositions of the hot spring fluids.

2 Geological and hydrothermal setting

The AVR is famous for a lot of hot springs and Quaternary volcanoes. It is located at the west margin of northeastern (NE) China, where volcanic eruptions were very violent in the Cenozoic Era and produced more than 590 volcanoes and about 50,000 km^2 of exposed basalt (Liu et al., 2001). The altitudes in the AVR range from 900 m to 1,700 m (Figure 1A). The annual mean temperature is −2.5°C, monthly averages of temperature range from 10.5°C to −31.2°C with the lowest temperature of -45.7°C recorded on 1st January 2001. Annual precipitation was 450 mm during 1951–2015, of which 80%–90% fell during June–September, whereas annual evaporation capacity is up to 1,116 mm (Gu et al., 2017; Chen et al., 2021).

The AVR tectonically belongs to the Greater Khingan Range orogenic belt that connects with the northern part of the continental rift valley on the east. There are mainly five groups of faults in the study area: NEE, NNE, NW, NNW, and EW trending faults. The NEE-trending Halaha River fault cuts the lithosphere with a length of ca. 500 km. The deep-cut faults provide two channels for Quaternary magma migration from the mantle: one displays a high temperature and fluid-enriched body approaching the depth of 10–12 km, and another has become cold above a depth of 30 km (Tang et al., 2005). The series of NNW-trending basement rifts deeply cut the crust, favoring the deep cycle of groundwater and the formation of hot springs.

Mesozoic igneous rocks are widely distributed in the AVR with a small area of Paleozoic clastic strata (Figure 1C). The Paleozoic strata are composed of Late Ordovician metamorphic clastic rocks and volcanic-sedimentary clastic rocks, Late Silurian metamorphic clastic rocks, and Early–Middle Devonian clastic rocks sandwiched with biogenic limestone. The Mesozoic strata are mainly Late Jurassic rhyolitic lava and volcanic clastic rocks. The Cenozoic strata are Neogene clastic rocks and black basalts and Quaternary sediments (Fan et al., 2011; Xie et al., 2011).

Magmatic rocks in the study area are mainly the Early Indosinian and the Late-Middle Yanshanian porphyroid potassic granite, monzonitic granite, and moyite and Neogene and Quaternary basalts (Figures 1C, D). Alkaline basalts in the Greater Khingan Range are characterized by high MgO and Ni concentrations, high CaO/Al_2O_3 ratios, enrichment of large lithophile elements and positive Nb-Ta anomalies, and moderately depleted Sr–Nb–Hf isotopic ratios. The basalts could be derived from the deep primary mantle, possibly from ancient primordial peridotite (Fan et al., 2003; Xue et al., 2019). Quaternary basalts in the AVR cover an area of ca. 100 km^2 and erupted from more than 54 craters in the Middle-Late Pleistocene and Holocene (Fan et al., 2011). The Yanshan Volcano is the youngest volcanic crater and has a radiocarbon age of 2,000 years (Bai et al., 2005).

Groundwaters in the study area can be classified into three types: (1) pore water in Quaternary fluvial sediments, discharging through river beds; (2) bedrock fissure water in Late Jurassic volcanic rocks, recharged by meteoric water and discharged through underflow to the river valley; and (3) vein-type fissure water in the fault zones (Chen et al., 2021). Surface waters include river water (the Halaha River and the Arshangole River), barrier lakes, and crater lakes. There are 45 hot springs around the Hot Spring Museum in Arxan town (Figure 1B), whose water temperatures range from 2 to 40°C. A unique phenomenon is that the distance between the low-temperature hot spring (2°C) and the high-temperature hot spring (40°C) is just 0.3 m, which could be caused by different amounts of deep-earth fluid recharge.

The heat flow in the Greater Khingan Range is 40.2 mW/m^2. The estimated Moho heat flow is 33.2 mW/m^2 (Sun, 1999). Though the regional heat flow is low, three geothermal fields have been found in the AVR (Qi et al., 2012). One is the Jinjiangguo (JJG) Valley geothermal field, which is composed of two geothermal zones controlled by the NE and NNW trending faults in granite and characterized by lower resistance. The geothermal water age was dated as 8,150 ± 90 a (Qi et al., 2012). The second one is the Yinjianggou Valley (YJG) geothermal field, which is controlled by a NNW-trending fault. The third one is the Wuliqiao geothermal field, which is controlled by EW- and NNW-trending faults (Qi et al., 2012). The thermal energy is derived from the mantle (magma) and radiogenic heat in the crust (Qi et al., 2012). The heat energy of the hot springs around the Hot Spring Museum could be mainly derived from radiogenic heat in the crust (Sun, 1999).

TABLE 1 Ion concentrations and isotopic ratios of the water samples from the Arxan volcanic region.

ID	Location	Type	T (°C)	EC (μS/cm)	PH	Li^+	Na^+	NH_4^+	K^+	Mg^{2+}	Ca^{2+}	F^-	Cl^-	NO_3^-	SO_4^{2-}	HCO_3^-	TDS	i.b %	$\delta^{18}O$	δD	Water type	Na*	Cl*
						mg/L													‰V-SMOW			%	
AW-0	VO	Rain	20.0	41.3	7.74	0.01	2.0	0.5	0.6	0.4	5.9	0.1	0.5	3.7	3.2	19.8	26.9	−0.32	−8.5	−94.4	$Ca\text{-}HCO_3$	98	85
AW-1	Dichi	Lake	19.2	95.8	7.66		7.9	0.4	1.8	3.5	10.2	0.4	1.4	0.9	6.9	56.2	61.4	−0.32	−13.1	−103.5	$Na\text{-}HCO_3$		
AW-2	TFL Tianchi	Lake	18.6	40.0	7.31		2.7	0.4	0.5	2.1	4.2	0.1	0.5	0.6	2.0	28.1	27.2	−0.34	−5.1	−61.3	$Na\text{-}Ca\text{-}HCO_3$		
AW-3	Dujuanhu	Lake	19.8	51.4	7.29		3.3	0.5	0.3	2.0	7.4	2.4	0.4	3.0	5.8	28.1	39.2	−0.33	−10.9	−87.6	$Ca\text{-}Mg\text{-}HCO_3$		
AW-4	Tianchi	Lake	21.8	40.3	6.92		2.4	0.3	0.2	2.2	3.7	0.8	0.7	1.3	1.2	22.1	23.8	−0.30	−4.1	−61.4	$Ca\text{-}Mg\text{-}HCO_3$		
AW-5	Budonghe	River	7.5	90.8	7.68	0.01	6.2	0.5	1.1	3.7	11.2	0.2	0.03	0.1	7.2	58.3	59.2	−0.32	−13.4	−106.2	$Ca\text{-}Mg\text{-}HCO_3$		
AW-6	JJG	HS	37.5	614.0	7.59	0.04	120.6	3.0	3.1	1.4	20.4	14.6	20.6	0.0	151.3	152.7	411.3	−0.48	−15.1	−111.7	$Na\text{-}HCO_3$		
AW-7	JJG	Well	19.9	577.0	7.58	0.04	121.3	3.5	3.2	1.5	22.4	9.8	18.1	0.1	137.9	152.7	394.0	−0.44	−15.0	−111.4	$Na\text{-}HCO_3$	98	83
AW-8	JJG	HS	27.4	471.0	7.79	0.03	81.7	3.6	2.7	2.9	30.4	6.3	12.8	1.8	101.4	158.7	323.9	−0.42	−14.6	−111.1	$Na\text{-}HCO_3$	96	76
AW-9	Wuliquan	HS	3.5	391.0	7.76	0.02	53.6	3.3	2.4	5.9	38.7	1.8	22.1	30.5	39.2	156.7	275.9	−0.32	−16.0	−118.4	$Na\text{-}HCO_3$	94	86
AW-10	HSM no. 34	HS	36.4	644.0	8.18	0.07	169.6	4.5	4.1	2.7	12.0	10.5	16.1	8.4	69.4	321.4	458.0	−0.41	−16.0	−116.8	$Na\text{-}HCO_3$	98	81
AW-11	HSM no. 35	HS	25.1	691.0	7.77	0.05	155.0	4.4	4.3	2.7	25.1	7.6	17.2	20.3	69.0	372.5	491.7	−0.43	−15.8	−115.0	$Na\text{-}HCO_3$	98	83
AW-12	HSM no. 36	HS	24.3	761.0	8.05	0.06	182.1	3.9	4.4	1.7	17.2	8.7	19.5	20.8	82.7	398.5	540.0	−0.46	−15.3	−113.8	$Na\text{-}HCO_3$	98	85
AW-13	HSM no. 45	HS	23.9	835.0	7.97	0.08	219.1	4.1	4.2	1.1	15.0	11.0	23.6	26.8	114.7	385.5	612.3	−0.45	−15.6	−114.4	$Na\text{-}HCO_3$	99	87
AW-14	HSM no. 7	HS	17.0	179.8	7.83	0.01	35.4	3.3	2.1	1.9	8.4	1.8	3.8	5.3	20.1	108.3	136.2	−0.44	−15.7	−119.9	$Na\text{-}HCO_3$	92	
AW-15	HSM no. 5	HS	16.6	211.3	7.71		21.8	2.5	1.5	4.1	24.8	1.4	11.2	21.1	22.2	80.1	150.5	−0.31	−15.4	−118.3	$Na\text{-}HCO_3$	86	73
AW-16	HSM no. 3	HS	17.0	408.0	7.97	0.03	78.3	4.4	3.2	3.2	22.6	3.3	15.8	35.5	46.4	175.4	300.3	−0.40	−15.3	−116.2	$Na\text{-}HCO_3$	96	81

VO - the volcano observatory; HS - hot spring; TFL - Tuofengling; JJG - Jinjiangguo; empty cell is less than the detection limit; Na* and Cl*- calculated percentages of Na^+ and Cl^- derived from deep-earth fluids.

10.3389/feart.2022.996583

3 Sample and method

The water and gas samples were collected from the AVR in August 2010 (Figure 1). The field measurements of water temperature, electrical conductivity (EC), and pH were conducted with the portable instruments. The samples for hydrochemical analysis were collected with the 250-ml plastic bottles, and for stable isotopic analysis of H and O with the 2-ml plastic bottles. The gas samples were collected by the gas drainage method in 1,000-ml glass bottles and sealed with rubber caps (Du et al., 2006). Totally, 17 water samples were collected from the springs, crater lakes, river, and rain, and eight gas samples were collected including seven bubbling gases and one dissolved gas in the water of the Budonghe River (at the sampling site V in Figure 1). The rain sample is the thundershower water dropped down from the building rooftop after filtering dust particles.

Concentrations of Li^+, Na^+, NH_4^+, K^+, Ca^{2+}, Mg^{2+}, F^-, Cl^-, NO_3^-, and SO_4^{2-} were measured with a Dionex ICS-900 ion chromatography system with the standard configuration (reproducibility within ±2%). The HCO_3^- concentrations were measured by the standard titration procedures with a ZDJ-100 potentiometric titrator (reproducibility within ±2%) (Chen et al., 2014). Ion charge balance errors (I.B.) of the hydrochemical data are less than ±5%. The total dissolved solid (TDS) value was calculated by, $\sum X_i - (HCO_3)/2$, subtracting total ion concentration minus the half of HCO_3^- concentration (Table 1). Stable isotope ratios of H and O were measured with a MAT 253 mass spectrometer at Hehai University, and the $\delta^{18}O$ and δD values were reported referring to the V-SMOW standard with errors of 0.1% and 2‰, respectively (Chen et al., 2021).

The N_2, O_2, Ar, CO_2, CH_4, and He concentrations of the gas sample were analyzed with a Finnigan MAT-271 mass spectrometer, with a precision of ±0.1%. Helium and neon isotope compositions of the gas samples were measured with an MM5400 mass spectrometer at the Laboratory of Gas Geochemistry, the Institute of Geology and Geophysics, the Chinese Academy of Sciences. $\delta^{13}C$ values of CH_4 and CO_2 were measured with the GC-IRMS analytical system, a gas chromatography (Agilent 6890)–stable isotope ratio mass spectrometer, and the values of $C^{13}C$ are reported relative to PDB in per mill with an error of ±0.5‰ (Li et al., 2007; Zhou et al., 2015). It is worthy of mention that the He concentration and $^4He/^{20}Ne$ ratios of dissolved gas in the Budonghe water are double of atmospheric values. The $^3He/^4He$ ratio was less than the atmospheric ratio, which indicates the sample was not contaminated by air during sampling and analysis.

4 Results

The temperatures of the hot spring waters are in a range of 2.3°C–37.5°C. The water temperatures of the springs no. 5 at the Hot Spring Museum and Wuliquan (at 2.5 km northwest Arxan town) are lower than those of Budonghe water (7.5°C). The water samples have low electric conductivity (40–835 μS/cm) and low TDS (23.83–540.00 mg/L). TDS values of the surface (river and lake) waters are lower than those of the hot spring waters. Abundance of the majority cations and anions is generally in the order of $Na^+ > Ca^{2+} > Mg^{2+} > K^+ > NH_4^+$ and $HCO_3^- > SO_4^{2-} > Cl^-$, $NO_3^- > F^-$, respectively. $\delta^{18}O$ and δD values of the water samples range from -4.1% to −16.0% and -61.3% to -119.9%, respectively. The lake waters are more enriched in heavy isotopes (^{18}O and D) than the hot spring waters (Table 1).

The molecular and isotope compositions of the gas samples are listed in Table 2 including some published data (Zhao et al., 2021) in the AVR for comparison. The N_2 concentrations of the gas samples from the AVR are more than 95%, and others together are less than 5%. $^3He/^4He$ ratios are in a range of 0.20×10^{-7} ~ 1.64×10^{-6}. $^4He/^{20}Ne$ ratios of the surface waters are approximately equal to the atmospheric value (0.32), but those of hot spring waters are much higher than the atmospheric value. CO_2 concentrations are lower (0.13%–0.41%) and $\delta^{13}C$ of CO_2 from -22.3% to -6.2%. $\delta^{13}C$ of methane (C_1) from Tianchi is -51.5%, indicating the biogenic origin of C_1, but $\delta^{13}C$ of C_1 from the geothermal well in JJG is 1.4‰, hinting at an abiogenic origin. $^{21}Ne/^{22}Ne$ and $^{20}Ne/^{22}Ne$ ratios are approximated by the atmospheric values (0.029 and 9.78, respectively).

5 Discussion

5.1 Origins of the water components

5.1.1 Isotopic compositions of hydrogen and oxygen

Most $\delta^{18}O$ and δD values of the water samples are scattered nearby the global meteoric water line (GMWL, $\delta D = 8.17\delta^{18}O + 10.35$, Rozanski et al., 1993) and the local meteoritic water line (LMWL) in NE China ($\delta D = 7.20\delta^{18}O - 2.39$, Li et al., 2012), but some shift far to the right side of the lines (Figure 2). The coordinates (−13.1% and −97.0%) of the intersection between the GMWL and LMWL can be regarded as the mean value of the initial source water (Han et al., 2019). The slop and intercept of the LMWL are smaller than those of the GMWL, indicating evaporation effect and multiple origins of waters (Tsujimura et al., 2007; Li et al., 2012; Han et al., 2019). The isotopic data of the spring and river waters in the AVR, the spring waters in Wudalianchi (Du et al., 1999) and CBV (Shangguan et al., 1996), and the river waters in Oita Plain, Japan (Amita et al., 2005), are scattered along the GMWL, indicating that those waters are mainly derived from the Pacific Ocean. This conclusion is supported by the fact that the meteoric water in northeastern China is mainly derived from the Pacific Ocean during the summer monsoon season. The wide ranges of $\delta^{18}O$ and δD values (Table 1) indicated that the different kinds of waters experienced different processes of isotopic fractionation.

TABLE 2 Molecular and isotope compositions of gases from the springs and lakes in the Arxan volcanic region.

Location	T ˚C	Sampling date	N_2	O_2	Ar	CO_2	N*	Ar*	CH_4 ×10^{-6}	He ×10^{-6}	$^3He/^4He$ ×10^{-6}	$^3He/^4He$	$^3He/^4He^*$	$\delta^{13}C_{CO2}$ ‰PDB	$\delta^{15}N$ ‰ Air	$^{20}Ne/^{22}Ne$	$^{21}Ne/^{22}Ne$	$^4He/^{20}Ne$ ×10^3	N_2/Ne	He (%)			
			(%)									(R/R_A)								Atm	LM	CR	PM
Dichi	19.2	2010.08	95.55	2.15	1.86	0.34	91.65	1.76	98.0	6.0	1.41	1.01	1.02	−15.9	1.9	9.96	0.028	0.44	0.12	56	21	23	5
TFL Tianchi	18.6	2010.08								7.0	1.64	1.17	1.53			11.50	0.028	0.36		68	23	9	6
Tianchi	21.8	2010.08								4.0	1.12	0.80	0.27			9.77	0.025	0.34		73	3	24	1
Budonghe	7.5	2010.08								9.0	0.92	0.66	0.44	−18.4		10.06	0.027	0.62		39	12	48	3
JJG HS	37.5	2010.08								8212.0	0.29	0.21	0.21			9.72	0.026	385.30		0	9	91	2
JJG HS	19.9	2010.08	97.19	0.56	1.73	0.41	96.17	1.70	12.0	7338.0	0.30	0.22	0.22	−21.0		10.05	0.023	293.45	0.12	0	9	90	2
HSM no. 34	27.4	2010.08								6469.0	0.23	0.16	0.16	−18.2		10.54	0.026	257.79		0	7	93	2
HSM no. 0	3.5	2010.08								1.0	0.27	0.19	0.16	−22.3		9.80	0.025	7.03		3	7	90	2
JJG HS[a]	36.6	2018.09	96.70	1.45	1.45	0.18	94.07	1.38		3191	0.238	0.17	0.17	−6.2				334	0.30	0	7	93	2
JJG HS[a]	36.6	2018.09	95.83	1.83	1.14	0.26	92.51	1.05		2840	0.196	0.14	0.14	−8.7	1.3			152	0.34	0	6	94	1
JJG HS[a]	24.8	2018.09	96.60	1.93	1.19	0.14	93.10	1.10		1457	0.252	0.18	0.18	−10.7	1.6			306	0.66	0	8	92	2
JJG HS[a]	24.8	2018.09	96.53	2.01	1.18	0.12	92.88	1.08		1585	0.224	0.16	0.16	−13.7	1.7			384	0.61	0	7	93	2
JJG HS[a]	24.8	2018.09	96.56	1.97	1.19	0.13	92.99	1.09															
Air			78.08	20.95	0.93	0.04			1.80	5.24		1.4		−7	0	9.78	0.029	0.318	149.3				
ASW[b]			17.070	9.409	0.459													0.245					

a. after Zhao et al. (2021); b. gas concentration in air-saturated water (ASW) at 3 ˚C (ml/L) after Weiss (1970, 1971); empty cell is no data; N*: excess N_2 corrected by the N_2/O_2 ratio of ASW at 3 ˚C, $N^*=N_2-1.814\ O_2$; Ar*: excess Ar corrected by the O_2/Ar ratio of ASW at 3 ˚C, $Ar^*=Ar-O_2/20.5$; $^3He/^4He^*$: ASW-corrected $^3He/^4He$ ratio; Atm: percentage of atmospheric He in the total He of the hot spring gases; LM: the estimated percentage of mantle-derived He considering the HNB $^3He/^4He$ ratio (2.1 R_A) as the local mantle helium source; CR: percentage of crustal He; PM: the estimated percentage of mantle helium considering the MORB $^3He/^4He$ ratio (8 R_A) as the primary mantle source; others are same as in Table 1.

10.3389/feart.2022.996583

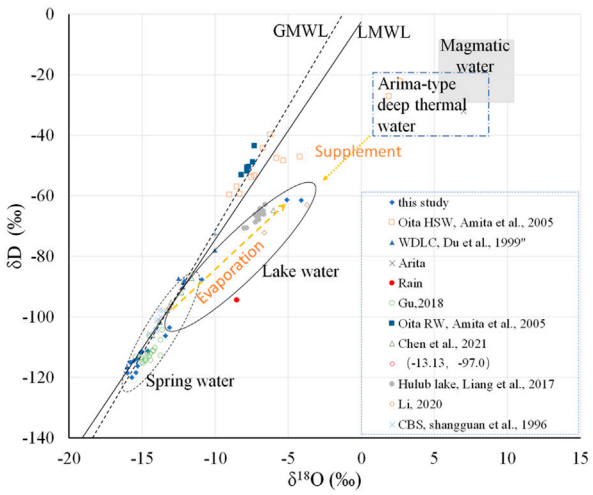

FIGURE 2
Plot of $\delta^{18}O$ vs. δD; dashed line (GMWL) is the global meteoric water line (Rozanski et al., 1993); sold line (LMWL) is the local meteoric water line (Li et al., 2012); red circle is the intersection of the GMWL and LMWL; red solid circle is the rain sample; for comparison, our data and the reported data of spring and river waters in the AVR (Gu et al., 2017; Li, 2020; Chen et al., 2021), Oita HSW and Oita RW - hot spring water and river water in Oita Plain and Arita - deep geothermal fluid in Japan (Amita et al., 2005), WDLC - spring water in the Wudalianchi volcanic area (Du et al., 1999), CBS - data of hot spring water in the Tianchi volcanic area in Changbai Mountains (Shangguan et al., 1996), and Hulun Lake - lake water data (Liang et al., 2017) were plotted.

$\delta^{18}O$ and δD values of the rain sample (AW-0) are scattered far from the LMWL (Figure 2). The heavier isotope compositions of the rain sample are concordant with those of rain in the Hulun Lake Basin (Liang et al., 2017), NE China (Li et al., 2012), and eastern Mongolia in summer (Tsujimura et al., 2007). Therefore, the heavier isotope compositions of the rain sample can be attributed to the seasonal isotopic variations of meteoric water. In the east-west extended climate zone from the Greater Khingan Range to the Mongolia Plateau, the isotopic compositions of H and O in meteoric water are characterized by obviously seasonal variation of more negative values in winter than those in summer (Tsujimura et al., 2007; Gao et al., 2018; Li, 2020).

The surface water samples (AW-1–AW-5) were relatively enriched in heavy isotopes but depleted in the TDS (<62 mg/L) (Table 1; Figure 2). $\delta^{18}O$ and δD values of water samples from the Dichi (a crater lake of the maar volcano) and Budonghe are similar. The water samples from the Tianchi and Tuofengling (TFL) Tianchi, two crater lakes on the volcanic cones, are more enriched in heavy isotopes. The Dujuehu is a barrier lake, whose water is more enriched in D (Table 1). The d-excess ($\delta D - 8.17\delta^{18}O$) of the lake water samples is much lower than that of the LMWL (Figure 2). Such isotopic shifts can be mainly attributed to the evaporation of raindrops and lake water caused by higher evaporation capacities.

δD and $\delta^{18}O$ values of seven water samples collected at the Hot Spring Museum and three water samples from the hot springs in JJG and previous results (Sun, 1999; Gu et al., 2017; Li, 2020; Chen et al., 2021) scattered nearby the LMWL, which indicates that the hot spring waters in the AVR mainly originated from meteoric water (Figure 2). The depletion of heavy isotopes in the hot spring waters can be explained by the air temperature effect because the isotopic fractionations of O and H in meteoric water are mainly related to the thermal dynamics of water vapor condensation. Both δD and $\delta^{18}O$ values of meteoric water and surface air temperature in north China (latitude higher than 36°N) have positive correlation. $\delta^{18}O/T$ gradient was 0.52‰/°C, and δD/T gradient was 4.27‰/°C (Zhang et al., 2008). Let us take the Hailun station in the Songliao Basin (47.45°N, 126.93°E, an altitude of 236 m, an annual mean of 5.5°C, and 480 km to NE Arxan) of the Chinese Network of Isotopes in Precipitation as a reference, the mean values of $\delta^{18}O$ and δD of meteoric water are −12.5% and −92.2% at the Hailun station (Liu et al., 2014). The temperature difference of 8.0°C between Hailun and Arxan results in the $\delta^{18}O$ and δD differences of 4.2% and 34.2%, respectively. Consequently, the $\delta^{18}O$ and δD values of meteoric water in Arxan are estimated to be, respectively, -16.7% and -126.4%. In reverse, the isotopic coordinates of intersection between the GMWL and LMWL, regarding the mean value of recharge source water, minus the O and H isotope fractionation caused by decreasing temperature, are equal to −17.3% and 121.2%, respectively, which are concordant with the isotopic ratios of the spring waters in the AVR (Table 1).

5.1.2 Ions in the waters

The TDS values of all water samples range from 23.83 to 540.00 mg/L, indicating the waters are fresh. The waters can be chemically classified into four groups, namely, Na-HCO_3, Ca-HCO_3, Ca·Mg-HCO_3, and Na·Ca-HCO_3 by Sokolov's method (Sokolov, 1966). All the spring water samples are Na-HCO_3 type, four samples from the crater lakes are Ca·Mg-HCO_3, Na·Ca-HCO_3, Ca-HCO_3, and Na-HCO_3, one from the Budonghe River is Ca·Mg-HCO_3, and a rain sample is Ca-HCO_3 type (Table 1).

The results of the correlation analysis for the hydrochemical parameters show that there is a strong positive correlation ($r > 0.8$, Table 3) between TDS and Li^+, Na^+, K^+, NH_4^+, HCO_3^-, Cl^-, F^-, and SO_4^{2-}, indicating that the TDS of the water samples is mainly controlled by deep-earth fluids and the dissolution of rocks. This is supported by the higher Na^+ and Cl^- concentrations, TDS, and temperatures of the hot spring waters and the residence time (Gu et al., 2017). Cui et al. (2022) reported that 85% of the TDS of continental meteoric water was composed of SO_4^{2-}, Ca^{2+}, NO_3^-, NH_4^+, and Cl^-, and NO_3^- was mainly anthropogenic origin. NO_3^- has shown an obviously positive correlation with NH_4^+, Cl^-, Ca^{2+}, and K ($r > 0.5$) and a weak positive correlation with TDS (Table 3), indicating the contribution of atmospheric and anthropogenic sources, While the weak negative correlation between the couple ions of Mg-Li, Mg-Na, SO_4-Mg, HCO_3-Mg, and TDS-Mg

TABLE 3 Correlation coefficient (r) of chemical components of the water samples.

	Li^+	Na^+	NH_4^+	K^+	Mg^{2+}	Ca^{2+}	F^-	Cl^-	NO_3^-	SO_4^{2-}	HCO_3^-	TDS
Li^+	1											
Na^+	0.9936	1										
NH_4^+	0.7984	0.8227	1									
K^+	0.9157	0.9390	0.9112	1								
Mg^{2+}	−0.2887	−0.2589	0.0544	−0.0504	1							
Ca^{2+}	0.2976	0.3527	0.6378	0.5139	0.5644	1						
F^-	0.8885	0.8784	0.6884	0.7909	−0.3739	0.3134	1					
Cl^-	0.8199	0.8467	0.8677	0.8654	0.0894	0.7310	0.7802	1				
NO_3^-	0.3756	0.4200	0.6027	0.5065	0.3748	0.5490	0.1018	0.6171	1			
SO_4^{2-}	0.7921	0.7978	0.6969	0.7531	−0.2884	0.4982	0.9334	0.8159	0.1103	1		
HCO_3^-	0.9288	0.9517	0.8197	0.9361	−0.1075	0.3734	0.7211	0.7880	0.5487	0.6158	1	
TDS	0.9659	0.9840	0.8762	0.9600	−0.1488	0.5075	0.8740	0.9162	0.4867	0.8369	0.9405	1

(Table 3) may reflect water–rock interaction (dissolution, ion exchange and deposition).

In the diagram of Na–Mg–Cl concentrations (Figure 3), the data of water samples from the AVR scatter far from the marine precipitation lines (Keene et al., 1986) and show evidently different slops, indicating the contribution of those ions from marine origin is negligible. The lines of Cl-Na and Cl-TDS in the water samples and solutions leaching granodiorite at ambient conditions (Du et al., 2010) have similar slopes and intersections, while those of Na-Mg are different. TDS, Cl, and Na in the samples are much higher than those in the leaching solutions (Figure 3), which indicate the ions mainly originate from Na-Cl-enriched deep geothermal fluids and the dissolution of Na-bearing minerals.

Plagioclase is a main component of the granite, granodiorite, and andesitic basalts that are widely distributed in the AVR (Figure 1). Na and Ca cations can be dissolved into solution through the reactions between plagioclase and CO_2-bearing water.

$$H_2O + CO_2 \rightarrow H_2CO_3 \text{ then } H_2CO_3 \rightarrow H^+ + HCO_3^- \quad (1)$$

$$CaAl_2Si_2O_8 + H_2CO_3 + 1/2O_2 \rightarrow Al_2Si_2O_5(OH)_4 + Ca^{2+} + CO_3^{2-} \quad (2)$$

$$2NaAlSi_3O_8 + H_2O + 2CO_2 \rightarrow 2Na^+ + 2HCO_3^- + 4SiO_2 + Al_2Si_2O_5(OH)_4 \quad (3)$$

$$3(Na, Ca)[Al(Si, Al)Si_2O_8] + 8H_2O + 4CO_2 + 5/2O_2 \rightarrow 3Na^+ + 3Ca^{2+} + 4HCO_3^- + 3SiO_2 + 3Al_2Si_2O_5(OH)_4 \quad (4)$$

The decomposition reactions of plagioclase can be promoted by an increase in temperature, CO_2 partial pressure, and a mixture of Cl-S-enriched deep-earth fluids.

The Mg/Na and K/Na ratios of the rain and surface water samples from the AVR are concordant with those of marine precipitation (Keene et al., 1986) and water-soluble ions (Mg/Na=0.6 and K/Na=0.4) in aerosol samples in NE China (Shen et al., 2007). This indicates that the ions in the rain sample and the surface waters are mainly derived from sources of continental aerosol, sea salt, and rock dissolution.

The Cl^- concentrations of the rain and surface water samples are much lower than those of the hot spring waters, except for the sample AW-14 (Table 1; Figure 3), indicating the contribution of atmospheric and anthropogenic Cl to the hot spring waters is neglectable. Additionally, the values of Cl^- and Na^+ concentrations and Mg/Na, Cl/Na, and Cl/Mg ratios of rock solutions differ from those of the hot spring water samples (Figure 3). The Na^+ concentration in the solution is about 2 magnitudes higher than Cl^- concentration if granitic and andesitic rocks are dissolved in equal proportion. The experiments of soaking basalt and trachyandesite grains display that concentrations of Cl^-, SO_4^{2-}, and Na^+ approach the highest values in short time, and then, the highest value of Cl^- of about 3 mg/L show no obvious variation with increasing soaking time, while others varied with soaking time (Du et al., 2010). Similarly, the observed and experimental results indicated that the meteoric waters picked up chloride more rapidly than they would be congruent dissolution of basalts, resulting in Cl^- of 1–5 mg/L in the spring water (Gislason and Hans, 1987; Gislason et al., 1993). Such data indicate that the amount of Cl^- in groundwater contributed by meteoric water dissolving igneous rocks ranges from 2 to 4 mg/L. Therefore, the ions in the hot spring water could be a mixture of rock solution and deep-earth fluids.

Cl^- percentages of dissolution of rock and deep-earth fluids in the hot spring waters can be estimated by the two-member linear mixing model (Figure 4). Assuming Cl^- concentration of the end member of dissolution of rock be 3 mg/L (Gislason and Hans, 1987; Du et al., 2010) and that of the end member of deep-earth fluids be 20,000 mg/L (Oita deep geothermal water Cl: 18,649–23,787 mg/L and Na: 12,213–15,813 mg/L (Amita et al., 2005)), the volume percentages of deep-earth fluids in the AVR

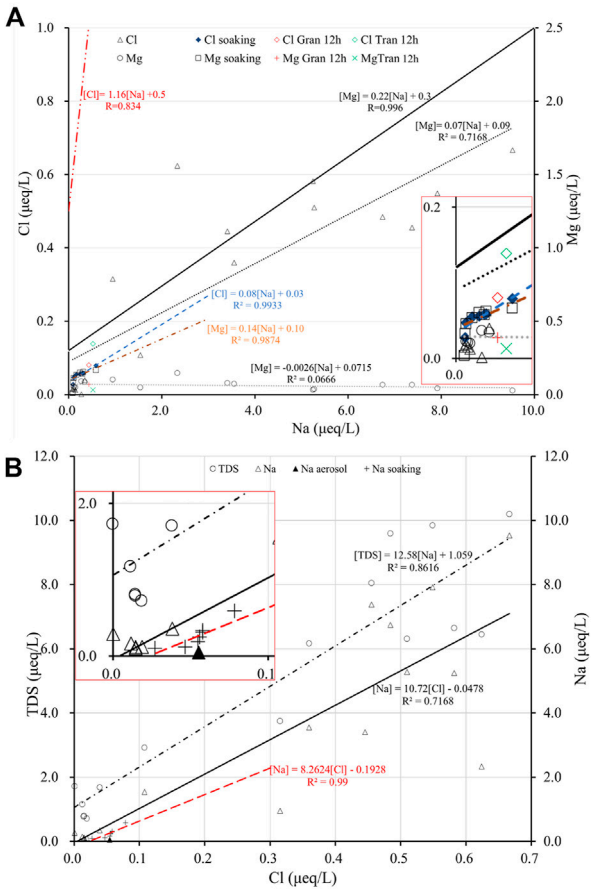

FIGURE 3
(A) Diagram of Na–Mg–Cl concentrations; the inset is at the enlarged left bottom corner; red dashed point and black solid lines stand for marine precipitation data from Keene et al. (1986); blue-dashed and brown-dashed point lines for solutions of soaking granodiorite grains for 168 h, which were extended for comparison, and two points for data of soaking 2,000-μm grains of granodiorite (Gran) and trachyandesite (Tran) under the ambient condition for 12 h (Du et al., 2010); point lines for data of this study. **(B)** Diagram of Na-TDS-Cl; the inset is at the enlarged left bottom corner; the short extended dashed line for data of solutions of soaking granodiorite grains of different sizes under the ambient condition for 168 h (Du et al., 2010).

hot spring waters were estimated in the range from 0.041 to 0.103; in other words, 73%–87% of Cl^- in the hot spring waters were derived from deep-earth fluids. Moreover, taking the Na^+ concentration of 3 mg/L in the 168-h soaking solution (Du et al., 2010) as the end member of dissolution of igneous rocks and that of 13,000 mg/L in Oita deep-earth fluids as another, the volume percentages of deep-earth fluids in the spring waters were estimated in the range of 0.14–1.66; that is, 86%–99% of Na^+ in the hot spring waters were derived from deep-earth fluids (Table 1). Obviously, less than 1 vol% of deep-earth fluids mixed in the hot spring waters can be ignored when assessing groundwater volume, but the contributions of ions and heat energy from the deep-earth fluids to the geothermal system are significant.

5.2 Origins of gases

5.2.1 Molecular compositions of the hot spring gases

The measured N–He–Ar abundance system in AVR obviously differs from the gaseous components in air-saturated water (ASW) (Table 2). The ratios of N_2/O_2 and Ar/O_2 of the samples are 44–67 and 0.07–1.11, respectively, except for 137.6 and 3.1 of the gas samples from the hot springs in JJG, which obviously differ from those of air (3.7 and 0.04) and those in ASW (1.81 and 0.03 (Weiss, 1970)). The N_2/He ratios of the gas samples range from 116.4 to 663.0, obviously differing from the atmospheric (15,000) and ASW values (11,400 (Weiss, 1970; Taran, 2011)). He concentrations in the gas samples are approximately 4 magnitudes larger than the atmospheric value, but the N_2/He ratios are about 2 magnitudes lower than ASW's value, and the $^4He/^{20}Ne$ ratios of 257.8–385.3 of the hot spring gases are much higher than the atmospheric value (0.318 (Porcelli et al., 2002)) and ASW's value (0.222 at 3°C (Weiss, 1971)). The disparities of molecular parameters between the samples and air or ASW likely indicate that amounts of atmospheric N_2 and He carried by meteoric water to the hot spring gases are not significant.

Sources of gases can be illustrated by the He–Ar–N_2 ternary diagram (Giggenbach et al., 1993; Rizzo et al., 2019; Bini et al., 2022). O_2 and Ar in hot springs are often considered to be derived from air based on the fact that O_2 and Ar concentrations in the atmosphere are much higher than those in the lithosphere, and hot spring water is mainly derived from meteoric water. In the case where all gaseous components in underground water originate from air, a part or all of the oxygen consumed by microbe respiration and the oxidation of organic and inorganic matter in the water circuit may result in N_2-rich gas. The low CO_2 concentrations in the gas samples indicate that the O_2 consumption of microbe respiration and the oxidation of organic matter in the hydrological circuit are neglectable. Data of our two gas samples are plotted nearby a magmatic source in the He–Ar–N_2 ternary diagram (Figure 5, Taran, 2011), indicating the gaseous components mainly originate from deep-earth fluids (Benavente et al., 2016). The data of the same hot springs obtained at different times (Zhao et al., 2021) shift to the air source in Figure 5, probably hinting at temporal variation or air contamination. The excess N_2 (N_2*), Ar (Ar*), and amount of non-atmospheric components can be estimated using the concentration of N_2/O_2 and Ar/O_2 ratios of ASW (Taran, 2009). Assuming the measured O_2 is derived from air and without consideration of O_2 consume in the hydrological circuit, Ar* can be estimated by Ar*= (Ar-O_2/20.5)/Ar, and excess N_2 can be estimated by N* =(N_2-

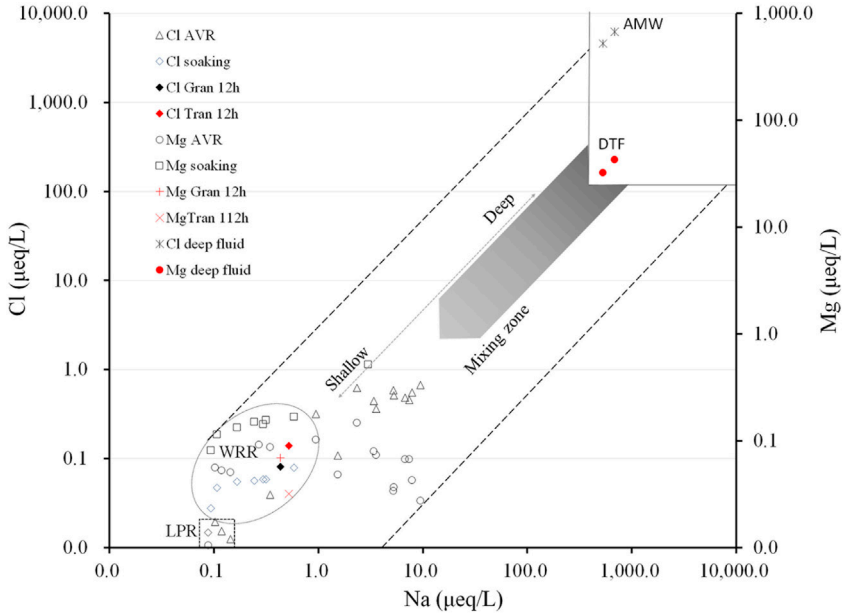

FIGURE 4
Source partitioning of Na–Mg–Cl ions in the AVR waters; data of deep-earth fluid after Amita et al. (2005); Cl AVR and Mg AVR are in this study; others (solutions of soaking granodiorite and trachyandesite) are after Du et al. (2010); LPR is the local precipitation region (rectangle); WRR is the water–rock reaction region (oval); DTR is the deep-earth fluid region; AMW displays approximately andesitic-magmatic water.

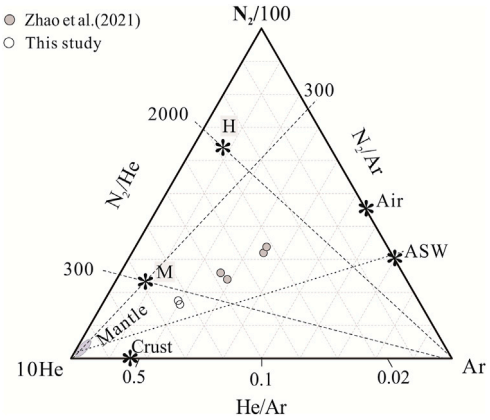

FIGURE 5
Diagram of He–Ar–N_2 concentrations of the hot spring gases in the Arxan volcanic region, M - magmatic source; H - hydrothermal source (Taran, 2011).

1.814 O_2)/N_2 (Table 2). The calculated results indicated that more than 95% of N_2 and more than 91% of Ar in the gas samples were of no-atmospheric origin (Table 2). N_2*/Ar* ratios ranged from 52.21 to 88.04, less than those of geothermal gases in the volcanic arc (107–388 (Roulleau et al., 2015)) and mantle (350 (Taran, 2011)). The low N_2*/Ar* ratios can be attributed to the contribution of radiogenic Ar produced by ^{40}K that is relatively enriched in the granodiorite and alkaline basaltic rocks (Figure 1). Higher concentration He can be attributed to mantle-derived He and radiogenic He produced by the U-Th series enriched in the granodiorite and acid-intermediate volcanic rock in the crust.

5.2.2 Isotopic ratios of helium, carbon, and neon

5.2.2.1 He

In most cases, helium in geothermal fluids originates from atmospheric, crustal, and mantle sources (Sano et al., 1985; Ballentine et al., 2002; Zhou et al., 2015; Bini et al., 2022). Several methods were proposed for source partitioning of He in geothermal gases. For example, Sano et al. (1985) used an equation set to calculate the He percentages of atmospheric, crust, and mantle sources on the basis of the given ^{3}He/^{4}He and ^{20}Ne/^{4}He ratios of those sources. Using a plot of CO_2/^{3}He vs. δ^{13}C with the given values of the same parameters for the atmospheric, crust, and mantle sources, the source partitioning of He and CO_2 in the geothermal gases can be illustrated (Sano and Marty, 1995; Hilton, 1996). Using the corrected ^{3}He/^{4}He ratios deducted for atmospheric He by the ^{4}He/^{20}Ne ratio of air or ASW, the no-atmospheric He can be estimated by the two-end member model of crust and mantle sources (Ballentine et al., 2002; Zhou et al., 2015).

The samples of gases in the hot springs in AVR are characterized by low ^{3}He/^{4}He and CO_2/^{3}He ratios (Table 2), which obviously differ from those of hydrothermal fluids in the

Wudalianchi volcanic area (low $^3He/^4He$ and high $CO_2/^3He$) in the rift valley (Du et al., 1999; Xu et al., 2013) and Tianchi volcanic area (high $^3He/^4He$ and low $CO_2/^3He$) neighboring the rift valley to the west in NE China (Shangguan et al., 1996), and much less than those of volcanic and geothermal gases in the volcanic arc and middle ocean ridge (Sano and Marty, 1995; Shaw et al., 2003). The $^4He/^{20}Ne$ ratios of the gas samples are in the range of 0.34–385.3, and ^4He concentrations and $^3He/^4He$ ratios of the spring gases are independent (Table 2). The $CO_2/^3He$ ratios of the gas samples are 3 magnitudes less than those of the mantle (MORB-type) (1.5×10^9 (Sano and Marty, 1995)), 3–5 magnitudes less than the values of fumaroles and hot springs in the volcanic areas in Japan (7.74×10^9–1.18×10^{11} (Sano and Marty, 1995)) and in the Nicaraguan volcanic front (Shaw et al., 2003), and 8 magnitudes less than the values of sediment and limestone (1×10^{13} (Sano and Marty, 1995; Xu et al., 2013)). Therefore, it can be concluded that that He in the gas samples has multiple origins.

The $^{20}Ne/^{22}Ne$ ratios of the gas samples are close to the atmospheric value, and the $^{21}Ne/^{22}Ne$ ratios are slightly less than the atmospheric value (Table 2), indicating that Ne is mainly derived from air. Assuming all the ^{20}Ne in the geothermal gases is derived from air, the measured $^3He/^4He$ ratios of geothermal gases can be corrected by $^4He/^{20}Ne$ ratios of air or air-saturated water (Hilton, 1996; Ballentine et al., 2002; Xu et al., 2013; Zhou et al., 2015; Zhao et al., 2021). For eliminating the air contribution resulted from air dissolved in meteoric water into groundwater, the measured $^3He/^4He$ ratios were corrected by the ASW's $^4He/^{20}Ne$ ratio using the equation, $(^3He/^4He)^* = \{(^3He/^4He)_{sample}—r\}/(1—r)$, where $r = (^4He/^{20}Ne)_{(air\ or\ ASW)}/(^4He/^{20}Ne)_{sample}$ (Xu et al., 2013). ASW's $^4He/^{20}Ne$ ratio was calculated using the data of He and Ne solubility in water at 3 °C (4.814×10^{-5} ml/kg and 21.71×10^{-5} ml/kg (Weiss, 1971)), and ^{20}Ne content is 90.48% of total Ne (Porcelli et al., 2002), regardless of isotopic fractionations of He and Ne caused by air dissolution. The corrected $^3He/^4He$ ratios of the gas samples from the Tianchi, JJG Tianchi crater lakes, the Budonghe water, and spring no. 0 differ evidently from the measured ratios, but those of the hot spring gas samples with high $^4He/^{20}Ne$ ratios and high He concentrations show no change (Table 2). The percentages of atmospheric He and no-atmospheric He in the gas samples can be calculated by the following equation:

$$\frac{^3He}{^4He} = Atm\left(\frac{^3He}{^4He}\right)_a + (1 - Atm)\left(\frac{^3He}{^4He}\right)^*, \quad (5)$$

where $(^3He/^4He)$ is the measured value; Atm is the percentage of atmospheric He, $(^3He/^4He)_a$ is the atmospheric ratio; and $(^3He/^4He)^*$ is the ASW-corrected ratio or no-atmospheric He. The calculation results show the percentages of atmospheric He (Atm) in the hot spring gases are less than 73, and those of no-atmospheric He range from 27 to 100 (Figure 6; Table 2).

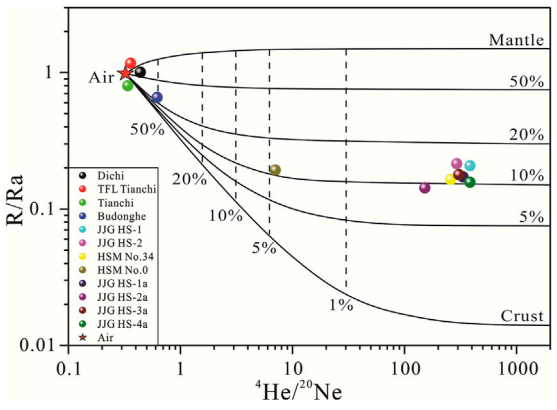

FIGURE 6
Diagram of $^3He/^4He$ vs. $^4He/^{20}Ne$.

Helium derived from the crustal and mantle origins can be quantitatively estimated by the two-member mixing model using the ASW (or air)-corrected $^3He/^4He$ ratios (Ballentine et al., 2002; Zhou et al., 2015; Seki et al., 2019; Zhao et al., 2021). Traditionally, assuming the mantle be homogenous, the $^3He/^4He$ ratios of the mantle and crust sources were proposed to be 8 ± 1 R_A and 0.02 R_A, respectively (Sano and Marty, 1995). However, the chemical heterogeneity of the upper mantle must be emphasized to estimate the amount of mantle-derived He in the hot spring gas, which is involved in assessing heat flux and potential heat resources in the geothermal fields. The $^3He/^4He$ ratios of basalts and mantle xenoliths in the different tectonic regions such as the mid-ocean ridge, volcanic arc, subcontinent, and orogenic zone evidently differ from each other and vary in a wide region within the same tectonic unit (Graham, 2002; Porcelli et al., 2002; Xu and Liu, 2002; Zhao et al., 2021; Randazzo et al., 2022). The $^3He/^4He$ ratio for the European subcontinental lithospheric mantle source was proposed as 6.1 ± 0.9 R_A (Randazzo et al., 2022). The isotopic compositions of noble gases in mantle peridotite xenoliths in eastern China vary from place to place and are obviously lower than MORB values (Cui et al., 2022). The lithospheric mantle and the asthenosphere in the continent area are important sources of gases in the upper mantle, which differs from the orogenic ranges to the rift valley in NE China (Xu et al., 2013). The mantle peridotite xenoliths in the Arxan–Chahe region (Liu et al., 2001; Sui et al., 2012) are geochemically similar to those in the Hannuoba region (Song and Frey, 1989; E and Zhao, 1987). Both the Arxan and Hannuoba volcanic regions are located in the orogenic belt of the Greater Khingan Range–Taihang Mountains, neighboring the rift valley on the east. The alkali basalts in the two regions formed in Miocene–Holocene, of which the REE pattens and spiderweb diagrams are similar (Zhao, 2010). The mantle xenoliths found in the two regions are mainly Al-rich lherzolites (E and Zhao, 1987). Therefore, the upper mantle from

the Hannuoba region to the south part of the Greater Khingan Range can be considered the same, implying that there is no obvious difference between the mantle sources of He in both the AVR and Hannuoba region in the Cenozoic Era. Therefore, $^3He/^4He$ of the mantle source in the AVR can be represented by the average (2.1×10^{-6}) of $^3He/^4He$ (n=31) of mantle peridotite xenoliths in the Hannuoba region (Cui et al., 2022). On the assumption that the $^3He/^4He$ ratios of the crustal and upper mantle sources are 2×10^{-8} and 2.1×10^{-6}, respectively, contributions of mantle-derived He to the total He of the hot spring gases were estimated in a range of 3%–23% using the ASW-corrected $^3He/^4He$ ratios and percentages of no-atmospheric He in the total He and percentages of crustal He range from 9 to 94 (Table 2). Source partitioning can be illustrated by the diagram of $^3He/^4He$ vs. $^4He/^{20}Ne$ (Figure 6). The percentages of mantle-derived He in the high-temperature spring gases in Figure 6 are slightly higher than the calculated values (Table 2). In consideration of the uncertainty of the different methods, however, it is clear that the calculated results are in general comparable with the diagram of $^3He/^4He$ vs. $^4He/^{20}Ne$ (Figure 6). He percentages of the primary mantle source in the gas samples range from 1% to 6%, estimated with the MORB value (Table 2). The bubble gas in the Tuofenglin crater lake has the highest percentage of mantle He and is composed of 68% of atmospheric He, 23% of mantle He, and 9% of crustal He. The high percentages of mantle He are found in the crater lakes (Figure 1), indicating that the mantle He migrates upwards to the surface through fractures in the channel of magma migration and mixes with atmospheric and crustal He during migration. The contribution of atmospheric He to the gases in the high-temperature hot springs in the Jinjianggou area is negligible. Gas in the low-temperature spring of no. 0 around the Hot Spring Museum (Figure 1B) contains about 3% of atmospheric He, but gas in the high-temperature hot spring on no. 34 lack of atmospheric He (Table 2; Figure 6). Such a small amount of atmospheric He may be carried into the spring by cool water recharge containing dissolved atmospheric He. Specially, the amount of mantle-derived He in the Budonghe water was estimated as high as 12%, which indicated that plenty of heat energy was transported by deep-earth fluids from the upper mantle to the Budonghe area in the Wuliqiao geothermal field. He in the hot spring gases with high concentrations is predominantly of crust origin, with less than 10% of mantle-derived He, indicating He accumulation in the geothermal reservoirs. The mantle-derived He emits upwards to the surface through the deep-cut faults and transports plenty of heat energy to the geothermal systems, which is supported by the data that about 80% of total heat flow is derived from the mantle in the study area (Sun, 1999).

5.2.2.2 CO_2

Concentrations of CO_2 in the hot spring gases in the AVR are less than 1%, and $\delta^{13}C$ values are in the range of −15.9–−22.3% (Table 2). There are three scenarios for the origin of CO_2 in the spring gases in the AVR. The first one is that CO_2 in the hot springs is likely derived from the mantle based on the mean value of −22.6% (n = 105) of CO_2 in mantle xenoliths and minerals enclosed in Cenozoic basalts in eastern China (Cui et al., 2022). The statistical result of the $\delta^{13}C$ values of CO_2 in the mantle xenoliths worldwide also shows a bimodal distribution with peak values of −5% and -25% (Deines, 2002). The second one is that the CO_2 is likely to have originated from biogenic and metamorphic gases in the crust. The $\delta^{13}C$ values of CO_2 originating from Jurassic coal seams are in a range of −11%–−28% (Du and Liu, 1991). Biogenic CO_2 of concentrations less than 6% in the gas reservoirs and gas seepages in China has $\delta^{13}C$ values between −10% and −22% (Dai et al., 1996). The third one is that the CO_2 is most likely a mixture of biogenic and abiogenic CO_2. $\delta^{13}C$ data (−4.7%–-6.4%) of CO_2 in the fumarolic gases at the Longonot Volcano, Kenya, indicated a magmatic origin with minor contributions from biogenic CO_2 (Robertson et al., 2016).

5.2.2.3 N_2

Nitrogen, in some instances, is the main component in hot spring, fumarole, and volcanic gases, which were identified as a mixture of atmospheric, mantle, and crustal N_2 (Roulleau et al., 2015; Tardani et al., 2016; Zhao et al., 2021). N_2 is the predominant component in the hot spring gases in the AVR, and $\delta^{15}N$ values are in a range of +1.3–+1.9% (Table 2). The excess N_2 content is larger than 92%. Combining with $^4He/^{20}Ne$ and $^3He/^4He$ ratios and the lack of organic matter to produce lot of metamorphic nitrogen in the study area, it can be considered that the excess N_2 mainly originated from the mantle with mixing crust-derived N_2, as reported by Zhao et al. (2021).

6 Conclusion

The origins of the spring water and gases in the AVR were traced by the hydro- and gas-chemical data. Contributions of deep-earth fluids to the geothermal systems were estimated using Cl^- and Na^+ concentrations, ASW-corrected $^3He/^4He$ ratios, and the regional mantle helium isotope ratio in consideration of the heterogeneity of the upper mantle. The conclusions are remarked as follows:

1 H_2O in the river, lakes, and spring waters predominantly originate from meteoric water. The small amount (<1%) of H_2O derived from deep-earth fluids seems negligible for assessing the volume of geothermal fluid, but the ion contributions of deep-earth fluids to the hot spring water are significant. Ions in the rain sample were mainly derived from sea salt and continental aerosol. Ions in the surface waters have multiple sources of the continental aerosol, sea salt, rock dissolution, and anthropogenic sources, while ions in the hot spring waters are

predominantly derived from deep-earth fluids. That 73%–87% of Cl^- and 86%–99% of Na^+ in the hot spring waters may be derived from deep-earth fluids.

2 Enrichment of heavy isotopes in the rainwater can be attributed to isotopic fractionation caused by raindrop evaporation. Heavier isotope compositions of the waters in the crater lakes may be caused by the evaporation process due to the higher evaporation capacity in the study area.

3 Atmospheric neon dissolution in the lake waters likely approached the balance state. CH_4 in the hot springs isotopically displays a biogenic origin. Excess N_2, Ar, and CO_2 in the hot spring gases could be predominantly derived from both the crust and upper mantle sources.

4 Contributions of the mantle-derived He to bubble gases in the hot spring were estimated in a range of 3%–23%. High percentages of mantle-derived He in the bubbling gases in the crater lakes indicate gases in the mantle emit upwards through the channel for magma migration; 12% of the total He of dissolved gas in the Budonghe water is derived from the mantle, indicating deep-earth fluids transport continuously plenty of heat to the Budonghe and the geothermal systems.

Data availability statement

The original contributions presented in the study are included in the article/Supplementary Material; further inquiries can be directed to the corresponding authors.

Author contributions

YC, LL, CX, JL, ZC, and JD conducted the field survey. YC and JD processed the data and prepared the first draft. All co-authors edited the manuscript.

Funding

This work was supported by the National Key Research and Development Program (2019YFC1509203), the Open Foundation of the United Laboratory of High Pressure Physics and Earthquake Science (2019HPPES08), and the National Natural Science Foundation of China (41403099).

Acknowledgments

The authors are grateful to Ruijie Zhang in the Arxan Observatory of Volcano for his help in the field trip and Zhaofei Liu and Jianan Huang for drawing the figures. They are extremely grateful to the four reviewers for their constructive comments and patience during discussion.

Conflict of interest

The authors declare that the research was conducted in the absence of any commercial or financial relationships that could be construed as a potential conflict of interest.

The handling editor MZ declared a past co-authorship with the author YL.

Publisher's note

All claims expressed in this article are solely those of the authors and do not necessarily represent those of their affiliated organizations, or those of the publisher, the editors, and the reviewers. Any product that may be evaluated in this article, or claim that may be made by its manufacturer, is not guaranteed or endorsed by the publisher.

References

Amita, K., Ohsawa, S., Du, J., and Yamada, M. (2005). Origin of Arima-type deep thermal water from hot spring wells in Oita Plain, eastern Kyushu, Japan. *Hot Spring Sci.* 55 (2), 64–77. (in Japanese wiith English abstract).

Bai, Z., Tian, M., and Wu, F. (2005). Yanshan, gaoshan: Two active volcanoes of the volcanic cluster in arxan, inner Mongolia. *Earthq. Res. China* 21 (1), 113–117. (In Chinese with English abstract).

Ballentine, C. J., Burgess, R., and Marty, B. (2002). "Tracing fluid origin, transport and interaction in the crust," in *Mineralogy and Geochemistry* 47 (1), 539–614.doi:10.2138/rmg.2002.47.13

Barry, P. H., Negrete-Aranda, R., Spelz, R. M., Seltzer, A. M., Bekaert, D. V., Virrueta, C., et al. (2020). Volatile sources, sinks and pathways: A helium-carbon isotope study of baja California fluids and gases. *Chem. Geol.* 550, 119722. doi:10.1016/j.chemgeo.2020.119722

Benavente, O., Tassi, F., Reich, M., Aguilera, F., Capecchiacci, F., Gutiérrez, F., et al. (2016). Chemical and isotopic features of cold and thermal fluids discharged in the Southern Volcanic Zone between 32.5°S and 36°S: Insights into the physical and chemical processes controlling fluid geochemistry in geothermal systems of Central Chile. *Chem. Geol.* 420, 97–113. doi:10.1016/j.chemgeo.2015.11.010

Bini, G., Chiodini, G., Caliro, S., Tassi, F., Vaselli, O., Rizzo, A. L., et al. (2022). Nitrogen, helium, and argon reveal the magmatic signature of fumarole gases and episodes of outgassing from upper-crustal magma reservoirs: The case of the Nisyros caldera (Aegean Arc, Greece). *Geochim. Cosmochim. Acta* 335, 68–84. doi:10.1016/j.gca.2022.08.028

Chen, J., Wang, W., and Ma, F. (2021). Recharge source and Genesis analysis of Cenozoic basalt groundwater in Arshan. *J. Hohai Univ. Nat. Sci.)* 49 (3), 249–256. (In Chinese with English abstract). doi:10.3876/j.issn.1000-1980.2021.03.007

Chen, Z., Du, J., Zhou, X., Yi, L., Liu, L., Xie, C., et al. (2014). Hydrochemistry of the hot springs in Western Sichuan province related to the Wenchuan M_S 8.0 earthquake. *Sci. World J.* 2014 (1), 1–13. doi:10.1155/2014/901432

Cui, Y., Sun, F., and Du, J. (2022). Methods for identification of seismic geochemical precursors and source partitioning of hot spring fluids in Eastern Chinese Mainland. *J. Seismol. Res.* 45 (2), 199–216. (In Chinese with English abstract). doi:10.20015/j.cnki.ISSN1000-0666.2022.0053

Dai, J., Song, Y., and Da, C. (1996). Geochemistry and accumulation of carbon dioxide gases in China. *Am. Assoc. Pet. Geol. Bull.* 80, 1615–1626. doi:10.1306/64EDA0D2-1724-11D7-8645000102C1865D

Deines, P. (2002). The carbon isotope geochemistry of mantle xenoliths. *Earth. Sci. Rev.* 58 (3-4), 247–278. doi:10.1016/S0012-8252(02)00064-8

Du, J., Amida, K., Ohsawa, S., Zhang, Y., Kang, C., and Yamada, M. (2010). Experimental evidence on imminent and short-term hydrochemical precursors for earthquake. *App. Geochem.* 25, 586–592. doi:10.1016/j.apgeochem.2010.01.015

Du, J., Cheng, W., Zhang, Y., Jian, C., Guan, Z., Liu, W., et al. (2006). Helium and carbon isotopic compositions of thermal springs in the earthquake zone of Sichuan, Southwestern China. *J. Asian Earth Sci.* 26, 533–539. doi:10.1016/j.jseaes.2004.11.006

Du, J., Li, S., Zhao, Y., Ren, J., Sun, R., and Duanmu, H. (1999). Geochemical characteristics of gases from the volcanic area Wudalianchi, Northeastern China. *Acta Geol. Sin.* 73 (2), 103–107. doi:10.1111/j.1755-6724.1999.tb00830.x

Du, J., Liu, C., Fu, B., Zhang, Y., Wang, C., Wang, H., et al. (2005). Variations of geothermometry and chemical-isotopic compositions of hot spring fluids in the Rehai geothermal field, southwestern China. *J. Volcanol. Geotherm. Res.* 142 (3-4), 243–261. doi:10.1016/j.jvolgeores.2004.11.009

Du, J., and Liu, W. (1991). Isotopic geochemistry of nonhydrocarbons in natural gas from sanshui basin, guangdong province. *Chin. J. Geochem.* 10 (4), 318–325. doi:10.1007/BF02841092

Fan, Q., Zhao, Y., Li, D., Wu, Y., Sui, J., and Zheng, D. (2011). Studies on Quaternary volcanism stages of Halahe river and Chaoer river area in the Great Xing'an Range: Evidence from K-Ar dating and volcanic geology features. *Acta Pet. Sin.* 27 (10), 2827–2832.

Fan, W., Guo, F., Wang, Y. J., and Lin, G. (2003). Late Mesozoic calc-alkaline volcanism of post-orogenic extension in the northern Da Hinggan Mountains, northeastern China. *J. Volcanol. Geotherm. Res.* 121 (1), 115–135. doi:10.1016/S0377-0273(02)00415-8

Gao, H., Li, C., Sun, B., Shi, X., Zhao, S., and Fan, C. (2018). Characteristics of hydrogen and oxygen stable isotopes in Lake Hulun Basin and its indicative function in evaporation. *J. Lake Sci.* 30 (1), 211–219. doi:10.18307/2018.0121

Giggenbach, W. F., Sano, Y., and Wakita, H. (1993). Isotopes of He, and CO_2 and CH_4 contents in gases produced along the New Zealand part of a convergent plate boundary. *Geochim. Cosmochim. Acta* 57, 3427–3455. doi:10.1016/0016-7037(93)90549-C

Gislason, S. R., and Hans, P. E. (1987). Meteoric water-basalt interactions. I: A laboratory study. *Geochim. Cosmochim. Acta* 51 (10), 2827–2840. doi:10.1016/0016-7037(87)90161-X

Gislason, S. R., Veblen, D. R., and Livi, K. J. T. (1993). Experimental meteoric water-basalt interactions: Characterization and interpretation of alteration products. *Geochim. Cosmochim. Acta* 57 (7), 1459–1471. doi:10.1016/0016-7037(93)90006-I

Graham, D. W. (2002). "Noble gas isotope geochemistry of mid-ocean ridge and ocean island basalts: Characterization of mantle source reservoirs," in *Mineralogy and Geochemistry* (1), 47, 247–318.doi:10.2138/rmg.2002.47.8

Gu, X., Zhang, Q., Cui, Y., Shao, J., Xiao, Y., Zhang, P., et al. (2017). Hydrogeochemistry and genesis analysis of thermal and mineral springs in arxan, northeastern China. *Water* 9 (1), 61–17. doi:10.3390/w9010061

Han, Z., Shi, X., Jia, K., Sun, B., Zhao, S., and Fu, C. (2019). Determining the discharge and recharge relationships between lake and groundwater in Lake Hulun using hydrogen and oxygen isotopes and chloride ions. *Water* 11 (2), 264. doi:10.3390/w11020264

Hilton, D. R. (1996). The helium and carbon isotope systematics of a continental geothermal system: results from monitoring studies at Long Valley caldera (California, U.S.A.). *Chem. Geol.* 127, 269–295. doi:10.1016/0009-2541(95)00134-4

Jia, Z., and Zhang, G. (2020). Teleseismic tomography for imaging the upper mantle beneath northeast China. *Appl. Sci. (Basel).* 10 (13), 4557. doi:10.3390/app10134557

Keene, W. C., Pszenny, A. A. P., Galloway, J. N., and Hawley, M. E. (1986). Sea-salt corrections and interpretation of constituent ratios in marine precipitation. *J. Geophys. Res.* 91 (D6), 6647. doi:10.1029/JD091iD06p06647

Li, J. (2020). "Isotopic hydrochemical study of geothermal fluids in volcanic geothermal system,". M.A. thesis (Xi'an, China: Chang'an University). (In Chinese with English abstract).

Li, X., Zhang, M., Ma, Q., Li, Y., Wang, S., and Wang, B. (2012). Characteristics of stable isotopes in precipitation over northeast China and its water vapor sources. *J. Env. Sci.* 33 (9), 2924–2931. (In Chinese with English abstract).

Li, Y., Gao, R., Yao, Y., Mi, S., Li, W., Xiong, X., et al. (2014). The crust velocity structure of Da Hinggan Ling orgenic belt and the basins on both sides. *Prog. Geophys.* 29 (1), 315–541. doi:10.6038/pg20140110

Li, Z., Tao, M., Li, L., Wang, Z., Du, L., and Zhang, M. (2007). Determination of isotope composition of dissolved inorganic carbon by gas chromatography-conventional isotope-ratio mass spectrometry. *Chin. J. Anal. Chem.* 35, 1455–1458. doi:10.1016/S1872-2040(07)60089-9

Liang, L., Li, C., Shi, X., Sun, B., Wang, J., and Zhou, J. (2017). Characteristics of hydrogen and oxygen isotopes of surface and ground water and the analysis of source of Lake water in Hulun Lake. *Wetl. Sci.* 15 (3), 385–390. doi:10.13248/j.cnki.wetlandsci.2017.03.010

Liu, J., Han, J., and Fyfe, W. S. (2001). Cenozoic episodic volcanism and continental rifting in northeast China and possible link to Japan Sea development as revealed from K-Ar geochronology. *Tectonophysics* 339, 385–401. doi:10.1016/S0040-1951(01)00132-9

Liu, J., Song, X., Yuan, G., Sun, X., and Yang, L. (2014). Stable isotopic compositions of precipitation in China. *Tellus B Chem. Phys. Meteorology* 66 (1), 22567. doi:10.3402/tellusb.v66.22567

Porcelli, D., Ballentine, C. J., and Wieler, R. (2002). "An overview of noble gas geochemistry and cosmochemistry," in *Noble gases in Geochemistry and cosmochemistry*. Editors D. Porcelli, C. Ballentine, and R. Wieler Rev. Mineral. Geochem. (Washington DC: Mineralogical Society of America), 47, 1–19.

Qi, F., Zhang, F., Lu, S., and Sun, Y. (2012). The geothermal geological features of Arxan mountains. *Jinlin Geol.* 31 (2), 109–102. (In Chinese with English abstract).

Randazzo, P., Caracausi, A., Aiuppa, A., Cardellini, C., Chiodini, G., Apollaro, C., et al. (2022). Active degassing of crustal CO_2 in areas of tectonic collision: A case study from the Pollino and Calabria sectors (Southern Italy). *Front. Earth Sci.* 10, 946707. doi:10.3389/feart.2022.946707

Rizzo, A. L., Caracausi, A., Chavagnac, V., Nomikou, P., Polymenakou, P. N., Mandalakis, M., et al. (2019). Geochemistry of CO_2-rich gases venting from submarine volcanism: The Case of Kolumbo (Hellenic Volcanic Arc, Greece). *Front. Earth Sci.* 7, 60. doi:10.3389/feart.2019.00060

Robertson, E., Biggs, J., Edmonds, M., Clor, L., Fischer, T. P., Vye-Brown, C., et al. (2016). Diffuse degassing at Longonot volcano, Kenya: Implications for CO_2 flux in continental rifts. *J. Volcanol. Geotherm. Res.* 327, 208–222. doi:10.1016/j.jvolgeores.2016.06.016

Roulleau, E., Vinet, N., Sano, Y., Takahata, N., Shinohara, H., Ooki, M., et al. (2015). Effect of the volcanic front migration on helium, nitrogen, argon, and carbon geochemistry of hydrothermal/magmatic fluids from Hokkaido volcanoes, Japan. *Chem. Geol.* 414, 42–58. doi:10.1016/j.chemgeo.2015.08.006

Rozanski, K., Araguas-Araguas, L., and Gonfiantinni, R. (1993). "Isotopic patterns in modern global precipitation," in *The climate change in continental isotopic records*. Editors P. K. Swart, K. C. Lohmann, and J. McKenzie (Washington, DC, USA: American Geophysical Union), 78, 1–36. doi:10.1029/GM078p0001

Sano, Y., and Marty, B. (1995). Origin of carbon in fumarolic gas from island arcs. *Chem. Geol.* 119 (1-4), 265–274. doi:10.1016/0009-2541(94)00097-R

Sano, Y., Nakamura, Y., and Wakita, H. (1985). Areal distribution of $^3He/^4He$ ratios in the Tohoku district, Northeastern Japan. *Chem. Geol. Isot. Geosci. Sect.* 52 (1), 1–8. doi:10.1016/0168-9622(85)90004-1

Seki, K., Ohba, T., Aoyama, S., Ueno, Y., Sumino, H., Kanda, W., et al. (2019). Variations in thermal state revealed by the geochemistry of fumarolic gases and hot-spring waters of the Tateyama volcanic hydrothermal system, Japan. *Bull. Volcanol.* 81, 8. doi:10.1007/s00445-018-1264-7

Shangguan, Z., Kong, L., Sun, F., and Gao, S. (1996). Deep-seated fluid components and stable isotopic compositions in Tianchi volcanic area, Changbaishan Mountains. *Chin. J. Geol.* 31 (1), 54–64. (In Chinese with English abstract).

Shaw, A. M., Hilton, D. R., Fischer, T. P., Walker, J., and Alvarado, G. (2003). Contrasting He–C relationships in Nicaragua and Costa Rica: insights into C cycling through subduction zones. *Earth Planet. Sci. Lett.* 214, 499–513. doi:10.1016/S0012-821X(03)00401-1

Shen, Z., Cao, J., Arimoto, R., Zhang, R., Jie, D., Liu, S., et al. (2007). Chemical composition and source characterization of spring aerosol over Horqin sand land in northeastern China. *J. Geophys. Res.* 112, D14315. doi:10.1029/2006JD007991

Sokolov, D. S. (1966). *Hydrogeology in U.S.S.R* (Moscow: Publishing House Nedra), 1, 432. (in Russian).

Song, Y., and Frey, F. A. (1989). Geochemistry of peridotite xenoliths in basalt from Hannuoba, Eastern China: Implications for subcontinental mantle heterogeneity. *Geochim. Cosmochim. Acta* 53, 97–113. doi:10.1016/0016-7037(89)90276-7

Sui, J., Fan, Q., and Xu, Y. (2012). Discovery of peridotite xenoliths from the Nuomin river Quaternary volcaniv field, the Grea Xing'an Range, and its geological significance. *Acta petro. Sin.* 28 (4), 1130–1138.

Sun, C. (1999). "Study of geothermal structure of hot springs in Arxan,". master's thesis (Changchun, China: Jilin University). (In Chinese with English abstract).

Sun, Y., Guo, Z., and Fortin, D. (2020). Carbon dioxide emission from monogenetic volcanoes in the Mt. Changbai volcanic field, NE China. *Int. Geol. Rev.* 63 (14), 1803–1820. doi:10.1080/00206814.2020.1802782

Tang, J., Wang, J., Chen, X., Zhao, G., and Zhan, Y. (2005). A Preliminary Investigation on Electric Structure of the Crust and Upper Mantle in Arxan Volcanic Area. *Chin. J. Geophys.* 48 (1), 214–221. doi:10.1002/cjg2.642

Tang, S. (1984). Feature of the Late Jurassic volcanic structure and genetic mechanism of hot springs in Arxan. *Jilin Geol.* 38(1), 54–65. (In Chinese with English abstract).

Taran, Y. A. (2009). Geochemistry of volcanic and hydrothermal fluids and volatile budget of the Kamchatka–Kuril subduction zone. *Geochim. Cosmochim. Acta* 73, 1067–1094. doi:10.1016/j.gca.2008.11.020

Taran, Y. A. (2011). N_2, Ar, and He as a tool for discriminating sources of volcanic fluids with application to Vulcano. *Bull. Volcanol.* 73 (4), 395–408. doi:10.1007/s00445-011-0448-1

Tardani, D., Reich, M., Roulleau, E., Takahata, N., Sano, Y., Pérez-Flores, P., et al. (2016). Exploring the structural controls on helium, nitrogen and carbon isotope signatures in hydrothermal fluids along an intra-arc fault system. *Geochim. Cosmochim. Acta* 184, 193–211. doi:10.1016/j.gca.2016.04.031

Tsujimura, M., Abe, Y., Tanaka, T., Shimada, J., Higuchi, S., Yamanaka, T., et al. (2007). Stable isotopic and geochemical characteristics of groundwater in Kherlen River basin, a semi-arid region in eastern Mongolia. *J. Hydrol. X.* 333 (1), 47–57. doi:10.1016/j.jhydrol.2006.07.026

Wei, F., Xu, J., Shangguan, Z., Pan, B., Yu, H., Wei, W., et al. (2016). Helium and carbon isotopes in the hot springs of Changbaishan Volcano, northeastern China: A material connection between Changbaishan Volcano and the west Pacific plate? *J. Volcanol. Geotherm. Res.* 327, 398–406. doi:10.1016/j.jvolgeores.2016.09.005

Weiss, R. F. (1971). Solubility of helium and neon in water and seawater. *J. Chem. Eng. Data* 16 (2), 235–241. doi:10.1021/je60049a019

Weiss, R. F. (1970). The solubility of nitrogen, oxygen and argon in water and seawater. *Deep Sea Res. Oceanogr. Abstr.* 17 (4), 721–735. doi:10.1016/0011-7471(70)90037-9

Xie, H., Tian, J., Wu, L., Zhu, Y., Wu, C., Shen, K., et al. (2011). Age of ore-forming granites in Aershan area of Inner Mongolia and its significance for prospecting. *J. Jilin Univ. (Earth Sci. Ed.)* 41 (5), 1432–1440.

Xu, S., and Liu, C. (2002). Abundance and isotope ratios of noble gas in mantle xenoliths from northeastern China. *Chin. Sci. Bull.* 47 (2), 141–146. (In Chinese).

Xu, S., Zheng, G., Nakai, S., Wakita, H., Wang, X., and Guo, Z. (2013). Hydrothermal He and CO_2 at Wudalianchi intra-plate volcano, NE China. *J. Asian Earth Sci.* 62, 526–530. doi:10.1016/j.jseaes.2012.11.001

Xue, X., Chen, L., Liu, J., He, Y., Wang, X., Zeng, G., et al. (2019). Primordial peridotitic mantle component in asthenosphere beneath Northeast China: Geochemical evidence from Cenozoic basalts of Greater Khingan Range. *Earth Sci.* 44 (4), 1143–1158. doi:10.3799/dqkx.2019.951

Zhang, L., Chen, Z., Nie, Z., Liu, F., Jia, Y., and Zhang, X. (2008). Correlation between $\delta^{18}O$ in precipitation and surface air temperature on different time-scale in China. *Nucl. Tech.* 31(9), 715–720. (In Chinese with English abstract).

Zhang, P. (2017). "Hydrochemical characteristics and water rock interaction of Arxan Springs,". master's theses (Beijing, China: China University of Geosciences).

Zhang, W., Du, J., Zhou, X., and Wang, F. (2016). Mantle volatiles in spring gases in the Basin and Range Province on the west of Beijing, China: Constraints from helium and carbon isotopes. *J. Volcanol. Geotherm. Res.* 309, 45–52. doi:10.1016/j.jvolgeores.2015.10.024

Zhao, D. (1987). *Cenozoic Basalts and Plutonic Inclusions in Eastern China*, Beijing, China: Science Press, 490. (In Chinese)

Zhao, W., Guo, Z., Lei, M., Zhang, M., Ma, L., Fortin, D., et al. (2019). Volcanogenic CO_2 degassing in the Songliao continental rift system, NE China. *Geofluids* 2019, 1–14. doi:10.1155/2019/8053579

Zhao, W., Guo, Z., Liu, J., Zhang, M., Sun, Y., Lei, M., et al. (2021). Fluxes and Genesis of carbon dioxide emissions from Cenozoic volcanic fields in NE China. *Ata Pet. Sin.* 37 (4), 1255–1269. doi:10.18654/1000-0569/2021.04.17

Zhao, Y. (2010). dissertation. Beijing, China: Institute of Geology, China Earthquake Administration.Study on Geology and Geochemistry of Quaternary Volcanoes in the Da Hinggan Ling Mountains,

Zhou, X., Wang, W., Chen, Z., Yi, L., Liu, L., Xie, C., et al. (2015). Gas geochemistry of hot springs in Western Sichuan Province, China after the Wenchuan M_S 8.0 earthquake. *Terr. Atmos. Ocean. Sci.* 26 (4), 361–373. doi:10.3319/tao.2015.01.05.01(tt)

frontiers | Frontiers in Earth Science

TYPE Original Research
PUBLISHED 16 January 2023
DOI 10.3389/feart.2022.1015134

OPEN ACCESS

EDITED BY
Maodu Yan,
Institute of Tibetan Plateau Research, Chinese Academy of Sciences (CAS), China

REVIEWED BY
Vivek Walia,
National Center for Research on Earthquake Engineering, Taiwan
Dongliang Liu,
Chinese Academy of Geological Sciences (CAGS), China

*CORRESPONDENCE
Xiaocheng Zhou,
zhouxiaocheng188@163.com
Ying Li,
subduction6@hotmail.com

SPECIALTY SECTION
This article was submitted to Geochemistry, a section of the journal Frontiers in Earth Science

RECEIVED 09 August 2022
ACCEPTED 25 October 2022
PUBLISHED 16 January 2023

CITATION
Liu J, Zhou X, Li Y, He M, Li J, Dong J, Tian J, Yan Y, Ouyang S and Liu F (2023), Relationship between hydrogeochemical characteristics of hot springs and seismic activity in the Jinshajiang fault zone, Southeast Tibetan Plateau.
Front. Earth Sci. 10:1015134.
doi: 10.3389/feart.2022.1015134

Relationship between hydrogeochemical characteristics of hot springs and seismic activity in the Jinshajiang fault zone, Southeast Tibetan Plateau

Jie Liu[1], Xiaocheng Zhou[2]*, Ying Li[2]*, Miao He[2], Jingchao Li[2], Jinyuan Dong[2], Jiao Tian[2], Yucong Yan[2], Shupei Ouyang[2] and Fengli Liu[2]

[1]Shaanxi Earthquake Agency, Xi'an, China, [2]United Laboratory of High-Pressure Physics and Earthquake Science, Institute of Earthquake Forecasting, CEA, Beijing, China

Significant anomalous hydrogeochemical changes in hot spring water are detected during strong seismic cycles. It is now necessary to clarify the relationship between tectonic movements, earthquakes and the evolution of hot springs. In this paper, laboratory analyses of major, trace elements, δD, $\delta^{18}O$ and $^{87}Sr/^{86}Sr$ values of 28 hot spring waters in the Jinshajiang fault zone (JSJFZ) in the northwestern boundary of the Sichuan-Yunnan block were conducted. The results showed that the primary source of water for JSJFZ hot springs was atmospheric precipitation. The geothermal reservoir temperature variation based on the silicon enthalpy mixing model ranged from 73 to 272°C. And the circulation depth range was 1.2–5.4 km. The segmentation characteristics of the $^{87}Sr/^{86}Sr$ values were related to the influence of source rocks on groundwater cycle processes. A conceptual model of the hydrologic cycle of hot springs explained the spatial distribution of earthquakes associated with tectonic movements. The Batang segment had the strongest water-rock reaction, the highest reservoir temperature and the deepest circulation depth; meanwhile, it was also an earthquake prone area. The fluid circulation of the JSJFZ corresponds well with the seismicity, which indicates that the hydrological characteristics of the hot spring water in a fracture zone play a crucial role in receiving information on seismic activity.

KEYWORDS

thermal spring, hydrogeochemistry, seismic activity, jinshajiang fault zone, southeast Tibetan plateau

1 Introduction

Underground water geochemistry has played an important role in inferring geotectonic activity. Hydrological effects occurring during strong earthquake cycles have been observed both recently and historically (Scholz et al., 1973; King, 1986; Linde et al., 1988; Thomas, 1988; Kitagawa et al., 1996; Wang et al., 2001; Jonsson et al., 2003; Yang et al., 2011; Li et al., 2014; Skelton, 2014; Yan et al., 2014; Yuce et al., 2014; Manga and Wang, 2015; Rosen et al., 2018; Martinelli and Tamburello, 2020; Nakagawa et al., 2020; Fu et al., 2021; Zhang et al., 2021; Zhou et al., 2021). Large, localized, and sustained fluid pressures could account for weakness of deep-seated fault (Fulton and Saffer, 2009). In particular, geothermal hot springs are important conduits for the discharge of deep source fluids to the surface. The hot springs in the deep-seated fault zone have deep circulation. Due to high temperature and strong water-rock interaction in deep-cycle process, they can dissolve different kinds of minerals, resulting in different geochemical characteristics (Bo et al., 2015; Guo et al., 2014; Tian et al., 2021). Such changes are always considered to be beneficial for fault tectonic and seismic studies.

The Jinshajiang fault zone (JSJFZ) is located in the southeast of the Tibetan Plateau. It has unique advantages in studying the relationship between earthquake and hydrochemistry of hot springs. Firstly, its major faults cut deeply into the crust and even through the asthenosphere (Wang et al., 2018). Secondly, it is an earthquake-prone area that has been hit by several Ms ≥ 6 earthquakes since records began. Among them, the largest earthquake was the Batang M7¼ earthquake in 1870 (Li et al., 2014). Since then, several earthquakes swarms with Ms ≥ 6 had occurred in this region. Recently, the small and intermediate seismic activities in Batang have been more active. More importantly, the Batang geothermal field is a significant part of the eastern Tibetan Plateau geothermal belt (Tang et al., 2017). It is the geothermal field with the highest reservoir temperature (200°C–225°C) along the Sanjiang Orogenic belt, and it has experienced a deep cycle (Yi et al., 2021).

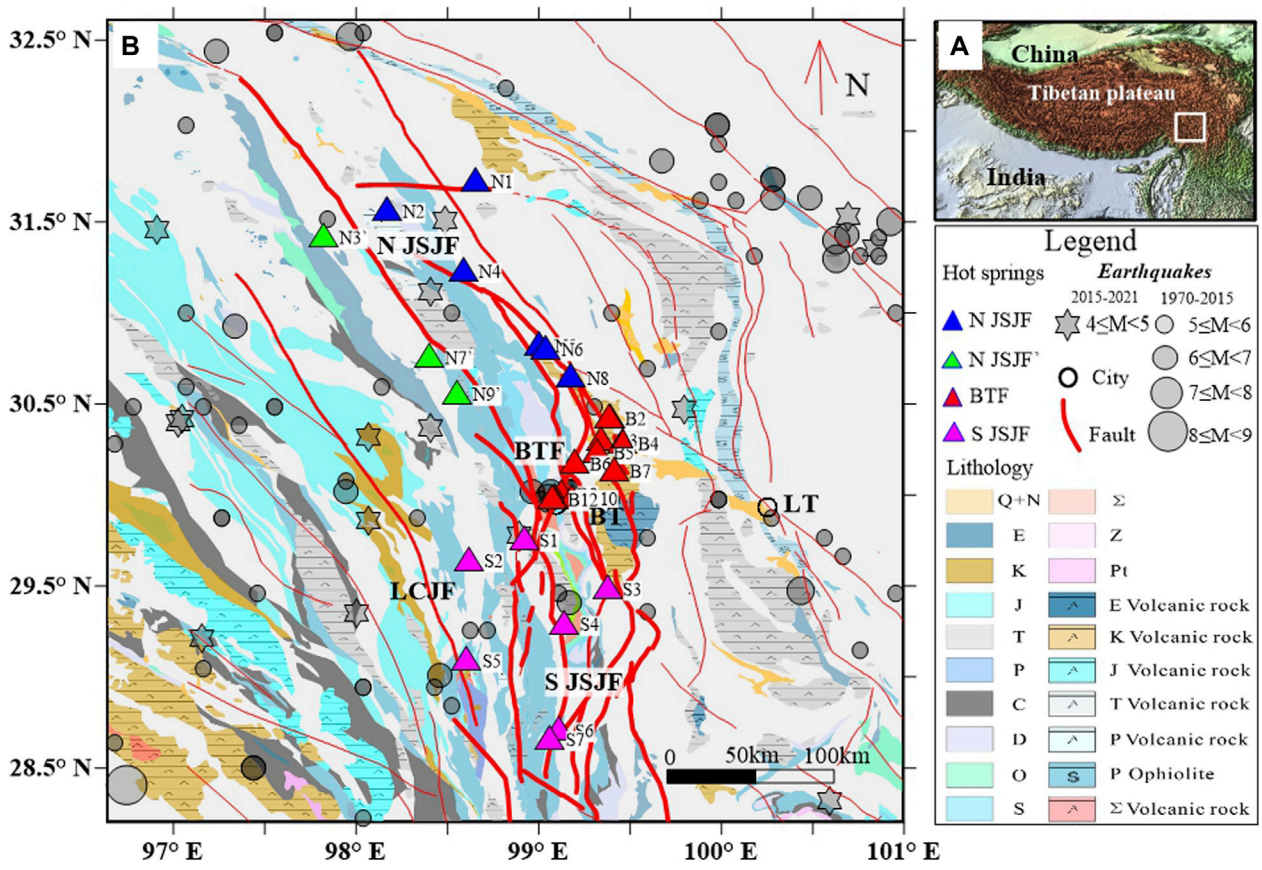

FIGURE 1
The plot of sampling site distribution. **(A)** Geological map showing the location of the study area. **(B)** Tectonic and tectonic and lithological features of the JSJFZ. Notes: The statistical earthquakes were divided into two parts, one is between 1970 and 2015 (grey circle), and the other is between 2015 and 2021 (grey polygon). The hot springs in the JSJFZ are divided into four parts (colored triangle). The background represents the lithology of the study area. The red line represents the fault.

TABLE 1 Geothermal water sampling sites information in the study area.

No	Segment	Longitude (°)	Latitude (°)	Altitude (m)	Sapmling time	Fault zone	Lithology and stratigraphic age
1	N1	98.66	31.69	3,285	2018.7.23	Northern JSJ fault	Limestone (T)
2	N2	98.17	31.52	3,994	2018.7.23	Northern JSJ fault	Sandstone, Mudstone, Volcanic rock (T)
3	N3′	97.83	31.38	4,107	2019.6.18	Northern JSJ fault	Limestone (T)
4	N4	98.59	31.20	2,906	2017.6.28	Northern JSJ fault	Limestone (T)
5	N5	99.00	30.80	2,945	2017.6.25	Northern JSJ fault	Limestone (T)
6	N6	99.04	30.78	2,964	2017.6.25	Northern JSJ fault	Limestone (T)
7	N7′	98.40	30.73	3,802	2019.6.17	Northern JSJ fault	Conglomerate, Sandstone, Mudstone (N)
8	N8	99.18	30.62	3,313	2018.7.21	Northern JSJ fault	Sandstone, Slate, limestone (T)
9	N9′	98.56	30.54	3,952	2019.6.17	Northern JSJ fault	Limestone (T)
10	B1	99.39	30.40	3,562	2019.6.15	BT Fault	Metamorphic clastic rock, limestone (T)
11	B2	99.38	30.40	3,562	2019.6.15	BT fault	Metamorphic clastic rock, limestone (T)
12	B3	99.34	30.28	3,287	2019.6.15	BT fault	Metamorphic sand slate, limestone (T)
13	B4	99.45	30.27	3,933	2019.6.15	BT fault	Metamorphic clastic rock, limestone (T)
14	B5	99.32	30.22	3,167	2016.4.26	BT fault	Carbonate rock (P)
15	B6	99.19	30.16	2,726	2019.6.15	BT fault	Metamorphic clastic rock, limestone (T)
16	B7	99.41	30.12	3,952	2019.6.16	BT fault	Metamorphic sand slate, limestone (T)
17	B8	99.12	29.99	2,668	2019.6.16	BT fault	Ophiolite group, limestone (P-T)
18	B9	99.08	29.98	2,517	2010.6.13	BT fault	Ophiolite group, limestone (P-T)
19	B10	99.18	29.97	3,079	2019.6.16	BT fault	Ophiolite group, limestone (P-T)
20	B11	99.08	29.97	2,519	2019.6.17	BT fault	Ophiolite group, limestone (P-T)
21	B12	99.07	29.96	2,513	2018.7.21	BT fault	Ophiolite group, limestone (P-T)
22	S1	98.92	29.74	2,646	2016.4.26	Southern JSJ fault	Ophiolite group, limestone (P-T)
23	S2	98.62	29.63	3,942	2018.7.22	Southern JSJ fault	Sandstone, Mudstone, Conglomerate (K)
24	S3	99.37	29.48	3,247	2017.6.26	Southern JSJ fault	Limestone (T)
25	S4	99.14	29.29	3,099	2017.6.26	Southern JSJ fault	Metamorphic clastic rock, limestone (T)
26	S5	98.61	29.09	2,655	2018.4.27	LCJ fault	Sandstone, Mudstone (J)
27	S6	99.11	28.71	3,270	2018.4.26	Southern JSJ fault	Carbonate rock (P)
28	S7	99.06	28.67	3,235	2018.4.26	Southern JSJ fault	Carbonate rock (P)

Previous studies have focused on the source of heat and chemical characteristics of some springs in this area (Shi and wang, 2017; Tang et al., 2017; Zhang, 2017; Hou et al., 2018; Tian et al., 2018, 2019; Zhou et al., 2020a; Yi et al., 2021; Liu et al., 2022). However, limited work has been reported on the relationship between the hydro-chemical characteristics of hot springs and fault activity. Such studies are important for evaluating the geothermal energy potential along the fracture zone. In this study, we focus on the hydrochemical properties and origin of 28 hot springs located in the JSJFZ. Major and trace elements, $^{87}Sr/^{86}Sr$ values, δD and $\delta^{18}O$ values are discussed to character the hydrochemical properties of these hot springs. Various methods were employed to calculate the reservoir temperature and depth of water circulation of these hot springs, so as to reveal their possible hydrochemical evolution processes. An attempt has been made to discuss the relationship between hot spring evolution and seismic activity through a conceptual model of hot spring hydrology cycle, and prospect its implications for future monitoring.

2 Geological setting

The JSJFZ is located in the southeastern Tibetan Plateau, which has long been controlled by the NS compression due to the collision between the Indian and Eurasian continents (Yin and Harrison, 2003). Since the late Cenozoic, because of the rapid northward growth and episodic eastward extrusion of the Tibetan Plateau, the Sichuan-Yunnan diamond-shaped block (SYDSB) has become the main channel for the escape of plateau materials to the east and southeast (Zhu et al., 2017). The JSJFZ is part of the northwestern margin of the SYDSB (Figure 1A). It is a multi-stage active suture, and the faults in this area are mainly right-lateral strike-slip and thrust faults (Wang et al., 2018). Its general trend is NW-SE oriented distribution,

TABLE 2 Hydrochemical properties, major chemial constituents of the geothermal water samples.

Segment	T (°C)	pH	K+ (mg/L)	Na+(mg/L)	Ca2+(mg/L)	Mg2+(mg/L)	Cl- (mg/L)	SO42- (mg/L)	CO32- (mg/L)	HCO3- (mg/L)	SiO2 (mg/l)	TDS	Hydrochemical type
N1	15.80	7.77	3.68	27.06	72.15	13.54	2.57	46.50	26.40	234.85	18.40	310.13	HCO3-Ca•Na
N2	40.50	7.14	3.00	37.38	412.64	21.56	2.53	1115.43	29.04	269.07	44.30	1757.77	SO4•HCO3-Ca
N3′	58.80	7.74	38.02	511.06	91.53	7.71	292.21	301.89	90.08	782.25	68.27	1730.79	HCO3-Na
N4	33.00	6.57	3.92	40.97	298.45	37.83	5.81	22.57	—	953.89	27.39	888.46	HCO3-Ca
N5	48.50	7.22	52.36	369.16	131.88	41.33	15.58	116.52	—	1260.54	50.08	1365.63	HCO3-Na
N6	23.00	7.76	1.30	10.57	75.47	17.84	1.37	29.76	—	217.92	12.09	254.83	HCO3-Ca
N7′	10.57	7.37	78.60	12,979	1258.70	95.52	25,238	3708.77	64.63	107.66	9.10	43,542	Cl-Na
N8	35.20	7.05	12.21	80.99	161.85	26.97	2.99	74.57	56.10	597.86	30.82	717.55	HCO3-Ca•Na
N9′	73.80	8.25	13.61	301.41	40.09	6.33	8.87	212.29	91.45	562.04	93.30	959.21	HCO3-Na
B1	86.10	8.89	29.94	338.72	4.17	0.92	41.69	26.27	151.27	499.83	—	867.72	HCO3-Na
B2	82.00	8.57	14.34	240.10	12.02	0.34	31.27	115.19	—	488.00	323.14	673.19	HCO3-Na
B3	60.00	7.12	18.89	273.54	73.84	16.09	11.57	99.70	123.08	695.56	106.14	968.68	HCO3-Na
B4	65.80	7.32	19.80	258.94	27.50	1.47	12.87	4.21	92.14	611.68	90.31	732.70	HCO3-Na
B5	50.00	7.27	30.42	197.80	167.69	39.57	16.97	103.98	—	917.93	—	1018.01	HCO3-Na•Ca
B6	52.80	7.16	24.84	288.79	127.39	35.90	9.09	147.37	148.52	938.14	78.97	1254.35	HCO3-Na•Ca
B7	79.80	7.55	9.73	123.42	14.61	3.34	5.30	30.57	61.88	234.88	137.82	378.96	HCO3-Na
B8	36.40	7.13	11.33	99.48	124.90	45.53	3.24	104.45	102.45	540.37	41.94	763.46	HCO3-Ca•Na
B9	31.50	8.50	23.70	80.08	116.56	91.82	4.62	66.56	—	215.20	—	492.39	HCO3-Ca•Mg
B10	35.70	7.21	18.22	162.87	166.56	31.94	15.10	49.43	100.39	862.64	45.15	978.25	HCO3-Ca•Na
B11	46.40	7.69	27.58	153.11	146.97	35.71	11.50	163.55	47.44	770.36	52.43	974.48	HCO3-Na•Ca
B12	45.50	7.14	31.60	137.08	130.84	67.24	10.95	162.33	69.30	737.43	85.17	980.84	HCO3-Na•Ca
S1	56.50	7.85	10.87	261.44	22.02	2.02	9.89	22.95	—	625.86	—	647.54	HCO3-Na
S2	17.60	7.59	8.65	158.73	65.88	8.39	2.42	23.59	48.18	532.10	—	585.92	HCO3-Na•Ca
S3	45.00	6.73	53.16	216.58	134.58	26.94	20.63	0.49	—	1128.75	60.56	1025.98	HCO3-Na•Ca
S4	45.00	7.33	11.24	458.28	46.56	4.08	48.50	51.98	—	1099.39	61.20	1176.85	HCO3-Na
S5	73.50	8.21	7.79	112.90	8.92	0.84	14.84	29.34	25.90	198.88	48.06	315.32	HCO3-Na
S6	58.60	7.32	23.90	448.19	47.19	22.83	98.60	32.35	141.09	972.92	79.40	1313.54	HCO3-Na
S7	57.60	7.25	20.40	284.82	35.67	2.77	27.97	50.18	—	799.68	95.54	833.20	HCO3-Na

10.3389/feart.2022.1015134

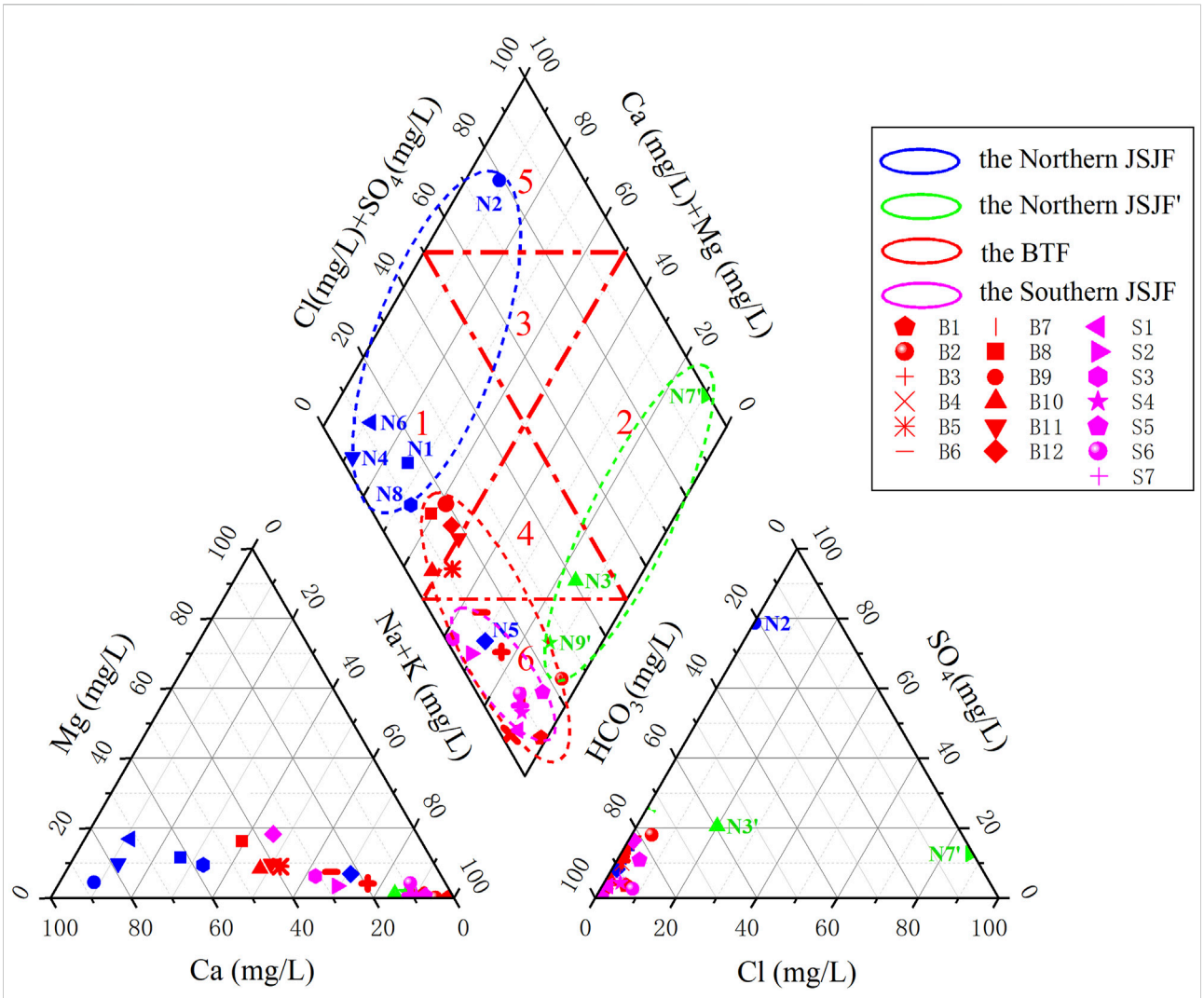

FIGURE 2
Piper diagram showing major ion chemistry of the sampled points. Notes: The hot springs in the blue and green sashed circular area are located in the Northern JSJF, and they are divided into two parts. The hot springs in the red sashed circular area are located in the BTF. The hot springs in the purple sashed circular area are located in the Southern JSJF.

with a total length of 1,200 km and a width of 50–70 km (Xia and Zhu, 2020). In particular, its major faults cut deeply into the crust and even through the asthenosphere. Tectonically, the JSJFZ is cut into two segments by the NNE Batang fault (BTF) (Figure 1B), namely the Northern Jingshajiang fault (NJSJF) and the Southern Jinshajiang fault (SJSJF). The BTF is a dextral fault that strikes N30°E and dips to the northwest at a sharp angle, with a total length of about 200 km. High-temperature hot springs are distributed along the JSJF and BTF. Particularly, hot springs with temperature higher than 80°C have been found in the Batang geothermal field.

The area is covered by widespread Triassic limestone with multi-stage magmatic activity. It owns a well-developed fracture system and frequent earthquakes. Since 780 B.C., two large earthquakes with magnitude >7.0 have occurred in this region, and minor to intermediate seismic events are frequent (Figure 1B). For the SJSJF, the dextral strike-slip rate is 4.9 mma^{-1} during the last 20 years, with a locking depth of approximately 20 km, while the slip rate of the NJSJF is not significant (Xu et al., 2020). For the BTF, the dextral strike-slip rate was 10.8 ± 2.3 mma^{-1} during 1999–2007 (Li et al., 2014), and its slip rate is consistent with that of the SJSJF in recent years (Xu et al., 2020).

3 Sampling and analysis

A total of 28 hot spring water samples were collected from the JSJFZ in 2018–2019. Based on the geological structure, the 28 hot

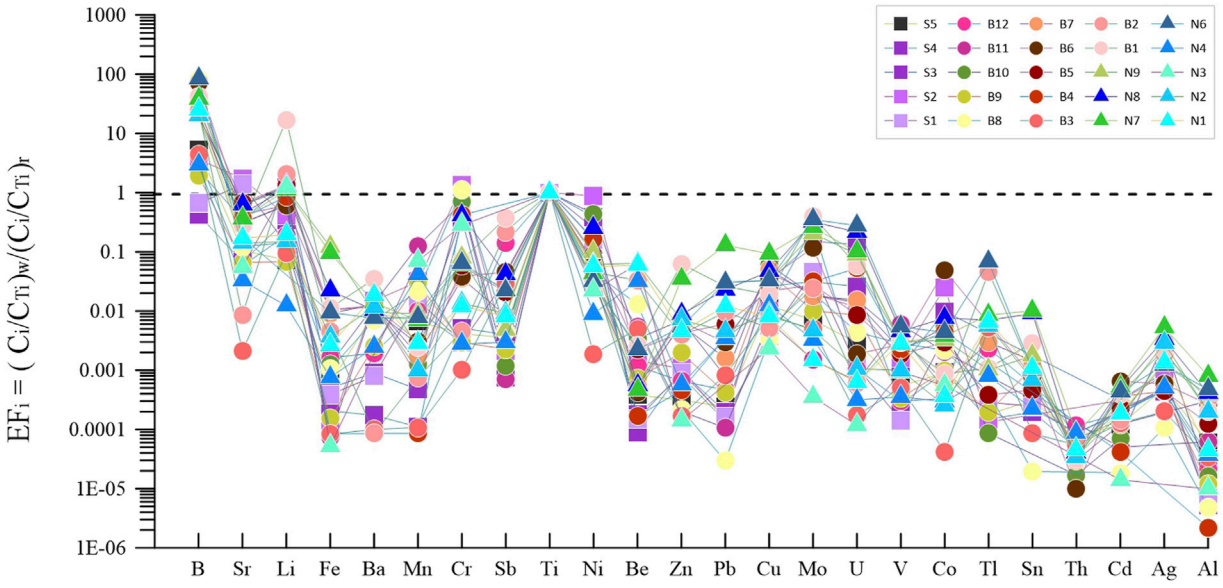

FIGURE 3
Trace element distribution in terms of enrichment coefficient (weight ratios) normalized to Ti for waters of the JSJFZ. Notes: The EFi means the degree of enrichment of an element in a given geological body, from which the source of trace elements in a hot spring can be determined qualitatively, and the EFi of Li, B, and Sr are relatively higher than the other elements.

springs were divided into three sections: N1-N9 in the NJSJF, B1-B12 in the BTF and S1-S7 in the SJSJF, respectively. Among them, hot springs N3, N7, and N9 were located in the secondary fault of NJSJF (Figure 1B). The main sampling information is listed in Table 1.

All water samples were collected in new, colorless, polyethylene terephthalate (PET) bottles that had been rinsed with the water samples. Specific conductivity, pH, dissolved oxygen and temperature of the spring water samples were measured *in situ* by placing multi-parameter probes into the spring vents. Reagent-quality HNO_3 was added to each sample to lower down the pH below 1. The concentrations of cations and anions were measured by a Dionex ICS-900 ion chromatograph and an AS40 automatic sampler at the Earthquake Forecasting Key Lab of China Earthquake Administration (https://www.ief.ac.cn/sysbygypt/), with the reproducibility within ±2% and detection limits 0.01 mg/L. For SiO_2 analysis, the geothermal water samples were diluted ten-fold using deionized water to prevent precipitation of SiO_2 in water. Trace elements were analyzed at the Test Center of the Research Institute of Uranium Geology (http://www.albriug.cn/) by Element XR ICP-MS (Thermo Fisher, Bremen, Germany). The hydrogen and oxygen isotopes were measured using a Finnigan MAT253 mass spectrometer, *via* the TC/EA method. Results were expressed as parts per thousand deviations from the Vienna Standard Mean Ocean Water (V-SMOW). Precisions of ±0.2% (2S.D.) and ±1% (2S.D.) were obtained for $\delta^{18}O$ and δD in a standard water sample, respectively (Wang et al., 2010).

4 Results and discussion

4.1 General hydrochemistry and origin of major ions

The 28 geothermal water samples in the study area were mainly divided into three categories, N1–N9, B1–B12, and S1–S7, respectively (Table 2). The Piper diagram in Figure 2 shows the distribution of the main cations (Ca^{2+}, Mg^{2+}, Na^+, K^+) and anions (HCO_3^-, Cl^- and SO_4^{2-}) of all water samples, which can be used to classify the hydrochemical characteristics of the water samples. It shows that Ca^{2+}, Na^+, and HCO_3^- are the main chemical components for most of the samples.

4.1.1 Hot springs from the NJSJF (N1-N9)

N1 - N9 are located in the major and secondary faults of the NJSJF. All these samples can be divided into two groups, N1, N2, N4, N5, N6, N8 in the major fault and N3′, N7′, N9′ in the secondary fault of the NJSJF. Except for N2 (Ca-SO_4•HCO_3) and N7' (Na-Cl), the hydrochemical types of these hot spring water samples are Na-HCO_3 and Ca•Na-HCO_3 in the major and secondary faults of NJSJF. The temperatures of these hot springs are in the range of 10.57°C to 73.8°C, and the pH values vary between 6.57 and 8.25. Most of the spring water samples have low total dissolved solids (TDS) values ranging from 254.83 mg/L to 1757.77 mg/L, except for N7', which has a TDS value of 43,542.98 mg/L.

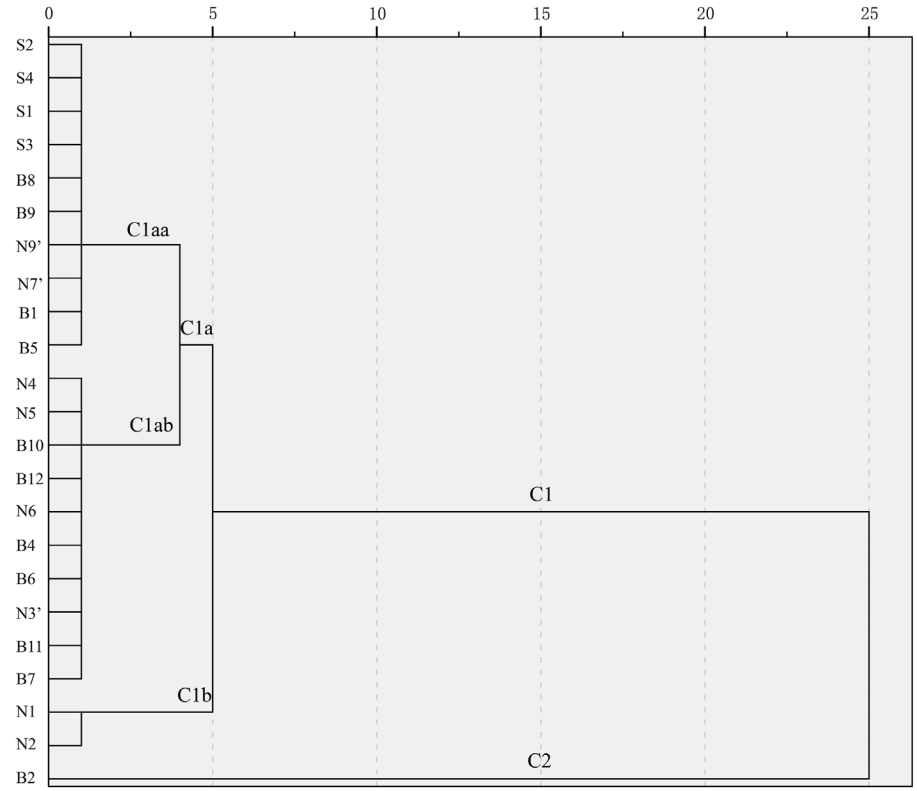

FIGURE 4
Cluster analysis of major ions of the spring water samples. Notes: All the samples can be divided into two parts, namely C1 and C2. And for C1, it can be divided into C1a and C1b. And furthermore, the C1a can be divided into C1aa and C1ab.

In the major fault of the NJSJF, as shown in Figure 2 (blue dots), most of hot spring water samples are distributed in "Zone 1", where the hardness of carbonic acid exceeds 50% and the chemical properties of groundwater are mainly alkaline earth metals and weak acids. Their aquifers are located in the Triassic limestone. As for sample N5, it locates in "Zone 6", where the carbonic alkali metal proportion is more than 50%. Na^+ in the spring water is mainly from the alternating dissolution and cation adsorption of albite, potassium feldspar, anorthite and other minerals. HCO_3^- mainly come from the dissolution of carbonate rocks such as limestone and dolomite (Yi et al., 2021). As for sample N2, it locates in "Zone 5", where non-carbonic acid hardness exceeds 50%. Generally, as the depth of groundwater infiltration depth increases, the leaching effect is enhanced and the concentration of SO_4^{2-} in the spring water increases. Sample N2 is located in Triassic sandstone, mudstone, volcanic strata and limestone. Oxidation of pyrite in aqueous medium can accelerate the dissolution of limestone, so as to enrich the SO_4^{2-} in spring water.

In the secondary fault of the NJSJF, as shown in Figure 2 (green dots), the concentrations of Cl^- (25,238.17 mg/L), SO_4^{2-} (3708.77 mg/L), Na^+ (12,979.57 mg/L) and Ca^{2+} (1258.70 mg/L) in N7′ are much higher than those in N3′, N9'. The TDS value of N7' (43,542.98 mg/L) is the highest one among the samples in the NJSJF. And N7′ is located near the top of the right side of "Zone 2", where non-carbonated alkali metal content is more than 50% and the groundwater chemistry is mainly alkali metal and strong acid. It may have originated from ancient seawater. During the water cycle, it was concentrated and finally became a deep brine with high salinity (Yan et al., 2021). Meanwhile, N9′ is located in "Zone 6", where the proportion of carbonic alkali metals exceeds 50%. Their origin is similar to that of N5.

4.1.2 Hot springs from the BTF (B1-B12)

B1–B12 are located in the BTF (Figure 2, red dots). The hydrochemical types of these hot spring water samples are mainly Na-HCO_3, Ca•Na-HCO_3 and Na•Ca-HCO_3. The temperature of these hot springs varies between 31.50°C and 86.1°C, and the pH value varies between 7.12 and 8.89. The TDS values of these spring water samples are relatively low, ranging from 378.96 mg/L ~ 1254.35 mg/L. Compared to the samples collected in the NSJSF, the hydrochemical types of hot spring water samples in the BTF do not change significantly, i.e., Na-HCO_3, Ca•Na-HCO_3 and Na•Ca-HCO_3. Only the hydro-chemical type of B9 is Ca•Mg-HCO_3. The Na-HCO_3 type waters are located in "Zone 6", while other samples are mainly located

TABLE 3 Hydrogen, oxygen and strontium isotopic compositions of the geothermal water samples.

Segment	δ^2H (‰)	$\delta^{18}O$ (‰)	$^{87}Sr/^{86}Sr$	Segment	Altitude (m)
N1	−131.50	−17.20	0.7134	N1	3,285
N2	−135.70	−17.90	0.7078	N2	3,994
N3′	−122.20	−14.90		N3	4,107
N4	−135.50	−17.40	0.7079	N4	2,906
N5	−148.20	−19.70	0.7142	N5	2,945
N6	−130.00	−17.20	0.7095	N6	2,964
N7′	−116.90	−15.40		N7	3,802
N8	−141.40	−18.10	0.7102	N8	3,313
N9′	−150.3	−20.2	0.7152	N9	3,952
B1	−151.20	−20.00	0.7124	B1	3,562
B2	−143.00	−24.20		B2	3,562
B3	−147.50	−20.00	0.7126	B3	3,287
B4	−158.20	−20.60	0.7158	B4	3,933
B5	—	—		B5	3,167
B6	−121.30	−15.30		B6	2,726
B7	−133.90	−17.50		B7	3,952
B8	−147.80	−19.50	0.7234	B8	2,668
B9	—	—		B9	2,517
B10	−144.70	−18.70	0.7206	B10	3,079
B11	−122.80	−15.40		B11	2,519
B12	−147.10	−18.90	0.7162	B12	2,513
S1	−148.60	−20.50		S1	2,646
S3	−158.70	−20.70	0.7208	S3	3,247
S4	−157.80	−20.80	0.7173	S4	3,099
S5	−143.80	−18.30		S5	2,655
S6	−145.60	−18.10		S6	3,270
S7	−144.60	−19.20		S7	3,235

in the transition region of "Zone 1" and "Zone 4". It indicates that their source rocks are mainly limestone, dolomite, calcareous sandstone and siltstone.

4.1.3 Hot springs from the SJSJF (S1-S7)

S1–S7 are located in the SJSJF (Figure 2, purple dots). The hydro-chemical types of these hot spring water samples are mainly Na-HCO_3 and Ca•Na-HCO_3. The temperature of these hot springs varies between 17.60°C and 73.50°C, and the pH value varies between 6.73 and 8.21. The TDS values of these spring water samples are relatively low, ranging from 315.32 mg/L~1313.54 mg/L. Minimal change of the hydro-chemical types of hot spring water samples is found in the SJSJF. All these spring waters are located in "Zone 6", which is the same with some of the samples in the BTF. It indicates that their source rocks are much more similar, mainly limestone, dolomite.

To sum up, all these spring water samples in the JSJFZ have the following characteristics. Congruent and incongruent dissolution of aquifer rocks, hydrothermal conditions, hydrodynamic power, together with cation exchange reactions may strongly influence the ionic concentration and facies types of the groundwater in the aquifer along the JSJFZ. Carbonate rocks are mainly developed in the study area, and HCO_3^- in the hot springs mainly comes from carbonate rocks, while Ca^{2+} and Mg^{2+} mainly come from soluble limestone ($CaCO_3$) and dolomite ($MgCO_3$) dissolved in the groundwater. In addition to dolomites, limestone, and carbonate rocks, sandstones and conglomerates are also developed in the study area, mainly including quartz, mica, feldspar and other aluminosilicate minerals, etc. Under high temperature and pressure, the recycled water reacts with aluminosilicate and carbonate rocks, causing a large amount of Na^+, silicic acid, and carbonate in the surrounding rocks to dissolve in water (Zhang et al., 2003).

4.2 Origin of trace elements hot spring waters

Water-rock reactions during the deep groundwater circulation are responsible for the variation in trace element

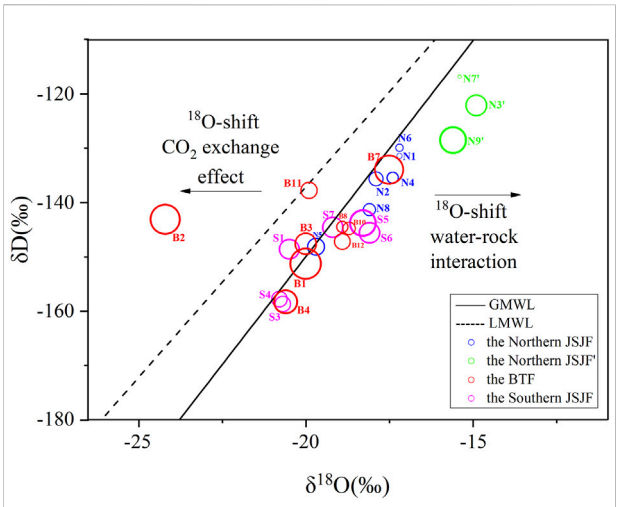

FIGURE 5
Stable hydrogen and oxygen isotope composition of samples in the JSJFZ. Notes: The circles with different colors represents hot springs in different faults. The size of the circles means the different reservoir temperatures, and the larger the size of the circle, the higher the reservoir temperature.

content. Therefore, the degree of water-rock reaction can be inferred to some extent by analyzing the trace element content characteristics. In this study, the trace elements measurements of 26 samples in the JSJFZ are shown in Supplementary Table S1. Twenty-four kinds of trace elements were determined, including Ti, V, Cr, Fe, Co, Ni, Cu, Zn, Ag, Cd, Sn, Sb, Pb, Li, Be, B, Al, Sr, Mo, Ba, Tl, Th, U, and Mn. The enrichment factor ($\mathbf{EF}_i$) is the degree of enrichment of an element in a given geological body, from which the source of trace elements in a hot spring can be determined qualitatively (Ji et al., 2017). The $\mathbf{EF}_i$ is calculated as follows:

$$\boldsymbol{EF}_i = (\boldsymbol{C}_i/\boldsymbol{C}_R)_W/(\boldsymbol{C}_i/\boldsymbol{C}_R)_r \quad (1)$$

Where $\mathbf{C}_R$ is the selected reference elemental content, $\mathbf{C}_i$ is the elemental content in the sample, w and r is the elemental content in the water sample and the rock, respectively. Titanium (Ti) was chosen as the reference element, and the average content of trace elements in typical granites was used as the reference values from Ji et al. (2017).

As shown in Figure 3, the $\mathbf{EF}_i$ of Li, B and Sr are relatively higher than the other elements. The mobile chalcophile elements may originate from external sources, such as sulfide-rich altered rocks. The content of alkali metal elements such as Li is generally lower than the major elements, but due to their active chemical properties, strong mobility, they are mainly enriched in acidic rocks with strong migration ability, and the content of some springs is close to or even exceeds the abundance of the surrounding rocks. The activity of Li may be a signature of deep fluid upwelling during deep fracture activity. Li-silicate minerals, such as lithium mica and chert, are usually formed in volcanic and magmatic rocks, and Li can enter water in a dissolved state under hydrolysis (Zhang et al., 2003). However, the Li concentration in the hot springs of the JSJFZ is not as high as that in the Kangding area, indicating a lack of magmatic source in the JSJFZ (Yi et al., 2021).

Studies have shown that the deeper the groundwater cycle, the higher the B content, because the solubility of B in groundwater increases with depth and pressure (Cai et al., 2001; Zhang et al., 2003). Hot springs with high B content are mainly located in the middle segment of the JSJFZ, i.e. the BTF, indicating that the circulation depth of hot springs in the BTF is larger.

Alkaline-earth metal Sr is a disperse element with high abundance in the crust, mantle and weak alkaline water with a pH of 7.0–8.5 (Cai et al., 2001). In addition, Sr is usually associated with calcium and potassium and is therefore present in calcium and potassium-rich minerals such as potassium feldspar and hornblende (Zhang et al., 2003). Volcanic and granitic rocks rich in potassium feldspar and hornblende are developed in this study area. The pH value of spring water samples in the JSJFZ ranged from 6.57 to 8.89 with a mean value of 7.53, which was favorable for Sr enrichment. Groundwater is heated and reacted at fracture depths, and is recycled into hot spring water after a series of reactions.

The cluster analysis of the major ions in the water samples from the JSJFZ shows that sample B2 in the BTF is different from the other samples (Figure 4) when the center distance is set as 10. Combined with the δD and $\delta^{18}O$ values of sample B2 (Table 3; Figure 5), it indicates that the water-rock reaction here is stronger than elsewhere.

4.3 Origin of hot spring waters

Stable oxygen and hydrogen isotopes have been widely used to determine the source, transit time of geothermal fluids (Tian et al., 2018). Therefore, the relationship between δDand $\delta^{18}O$ of water samples was plotted to trace the source of replenishment of geothermal fluids. In the study area, the δD and $\delta^{18}O$ values of geothermal water samples (Table 3) ranged from −158.7‰ to −116.9‰ and −24.2‰ to −14.9‰ (VSMOW). As shown in Figure 5, the majority of the geothermal waters is plotted close to the Global Meteoric Water Line (Craig, 1961) and the western Sichuan Meteoric Water Line (Chen et al., 2014), indicating the recharge source of meteoric water. An exception is the spring water sample (B2) in the BTF, which may be attributable to the isotopic exchange reaction between water and CO_2 isotopes (Pang et al., 2017). Groundwater is induced by precipitation recharging from high altitude regions. Aquifer rocks dissolved in the infiltrating water and freshening started, consisting of cation exchange during groundwater flow. δD and $\delta^{18}O$ values are more negative for springs at high mountains or high latitudes, and less negative for springs at low altitudes and low latitudes.

Sr concentration and $^{87/86}Sr$ values varied from 0.03 to 13.51 μg/L and 0.7078 to 0.7234, respectively. The spring

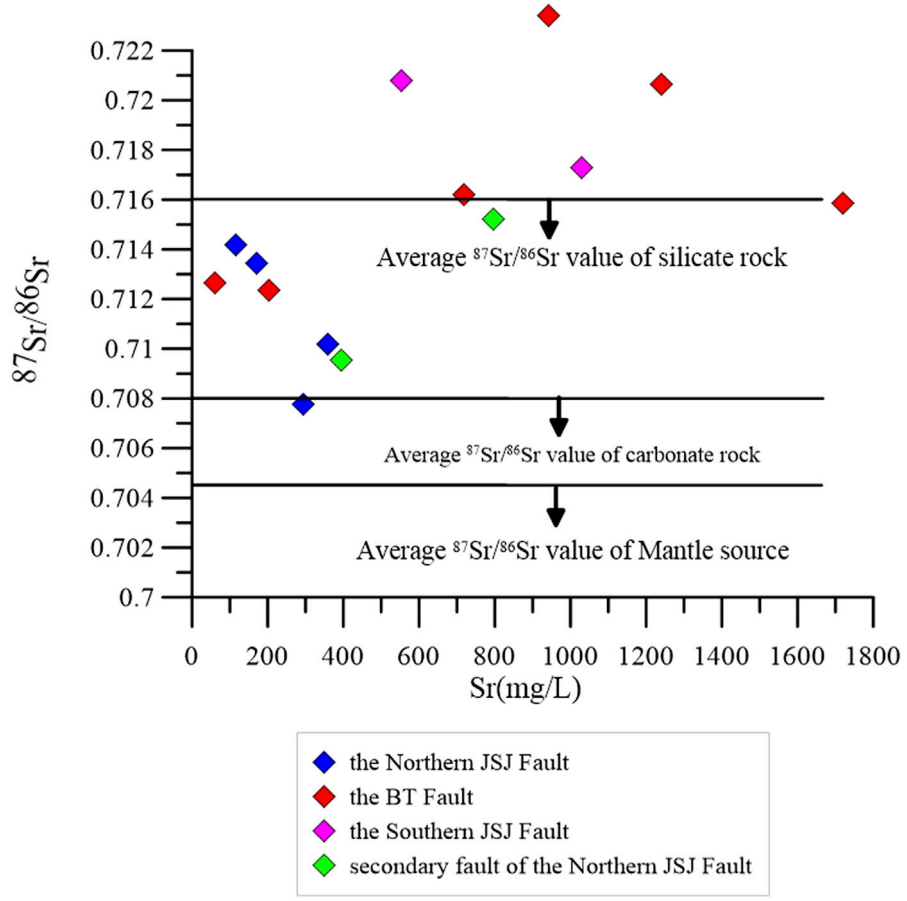

FIGURE 6
Strontium isotopes of the water samples in the JSJFZ.

waters in the NJSJF had lower Sr concentrations than those in the NJSJF and BTF. The $^{87}Sr/^{86}Sr$ values of the spring waters in the NJSJF were closer to the average $^{87}Sr/^{86}Sr$ value of carbonate rock (Figure 6), while the $^{87}Sr/^{86}Sr$ values of the spring waters in the BTF and the SJSJF belonged to the aluminosilicate weathering. The segmental characteristics of the different strontium isotopes suggest that the hot springs were formed by the interaction with Sr-bearing source rocks in the crust during the deep circulation of atmospheric precipitation in the local heat flow system. This is consistent with the geochemical characteristics of the hot spring waters and the lithology of the surrounding rocks.

4.4 Water-rock interaction of hot springs in the JSJFZ

4.4.1 The water-rock reaction equilibrium

The Na-K-Mg ternary diagram (Figure 7) can indicate the degree of ionic equilibrium reaction of the water sample. As shown in Figure 7, the blue and green circles represent water samples in the NJSJF. Except for sample N7′, the other samples are distributed in the "immature waters zone". The red circles represent the water samples in the BTF, which are distributed in the "immature waters zone" or the "partially equilibrated and mixed waters zone." And the purple circles represent water samples in the SJSJF that are distributed in the "immature waters zone" or the "partially equilibrated and mixed waters zone". It can be preliminarily estimated that the spring waters in the BTF have the highest reservoir temperatures in the JSJFZ.

4.4.2 Mineral saturation states

Mineral equilibrium calculations help predict the presence of reactive minerals and estimate mineral reactivity in groundwater systems. By using the saturation index (SI) approach, reactive minerals in host rocks and minerals that may precipitate during the extraction and use of thermal fluids can be predicted from groundwater data without the need to examine solid phases samples (Deutsch, 1997). The mineral saturation indices of hydrothermal minerals that may be present in the reservoirs of geothermal systems

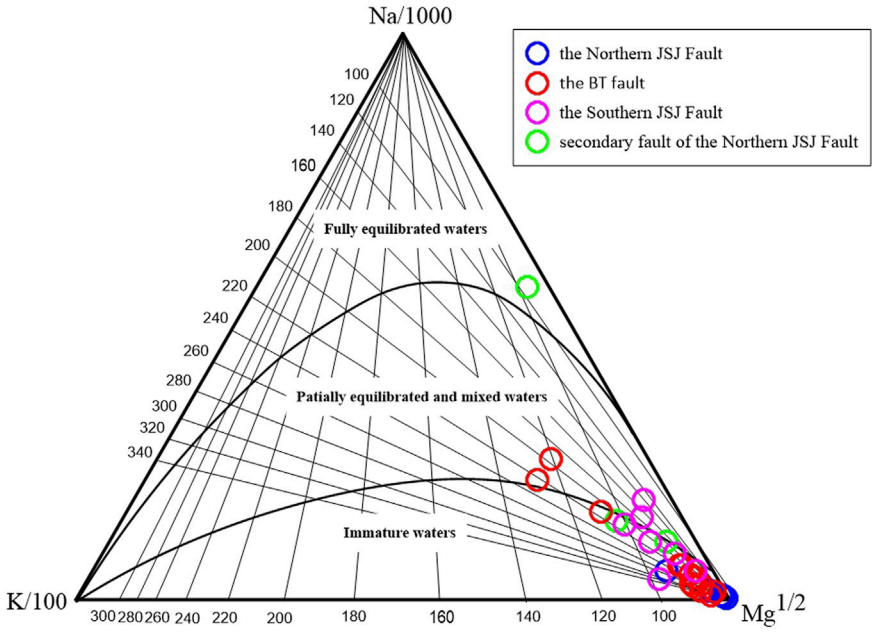

FIGURE 7
Distribution of aqueous samples on the Na-K-Mg ternary diagram.

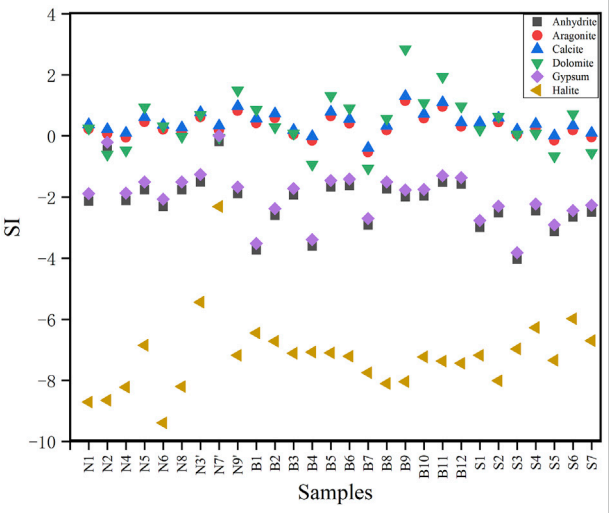

FIGURE 8
Saturation indices values of water samples with respect to minerals. Notes: The value of SI is divided by zero.

were calculated by PHREEQCI-2.12 (USGS) at their outlet temperatures and pH values. Results are presented in Figure 8. Almost all groundwater samples were supersaturated (SI > 0) relative to calcite at the sampling temperature, suggesting that CO_2 degassing may have occurred (Figure 8). Only the value of sample B7 was negative (−0.39), but it was also almost in equilibrium with calcite. This super-saturation state demonstrates the presence of substantial amounts of these minerals and sufficient residence time in the aquifer system (Rouabhia et al., 2012). Except for B4 and B7, groundwater samples were in equilibrium with dolomite (SI~0). The possible cause of B4 and B7's characteristics is that high CO_2 concentrations lead to lower pH values and lower dolomite SI values (Zhou et al., 2020a). Almost all groundwater samples are in under saturation with halite (SI <−4). The rest of minerals in Supplementary Table S2 have various saturation indices.

4.4.3 Reservoir temperature and circulation depth

Chemical geothermometers (including quartz and chalcedony) and cationic geothermometers (including Na-K and Na-Li system) are commonly used to estimate reservoir temperatures. The equations are as follows:

$$\mathbf{T}_{SiO2}(^{\circ}C) = (1309/(5.19 - \log(SiO_2)))-273.15\,(\text{Fournier, 1981}) \quad (2)$$

$$\mathbf{T}_{Na\text{-}K}(^{\circ}C) = (1217/(1.483 + \log(Na/K)))-273.15\,(\text{Fournier, 1981}) \quad (3)$$

$$\mathbf{T}_{Na\text{-}K}(^{\circ}C) = (1390/(1.75 + \log(Na/K)))-273.15\,(\text{Giggenbach, 1988}) \quad (4)$$

$$\mathbf{T}_{Na\text{-}Li}(^{\circ}C) = (1590/(0.779 + \log(Na/Li)))-273.15\,(\text{Kharaka and Mariner, 1984}) \quad (5)$$

These geothermometers consist of equations or models based on temperature-dependent chemical reactions, from

TABLE 4 Calculation of reservoir temperature and circulation depth of geothermal waters.

Sample no.	Toutlet (°C)	TNa-K (°C)	TNa-K (°C)	TNa-Li (°C)	TSiO2 (°C)	TSilicon enthalpy mixing model (°C)	Toptimum (°C)	Proportion of cold water (%)	DSiO2 (km)	DS-E (km)
	Fournier, 1981		Arnorsson, 1998		Kharaka and Mariner, 1984		Fournier, 1981		Fournier and Truesdell, 1974	
N1	16	227	242	—	60	—	60	—	0.9	—
N2	41	177	195	163	96	103	96	71	1.7	1.8
N3	59	192	209	230	117	85	117	34	2.1	1.5
N4	33	212	228	150	75	73	75	71	1.3	1.2
N5	49	248	261	160	102	102	102	62	1.8	1.8
N6	23	234	249	—	45	—	45	—	0.6	—
N7	11	55	77	21	36	—	36	—	0.4	—
N8	35	248	262	190	80	84	80	72	1.4	1.4
N9	73	157	176	165	133	125	133	48	2.5	2.3
B2	86	210	226	295	215	272	215	73	4.2	5.4
B3	66	190	208	204	140	153	140	63	2.6	2.9
B4	66	199	216	233	131	134	131	58	2.4	2.5
B6	53	203	220	159	124	149	124	72	2.3	2.8
B7	80	196	214	240	156	157	156	55	2.9	3.0
B8	35	233	248	204	93	136	93	85	1.6	2.5
B10	35	226	241	239	97	146	97	86	1.7	2.7
B11	46	272	284	225	104	115	104	70	1.9	2.1
B12	48	287	297	235	128	172	128	80	2.4	3.3
S3	45	307	315	187	111	140	111	77	2.0	2.6
S4	45	119	140	172	111	142	111	77	2.0	2.7
S5	74	186	204	190	100	—	100	—	1.8	—
S6	59	167	186	246	124	135	124	64	2.3	2.5
S7	58	189	207	226	134	158	134	71	2.5	3.0

T_{outlet} means the outlet temperature of hot spring; $T_{Na\text{-}K}$, $T_{Na\text{-}Li}$ and T_{SiO2} means reservoir temperature calculated by different geothermometers; $T_{optimum}$ means the most appropriate reservoir temperature; D_{SiO2} and $D_{S\text{-}E}$ means the depths calculated by SiO_2 geothermometers and silicon enthalpy mixing model, respectively.

which equilibrium temperatures can be calculated. In fact, due to the complex geological settings, different chemical geothermometers always yield very different reservoir temperatures. In this study, we compared these calculation results (Table 4). The Na-K-Mg triangle diagram method could help to judge the equibibrium state of the geothermal water (Giggenbach, 1988). In Figure 7, the spring water samples are almost belong to immature waters, indicating that they are not fully equilibrated with the reservoir rocks, so the cation ratio geothermometers cannot provide reliable results than silica geothermeter with no-steam loss. Finally, we chose the quartz geothermometers with no steam loss (Fournier, 1981) as the optimum one. The circulation depth of the spring waters and the proportion of cold water were also deduced using the reservoir temperatures calculated by the Silicon-enthalpy mixing model (Fournier and Truesdell, 1974). The results showed that the T_{SiO2} of the NJSJF, BTF and SJSJF ranged from 36 to 133°C, 93 to 215°C and 100 to 134°C, respectively; the $T_{S\text{-}E}$ of the NJSJF, BTF and SJSJF ranged from 73 to 125°C, 115 to 272°C and 135 to 158°C, respectively. The results are close to those of Tian et al. (2019) on the BTF hot springs. The spatial distribution of outlet temperature and thermal reservoir temperature was consistent with each other. The spring water temperaure in the southern segment of the JSJFZ was higher than that of the northern segment, with the peak located in the BTF.

The circulation depths were evaluated according to the following equation:

$$\boldsymbol{D}(\mathrm{km}) = ((\boldsymbol{T} - \boldsymbol{T}_0)/\Delta t) + h \tag{7}$$

D is the circulation depth; **T** is the reservoir temperature (°C); $\mathbf{T}_0$ is the temperature of the local average temperature (°C); Δt is the geothermal gradient (°C/km) and h is the depth of

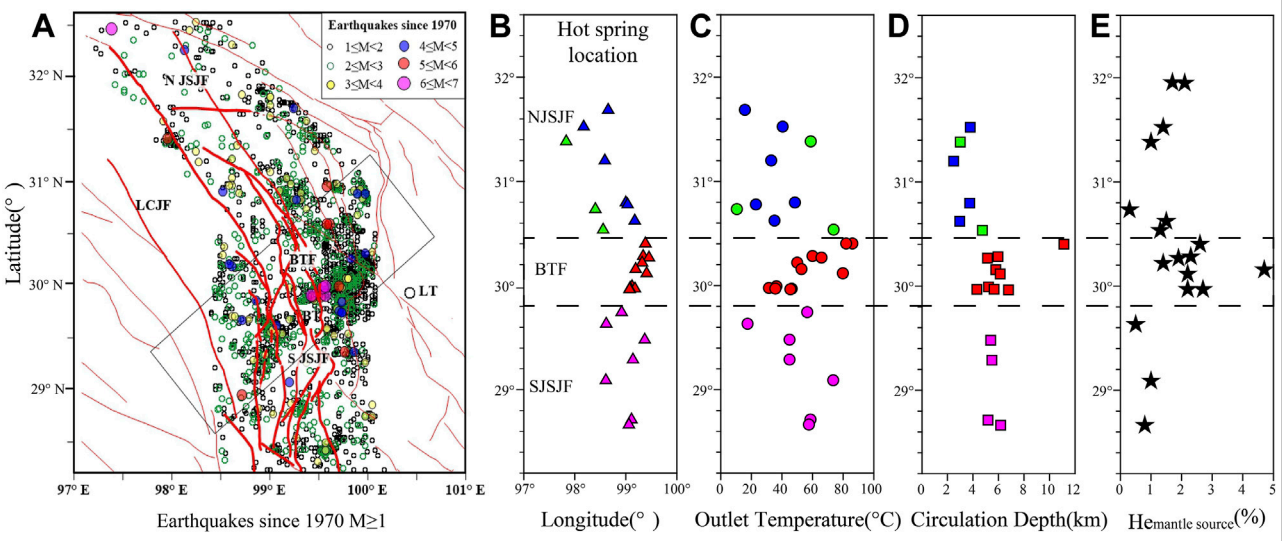

FIGURE 9
Earthquake (M ≥ 1) distribution in the JSJFZ since 1970 **(A)**, hot spring location **(B)**, outlet temperature **(C)**, circulation depth **(D)** and mantle source helium **(E)**, data from Zhou et al., 2020a).

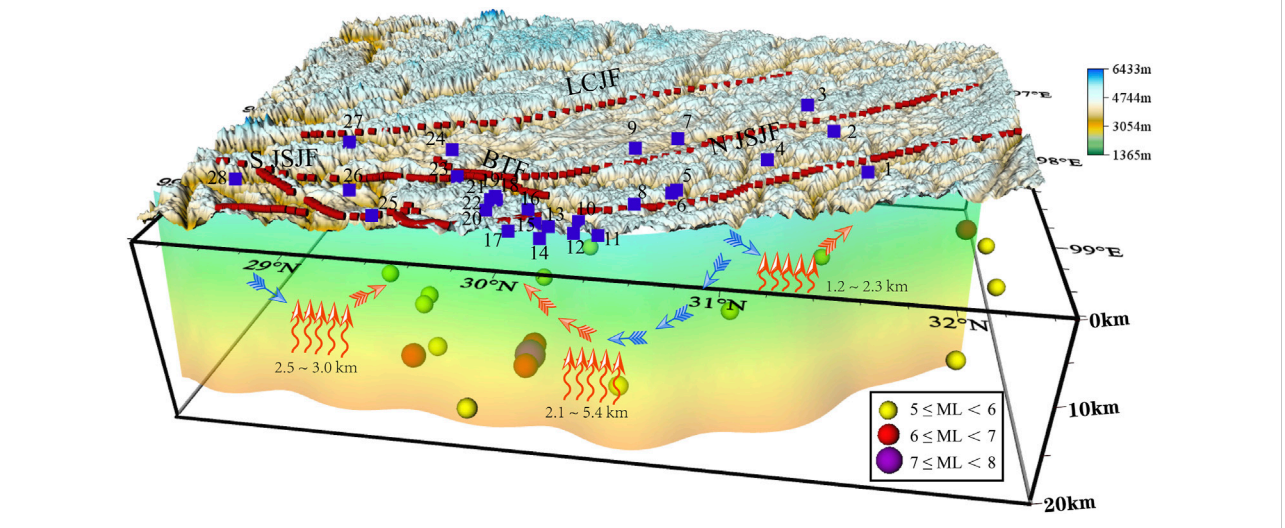

FIGURE 10
Conceptual model of the origin of groundwater and the hydrogeochemical cycling process in the JSJFZ. Notes: The red dashed line represents faults in the study area. The blue square represents the hot springs. The red and blue arrows represent runoff of hot and cold waters, respectively. The red curved arrow represents the suspected heat source location.

constant temperature zone (km). For the Sichuan province, Δt, T_0, h was assumed as 47.5°C/km, 16.42°C and 0.02km, respectively (Zhang et al., 2019).

The D_{SiO2} of the NJSJF, BTF and SJSJF was 0.4~2.5 km, 1.6~4.2 km and 1.8~2.3 km, respectively. And the D_{S-E} of the NJSJF, BTF and SJSJF was 1.2~2.3 km, 2.1~5.4 km and 2.5~3.0 km. Similarly, the circulation depth of the spring waters in the BTF was the deepest.

4.5 Correlation between hydro-geochemical changes and seismic activities

4.5.1 Segmental hydro-chemical characteristics and spatial distribution of earthquakes

Generally, the ranking of the JSJFZ spring waters in terms of temperature, thermal reservoir temperature, circulation depth,

water maturity, water-rock interaction intensity is roughly NJSJF < SJSJF < BTF. For historical earthquakes (M ≥ 5) in the JSJFZ (Figure 1), they used to appear in the NJSJF and BTF, and for recent earthquakes (M ≥ 1) in the JSJFZ, they gathered in the BTF (Figure 9A). It may be due to two mechanisms. The spring waters in the BTF contain more mantle derived materials (Zhou et al., 2017; Zhou et al., 2020a), which confirms that the BTF is characterized by a deep and large fault cutting through the crust or an ultra-crustal fault. Given its strong fault activity, the BTF became an earthquake-prone area. As shown in Figures 9B–E, the outlet temperature, circulation depth and mantle source helium in the hot springs of the BTF were the highest in the JSJFZ. Deep fluid circulation and facture coupling are important triggers of earthquakes. It can be inferred that the first mechanism is more consistent with the characteristics of the JSJFZ. In addition, the effects between fluids and earthquakes are mutual. On the one hand, deep-source fluids promote the occurrence of earthquakes, and on the other hand, the occurrence of earthquakes changes the crustal structure and fluid permeability (Manga and Wang, 2015).

Strong earthquakes may occur in the transition zone of geothermal anomalies (Liu et al., 2022). According to spatial distribution of the reservoir temperatures in the JSJFZ, the BTF coincides with the high and low temperature transition zone where the north-south segment intersects. Earthquakes are more expected to occur in the BTF rather than other areas due to its strong fluid activity characteristics and deep cutting depth. In fact, the BTF has been active since the late Quaternary. In 1870, the Batang M seven earthquake occurred here. According to the GPS measurements, the BTF has a dextral strike slip rate of 8.7 ± 2.1 mm/a (Wang et al., 2008). In the NJSJF, the fault slip is not significant, while in the BTF and the SJSJF, the slip rate reached ~4.9 mm/a (Xu et al., 2020). Correspondingly, the hot springs in the BTF were the most active, and a large number of earthquakes also gathered here. In the BTF and SJSJF area, the locking depth is about 20 km (Xu et al., 2020) and there is a certain degree of strain accumulation in the faults. Earthquakes usually occur on faults with accumulated stresses, especially in areas with strong and weak stress transitions. Based on fracture activity, seismic distribution and geochemical characteristics of the hot springs, the BTF is currently at higher seismic risk than other areas in the JSJFZ.

4.5.2 Conceptual model and evolution of geothermal fluid in JSJFZ

Deep fracture zones can serve not only as a channel for further infiltration of groundwater, but also as a channel for rapid ascent of deep-derived geothermal fluid. It is noted that deep source fluids can trigger earthquakes (Fairley et al., 2003; Shi and wang., 2017; Hou et al., 2018; Wang et al., 2021). When a large amount of fluid invades into a fault, it may change the pore pressure and the stress state in the fault zone. Therefore, it may increase the frequency of minor and intermediate earthquakes. Besides, heat sources, permeability pathways and fault activity also play important roles in formation of hot springs (Chen et al., 2014; Zhou et al., 2020b). Tracing the sources and migration pathways of groundwater in active fault zones is of paramount importance in terms of studying hydro-geochemical precursors in seismic hazards zones.

A conceptual model for the origin of groundwater and the hydro-geochemical cycling process in the JSJFZ is summarized in Figure 10 according to the results of this study. Meteoric waters permeates into the aquifers along the fractures between and around mountains and river terraces through the water-conducting fault zone. Due to the difference in circulation depth, reservoir temperature and degree of water-rock reaction, partially equilibrated water or immature water were formed in the NJSJF, the BTF and the SJSJF. The spring water may mix with cold surface water or shallow groundwater with different mixing ratios during fluid ascent in the fault channel. Finally, it became exposed to the earth's surface as a hot spring. When the crustal stress in the JSJFZ changes, the pressure in the aquifer system and the equilibrated state of hot spring water will be disrupted, resulting in the different hydro-chemical characteristics. The infiltrated waters in the BTF had a considerable deep circulation (~5.4 km) in a high heat flow reservoir. This is the reason for the high mantle helium contribution (Tian et al., 2018; Zhou et al., 2020a), and the frequent high-intensity earthquakes here. Deeply-sourced volatile emissions may have responded rapidly to the onset of sustained plateau growth (Zhang et al., 2021).

The Rayleigh-wave velocity of the NJSJF is higher than that of the southern SYDSB (Fan et al., 2015). The SJSJF is located in the low-velocity channel bounded by major strike-slip faults around the EHS and in the southeastern margin of Tibet (Bao et al., 2015; Hu et al., 2018). The high-resolution Q_{lg} model showed that the main flow channel emerged from the northern end of plateau, extended east and southeast, and then turned south after being blocked by the rigid Sichuan Basin (Zhao et al., 2013). Consistently, the conductance values present very high conductivity regions near the SJSJF. As the fluid content increases, the crust weakens and flows (Unsworth et al., 2005). And crustal flows can occur in orogenic belts and contribute to the uplift of plateau (Bai et al., 2011). High conductivity and low velocity layer is a relatively soft medium, which is prone to deformation, stress and strain conduction, concentration and accumulation. The BTF is located in the transition area of the NJSJF and SJSJF (Wang and Shen, 2020) that is prone to earthquakes. The geophysical and fluid geochemical signatures here are well confirmed by each other. In summary, the hydrological characteristics of hot spring water in fault zones play a crucial role in receiving information on tectonic movements and seismic activities in advance.

5 Conclusion

Fault structures and tectonic movements jointly control the formation and geochemical characteristics of hot springs. The

high-temperature geothermal system along the lithospheric-scale strike-slip JSJFZ was studied.

The geochemical characteristics of the 28 hot springs suggested that they were mainly recharged by atmospheric precipitation from the nearby mountains. Chemical geothermometry applications, together with silicon enthalpy mixing model calculation, presented a reservoir temperature range of 73 ~ 272°C. The proportion of cold water ranged from 34% to 86%. And the circulation depths varied from 1.2 km to 5.4 km.

A conceptual model for the hot spring water origin and circulation cycle showed that the meteoric water firstly seeped into the fault and was heated by the wall rocks. Then, it circulated along faults and fissures to the surface, where it eventually formed hot springs.

The segmental characteristics of the fault, the hydration characteristics together with the H, O, and Sr isotopes of the hot springs located in different segments of the JSJFZ and the seismic activities are closely related to each other. Notably, the hot springs in the BTF had deeper recharges source and high reservoir temperatures than those in the NJSJF and the SJSJF. And it was coincident with strong tectonic and seismological activity here in the BTF. Thus, the spatial distribution hot springs, the hydro-geochemical characteristics and the influence of controlling factors are of great importance to further exploration of strong seismic information.

Data availability statement

The original contributions presented in the study are included in the article/Supplementary Material, further inquiries can be directed to the corresponding authors.

Author contributions

JL as the first author of this manuscript, wrote the main part of the article. XZ and YL as the corresponding authors, controlled the article ideas. MH, JL, JD, and FL helped collect the water samples. JT, YY, and SO made their contributions in the data analysis.

Funding

The work was funded by the Natural Science Foundation of Shaanxi Province, China (2022JQ-254), Spark Program of Earthquake Sciences (XH21032), National Key Research and Development Project (2017YFC1500501-05 and 2019YFC1509203), the National Natural ScienceFoundation of China (41673106, 42073063, and 4193000170), the Special Fund of the Institute of Earthquake Forecasting, China Earthquake Administration (2021IEF0101, 2021IEF0201, and 2021IEF1201) and Open Fund for Earthquake Forecasting (2021EFOF03).

Acknowledgments

We thank the Editor and two reviewers for their constructive comments and suggestions.

Conflict of interest

The authors declare that the research was conducted in the absence of any commercial or financial relationships that could be construed as a potential conflict of interest.

Publisher's note

Supplementary Material

The Supplementary Material for this article can be found online at: https://www.frontiersin.org/articles/10.3389/feart.2022.1015134/full#supplementary-material

References

Bai, D. H., Unsworth, M. J., Meju, M. A., Ma, X., Teng, J., Kong, X., et al. (2011). Crustal deformation of the eastern Tibetan plateau revealed by magnetotelluric imaging. *Nat. Geosci.* 497, 358–362. doi:10.1038/ngeo830

Bao, X., Sun, X., Xu, M., Eaton, D. W., Song, X., Wang, L., et al. (2015). Two crustal low-velocity channels beneath SE Tibet revealed by joint inversion of Rayleigh wave dispersion and receiver functions. *Earth Planet. Sci. Lett.* 415, 16–24. doi:10.1016/j.epsl.2015.01.020

Bo, Y., Liu, C., Zhao, Y., and Wang, L. (2015). Chemical and isotopic characteristics and origin of spring waters in the lanping–simao basin, yunnan, southwestern China. *Geochemistry* 75 (3), 287–300. doi:10.1016/j.chemer.2015.04.002

Chen, Z., Du, J. G., Zhou, X. C., Yi, L., Liu, L., Xie, C., et al. (2014). Hydrochemistry of the hot springs in western sichuan province related to the WenchuanMS8.0 earthquake. *Sci. World J.* 2014, 1–13. doi:10.1155/2014/901432

Craig, H. (1961). Isotopic variations in meteoric waters. *Science* 133 (3465), 1702–1703. doi:10.1126/science.133.3465.1702

Deutsch, W. J. (1997). *Groundwater geochemistry: Fundamentals and applications to contamination*. New York, NY, USA: Lewis Publisher.

Fairley, J., Heffner, J., and Hinds, J. (2003). Geostatistical evaluation of permeability in an active fault zone. *Geophys. Res. Lett.* 30 (18), 1962. doi:10.1029/2003gl018064

Fan, L. P., Wu, J. P., and Fang, L. H. (2015). The characteristics of Rayleigh group velocities in the southeastern margin of the Tibetan Plateau and its tectonic implications. *Chin. J. Geophys.* 58 (5), 1555–1567. in Chinese. doi:10.6038/cjg20150509

Fournier, R. O. (1981). "Application of water geochemistry to geothermal exploration and reservoir engineering," in *Geothermal systems, principles and case histories*. Editors L. Rybach and L. J. P. Muffler (New York: Wiley), 109–143.

Fournier, R. O., and Truesdell, A. H. (1974). Geochemical indicators of subsurface temperature PartII, estimate of temperature and fractions of hot water mixed with cold water. *J. Res. U.S. Geol. Surv.* 2 (3), 263–270. doi:10.3133/ofr741032

Fu, C. C., Lai, C. W., Yang, T. F., Hilton, D. R., Chen, C. H., Walia, V., et al. (2021). An automatic system for continuous monitoring and sampling of groundwater geochemistry in earthquake-prone regions of SW Taiwan. *Front. Earth Sci. (Lausanne).* 9, 635913. doi:10.3389/feart.2021.635913

Fulton, P. M., and Saffer, D. M. (2009). Potential role of mantle-derived fluids in weakening the San Andreas Fault. *J. Geophys. Res.* 114, B07408. doi:10.1029/2008JB006087

Giggenbach, W. F. (1988). Geothermal solute equilibria. derivation of Na-K-Mg-Ca geoindicators. *Geochim. Cosmochim. Acta* 52, 2749–2765. doi:10.1016/0016-7037(88)90143-3

Hou, Y. Y., Shi, Z. M., and Mu, W. Q. (2018). Fluid geochemistry of fault zone hydrothermal system in the yidun-litang area, eastern Tibetan Plateau geothermal belt. *Geofluids* 2018, 1–13. doi:10.1155/2018/6872563

Hu, J. F., Badal, J., Yang, H. Y., Li, G., and Peng, H. (2018). Comprehensive crustal structure and seismological evidence for lower crustal flow in the southeastern margin of Tibet revealed by receiver functions. *Gondwana Res.* 55, 42–59. doi:10.1016/j.gr.2017.11.007

Ji, L., Liu, F. L., and Wang, F. (2017). Multiple granitic magma events in north middle segment of Diancangshan Ailaoshan complex zone: Impications for tectonic evolution. *Acta Pet. Sin.* 33, 2957–2974. in Chinese.

Jonsson, S., Segall, P., Pedersen, R., and Bjornsson, G. (2003). Post-earthquake ground movements correlated to pore-pressure transients. *Nature* 424, 179–183. doi:10.1038/nature01776

King, C. Y. (1986). Gas geochemistry applied to earthquake prediction: An overview. *J. Geophys. Res.* 91 (B12), 12269–12281. doi:10.1029/jb091ib12p12269

Kitagawa, Y., Koizumi, N., and Tsukuda, T. (1996). Comparison of postseismic groundwater temperature changes with earthquake-induced volumetric strain release: Yudani Hot Spring, Japan. *Geophys. Res. Lett.* 23 (22), 3147–3150. doi:10.1029/96GL02517

Li, Y. H., Hao, M., Ji, L. Y., and Qin, S. L. (2014). Fault slip rate and seismic moment deficit on major active faults in mid and south part of the Eastern margin of Tibet plateau. *Chin. J. Geophys.* 57 (4), 1062–1078. in Chinese. doi:10.6038/cjg20140405

Linde, A. T., Suyehiro, K., Miura, S., Sacks, I. S., and Takagi, A. (1988). Episodic aseismic earthquake precursors. *Nature* 334, 513–515. doi:10.1038/334513a0

Liu, W., Guan, L. F., Liu, Y., Xie, X., Zhang, M., Chen, B., et al. (2022). Fluid geochemistry and geothermal anomaly along the yushu-ganzi-xianshuihe fault system, eastern Tibetan plateau: Implications for regional seismic activity. *J. Hydrol. X.* 607, 127554. doi:10.1016/j.jhydrol.2022.127554

Manga, M., and Wang, C. Y. (2015). *Earthquake hydrology, treatise on geophysics*. Amsterdam: Elsevier.

Martinelli, G., and Tamburello, G. (2020). Geological and geophysical factors constraining the occurrence of earthquake precursors in geofluids: A review and reinterpretation. *Front. Earth Sci.* 8, 596050. doi:10.3389/feart.2020.596050

Nakagawa, K., Yu, Z. Q., Berndtsson, R., and Hosono, T. (2020). Temporal characteristics of groundwater chemistry affected by the 2016 Kumamoto earthquake using selforganizing maps. *J. Hydrol. X.* 582, 124519. doi:10.1016/j.jhydrol.2019.124519

Pang, Z. H., Kong, Y. L., Li, J., and Tian, J. (2017). An isotopic geoindicator in the hydrological cycle. *Procedia Earth Planet. Sci.* 17, 534–537. doi:10.1016/j.proeps.2016.12.135

Rosen, M. R., Binda, G., Archer, C., Pozzi, A., Michetti, A. M., and Noble, P. J. (2018). Mechanisms of earthquake-induced chemical and fluid transport to carbonate groundwater springs after earthquakes. *Water Resour. Res.* 54, 5225–5244. doi:10.1029/2017wr022097

Rouabhia, A., Djabri, L., Hadji, R., Baali, F., and FehdiHani, C. A. (2012). Geochemical characterization of groundwater from shallow aquifer surrounding Fetzara Lake NE Algeria. *Arab. J. Geosci.* 5, 1–13. doi:10.1007/s12517-010-0202-6

Scholz, C. H., Sykes, L. R., and Aggarwal, Y. P. (1973). Earthquake prediction: A physical basis. *Science* 181, 803–810. doi:10.1126/science.181.4102.803

Shi, Z. M., and Wang, G. C. (2017). Evaluation of the permeability properties of the Xiaojiang Fault Zone using hot springs and water wells. *Geophys. J. Int.* 209 (3), 1526–1533. doi:10.1093/gji/ggx113

Skelton, A., Andren, M., Kristmannsdottir, H., Stockmann, G., Morth, C. M., Sveinbjornsdottir, A., et al. (2014). Changes in groundwater chemistry before two consecutive earthquakes in Iceland. *Nat. Geosci.* 7, 752–756. doi:10.1038/ngeo2250

Tang, X. C., Zhang, J., Pang, Z. H., Hu, S., Wu, Y., and Bao, S. (2017). Distribution and Genesis of the eastern Tibetan Plateau geothermal belt, Western China. *Environ. Earth Sci.* 76 (1), 31. doi:10.1007/s12665-016-6342-6

Thomas, D. (1988). Geochemical precursors to seismic activity. *Pure Appl. Geophys.* 126, 241–266. doi:10.1007/BF00878998

Tian, J., Pang, Z. H., Guo, Q., Wang, Y., Li, J., Huang, T., et al. (2018). Geochemistry of geothermal fluids with implications on the sources of water and heat recharge to the Rekeng high-temperature geothermal system in the Eastern Himalayan Syntax. *Geothermics* 74, 92–105. doi:10.1016/j.geothermics.2018.02.006

Tian, J., Pang, Z. H., Wang, Y. C., and Guo, Q. (2019). Fluid geochemistry of the Cuopu high temperature geothermal system in the eastern Himalayan syntaxis with implication on its Genesis. *Appl. Geochem.* 110, 104422. doi:10.1016/j.apgeochem.2019.104422

Tian, J., Pang, Z., Liao, D. W., and Zhou, X. (2021). Fluid geochemistry and its implications on the role of deep faults in the Genesis of high temperature systems in the eastern edge of the Qinghai Tibet Plateau. *Appl. Geochem.* 131, 105036. doi:10.1016/j.apgeochem.2021.105036

Unsworth, M. J., Jones, A. G., Wei, W., Marquis, G., Gokarn, S. G., and Spratt, J. E. (2005). Crustal rheology of the Himalaya and Southern Tibet inferred from magnetotelluric data. *Nature* 438 (7064), 78–81. doi:10.1038/nature04154

Wang, B., Zhou, X. C., Zhou, Y. S., Yan, Y., Li, Y., Ouyang, S., et al. (2021). Hydrogeochemistry and precursory anomalies in thermal springs of Fujian (Southeastern China) associated with earthquakes in the Taiwan Strait. *Water* 13, 3523. doi:10.3390/w13243523

Wang, C. Y., Cheng, L. H., Chin, C. V., and Yu, S. B. (2001). Coseismic hydrologic response of an alluvial fan to the 1999 Chi-Chi earthquake, Taiwan. *Geol.* 29 (9), 831–834. doi:10.1130/0091-7613(2001)029<0831:chroaa>2.0.co;2

Wang, E. Q., Meng, K., Xu, G., Li, T. M., Ren, J. W., Qiao, X., et al. (2018). Cenozoic two-stage obduction of the Indian subcontinent: On the interaction between the Indian Ocean, Tethyan and Eurasian plates. *Acta Pet. Sin.* 34 (7), 1867–1875. in Chinese.

Wang, M., Shen, Z. K., Gan, W. J., Liao, H., Li, T. M., Ren, J. W., et al. (2008). GPS monitoring of temporal deformation of the Xianshuihe fault. *Sci. Chi. Ser. D-Earth Sci.* 51, 1259–1266. doi:10.1007/s11430-008-0095-3

Wang, M., and Shen, Z. K. (2020). Present-day crustal deformation of continental China derived from GPS and its tectonic implications. *J. Geophys. Res. Solid Earth* 125 (2), 1–22. doi:10.1029/2019JB018774

Wang, P., Song, X., Han, D., Zhang, Y., and Liu, X. (2010). A study of root water uptake of crops indicated by hydrogen and oxygen stable isotopes: A case in shanxi province, China. *Agric. Water Manag.* 97, 475–482. doi:10.1016/j.agwat.2009.11.008

Xia, J. W., and Zhu, M. (2020). Study on tectonic characteristics and activity of middle section of Jinshajiang main fault zoon. *Yangtze River* 51 (5), 131–137. in Chinese.

Xu, X. X., Ji, L. Y., Jiang, F. Y., and Zhang, W. T. (2020). Study on current activity features of Jinshajiang Fault Zone based on GPS and small earthquakes. *J. Geod. Geodyn.* 40 (10), 1062–1067. in Chinese. doi:10.14075/j.jgg.2020.10.013

Yan, R., Woith, H., and Wang, R. (2014). Groundwater level changes induced by the 2011 Tohoku earthquake in China mainland. *Geophys. J. Int.* 199, 533–548. doi:10.1093/gji/ggu196

Yan, Y. C., Liu, F. L., Guo, L. S., Zhou, X. C., Ouyang, S. P., Li, J. C., et al. (2021). Hydrogeochemical characteristics of the hot springs in the longmenshan fault zone. *J. Seismol. Res.* 44 (2), 96–110. in Chinese. doi:10.3969/j.issn.1000-0666.2021.02.005

Yang, T. F., Wen, H. Y., Fu, C. C., Lee, H. F., Lan, T. F., Chen, A. T., et al. (2011). Soil radon flux and concentrations in hydrothermal area of the tatun volcano group, northern taiwan. *Geochem. J.* 45 (6), 483–490. doi:10.2343/geochemj.1.0144

Yi, L., Qi, J. H., Li, X., Xu, M., Zhang, X., Zhang, Q., et al. (2021). Geochemical characteristics and Genesis of the high-temperature geothermal systems in the north section of the Sanjiang Orogenic belt in southeast Tibetan Plateau. *J. Volcanol. Geotherm. Res.* 414 (2021), 107244. doi:10.1016/j.jvolgeores.2021.107244

Yin, A., and Harrison, T. M. (2003). Geologic evolution of the Himalayan-Tibetan orogen. *Annu. Rev. Earth Planet. Sci.* 28 (28), 211–280. doi:10.1146/annurev.earth.28.1.211

Yuce, G., Italiano, F., and D'Alessandro, W. (2014). Origin and interactions of fluids circulating over the Amik Basin (Hatay-Turkey) and relationships with the hydrologic, geologic and tectonic settings. *Chem. Geol.* 388, 23–39. doi:10.1016/j.chemgeo.2014.09.006

Zhang, C. S., Zhang, Y. C., and Wu, M. L. (2003). Study on relationship between earthquake and hydro-geochemistry of groundwater in southern part of North-South earthquake belt in China. *J. Geomechaics* 9 (1), 21–30. in Chinese.

Zhang, J., Li, W., Tang, X., Tian, J., Wang, Y., Guo, Q., et al. (2017). Geothermal data analysis at the high-temperature hydrothermal area in Western Sichuan. *Sci. China Earth Sci.* 08 (60), 1507–1521. doi:10.1007/s11430-016-9053-2

Zhang, M. L., Guo, Z., Xu, S., Barry, P. H., Sano, Y., Zhang, L., et al. (2021). Linking deeply-sourced volatile emissions to plateau growth dynamics in southeastern Tibetan Plateau. *Nat. Commun.* 12, 4157. doi:10.1038/s41467-021-24415-y

Zhang, W., Wang, G. L., Xing, L. X., and Zhao, J. (2019). Geochemical response of deep geothermal processes in the Litang region, Western Sichuan. *Energy Explor. Exploitation* 2 (37), 626–645. doi:10.1177/0144598718812550

Zhao, L. F., Xie, X. B., He, J. K., Tian, X., and Yao, Z. X. (2013). Crustal flow pattern beneath the Tibetan Plateau constrained by regional Lg-wave Q tomography. *Earth Planet. Sci. Lett.* 383, 113–122. doi:10.1016/j.epsl.2013.09.038

Zhou, X. C., Liu, L., Chen, Z., Cui, Y., and Du, J. (2017). Gas geochemistry of the hot spring in the Litang fault zone, Southeast Tibetan Plateau. *Appl. Geochem.* 79, 17–26. doi:10.1016/j.apgeochem.2017.01.022

Zhou, X. C., Wang, W. L., Li, L. W., JianMin, H., LanTian, X., ZhongPing, L., et al. (2020a). Geochemical features of hot spring gases in the Jinshajiang-Red River fault zone, Southeast Tibetan Plateau. *Acta Pet. Sin.* 36 (7), 2197–2214. (in Chinese). doi:10.18654/1000-0569/2020.07.18

Zhou, Z. H., Tian, L., Zhao, J., Wang, H., and Liu, J. (2020b). Stress-related pre-seismic water radon concentration variations in the Panjin observation well, China (1994–2020). *Front. Earth Sci. (Lausanne).* 8. doi:10.3389/feart.2020.596283

Zhou, Z. H., Zhong, J., Zhao, J., Yan, R., Tian, L., and Fu, H. (2021). Two mechanisms of earthquake-induced hydrochemical variations in an observation well. *Water* 13 (17), 2385. doi:10.3390/w13172385

Zhu, J. S., Wang, X. B., Yang, Y. H., Fan, J., and Cheng, X. Q. (2017). The crustal flow beneath the eastern margin of the Tibetan Plateau and its process of dynamics. *Chin. J. Geophys.* 60 (6), 2038–2057. in Chinese. doi:10.6038/cjg20170602

frontiers | Frontiers in Earth Science

TYPE Original Research
PUBLISHED 19 January 2023
DOI 10.3389/feart.2022.1091052

OPEN ACCESS

EDITED BY
Long Li,
University of Alberta, Canada

REVIEWED BY
Cyril Aubaud,
UMR7154 Institut de Physique du Globe de Paris (IPGP), France
Kan Li,
Woods Hole Oceanographic Institution, United States

*CORRESPONDENCE
Maoliang Zhang,
mzhang@tju.edu.cn
Sheng Xu,
sheng.xu@tju.edu.cn

SPECIALTY SECTION
This article was submitted to Geochemistry, a section of the journal Frontiers in Earth Science

RECEIVED 06 November 2022
ACCEPTED 25 November 2022
PUBLISHED 19 January 2023

CITATION
Liu Y, Liu W, Zhou X, Zhong J, Zhang M and Xu S (2023), Carbon mobilization in response to the 2021 M_w 7.4 Maduo earthquake: Constraints from carbon isotope systematics of subsurface fluids. *Front. Earth Sci.* 10:1091052. doi: 10.3389/feart.2022.1091052

Carbon mobilization in response to the 2021 M_w 7.4 Maduo earthquake: Constraints from carbon isotope systematics of subsurface fluids

Yi Liu[1], Wei Liu[1], Xiaocheng Zhou[2], Jun Zhong[1], Maoliang Zhang[1,3]* and Sheng Xu[1]*

[1]School of Earth System Science, Tianjin University, Tianjin, China, [2]Institute of Earthquake Forecasting, China Earthquake Administration, Beijing, China, [3]Atmosphere and Ocean Research Institute, The University of Tokyo, Chiba, Japan

Active fault zones provide favorable channels for the discharge of carbon-bearing fluids from Earth's interior. Earthquakes, as a common fault-related dynamic process, can disturb the circulation of subsurface fluids and their interactions with country rocks and sediments on short timescales, which may cause changes in carbon mobilization processes and carbon sources of the discharged fluids. However, quantitative research on earthquake-induced changes in carbon mobilization at deep and shallow levels remains lacking. Here, we present a quantitative study on stable carbon isotopes ($\delta^{13}C$) and radiocarbon values ($\Delta^{14}C$) of dissolved inorganic carbon (DIC) in subsurface fluid samples from the surface rupture zone formed by the M_w 7.4 Maduo earthquake (22 May 2021) and the East Kunlun fault, NE Tibetan Plateau. Our results show that $\delta^{13}C_{DIC}$ values vary from −11.6‰ to 0.1‰, while $\Delta^{13}C_{DIC}$ values have a range of −980‰ to −46‰. Using a mass balance model based on $\delta^{13}C_{DIC}$ and DIC concentrations, we calculated the proportions of source components involved in DIC, including organic carbon, carbonates, and deeply-sourced carbon. On average, waters discharging from the surface rupture zone have higher inputs from organic carbon (28.1%) than those from the East Kunlun fault (18.6%), with the latter showing higher deeply-sourced carbon contributions (45.7% vs. 30.7%). This is consistent with the lower average $\Delta^{14}C_{DIC}$ value (−544‰) observed from the East Kunlun fault, suggesting more inputs from carbon source components that are devoid of ^{14}C (i.e., deeply-sourced carbon and carbonates). These findings indicate that seismic events can significantly affect the carbon mobilization processes at variable depths, especially the shallow soil organic carbon in the case of the 2021 Maduo earthquake. The potential effects of earthquake-induced changes in carbon mobilization processes should be taken into account in the modeling of tectonic carbon dioxide degassing and carbon cycle on longer timescales.

KEYWORDS

carbon mobilization processes, carbon isotope systematics, dissolved inorganic carbon, subsurface fluids, Maduo earthquake

1 Introduction

The discharge of carbon-bearing fluids is prevalent in active fault zones controlled by different tectonic regimes (e.g., Becker et al., 2008; Tamburello et al., 2018; Zhang et al., 2021). Previous studies indicate that active fault zone can act as a favorable channel for fluid transfer from Earth's interior to the surface (Williams et al., 2013), or as a barrier for fluid flows in the case of episodic fluid accumulation within fault-related traps (Miller et al., 2004; Han et al., 2019). The circulation of subsurface fluids in the active fault zones, as well as their interaction with country rocks or sediments at variable depths, is thus expected to affect the geochemical compositions of groundwaters (Newell et al., 2008; Crossey et al., 2009). Such fluid-rock or fluid-sediment interactions have established the basis for earthquake forecasting studies that integrate the geochemistry of subsurface fluids (e.g., natural spring waters) as an effective tool for evaluating the potential earthquake risk (Ingebritsen and Manga, 2014).

The kinematics and locking status of seismically active fault zones play an important role in controlling the decarbonation reactions of source materials and the migration of carbon-bearing fluids through the lithosphere (Faulkner et al., 2010; Zucchi, 2020). At a regional scale, the correlations between deeply-sourced CO_2 emissions, seismic activity, and fault types have been clearly demonstrated (Tamburello et al., 2018). Moreover, numerous studies have reported post-earthquake perturbations in geochemistry and fluxes of carbon-bearing fluids associated with specific earthquake events (e.g., Claesson et al., 2004; Skelton et al., 2014; Ünal-İmer et al., 2016; Girault et al., 2018; Bonini, 2022). From a dynamic point of view, earthquakes have the potential to disturb the circulation of subsurface fluids and their leaching effects on country rocks or sediments over short timescales (Rosen et al., 2018), giving rise to transient changes in geochemical proxies of the discharging fluids along active faults, such as concentrations and isotopic compositions of dissolved inorganic carbon (DIC) (Girault et al., 2018; Barbieri et al., 2020). As a result, carbon isotope systematics (e.g., $\delta^{13}C_{DIC}$ and $\delta^{13}C_{CO2}$; Barbieri et al., 2020) of deeply-sourced fluids, together with other hydrogeochemical and isotopic tracers (e.g., Cl^-, SO_4^{2-}, and $^3He/^4He$; Tsunogai and Wakita, 1995; Kulongoski et al., 2013; Bräuer et al., 2014), have been taken as potential precursors to earthquakes. Nevertheless, quantification of the earthquake-induced changes in carbon mobilization processes at deep and shallow levels remains loosely constrained, especially for earthquakes that occurred in the continental orogenic setting of the Tibetan Plateau and its surrounding regions.

In this study, we focus on carbon source quantification of a post-earthquake sample set of subsurface fluids from Maduo region in the Songpan-Ganzi block of NE Tibetan Plateau (Figure 1), based on stable carbon isotopes ($\delta^{13}C$) and radiocarbon values ($\Delta^{14}C$) of total DIC, which can contribute to understanding the carbon mobilization processes in response to the M_w 7.4 Maduo earthquake (98.34°E, 34.59°N, epicenter depth = 17 km; Zhu et al., 2021) occurred on 22 May 2021. The data of water chemistry, $\delta^{18}O_{H2O}$, δD_{H2O}, and $^{87}Sr/^{86}Sr$ of this sample set were reported in Lu et al. (2021), but carbon isotope systematics of DIC have not been investigated, resulting in an open question about the DIC sources and carbon mobilization mechanism associated with the 2021 Maduo earthquake. Spatially, carbon sources of subsurface fluids from boundary faults of the Songpan-Ganzi block (e.g., Yushu-Ganzi-Xianshuihe fault and Longmenshan fault; Figure 1A) have been reported (e.g., Zhou et al., 2015; Tian et al., 2021; Liu et al., 2022; Xu et al., 2022). In contrast, the carbon source components of the Jiangcuo fault in the block interior (Figure 1B), which was ruptured by the 2021 Maduo earthquake, are still largely unknown. Our results show that earthquake-induced changes in mobilization of soil organic carbon are prominent for the fluids discharging from the Maduo surface rupture zone, compared to the adjacent East Kunlun fault zone that is characterized by discharge of carbon-bearing fluids with more contributions from deeply-sourced carbon.

2 Geological background

Since the early Cenozoic, the continuous India-Asia continental collision has resulted in extensive crustal shortening, tectonic uplift, and lateral extrusion of the micro-continental blocks that constitute the Tibetan Plateau (Tapponnier et al., 2001). As a result, a series of active fault zones were formed primarily along the block boundary and also in the block interior (Figure 1). Generally, tectonic deformation of the block boundary faults controls outward expansion of the Tibetan Plateau and the occurrence of high-frequency strong earthquakes within the continental interiors (Liu and Stein, 2016). Our study area is located in the Songpan-Ganzi block, which is bounded by the East Kunlun fault to the north, the Yushu-Ganzi-Xianshuihe fault to the south, the Longmenshan fault to the east, and the western segment of the Altyn Tagh fault to the west (Figure 1A). There are a series of left-lateral strike-slip faults inside of the Songpan-Ganzi block near the East Kunlun fault zone, including the Maduo-Gande fault, Jiangcuo fault, South Gande fault, and Dari fault from north to south (Figure 1B). Permian and Triassic strata and Quaternary alluvial diluvium are mainly exposed in the study area; the main lithology assemblage includes sandstone, glutenite, limestone, slate, pyroclastic rock and sand gravel (Figure 1B).

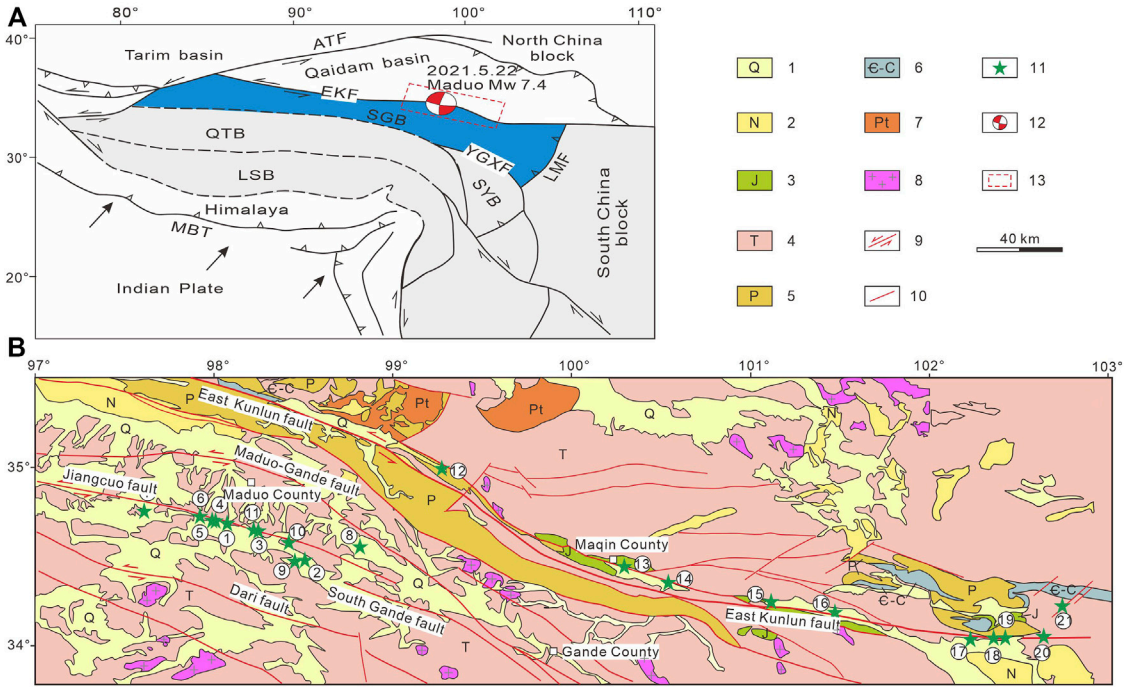

FIGURE 1
Simplified geological map showing tectonic features and sample distribution in the study area (modified from Wu et al., 2016). **(A)** Geological units and tectonic boundaries of the Tibetan Plateau and adjacent regions. Abbreviations: LSB, Lhasa block; QTB, Qiangtang block; SGB, Songpan-Ganzi block; SYB, Sichuan-Yunnan block; Tarim basin; Qaidam basin; ATF, Altyn Tagh fault; EKF, East Kunlun fault; LMF, Longmenshan fault; YGXF, Yushu-Ganzi-Xianshuihe fault; MBT, Main Boundary Thrust. **(B)** Regional geological information and sample distribution in the Maduo surface rupture zone and the East Kunlun fault zone. Numbers 1–21 in circles represent serial numbers of sampling sites (see Table 1). Legends are shown by numbers as follows: 1, Quaternary sediments; 2, Neogene sedimentary rocks; 3, Jurassic sedimentary rocks; 4, Triassic sedimentary rocks; 5, Permian sedimentary rocks; 6, Cambrian-carboniferous sedimentary rocks; 7, Precambrian metamorphic rocks; 8, Mesozoic granite; 9, Strike-slip fault; 10, Other types of faults; 11, Sampling sites; 12, Focal mechanism solution; 13, Location of study area shown in **(A)**.

As one of the most seismically active regions in mainland China, the boundary faults of the Songpan-Ganzi block, eight large earthquakes (mostly M>7.0) have occurred in the past 25 years (Pan et al., 2022), the largest of which was the 2008 M_w 7.9 Wenchuan earthquake (Hubbard and Shaw, 2009). Located to the NE of the 2021 Maduo earthquake, the East Kunlun fault is a large-scale left-lateral strike-slip fault with an inclination angle of about 55–85° and a total length of about 1900 km (Figure 1A). The slip rate of this fault decreases from 11 mm/yr to 2 mm/yr from east to west (Ren et al., 2013), which is still in an active state of intensive seismicity. A recent study by Yue et al. (2022) suggests that the Songpan-Ganzi block, although being controlled by a distributed shearing stress state, exhibits slip rates on its boundary faults (e.g., ~10 mm/y for the Xianshuihe fault) about one order of magnitude higher than that on the block interior faults (0–2 mm/y). The 2021 M_w 7.4 Maduo earthquake occurred along the Jiangcuo fault in the block interior (Pan et al., 2022), making it a relatively rare case of strong earthquake in the interior of the Songpan-Ganzi block.

Importantly, the 2021 Maduo earthquake provides a good opportunity for constraining the carbon sources of subsurface fluids and their changes in response to strong earthquakes in the block interior. After the Maduo earthquake on 22 May 2021, a nearly 70-km-long surface rupture zone with a NWW-SEE strike was formed along the Jiangcuo fault (Figure 1B), which is characterized by linear distribution of passes, fault triangles, gullies dislocation, twisted ridges, sag ponds, and the discharging spring waters near the surface rupture zone (Lu et al., 2021). The strong rupturing creates favorable conditions for the upward migration of subsurface fluids and controls the NWW-SEE trending distribution of springs (Figure 1B). These newly formed springs are considered in this study to make a comparison of quantitatively constrained carbon sources with natural springs along the East Kunlun fault zone.

3 Samples and methods

In May 2021, twenty-one spring water and surface water samples were collected from the surface rupture zone near the epicenter of the 2021 Maduo earthquake and the East Kunlun fault zone (Figure 1). Among them, nine samples (MDW1–6 and

MDW9–11) are from the Maduo surface rupture zone, and ten samples (MDW12–21) are from the East Kunlun fault zone. For comparison, two surface water samples were collected from the Eling Lake (MDW7) and the Yellow River (MDW8). A portable water parameter meter was used to measure the temperature and pH value of waters. All samples were stored in polyethylene bottles. Based on the data of water chemistry (cations and anions), basicity, temperature, and pH value (Lu et al., 2021), the partial pressure of carbon dioxide (pCO_2) and DIC concentration in water are calculated using software PHREEQC.

The stable carbon isotope and radiocarbon isotope compositions were analyzed in School of Earth System Science, Tianjin University. The stable carbon isotope of DIC was analyzed by the conventional stable isotope ratio mass spectrometer (Model Delta V Plus, Thermo Fisher, United States) coupled with a Gas Bench. 1 mL 85% phosphoric acid was injected into a glass reaction flask, which was purged with high-purity helium gas, and then an appropriate amount of water (0.05–0.33 mL in this study) was injected. After complete reaction (>18 h), CO_2 was introduced into the ion source of the mass spectrometer for analysis of $^{13}C/^{12}C$ ratio. Meanwhile, the international standard (NBS-18) was used during the analysis. The results were represented by $\delta^{13}C_{DIC}$ relative to the V-PDB standard, and the overall uncertainty in repeated measurements of the working standard NBS-18 is ±0.2‰ (2σ). For radioactive carbon isotope of DIC ($\Delta^{14}C_{DIC}$) analysis, the water samples were injected into pre-vacuumed bottles with 85% phosphoric acid. The produced gas was introduced in the vacuum system for separation between CO_2 and H_2O. The purified CO_2 was sealed in vacuum tube filled with iron powder and zinc powder in which the CO_2 gas reacted with zinc under the condition of Fe catalyst and 550 °C to form graphite. The graphite was pressed into a sample holder and loaded in the ion source of the 0.5 MV accelerator mass spectrometer (AMS, 1.5SDH-1, NEC, United States) to determine the $^{14}C/^{12}C$ ratio. Repeated measurements of the working standards indicate ~0.3% precision and accuracy on the $^{14}C/^{12}C$ ratio. The mass-dependent carbon isotopic fractionation effect has been corrected using the on-line AMS-measured $^{13}C/^{12}C$ ratios.

4 Results

The analytical results of water samples are summarized in Table 1. The pCO_2 values of the 21 water samples range from 0.0011 to 0.0417 atm, much higher than the local atmospheric pCO_2 value of 0.0003 atm. The $\delta^{13}C_{DIC}$ values of spring waters in Maduo surface rupture zone vary from −8.5‰ to −4.6‰, whereas samples in East Kunlun fault zone have a $\delta^{13}C_{DIC}$ range of −11.6‰ to 0.1‰ (Table 1). As a comparison, the $\delta^{13}C_{DIC}$ values of the Eling Lake water and Yellow River water are −7.3‰ and −11.3‰, respectively. The $\Delta^{14}C_{DIC}$ values of spring water samples range from −980‰ to −46‰, and one surface water sample from the Yellow River (MDW8) has a $\Delta^{14}C_{DIC}$ value of −58‰ (Table 1).

5 Discussion

5.1 Identification of candidate carbon source components

There are generally four candidate carbon end-member for the sources of DIC in spring waters (Chiodini et al., 2000): 1) atmospheric CO_2; 2) organic carbon; 3) dissolution of carbonate minerals; 4) deeply-sourced carbon (e.g., mantle-derived and/or metamorphic CO_2). Different carbon source components have specific ranges of $\delta^{13}C$ values, which on average are −8.5‰ for modern atmospheric CO_2 (Campeau et al., 2017); −26‰ and −12‰ for C_3 and C_4 plants, respectively; −4‰ for mantle-derived CO_2; and 0 ± 2‰ for marine carbonate rocks (Telmer and Veizer, 1999; Pineau et al., 2004; Newell et al., 2008). In addition to stable carbon isotope, radiocarbon isotope ($\Delta^{14}C$) is also an important geochemical indicator for identifying carbon sources (Wang et al., 2022). High $\Delta^{14}C$ values indicate the involvement of shallow carbon sources such as atmospheric CO_2 and modern organic carbon, while low $\Delta^{14}C$ values indicate the contribution from deep carbon sources such as carbonate dissolution, mantle-derived CO_2, and metamorphic CO_2 (Mayorga et al., 2005). Since the stable carbon isotopic compositions of different end-members overlap to some extent, and mixing of any two carbon end-members could lead to $\delta^{13}C$ values consistent with those of a particular end-member, further identification of carbon source based on stable carbon isotopes and radiocarbon can better constrain the relative contributions of deep and shallow sources of CO_2 (Xu et al., 2022).

According to the relationship between $\delta^{13}C_{DIC}$ and $\Delta^{14}C_{DIC}$ (Figure 2), compared with the springs in Xianshuihe-Anninghe fault zone (Xu et al., 2022), the springs and surface water in Maduo surface fracture zone and East Kunlun fault zone are basically in the mixing zone of modern organic carbon, atmospheric CO_2, dissolved carbonate, and deeply-sourced carbon. Most springs near the surface rupture zone are relatively rich in ^{14}C (average $\Delta^{14}C_{DIC}$ = −279‰), while most springs near the East Kunlun fault zone are relatively poor in ^{14}C (average $\Delta^{14}C_{DIC}$ = −544‰). The $\Delta^{14}C_{DIC}$ value of sample MDW21 (−980‰) is basically consistent with those of the springs of Xianshuihe-Anninghe fault zone, falling in the $\Delta^{14}C_{DIC}$ range of deeply-sourced carbon and carbonate components (Figure 2). Except for MDW21, the $\Delta^{14}C_{DIC}$ values of spring water samples in this study are higher than those of the Xianshuihe-Anninghe samples (−997‰ to −909‰; Xu et al., 2022), suggesting more inputs of modern organic

TABLE 1 Sample information, concentrations of major cations and anions, stable carbon isotopes and radiocarbon isotopes of the water samples.

No	Sample ID	Longitude (E)	Latitude (N)	Temperature* (°C)	pH*	Ca^{2+*} (mM)	Mg^{2+*} (mM)	HCO_3^{-*} (mM)	SO_4^{2-*} (mM)	DIC (mM)	pCO_2 (atm)	$\delta^{13}C_{DIC}$ (‰)	$\Delta^{14}C_{DIC}$ (‰)
1	MDW1	98.086	34.675	8	8.1	1.47	0.77	4.24	0.18	5.13	0.0019	−7.2	
2	MDW2	98.522	34.470	5	7.7	0.67	0.43	2.51	0.04	3.21	0.0029	−7.0	−46
3	MDW3	98.262	34.634	5	8.1	3.13	1.67	8.41	0.81	10.00	0.0035	−8.5	
4	MDW4	98.018	34.694	8	8.3	1.48	1.03	3.97	0.34	4.70	0.0011	−7.9	−209
5	MDW5	98.006	34.695	8	8.2	1.57	0.84	5.02	0.27	6.00	0.0018	−8.2	
6	MDW6	97.932	34.718	5	8.3	2.36	1.17	6.22	0.71	7.33	0.0017	−6.4	
7	MDW7**	97.625	34.750	8	8.2	1.88	0.57	5.03	0.17	6.01	0.0018	−7.3	
8	MDW8***	98.830	34.542	11	8.1	1.56	2.05	6.52	0.08	7.75	0.0030	−11.3	−58
9	MDW9	98.466	34.466	11	8.2	1.36	1.30	3.70	0.36	4.40	0.0013	−4.6	−648
10	MDW10	98.432	34.572	3	8.1	0.93	0.91	3.63	0.10	4.44	0.0016	−5.9	
11	MDW11	98.233	34.643	5	8.2	1.57	0.83	3.96	0.18	4.75	0.0014	−8.4	−211
12	MDW12	99.289	34.985	4.5	8.1	3.64	1.84	6.51	2.16	7.73	0.0027	−2.0	−519
13	MDW13	100.310	34.441	10	8.1	2.52	1.57	7.21	0.78	8.56	0.0032	−6.3	
14	MDW14	100.556	34.357	4.5	8.2	1.64	0.57	4.92	0.07	5.92	0.0017	−11.6	−221
15	MDW15	101.132	34.242	6.5	7.9	2.52	0.84	8.33	0.15	10.19	0.0058	−10.2	−201
16	MDW16	101.488	34.182	9.5	7.8	3.11	0.41	8.15	0.05	10.02	0.0074	−10.9	
17	MDW17	102.266	34.015	9	8.0	2.39	0.83	6.66	0.05	8.03	0.0038	−5.4	
18	MDW18	102.389	34.024	4.5	7.9	2.52	1.12	9.41	0.01	11.53	0.0063	−6.6	−798
19	MDW19	102.458	34.019	12	8.0	1.91	0.89	6.51	0.10	7.85	0.0038	−6.4	
20	MDW20	102.680	34.035	28	8.0	2.17	0.75	7.08	0.10	8.35	0.0051	−3.8	
21	MDW21	102.783	34.203	49	7.6	5.66	2.77	17.8	2.39	20.61	0.0417	0.1	−980

Notes: * Data from Lu et al. (2021); ** Eling Lake water; *** Yellow River water.

10.3389/feart.2022.1091052

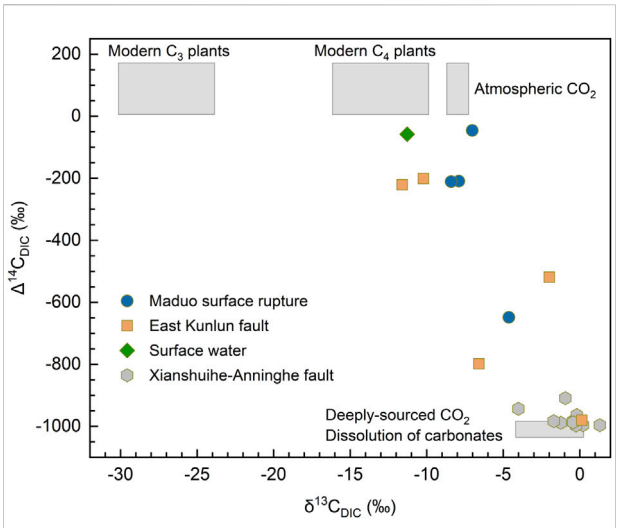

FIGURE 2
Plot of $\Delta^{14}C_{DIC}$ *versus* $\delta^{13}C_{DIC}$ for spring and surface water samples in the study area. Data of the Xianshuihe-Anninghe fault zone are from Xu et al. (2022).

carbon to subsurface fluids along the Maduo surface rupture zone and East Kunlun fault zone.

The pCO_2 values in spring and surface waters near the Maduo surface rupture zone and the East Kunlun fault zone are at least over three times higher than the atmospheric CO_2 partial pressure (~0.0003 atm; Liu et al., 2022); and therefore, the contribution of atmospheric CO_2 to DIC in the spring and surface waters can be largely excluded. In addition, the infiltrating waters contain a mixed DIC component of atmospheric CO_2 and biospheric organic carbon in the soils, but generally have a $\delta^{13}C$ value close to the organic carbon end-member (Chiodini et al., 2000). Therefore, the DIC in spring waters is mainly derived from modern organic carbon, carbonate-dissolved carbon, and deeply-sourced carbon. In addition, according to $\Delta^{14}C_{DIC}$ values, DIC of MDW2 (−46‰) and MDW8 (the Yellow River water, −58‰) exhibits clear organic inputs to radiocarbon isotopes, in contrast to the DIC of MDW21 (−980‰) that is depleted in ^{14}C due to contributions from deeply-sourced carbon and carbonate dissolution.

5.2 Quantification of carbon source contributions

It is generally accepted that Ca^{2+} and Mg^{2+} dissolved in water (including surface water and groundwater) are mainly derived from dissolution of carbonate minerals (Liu et al., 2022 and references therein), but sulfate minerals may also contribute to part of them (Chiodini et al., 2004). Assuming that Ca^{2+}, Mg^{2+} and SO_4^{2-} in springs are all contributed by dissolution of carbonate and sulfate minerals, the DIC ascribed to carbonate mineral dissolution (C_{carb}) can be calculated according to Eq. 1. After deducting the contribution from carbonate dissolved carbon using Eq. 2, the DIC from external carbon (C_{ext}, non-carbonate dissolved carbon) can be obtained (Chiodini et al., 2000). As shown in Table 2, the C_{carb} and C_{ext} values of spring waters in the Maduo surface rupture zone are 1.05–3.98 mmol L^{-1} and 2.09–6.02 mmol L^{-1}, respectively, while the C_{carb} and C_{ext} values of spring waters in the East Kunlun fault zone are 2.14–6.04 mmol L^{-1} and 3.78–14.57 mmol L^{-1}, respectively. According to Eq. 3, the isotopic composition of external carbon can be calculated to further constrain its sources (Chiodini et al., 2004).

$$C_{carb} = Ca^{2+} + Mg^{2+} - SO_4^{2-} \quad (1)$$

$$C_{ext} = DIC - C_{carb} \quad (2)$$

$$\delta^{13}C_{DIC} \times DIC = \delta^{13}C_{ext} \times C_{ext} + \delta^{13}C_{carb} \times C_{carb} \quad (3)$$

In Eq. 3, $\delta^{13}C_{ext}$ represents the isotopic composition of external carbon, and $\delta^{13}C_{carb}$ represents the isotopic composition of dissolved carbon from carbonates. The reference $\delta^{13}C$ value of marine carbonates (0‰; Hoefs, 2009) was used to calculate the isotopic composition of external carbon. In addition, if the water sample before acquisition is affected by CO_2 degassing or carbonate mineral precipitation, the C_{ext} value will be underestimated and the $\delta^{13}C_{ext}$ value will be overestimated (Chiodini et al., 2004). The effects of CO_2 degassing or carbonate precipitation on $\delta^{13}C$ values in springs cannot be constrained based on available data in this study. Nevertheless, following Chiodini et al. (2000), the effect of CO_2 degassing or carbonate precipitation in the calculation is probably negligible when pCO_2 and DIC values are much lower than ~1 atm and 0.0695 mol/L, respectively. Considering the DIC concentrations (3.21–20.61 mmol/L) and pCO_2 values (0.0011–0.0417 atm) of water samples in this study (Table 1), we suggest that the effect of significant CO_2 degassing or carbonate precipitation was probably negligible for the calculation of C_{ext} and $\delta^{13}C_{ext}$ values in spring waters.

The calculated results (Table 2) show that the $\delta^{13}C_{ext}$ values of spring waters in Maduo surface rupture zone range from −15.7‰ to −9.7‰; the $\delta^{13}C_{ext}$ values in the East Kunlun fault zone vary from −18.2‰ to 0.2‰. As shown in Figure 3, the C_{ext} and $\delta^{13}C_{ext}$ of springs indicate two candidate sources for external carbon, namely organic carbon and deeply-sourced carbon (i.e., endogenic carbon). The curves represent theoretical mixing of organic carbon end-member with different C_{ext} concentrations and deeply-sourced carbon end-member (Figure 3), which can well explain source components of external carbon in spring waters from the Maduo surface rupture zone and East Kunlun fault zone. In particular, most springs of the East Kunlun fault zone are more enriched in ^{13}C than those from the Maduo surface rupture zone.

The proportions of source components involved in external carbon can be quantitatively constrained by the binary mixing model following Eq. 4.

TABLE 2 Proportions of organic carbon, deeply-sourced carbon, and carbonate involved in DIC of the water samples.

No	Sample ID	Locality	C_{carb} (mM)	C_{ext} (mM)	$\delta^{13}C_{ext}$ (‰)	C_{org} (%)	C_{endo} (%)	C_{carb} (%)
1	MDW1	MSRZ	2.05	3.07	−12.0	28.5	31.4	40.1
2	MDW2	MSRZ	1.05	2.16	−10.4	28.2	39.1	32.7
3	MDW3	MSRZ	3.98	6.02	−14.1	32.9	27.3	39.8
4	MDW4	MSRZ	2.17	2.53	−14.7	30.5	23.3	46.2
5	MDW5	MSRZ	2.14	3.86	−12.7	32.1	32.3	35.6
6	MDW6	MSRZ	2.82	4.51	−10.4	25.6	35.9	38.5
7	MDW7	Eling Lake	2.28	3.74	−11.7	28.8	33.4	37.8
8	MDW8	Yellow River	3.53	4.22	−20.7	42.4	12.1	45.5
9	MDW9	MSRZ	2.31	2.09	−9.8	18.7	28.7	52.6
10	MDW10	MSRZ	1.74	2.69	−9.7	23.8	36.9	39.3
11	MDW11	MSRZ	2.21	2.54	−15.7	32.3	21.2	46.5
12	MDW12	EKFZ	3.31	4.42	−3.5	10.0	47.2	42.8
13	MDW13	EKFZ	3.31	5.25	−10.3	25.4	35.9	38.7
14	MDW14	EKFZ	2.14	3.78	−18.2	44.1	19.8	36.1
15	MDW15	EKFZ	3.22	6.98	−14.9	39.5	29.0	31.5
16	MDW16	EKFZ	3.46	6.56	−16.7	41.8	23.7	34.5
17	MDW17	EKFZ	3.17	4.87	−8.9	22.2	38.4	39.4
18	MDW18	EKFZ	3.63	7.90	−9.6	26.7	41.8	31.5
19	MDW19	EKFZ	2.70	5.16	−9.7	25.9	39.8	34.3
20	MDW20	EKFZ	2.81	5.54	−5.7	16.7	49.7	33.6
21	MDW21	EKFZ	6.04	14.57	0.2	3.3	67.4	29.3

MSRZ, Maduo surface rupture zone; EKFZ, East Kunlun fault zone. For the East Kunlun fault zone, the average proportions of organic carbon (C_{org}), deeply-sourced carbon (C_{endo}), and carbonate (C_{carb}) end-members are 18.6% (3.3–26.7%), 45.7% (35.9–67.4%) and 35.7% (29.3–42.8%), respectively, which do not take into account samples MDW14 to MDW16 due to possible shallow fluid sources that fail to reflect the properties of deep fluid circulation in the East Kunlun fault zone (see details in Section 5.3 of the main text). Similarly, the average proportions of C_{org}, C_{endo}, and C_{carb} calculated for water samples from the Maduo surface rupture zone are 28.1% (18.7–32.9%), 30.7% (21.2–39.1%), and 41.2% (32.7–52.6%), respectively.

$$\delta^{13}C_{ext} \times C_{ext} = \delta^{13}C_{org} \times C_{org} + \delta^{13}C_{endo} \times C_{endo} \quad (4)$$

The results show that the C_{org} and C_{endo} values of springs near the Maduo surface rupture zone are 0.82–3.29 mmol L^{-1} and 1.01–2.73 mmol L^{-1}, respectively; the C_{org} and C_{endo} values of springs along the East Kunlun fault zone are 0.67–4.18 mmol L^{-1} and 1.17–13.90 mmol L^{-1}, respectively. For most springs of the East Kunlun fault zone, the average proportions of organic carbon, deeply-sourced carbon, and carbonate end-members are 18.6% (3.3–26.7%), 45.7% (35.9–67.4%) and 35.7% (29.3–42.8%), respectively (Table 2). In contrast, the spring waters in the Maduo surface rupture zone yield average end-member proportions of 28.1% (18.7–32.9%) for organic carbon, 30.7% (21.2–39.1%) for deeply-sourced carbon, and 41.2% (32.7–52.6%) for carbonate, respectively (Table 2). Irrespective of sample locations, the DIC in the studied spring waters are generally derived from dissolution of carbonates (average = 38.1%), followed by deeply-sourced carbon (average = 35.2%) and organic carbon (average = 26.7%). Notably, spring waters from the Maduo surface rupture zone have higher inputs from organic carbon (28.1%) than those from the East Kunlun fault zone (18.6%), with the latter showing higher contributions from deeply-sourced carbon (45.7% vs. 30.7%).

5.3 Mechanism of earthquake-induced carbon mobilization

Previous studies have reported that anomalies in chemical compositions and isotope ratios of carbon-bearing fluids before and after seismic events could reflect earthquake-induced fluid release as well as changes in fluid migration pathways (e.g., Weise et al., 2001; Bräuer et al., 2007; Chiodini et al., 2011; Bräuer et al., 2014). Generally, the geochemical anomalies can be explained by fluid discharge from isolated pores and fractures, mixing of components from different aquifers, and increased inputs of surface flow or deeply-sourced fluids (Rosen et al., 2018; Barbieri et al., 2020).

In this study, springs in the Maduo surface rupture zone show more organic carbon contribution compared to most springs in the East Kunlun fault zone. These springs reflect the post-earthquake upwelling of mostly shallow groundwater and recharged surrounding water (Lu et al., 2021). Due to the

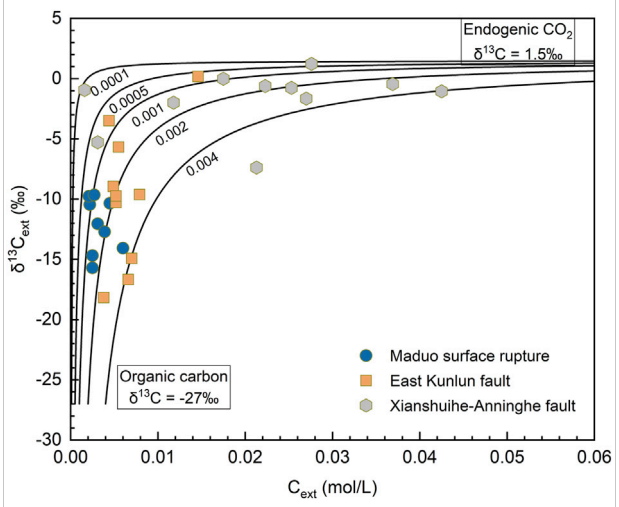

FIGURE 3
Plot of $\delta^{13}C_{ext}$ *versus* C_{ext} for spring samples in the study area. Data of the Xianshuihe-Anninghe fault zone are from Xu et al. (2022). The modeling parameters of end-members are as follows: (1) Organic carbon: $\delta^{13}C_{org}$ = −27‰, C_{ext} = 0.0001–0.004 mol L^{-1}; (2) Endogenic (deeply-sourced) carbon: $\delta^{13}C_{endo}$ = 1.5‰, C_{ext} >> 0.06 mol L^{-1}. The $\delta^{13}C$ value of deeply-sourced carbon end-member represents a mixture of carbon from mantle degassing and decomposition of marine limestones. The $\delta^{13}C$ value of metamorphic CO_2 depends on that of source rocks, and we cannot discriminate carbon from mantle degassing and metamorphic decarbonation due to the lack of further geochemical data (e.g., $^3He/^4He$) in this study. The numbers (i.e., 0.0001, 0.0005, 0.001, 0.002, and 0.004) near corresponding mixing curves represent carbon contents (shown in C_{ext}) of organic carbon end-member.

mixing between surface water and groundwater in the rupture zone formed by the Maduo earthquake, we suggest that more modern soil CO_2 entered into the spring waters (Figure 4A), consistent with our carbon isotope results (Tables 1 and 2). Geophysical data show that the Jiangcuo fault, along which the Maduo earthquake occurred, mainly extends to the brittle upper crustal depths (0–30 km; Yue et al., 2022), as indicated by the epicenter of about 17 km (Zhu et al., 2021). In this case, the inputs of deeply-sourced carbon would be less than those of shallow organic carbon and sedimentary carbonates. The enhanced release of organic carbon after earthquakes has also been observed in other seismically active regions (Wang et al., 2016; Bonini, 2022). For example, Rosen et al. (2018) reported a decrease in $\delta^{13}C_{DIC}$ values from −11.6‰ to −17.3‰ for the Nerea spring after the 2016 Amatrice-Norcia earthquake, which was probably due to soil CO_2 release. After the 2008 Wenchuan earthquake, Zheng et al. (2013) also observed emissions of biogenic gases from shallow reservoirs through faults or fractures.

As an important boundary fault of the Songpan-Ganzi block, the East Kunlun fault zone cut deep into the middle and lower crust (Sun et al., 2019), which is conducive to the upward migration of deep fluids. Therefore, most springs near the East Kunlun fault zone show high contributions from deeply-sourced carbon components as shown in Figure 4B. Similarly, after the 2016 Amatrice-Norcia earthquake, Rosen et al. (2018) observed an increase of $\delta^{13}C_{DIC}$ (~6‰) in the Santa Susanna Spring. Such abrupt change was attributed to increased inputs from deeply-sourced carbon, or the addition of groundwater enriched in heavier carbon isotopes (such as the groundwater from reservoirs with long residence time or intense water-rock interaction). Notably, relatively higher organic carbon contributions are observed in three springs (MDW14, MDW15, and MDW16; Table 2) along the East Kunlun fault. Since their $\delta^{13}C_{DIC}$ values are similar to that of the Yellow River water (MDW8). It is possible that fluid sources of the three springs are influenced by shallow waters such as rivers or streams, which thus fails to reflect the deep fluid circulation related to deep-cutting nature of the East Kunlun fault zone.

The above findings suggest that seismic events such as the 2021 Maduo earthquake can affect carbon mobilization processes at variable depths, especially shallow organic carbon that tends to be released from the newly formed rupture zones (Figure 4). The

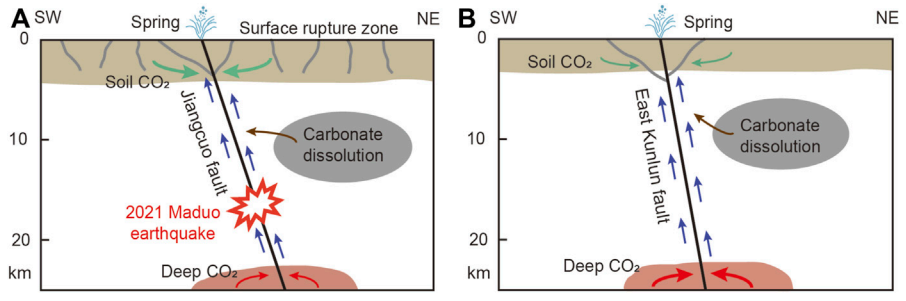

FIGURE 4
Schematic model showing carbon mobilization processes in the Maduo surface rupture zone **(A)** and the East Kunlun fault zone **(B)**. Note that inputs from organic carbon in soils are higher (thicker green arrows; Figure 4A) in the spring waters discharging from the surface rupture zone formed by 2021 Maduo earthquake, while the spring waters in the East Kunlun fault zone have higher inputs from deep CO_2 (thicker red arrows in Figure 4B).

combination of changes in hydrogeochemical and isotopic signatures of groundwater before and after earthquake could further reveal the mechanism of carbon emissions induced by perturbations in carbon mobilization processes at deep and shallow levels (Rosen et al., 2018). Moreover, it is also of considerable significance to take into account the potential effects of earthquake-induced CO_2 emissions in modeling of tectonic evolution and carbon cycling over longer timescales (Wang et al., 2016).

6 Conclusion

Based on stable carbon isotope and radiocarbon isotope of the DIC in spring and surface waters, combined with regional geological and geophysical evidence, our study quantitatively constrained the carbon source components involved in the discharging subsurface fluids after the 2021 Maduo earthquake. Overall, the DIC in spring waters is mainly derived from dissolved carbonate minerals (38.1%), modern soil organic carbon (26.7%), and deeply-sourced carbon (35.2%). Spatially, spring waters discharging from the Maduo surface rupture zone have higher inputs from modern soil organic carbon (28.1%) than those observed in the East Kunlun fault zone (18.6%), suggesting enhanced mobilization of organic carbon as a result of earthquake-induced fault rupturing that is suggested to be confined within upper crustal depths. In contrast, the higher inputs of deeply-sourced carbon (45.7%) to spring waters from the East Kunlun fault zone suggest higher probability of decarbonation processes at larger depths in the case of deep cutting of the East Kunlun strike-slip fault system. We suggest that the earthquake-induced release of organic carbon, as indicated by our observations after the 2021 M_w 7.4 Maduo earthquake, could shed new insights into the potential relationships between tectonic evolution and global carbon cycle.

Data availability statement

The original contributions presented in the study are included in the article/Supplementary Material, further inquiries can be directed to the corresponding authors.

Author contributions

SX and MZ conceived the study based on samples collected by XZ. YL analyzed the samples, performed data modeling, and wrote the manuscript with contributions from SX, MZ, WL, and JZ. WL helped with model visualization. SX and MZ revised the manuscript based on comments from other authors.

Funding

This work was supported by National Key Research and Development Project (Grant No. 2020YFA0607700) and National Natural Science Foundation of China (Grant Nos. 41930642 and 42072327). MZ is supported as an Overseas Researcher under a Postdoctoral Fellowship (Grant No. P20025) of the Japan Society for the Promotion of Science (JSPS).

Acknowledgments

Yue Zheng is appreciated for polishing English language of the draft manuscript. We thank editorial handling by Associate Editor Long Li and constructive comments and suggestions from Cyril Aubaud and Kan Li.

Conflict of interest

The authors declare that the research was conducted in the absence of any commercial or financial relationships that could be construed as a potential conflict of interest.

Publisher's note

References

Barbieri, M., Boschetti, T., Barberio, M. D., Billi, A., Franchini, S., Iacumin, P., et al. (2020). Tracing deep fluid source contribution to groundwater in an active seismic area (central Italy): A combined geothermometric and isotopic ($\delta^{13}C$) perspective. *J. Hydrol. X.* 582, 124495. doi:10.1016/j.jhydrol.2019.124495

Becker, J. A., Bickle, M. J., Galy, A., and Holland, T. J. B. (2008). Himalayan metamorphic CO_2 fluxes: Quantitative constraints from hydrothermal springs. *Earth Planet. Sci. Lett.* 265, 616–629. doi:10.1016/j.epsl.2007.10.046

Bonini, M. (2022). Can coseismic static stress changes sustain postseismic degassing? *Geology* 50, 371–376. doi:10.1130/G49465.1

Bräuer, K., Kämpf, H., Koch, U., Niedermann, S., and Strauch, G. (2007). Seismically induced changes of the fluid signature detected by a multi-isotope approach (He, CO_2, CH_4, N_2) at the Wettinquelle, Bad Brambach (central Europe). *J. Geophys. Res.* 112, B04307. doi:10.1029/2006JB004404

Bräuer, K., Kämpf, H., and Strauch, G. (2014). Seismically triggered anomalies in the isotope signatures of mantle-derived gases detected at degassing sites along two neighboring faults in NW Bohemia, central Europe. *J. Geophys. Res. Solid Earth* 119, 5613–5632. doi:10.1002/2014JB011044

Campeau, A., Wallin, M. B., Giesler, R., Löfgren, S., Mörth, C.-M., Schiff, S., et al. (2017). Multiple sources and sinks of dissolved inorganic carbon across Swedish

streams, refocusing the lens of stable C isotopes. *Sci. Rep.* 7, 9158. doi:10.1038/s41598-017-09049-9

Chiodini, G., Caliro, S., Cardellini, C., Frondini, F., Inguaggiato, S., and Matteucci, F. (2011). Geochemical evidence for and characterization of CO_2 rich gas sources in the epicentral area of the Abruzzo 2009 earthquakes. *Earth Planet. Sci. Lett.* 304, 389–398. doi:10.1016/j.epsl.2011.02.016

Chiodini, G., Cardellini, C., Amato, A., Boschi, E., Caliro, S., Frondini, F., et al. (2004). Carbon dioxide Earth degassing and seismogenesis in central and southern Italy. *Geophys. Res. Lett.* 31, L07615. doi:10.1029/2004GL019480

Chiodini, G., Frondini, F., Cardellini, C., Parello, F., and Peruzzi, L. (2000). Rate of diffuse carbon dioxide Earth degassing estimated from carbon balance of regional aquifers: The case of central apennine, Italy. *J. Geophys. Res.* 105, 8423–8434. doi:10.1029/1999JB900355

Claesson, L., Skelton, A., Graham, C., Dietl, C., Mörth, M., Torssander, P., et al. (2004). Hydrogeochemical changes before and after a major earthquake. *Geol.* 32, 641–644. doi:10.1130/G20542.1

Crossey, L. J., Karlstrom, K. E., Springer, A. E., Newell, D., Hilton, D. R., and Fischer, T. (2009). Degassing of mantle-derived CO_2 and He from springs in the southern Colorado plateau region—neotectonic connections and implications for groundwater systems. *Geol. Soc. Am. Bull.* 121, 1034–1053. doi:10.1130/b26394.1

Faulkner, D. R., Jackson, C. A. L., Lunn, R. J., Schlische, R. W., Shipton, Z. K., Wibberley, C. A. J., et al. (2010). A review of recent developments concerning the structure, mechanics and fluid flow properties of fault zones. *J. Struct. Geol.* 32, 1557–1575. doi:10.1016/j.jsg.2010.06.009

Girault, F., Adhikari, L. B., France-Lanord, C., Agrinier, P., Koirala, B. P., Bhattarai, M., et al. (2018). Persistent CO_2 emissions and hydrothermal unrest following the 2015 earthquake in Nepal. *Nat. Commun.* 9, 2956. doi:10.1038/s41467-018-05138-z

Han, G., Han, W. S., Kim, K.-Y., Park, J. G., Piao, J., and Yun, T. K. (2019). Roles of fault structures and regional formations on CO_2 migration and distribution in shallow saline aquifer in Green River, Utah. *J. Hydrol. X.* 570, 786–801. doi:10.1016/j.jhydrol.2019.01.027

Hoefs, J. (2009). *Stable isotope geochemistry*. Berlin: Springer-Verlag.

Hubbard, J., and Shaw, J. H. (2009). Uplift of the longmen Shan and Tibetan plateau, and the 2008 wenchuan (M = 7.9) earthquake. *Nature* 458, 194–197. doi:10.1038/nature07837

Ingebritsen, S. E., and Manga, M. (2014). Hydrogeochemical precursors. *Nat. Geosci.* 7, 697–698. doi:10.1038/ngeo2261

Kulongoski, J. T., Hilton, D. R., Barry, P. H., Esser, B. K., Hillegonds, D., and Belitz, K. (2013). Volatile fluxes through the big bend section of the san andreas fault, California: Helium and carbon-dioxide systematics. *Chem. Geol.* 339, 92–102. doi:10.1016/j.chemgeo.2012.09.007

Liu, M., and Stein, S. (2016). Mid-continental earthquakes: Spatiotemporal occurrences, causes, and hazards. *Earth. Sci. Rev.* 162, 364–386. doi:10.1016/j.earscirev.2016.09.016

Liu, W., Guan, L., Liu, Y., Xie, X., Zhang, M., Chen, B., et al. (2022). Fluid geochemistry and geothermal anomaly along the Yushu-Ganzi-Xianshuihe fault system, eastern Tibetan Plateau: Implications for regional seismic activity. *J. Hydrol. X.* 607, 127554. doi:10.1016/j.jhydrol.2022.127554

Lu, C., Zhou, X., Li, Y., Liu, L., Yan, Y., and Xu, Y. (2021). Hydrogeochemical characteristics of groundwater in the surface rupture zone of Madoi M_s 7.4 earthquake and hot springs in the East Kunlun Fault. *Seismol. Geol.* 43, 1101–1126. in Chinese with English abstract. doi:10.3969/j.issn.0253-4967.2021.05.005

Mayorga, E., Aufdenkampe, A. K., Masiello, C. A., Krusche, A. V., Hedges, J. I., Quay, P. D., et al. (2005). Young organic matter as a source of carbon dioxide outgassing from Amazonian rivers. *Nature* 436, 538–541. doi:10.1038/nature03880

Miller, S. A., Collettini, C., Chiaraluce, L., Cocco, M., Barchi, M., and Kaus, B. J. P. (2004). Aftershocks driven by a high-pressure CO_2 source at depth. *Nature* 427, 724–727. doi:10.1038/nature02251

Newell, D. L., Jessup, M. J., Cottle, J. M., Hilton, D. R., Sharp, Z. D., and Fischer, T. P. (2008). Aqueous and isotope geochemistry of mineral springs along the southern margin of the Tibetan plateau: Implications for fluid sources and regional degassing of CO_2. *Geochem. Geophys. Geosyst.* 9, Q08014. doi:10.1029/2008gc002021

Pan, J., Li, H., Chevalier, M.-L., Tapponnier, P., Bai, M., Li, C., et al. (2022). Co-seismic rupture of the 2021, M_w7.4 Maduo earthquake (northern Tibet): Short-cutting of the Kunlun fault big bend. *Earth Planet. Sci. Lett.* 594, 117703. doi:10.1016/j.epsl.2022.117703

Pineau, F., Shilobreeva, S., Hekinian, R., Bideau, D., and Javoy, M. (2004). Deep-sea explosive activity on the mid-atlantic ridge near 34°50′N: A stable isotope (C, H, O) study. *Chem. Geol.* 211, 159–175. doi:10.1016/j.chemgeo.2004.06.029

Ren, J., Xu, X., Yeats, R. S., and Zhang, S. (2013). Millennial slip rates of the Tazang fault, the eastern termination of Kunlun fault: Implications for strain partitioning in eastern Tibet. *Tectonophysics* 608, 1180–1200. doi:10.1016/j.tecto.2013.06.026

Rosen, M. R., Binda, G., Archer, C., Pozzi, A., Michetti, A. M., and Noble, P. J. (2018). Mechanisms of earthquake-induced chemical and fluid transport to carbonate groundwater springs after earthquakes. *Water Resour. Res.* 54, 5225–5244. doi:10.1029/2017WR022097

Skelton, A., Andrén, M., Kristmannsdóttir, H., Stockmann, G., Mörth, C.-M., Sveinbjörnsdóttir, Á., et al. (2014). Changes in groundwater chemistry before two consecutive earthquakes in Iceland. *Nat. Geosci.* 7, 752–756. doi:10.1038/ngeo2250

Sun, X., Zhan, Y., Zhao, L., Chen, X., Sun, J., Li, C., et al. (2019). Electrical structure of the Kunlun–Qinling fault system, northeastern Tibetan Plateau, inferred from 3-D inversion of magnetotelluric data. *J. Asian Earth Sci.* 181, 103910. doi:10.1016/j.jseaes.2019.103910

Tamburello, G., Pondrelli, S., Chiodini, G., and Rouwet, D. (2018). Global-scale control of extensional tectonics on CO_2 Earth degassing. *Nat. Commun.* 9, 4608. doi:10.1038/s41467-018-07087-z

Tapponnier, P., Zhiqin, X., Roger, F., Meyer, B., Arnaud, N., Wittlinger, G., et al. (2001). Oblique stepwise rise and growth of the Tibet Plateau. *Science* 294, 1671–1677. doi:10.1126/science.105978

Telmer, K., and Veizer, J. (1999). Carbon fluxes, pCO_2 and substrate weathering in a large northern river basin, Canada: Carbon isotope perspectives. *Chem. Geol.* 159, 61–86. doi:10.1016/S0009-2541(99)00034-0

Tian, J., Pang, Z., Liao, D., and Zhou, X. (2021). Fluid geochemistry and its implications on the role of deep faults in the Genesis of high temperature systems in the eastern edge of the Qinghai Tibet Plateau. *Appl. Geochem.* 131, 105036. doi:10.1016/j.apgeochem.2021.105036

Tsunogai, U., and Wakita, H. (1995). Precursory chemical changes in ground water: Kobe earthquake, Japan. *Science* 269, 61–63. doi:10.1126/science.269.5220.61

Ünal-İmer, E., Uysal, I. T., Zhao, J.-X., Işık, V., Shulmeister, J., İmer, A., et al. (2016). CO_2 outburst events in relation to seismicity: Constraints from microscale geochronology, geochemistry of late Quaternary vein carbonates, SW Turkey. *Geochim. Cosmochim. Acta* 187, 21–40. doi:10.1016/j.gca.2016.05.006

Wang, J., Jin, Z., Hilton, R. G., Zhang, F., Li, G., Densmore, A. L., et al. (2016). Earthquake-triggered increase in biospheric carbon export from a mountain belt. *Geology* 44, 471–474. doi:10.1130/G37533.1

Wang, S.-L., Lin, Y.-S., Burr, G. S., Wang, P.-L., and Lin, L.-H. (2022). Radiocarbon and stable carbon isotope constraints on the propagation of vent CO_2 to fluid in the acidic Kueishantao shallow water hydrothermal system. *Geochem. Geophys. Geosyst.* 23, e2022GC010508. doi:10.1029/2022GC010508

Weise, S. M., Bräuer, K., Kämpf, H., Strauch, G., and Koch, U. (2001). Transport of mantle volatiles through the crust traced by seismically released fluids: A natural experiment in the earthquake swarm area vogtland/NW bohemia, central europe. *Tectonophysics* 336, 137–150. doi:10.1016/S0040-1951(01)00098-1

Williams, A. J., Crossey, L. J., Karlstrom, K. E., Newell, D., Person, M., and Woolsey, E. (2013). Hydrogeochemistry of the Middle Rio Grande aquifer system — fluid mixing and salinization of the Rio Grande due to fault inputs. *Chem. Geol.* 351, 281–298. doi:10.1016/j.chemgeo.2013.05.029

Wu, C., Yin, A., Zuza, A. V., Zhang, J., Liu, W., and Ding, L. (2016). Pre-Cenozoic geologic history of the central and northern Tibetan Plateau and the role of Wilson cycles in constructing the Tethyan orogenic system. *Lithosphere* 8, 254–292. doi:10.1130/L494.1

Xu, S., Guan, L., Zhang, M., Zhong, J., Liu, W., Xie, X. g., et al. (2022). Degassing of deep-sourced CO_2 from Xianshuihe-Anninghe fault zones in the eastern Tibetan Plateau. *Sci. China Earth Sci.* 65, 139–155. doi:10.1007/s11430-021-9810-x

Yue, H., Shen, Z.-K., Zhao, Z., Wang, T., Cao, B., Li, Z., et al. (2022). Rupture process of the 2021 M7.4 Maduo earthquake and implication for deformation mode of the Songpan-Ganzi terrane in Tibetan Plateau. *Proc. Natl. Acad. Sci. U. S. A.* 119, e2116445119. doi:10.1073/pnas.2116445119

Zhang, M., Guo, Z., Xu, S., Barry, P. H., Sano, Y., Zhang, L., et al. (2021). Linking deeply-sourced volatile emissions to plateau growth dynamics in southeastern Tibetan Plateau. *Nat. Commun.* 12, 4157. doi:10.1038/s41467-021-24415-y

Zheng, G., Xu, S., Liang, S., Shi, P., and Zhao, J. (2013). Gas emission from the qingzhu river after the 2008 wenchuan earthquake, southwest China. *Chem. Geol.* 339, 187–193. doi:10.1016/j.chemgeo.2012.10.032

Zhou, X., Wang, W., Chen, Z., Yi, L., Liu, L., Xie, C., et al. (2015). Hot spring gas geochemistry in Western sichuan province, China after the wenchuan ms 8.0 earthquake. *Terr. Atmos. Ocean. Sci.* 26, 361–373. TT. doi:10.3319/tao.2015.01.05.01(tt)

Zhu, Y., Diao, F., Fu, Y., Liu, C., and Xiong, X. (2021). Slip rate of the seismogenic fault of the 2021 Maduo earthquake in Western China inferred from GPS observations. *Sci. China Earth Sci.* 64, 1363–1370. doi:10.1007/s11430-021-9808-0

Zucchi, M. (2020). Faults controlling geothermal fluid flow in low permeability rock volumes: An example from the exhumed geothermal system of eastern Elba Island (northern Tyrrhenian Sea, Italy). *Geothermics* 85, 101765. doi:10.1016/j.geothermics.2019.101765

frontiers | Frontiers in Earth Science

TYPE Original Research
PUBLISHED 02 February 2023
DOI 10.3389/feart.2023.1100039

OPEN ACCESS

EDITED BY
Maoliang Zhang,
Tianjin University, China

REVIEWED BY
Xiaocheng Zhou,
China Earthquake Administration, China
Yutao Sun,
Hebei GEO University, China

*CORRESPONDENCE
Xiaopeng Liu,
2641996568@qq.com

SPECIALTY SECTION
This article was submitted to Geochemistry, a section of the journal Frontiers in Earth Science

RECEIVED 16 November 2022
ACCEPTED 18 January 2023
PUBLISHED 02 February 2023

CITATION
Li X, Liu X, Zeng X, Wang X, Luo H, Li M, He J and Shi H (2023), Spatial variations of Rn and CO_2 emissions in the Wuzhong–Lingwu region, northwest China.
Front. Earth Sci. 11:1100039.
doi: 10.3389/feart.2023.1100039

Spatial variations of Rn and CO_2 emissions in the Wuzhong–Lingwu region, northwest China

Xinyan Li[1,2], Xiaopeng Liu[1,3]*, Xianwei Zeng[2], Xiaotao Wang[2], Hengzhi Luo[2], Mengya Li[2], Jiawei He[2] and Haikuo Shi[2]

[1]School of Civil and Hydraulic Engineering, Ningxia University, Yinchuan, China, [2]Earthquake Agency of Ningxia Hui Autonomous Region, Yinchuan, China, [3]School of Geography and Planning, Ningxia University, Yinchuan, China

Soil gas Rn and CO_2 in surface rupture and deep-seated fault zones are important indicators for tectonic and seismic activities. The spatial distributions of Rn and CO_2 concentrations and their relationships with earthquakes and stress state in the Wuzhong–Lingwu area of Ningxia, Northwest China, were investigated through field observations based on 76 measurement points, spatial interpolation and six crossing-fault profiles along Yellow River Fault zone (YRF). Observed results of the soil gas Rn and CO_2 in different segments of Yellow River Fault zone illustrated that YRF has features of both strike-slip and certain normal fault characteristics. Moreover, the difference in seismic activity could also account for the differences in gas concentration and relative activity intensity (RAI) in the Yellow River Fault zone. Significant differences in the spatial distributions of Rn and CO_2 were identified in gridded observation mode. By comparing these spatial distributions with the surface latent heat flux (SLHF), volumetric soil water layer (SWVL), and lithology, an anomalous high-Rn area was identified in the east and south Qingtongxia, and associated with Permian sandstone and mudstone in a piedmont setting. Away from a strong impact of irrigation in the Yinchuan Basin, CO_2 anomalies were identified in the transition area between the Yinchuan Basin and the mountains and coincided with a dramatic negative variation of surface latent heat flux, which was considered to reflect humus accumulation, rich organic matter, and strong soil microorganism activity in loosely accumulated mountain alluvial deposits. After excluding gas anomalies related to shallow soils and surface geology, anomalies of Rn and CO_2 in the west of Lingwu were consistent with the distribution of low seismic b-values and frequent seismic activity in plane and profile. According to similar studies in the north-south seismic belts, it is believed that high stress and strong seismic activity increased the permeability of rocks and boosted the gas emission in the west of Lingwu. Base on a crustal thickness variation belt, high-velocity bodies, and in this region, an higher seismic hazard was illustrated. This study offers new insight into combining geochemical characteristics of soil gas and seismological methods to estimate regional seismic hazards.

KEYWORDS

Rn, CO_2, irrigation, b-value, seismic hazards

Introduction

The emission of gases, such as Rn, CO_2, CH_4, and He, from the solid Earth to the near-surface can be increased by tectonic and seismic activity (King et al., 1996; Giammanco et al., 1998; Fu et al., 2005; Al-Hilal and Abdul-Wahed, 2007; Zhou et al., 2010; Fu et al., 2016; Yuce et al., 2017). Previous studies have demonstrated that a difference in stress state can affect the

concentration and type of soil gas, and soil gas surveys have been performed to assess the potential for seismic hazard prediction (Fu et al., 2008; Kumar et al., 2009; Sun et al., 2021). However, along with regional stress state and seismic activity, the concentration of soil gas can also be related to soil types, lithological characteristics, meteorological parameters, crustal thickness and structure, permeable pathways for gas migration, and human activities (Hinkle, 1994; Han et al., 2014; Szabó et al., 2014). Thus, various soil gas sources have been observed around fault zones, among which meteorological sources can be easily distinguished due to their values being significantly lower. Deep crustal/mantle sources usually have higher concentrations than meteorological sources (Yang et al., 2003; Hong et al., 2010; Yuce et al., 2017). However, soil gas compositions in the near-surface were easily contaminated by the environment (Biological activity, agricultural production and industrial pollution, etc.). Therefore, it is necessary to account for anomalies, meteorological factors, and near-surface influences when analyzing the relationship between soil gas variation and seismic activity. Soil gas studies have been conducted in surface fracture zones produced by large earthquakes (Dogan, et al., 2007; Li et al., 2009; Zhou et al., 2010), faults in basins or valleys controlled by structural patterns (Guerra and Lombardi., 2001; Ciotoli et al., 2007; Al-Hilal et al., 2016), deep-seated faults with frequent moderate and strong earthquakes (Weinlich, 2014; Zhou et al., 2017; Sun et al., 2021), and along active faults on a volcanic field (Neri et al., 2011). These studies found that variations in different gas compositions are spatially synchronized, particularly CO_2 and Rn (Guerra and Lombardi., 2001; Ciotoli et al., 2007; Li et al., 2013; Yuce et al., 2017). However, few soil gas studies have been reported in areas affected by human activities, especially agriculture and irrigation; consequently, the sources and distributions of soil gases in agricultural areas remain unclear. Therefore, to prevent possible earthquake hazards and disasters and assess the seismic risk in human activity areas, the primary goals of soil gas investigation were to understand the various factors of soil gas and obtain anomalies boosted by seismic activity.

As a product of uranium (^{238}U) decay, Rn is a natural radioactive idle gas without stable or synthetic isotopes. It is believed that Rn in Earth's substrata continuously escapes from the surface, resulting in detectable surface concentrations (Khilyuk et al., 2000). In addition to its ability to be measured in minute amounts, Rn is relatively non-reactive to other compounds. He, CH_4, H_2, and CO_2 can serve as carrier gases to transport Rn from depth to the surface (Yang et al., 2003). Based on its origin depth and radioactive characteristics, Rn offers the possibility to determine and quantify changes in gas migration duo to tectonic activity. The parent isotope, surface degassing rate, and carrier gas play essential roles in Rn concentration variation. Among the carrier gases, CO_2 is one of the most important. Numerous CO_2 sources have been identified in structurally active zones, including mantle degassing, carbonate metamorphism, and decomposition of organic matter (Irwin and Barnes, 1980); this CO_2 can be transported along deep-seated faults (Baubron et al., 2002). A higher concentration of CO_2 at the surface indicates higher pore pressure in the subsurface, which can contribute to identifying potential seismic zones (Irwin & Barnes., 1980; Ciotoli et al., 2007). However, CO_2 can also offer evidence of shallow sources (Khilyuk et al., 2000), and simultaneous observations of soil gas Rn and CO_2 can facilitate the elimination of interference factors and the identification of deep gas sources.

Ningxia is a sizeable agricultural area located on the upper reaches of the Yellow River; Wuzhong–Lingwu is an important part of the Hetao irrigation area, and is notable for its rice production. The Wuzhong–Lingwu area is also one of the seismically active regions in Ningxia, with moderately strong earthquakes and complex tectonics (Liao et al., 2000; Chai et al., 2001; Ma et al., 2006; Zeng et al., 2021). Owing to the large population and high level of economic development, geophysical observations in this region are significantly affected by human-related factors, making it more challenging to detect effective earthquake precursors. In this study, we measured the spatial distributions of Rn and CO_2 concentrations in soil gas around the main seismogenic faults of the Wuzhong–Lingwu area to identify soil gas anomalies associated with seismic activity and assess regional seismic risk.

Materials and methods

Seismogeological setting

Wuzhong–Lingwu is an arid/semi-arid inland region of northwest China (Figure 1). The south of the region is characterized by folded mountains. The north is the alluvial Yinchuan Basin, formed by the south–north flow of the Yellow River, forming an important agricultural area. The basin is underlain by thick Quaternary sediments. Based on teleseismic P-wave data, the regional crustal thickness is 40–50 km; more specifically, it is 40–49 km in the Wuzhong–Lingwu area (47–49 km in Lingwu; Xu et al., 2018) and 40–43 km in southern Qingtongxia and Guangwu. P-wave tomography indicates a high-velocity anomaly at shallow mid–crustal depths beneath Lingwu town (Zeng et al., 2017). There are eight strike-slip or normal active faults in the study area, including the Yellow River fault (YRF), Niushou Mountain fault (NSMF), Sanguankou fault (SGKF), Luoshan fault (LSF), Chongxing fault (CXF), Xinhuaqiao fault (XHQF), and Yinchuan blind fault (YCBF). The NSMF forms a boundary with Tertiary sediments of the southern Yinchuan graben (Chai et al., 2001). The region experiences moderate to strong seismic activity owing to neotectonic movements; five earthquakes of $M > 5$ have occurred in the Wuzhong–Lingwu area since 1970 (Ma et al., 2006).

Field measurements

According to the distribution of earthquakes and major fault zones, field measurements were taken at 76 sites within 5–10 km of each other in the Wuzhong–Lingwu area during July 2020 (Figure 1). The sample sites are set to gridded observation mode, and the easternmost measuring sites are located along the Yellow River fault, while the westernmost measuring point is located in front of Helan Mountain. Except for sites along fault zones, the site distribution covered the Wuzhong–Lingwu area as evenly as possible. All sample sites shared the same land use type and daily observation period (09:00–17:00 UTC+8) to minimize the influence of meteorology and surface vegetation on soil gas concentrations. To avoid abnormal gas variations caused by significant differences in soil humidity, move the sites when they are located in areas with high humidity area (canals, the Yellow River, freshly irrigated farmland, etc.). The measuring sites should also be located in the thick surface cover layers to facilitate the occurrence of gases. Six profiles were constructed along the YRF in order to explore the relationship

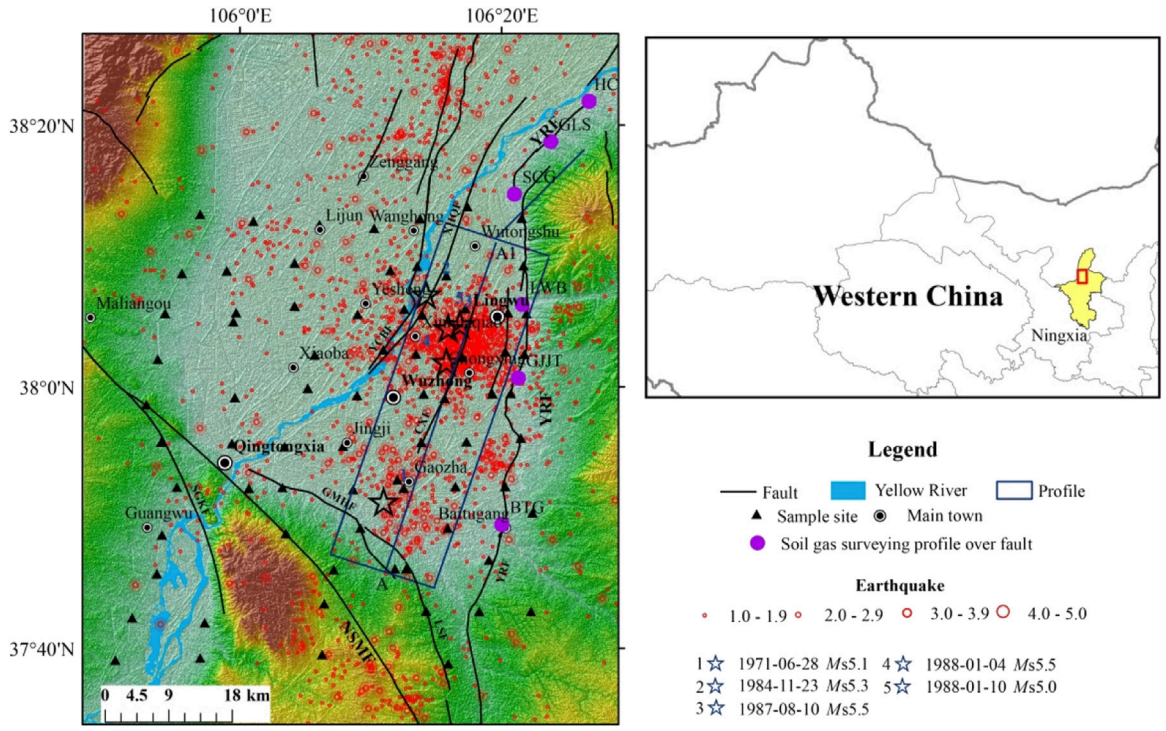

FIGURE 1
Topographical map of the study region showing the main faults, earthquake epicenters, and sampling locations. Abbreviations of the profiles: BTG, Baitugang profile; GJJT, Guojiajiantan profile; LWB, Lingwubei profile; SCG, Shuangchagou profile; GLS, Ganlusi profile; HC, Hengcheng profile. Abbreviations of the faults: YRF, Yellow River fault; NSMF, Niushou Mountain fault; SGKF, Sanguankou fault; LSF, Luoshan fault; CXF, Chongxing fault; XHQF, Xinhuaqiao fault YCBF, Yinchuan blind faul.

between the geochemistry characteristics of soil gas and seismic activity in different segments, including three profiles at the northern segment of Yellow River Fault (YRF_N), two profiles at the middle segment of Yellow River Fault (YRF_M), and one profile at the southern segment of Yellow River Fault (YRF_S). Approximately 14–15 survey points are located on each cross-fault survey line, starting from the center of the fault and extending to both sides (Li et al., 2009). As a starting point, the distance between the two measuring points is 5 m, and it increases successively by 10 m, 15 m, 20 m, 40 m, and 50 m so that the total length of the measuring line is about 240 m–280 m. Soil samples were collected from ~0.8 m depth using a 12-hole hollow steel sampler. Rn concentrations were analyzed using a RAD7 Radon Detector and expressed in Bq/m^3; analytical precision was within 10%, and the detection sensitivity was 9.25 Bq/m^3 operating in the Sniff mode. The Rn concentration for each site was taken as the average of at least three consecutive observations; the error was within ±5%. CO_2 concentrations were measured using an ATG-C60 CO_2 detector (Adtech, China) with a measuring resolution and accuracy of 0.001% and 4%, respectively. The CO_2 concentration for each site was calculated as the average of three measurements; the error was within ±5% under a stable state of continuous measurement.

Data processing

Ordinary kriging (OK) and inverse distance weight (IDW) interpolation were applied to obtain the spatial variation of Rn and CO_2 based on data from the 76 sites. The skewness coefficients of Rn and CO_2 were >0, and kurtosis was >3 (Table 1), indicating that the data did not have a normal distribution. Therefore, logarithmic transformation was performed on the original soil gas data and spatial interpolation was applied to the transformed data, which conformed to a normal distribution. For IDW, we set the inverse distance power value to 2; for OK, a variogram was used to select the spherical function. To assess the accuracy of the spatial interpolation, we used the mean absolute error (MAE; Eq. 1) and root mean square error (RMSE; Eq. 2), which were calculated as follows:

TABLE 1 Statistics of soil gas Rn and CO_2 in gridded observation mode.

CO_2 (%)					Rn (kBq/m^3)				
Max	Min	Ave	Skew	Kurt	Max	Min	Ave	Skew	Kurt
3.95	0.07	0.95	1.69	2.56	36.70	0.07	4.19	3.50	14.94

Max is short for the maximum, and Min is short for the minimum. Skew is short for Skewness, and Kurt is short for Kurtosis.

TABLE 2 CO_2 and Rn concentrations of soil gas at each site in the Wuzhong–Lingwu area.

Site. No	Lon (°E)	Lat (°N)	Date	CO_2 (%)	Rn (kBq/m^3)	Site. No	Lon (°E)	Lat (°N)	Date	CO_2 (%)	Rn (kBq/m^3)
1	106.2295	38.2142	2020/7/14	0.28	3.88	14	106.3412	38.0945	2020/7/15	0.28	0.35
2	106.1706	38.2021	2020/7/14	0.81	1.73	15	105.9491	38.2200	2020/7/16	0.14	6.73
3	106.1010	38.2066	2020/7/14	0.91	2.45	16	105.9258	38.1445	2020/7/16	0.11	2.82
4	106.0171	38.2112	2020/7/14	0.93	1.48	17	105.9045	38.0935	2020/7/16	0.44	9.83
5	105.9831	38.1477	2020/7/14	2.33	7.75	18	105.8951	38.0353	2020/7/16	0.45	3.79
6	106.0693	38.1576	2020/7/14	0.25	0.07	19	105.8807	37.9771	2020/7/16	0.17	2.61
7	106.1914	38.1484	2020/7/14	0.30	0.14	20	106.0864	37.9981	2020/7/16	0.87	3.96
8	106.3650	38.0933	2020/7/15	0.95	0.92	21	105.8995	37.9297	2020/7/16	1.33	12.10
9	106.3308	38.1612	2020/7/15	0.15	0.10	22	105.9897	37.9279	2020/7/16	0.61	1.81
10	106.3612	38.1544	2020/7/15	1.29	2.26	23	106.0565	37.9236	2020/7/16	0.91	24.52
11	106.3588	38.2147	2020/7/15	3.84	4.88	24	106.1313	37.9242	2020/7/16	0.74	3.23
12	106.2895	38.2297	2020/7/15	1.07	2.45	25	106.0950	38.0403	2020/7/17	0.13	0.35
13	106.2628	38.1418	2020/7/15	2.65	5.00	26	105.9935	37.9863	2020/7/17	1.36	1.42
Site. No	Lon (°E)	Lat (°N)	Date	CO_2 (%)	Rn (kBq/m^3)	Site. No	Lon (°E)	Lat (°N)	Date	CO_2 (%)	Rn (kBq/m^3)
27	106.2870	38.0999	2020/7/15	1.42	35.44	41	105.9914	38.0831	2020/7/17	0.35	0.59
28	105.9947	38.0946	2020/7/17	0.29	0.78	42	106.3623	38.0415	2020/7/21	0.43	0.66
29	106.0695	38.1028	2020/7/17	1.67	2.87	43	106.3448	37.9917	2020/7/21	0.90	1.10
30	106.1500	38.0922	2020/7/17	0.52	0.10	44	106.3216	37.9909	2020/7/21	0.27	0.38
31	106.1826	38.0473	2020/7/17	0.65	1.06	45	106.2310	37.9294	2020/7/22	0.23	0.99
32	106.2093	38.0993	2020/7/17	0.31	1.13	46	106.2084	37.8708	2020/7/22	3.18	4.96
33	105.8409	37.6518	2020/7/20	0.36	1.07	47	106.2006	37.8819	2020/7/22	3.26	4.83
34	105.8625	37.7059	2020/7/20	2.40	6.88	48	106.2115	37.7683	2020/7/22	0.70	1.73
35	105.8939	37.7618	2020/7/20	0.62	0.90	49	106.1974	37.7681	2020/7/22	3.91	9.70
36	105.9004	37.8114	2020/7/20	0.73	4.28	50	106.2371	37.7143	2020/7/22	1.01	1.66
37	105.9196	37.8721	2020/7/20	0.91	3.15	51	106.2652	37.6470	2020/7/22	0.16	2.94
38	106.1492	37.9889	2020/7/21	0.81	6.49	52	106.1044	37.6591	2020/7/23	0.13	1.65
39	106.2341	37.9911	2020/7/21	0.62	0.62	53	106.1073	37.7238	2020/7/23	0.10	2.57
40	106.2606	37.9852	2020/7/21	1.04	1.68	54	106.1195	37.7672	2020/7/23	0.54	2.32
Site. No	Lon (°E)	Lat (°N)	Date	CO_2 (%)	Rn (kBq/m^3)	Site. No	Lon (°E)	Lat (°N)	Date	CO_2 (%)	Rn (kBq/m^3)
55	106.2829	38.0380	2020/7/21	0.41	0.28	66	106.1533	37.8202	2020/7/23	0.57	1.19
56	106.3378	38.0451	2020/7/21	1.08	3.66	67	106.1441	37.8693	2020/7/23	0.52	0.14
57	106.0539	37.8720	2020/7/23	2.80	32.50	68	106.2886	37.9302	2020/7/24	1.00	2.57
58	106.0584	37.8130	2020/7/23	0.15	3.51	69	106.3706	37.7138	2020/7/25	0.22	3.08
59	106.0112	37.8708	2020/7/23	1.14	3.64	70	106.3046	37.7139	2020/7/25	0.07	2.57
60	106.2742	37.8730	2020/7/24	1.79	1.53	71	106.3170	37.7793	2020/7/25	0.51	2.71
61	106.2646	37.8201	2020/7/24	1.41	1.73	72	105.9492	37.6545	2020/7/25	1.00	2.40
62	106.3358	37.8290	2020/7/24	0.98	3.30	73	105.9548	37.6994	2020/7/25	1.47	36.70

(Continued on following page)

TABLE 2 (*Continued*) CO_2 and Rn concentrations of soil gas at each site in the Wuzhong–Lingwu area.

Site. No	Lon (°E)	Lat (°N)	Date	CO_2 (%)	Rn (kBq/m^3)	Site. No	Lon (°E)	Lat (°N)	Date	CO_2 (%)	Rn (kBq/m^3)
63	106.3724	37.8395	2020/7/24	0.56	2.59	74	106.2240	38.0422	2020/7/27	0.32	0.14
64	106.3379	37.8728	2020/7/24	0.80	2.01	75	106.2319	38.0917	2020/7/27	0.14	0.10
65	106.3577	37.9346	2020/7/24	1.83	1.61	76	106.2256	38.1536	2020/7/27	2.61	1.45

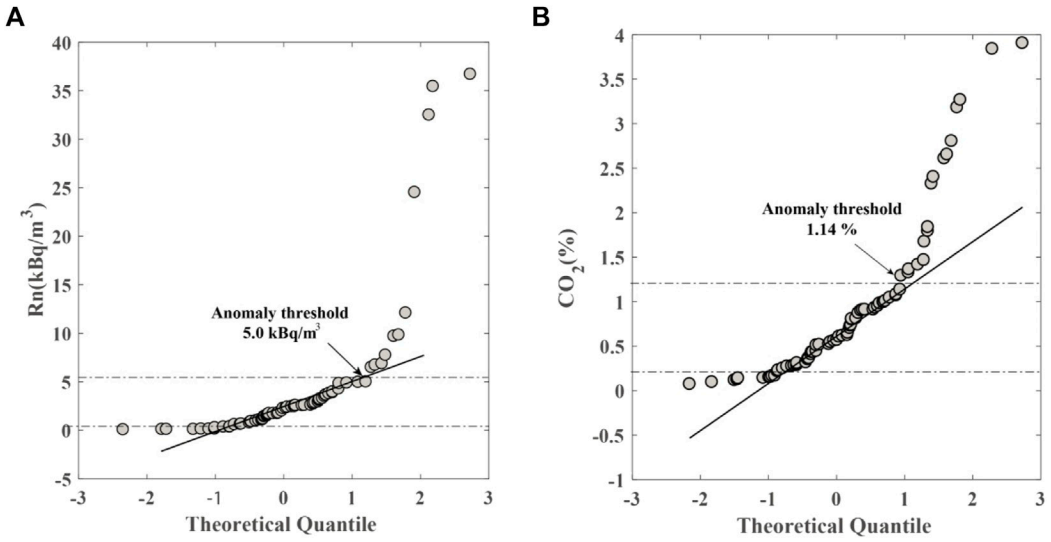

FIGURE 2
Anomaly thresholds of soil gas **(A)** Rn and **(B)** CO_2 estimated by the Q–Q plot method.

TABLE 3 Evaluation of spatial interpolation precision.

Interpolation method	Raster size (km)	Rn	CO_2		
		MAE	RMSE	MAE	RMSE
IDW	1×1	11.46	7.09	0.36	2.55
OK	1×1	98.70	179.53	230.81	424.61

IDW, inverse distance weight interpolation; OK, ordinary kriging; RMSE, root mean square error; MAE, mean absolute error.

$$MAE = \frac{1}{n}\sum_{i=1}^{n}\left|C_{f(i)} - C_{o(i)}\right| \quad (1)$$

$$RMSE = \sqrt{\frac{1}{n}\sum_{i=1}^{n}\left(C_{f(i)} - C_{o(i)}\right)^2} \quad (2)$$

where n is the measured sequence or predicted sequence length, and *Cf(i)* and *Co.(i)* are the measured and predicted values of soil gas, respectively. The method with the smallest error and highest interpolation accuracy was selected to determine the spatial distribution of Rn and CO_2.

Owing to the numerous sources of soil gas, obtaining an anomaly threshold for soil gas is essential for identifying sources related to seismic or tectonic activity. The interquartile range, Z-score, Q–Q plot, and RST methods are widely applied in identifying gas anomalies (Beaubien et al., 2003; Cui et al., 2013; Tramutoli et al., 2013; Jiao et al., 2018). We employed a Q–Q plot to determine the upper and lower limits of the outliers in the Rn and CO_2 data.

The b-value data were obtained from the literature (Zeng et al., 2017; Zeng et al., 2021). Geological records were obtained from the China' Spatial Database of 1:2.5 million digital geological maps. In addition, to examine the influence of surface cover on soil gas concentrations, the monthly data of surface latent heat flux (SLHF; a parameter that reflects heat and moisture exchange between the surface and near-surface atmosphere; Ando and Ueyama, 2017) and volumetric soil water layer (SWVL) data with a spatial resolution of 0.1° × 0.1° were derived from ERA5 land products, they can be download from the Climate Data Store (CDS; https://cds.climate.copernicus.eu); these data were sampled between 09:00 and 17:00 UTC+8. To account for, The background values of SLHF and SWVL were represented by the average value of July from 2016 to 2020 to examine the effect of the hydrothermal characteristics and long-term irrigation processes on soil gas

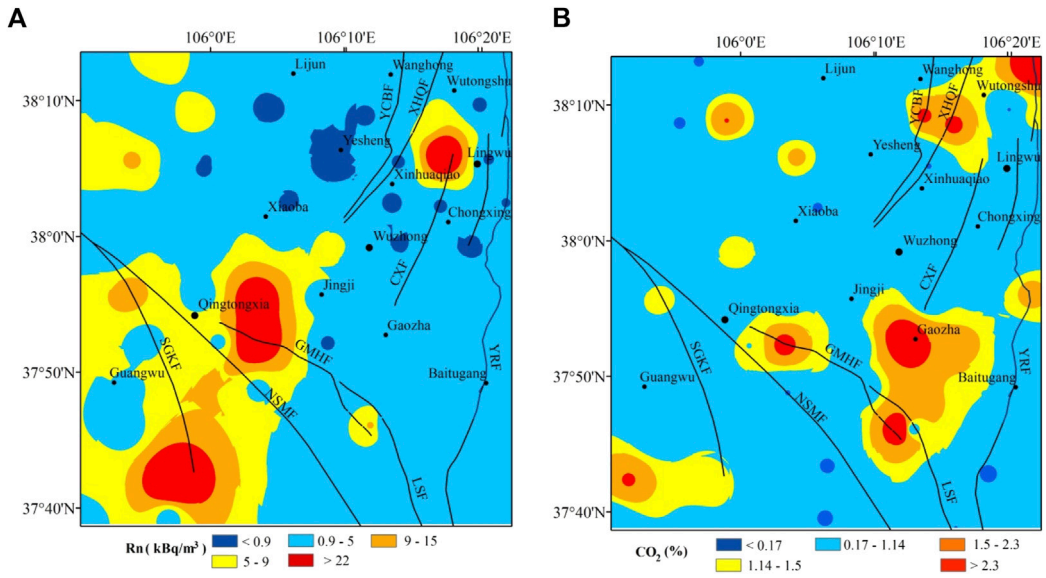

FIGURE 3
Spatial distribution of **(A)** Rn and **(B)** CO_2 concentrations in the Wuzhong–Lingwu area.

TABLE 4 Observed results of the soil gas Rn and CO_2 in the 6 survey profiles in the Yellow River Fault zone.

Profile	Num	Date	Rn (kBq/m³)							CO_2(%)						
			M	M_{max}	M_{min}	Std	A_U	A_L	RAI	M	M_{max}	M_{min}	Std	A_U	A_L	RAI
HC	14	2021.4.14	2.17	5.72	0.27	1.81	3.08	1.27	2.64	0.07	0.16	0.03	0.05	0.10	0.05	2.29
GLS	14	2021.4.20	2.57	4.77	1.12	1.17	3.15	1.98	1.86	0.23	0.43	0.12	0.10	0.28	0.18	1.84
SCG	15	2021.4.19	2.22	5.20	0.81	1.31	2.87	1.56	2.35	0.08	0.15	0.05	0.02	0.09	0.07	1.90
LWB	14	2021.4.26	1.14	1.61	0.48	0.31	1.30	0.99	1.41	0.42	0.67	0.18	0.17	0.51	0.34	1.60
GJJT	14	2021.4.25	2.11	6.96	0.48	2.11	3.17	1.06	3.29	0.49	1.83	0.17	0.48	0.73	0.25	3.74
BTG	14	2021.4.15	1.34	5.72	0.03	1.65	2.16	0.51	4.27	0.67	2.64	0.03	1.04	1.19	0.15	3.93

Num is short for the number of samples, M_{max} is the maximum and M_{min} is s the minimum. Std is short for standard deviation. A_u and A_L, is the upper limit and lower limit of gas anomaly, respectively. RAI, is represent the Relative Activity Intensity. Abbreviations of the profiles: BTG, baitugang profile; GJJT, guojiajiantan profile; LWB, lingwubei profile; SCG, shuangchagou profile; GLS, ganlusi profile; HC, hengcheng profile.

concentration. Equation 3 was used to calculate local spatial variance in SLHF to determine the influence of SLHF on soil gas concentration. (Tramutoli et al., 2005):

$$Diff_r = S_r - S_m \quad (3)$$

where $Diff_r$ is the difference between the SLHF value of the current pixel r (S_r) and its spatial average in a homogenous region (S_m). According to a digital elevation mode; (DEM), the Wuzhong–Lingwu area was divided into mountain and basin regions to calculate local differences.

Following the fault activity determination method used in the past, the mean value M), maximum (M_{max}), minimum (M_{min}), standard deviation (Std) and relative activity intensity (RAI) of soil gas Rn and CO_2 concentration were calculated. Assume the average of each sample site along each line is the background value B), and The upper limit (A_U) and lower limit (A_L) of abnormal Rn and CO_2 concentration in soil gas were calculated by adding 0.5 times standard deviation to the background mean (Yang et al., 2021; Liu et al., 2022). The measured value higher than the upper limit of the anomaly is regarded as the anomaly value related to the fault, and the ratio of the maximum measured value in the anomaly area to the background value is defined as the RAI (Shao et al., 2012):

$$RAI = M_{max}/M \quad (4)$$

Results and discussion

The soil gas Rn and CO_2 results for Wuzhong–Lingwu are shown in Table 2. Rn ranged from 0.07 to 36.7 kBq/m³, with an average value of 4.19 kBq/m³; CO_2 concentration ranged from 0.07% to 3.9%, with an average value of 0.93%. The resultant anomaly threshold values derived using the Q–Q plot method were 5.0 kBq/m³ for Rn and 1.14%

10.3389/feart.2023.1100039

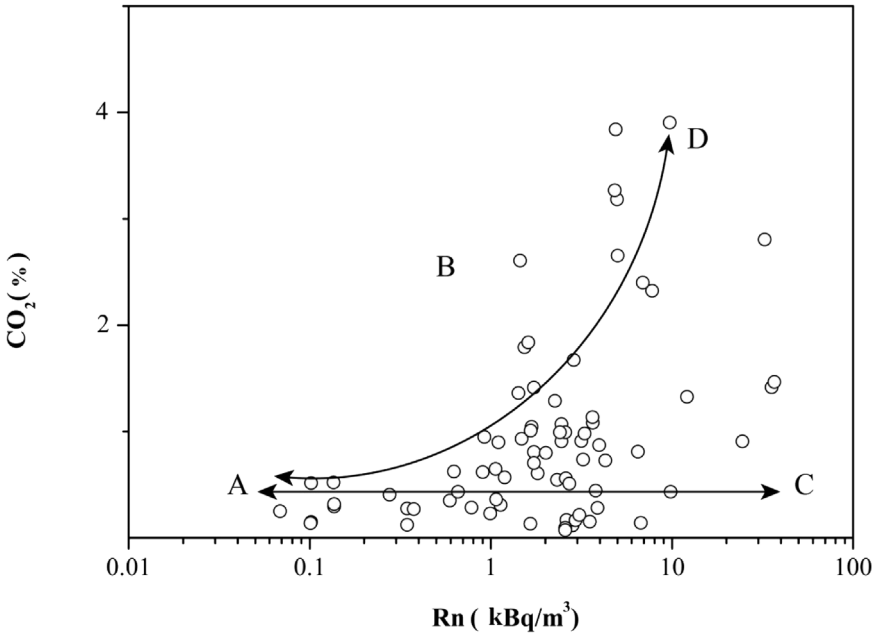

FIGURE 4
Variation diagram of Rn with CO_2 (Part A represents meteorological sources, part C and part B represent shallow sources, Part D represents deep sources).

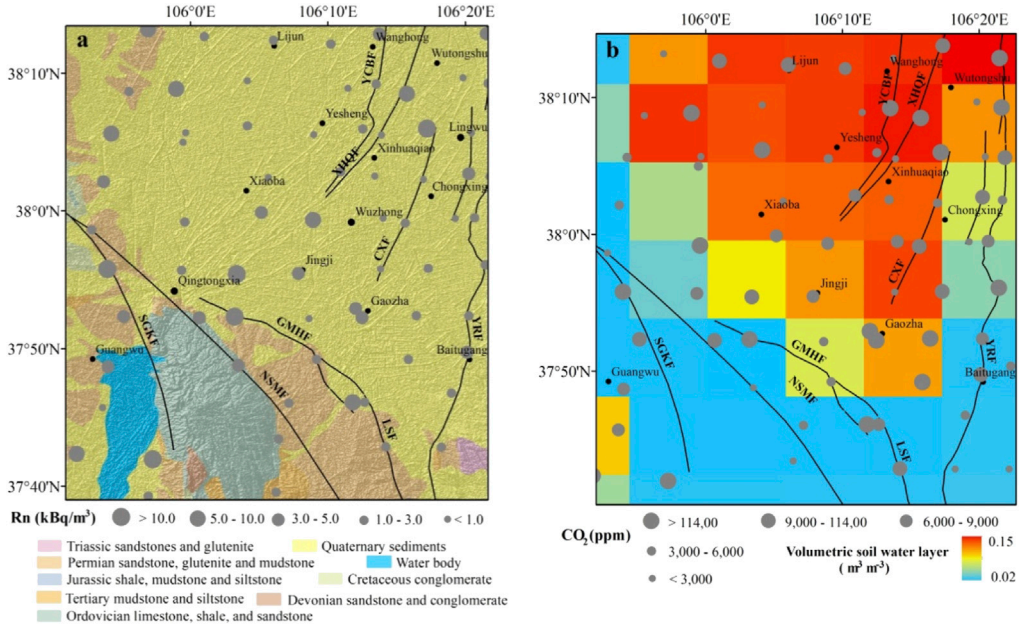

FIGURE 5
(A) Lithology and **(B)** local variance of surface latent heat flux in the Wuzhong–Lingwu area.

for CO_2 (Figure 2). The proportions of sample sites exceeding the Rn and CO_2 thresholds were 15.7% and 23.7%, respectively.

The spatial distributions of Rn and CO_2 concentrations interpolated by the IDW method were closer to measured values (i.e., smaller MAE and RMSE) than those from the OK method (Table 3). Accordingly, the spatial distributions derived using the IDW method were used for analysis. High-Rn anomalies were mainly distributed in two areas (Figure 3A): 1) western Lingwu, where the maximum value exceeded 20 kBq/m^3; and 2) southern and eastern Qingtongxia. Low-Rn areas (Rn < 0.9 kBq/m^3) were sporadically distributed to the west and south of Lingwu.

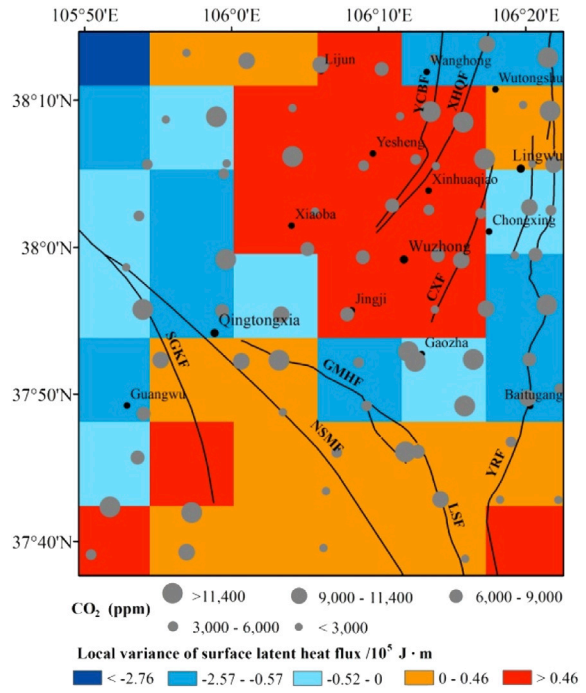

FIGURE 6
Relationship between the spatial distribution of surface latent heat flux (SLHF) and CO_2 in the Wuzhong–Lingwu area.

High-CO_2 anomalies were similar to those of Rn in eastern Qingtongxia and west of Lingwu, with the maximum value reaching 3.0% (Figure 3B). However, large areas with elevated CO_2 were also identified to the south of Gaozha, where the maximum value reached >2.3%.

A comparison of the soil gas results of the six profiles is shown in Table 4. The background value of Rn concentration in the HC, GLC, and SC profiles is slightly larger than in other YRF profiles, while the RAI is largest in the BTG and GJJT profiles. Both the background value of CO_2 concentration and the RAI on the YRF_S and YRF_M profiles are greater than the value of YRF_N.

Rn and CO_2 variation

Trace gases from Earth's subsurface can migrate to the surface together with other carrier gases; CO_2 is one of the main carrier gases for Rn (Toutain & Baubron., 1999; Yang et al., 2003; Fu et al., 2016). Gases from meteorological sources are primarily influenced by surface processes, such as air dilution and soil respiration (Sun et al., 2021); deep-seated gases are related to crustal and mantle degassing along fault zones (Sciarra et al., 2020). Figure 4 shows the variation in Rn concentration with CO_2 concentration; meteorological sources are represented by part A (low Rn and CO_2), and deep crustal and mantle gases are represented by part D (high Rn and CO_2). The Rn and CO_2 concentrations are not coupled in parts C and B. In part C, CO_2 concentrations do not increase with increasing Rn; in part B, high CO_2 (>1.0%) is found together with moderate Rn (2.0–10.0 kBq/m^3). Parts C and B can be considered shallow sources of soil and rocks. The data show that the origins of soil gas in the Wuzhong–Lingwu area are complex, with Rn and CO_2 generally derived from different sources.

Influence of surface overburden layer on soil gas Rn and CO_2

The rock type, soil type, and hydrothermal conditions of overlying strata play an important role in the distribution of soil gas concentrations, especially in areas affected by human activity. The highest Rn contents are in granite and acidic volcanic units, followed by shale, limestone, sandstone, and mafic dikes (Baixeras et al., 2001; El-Arabi et al., 2006). In the study area, the distribution of high-Rn anomalies is strongly related to Permian sandstones and mudstones in a piedmont setting (Figure 5A). Most high-CO_2 anomalies (8 of 12) are concentrated in the transition area between the mountains and basin, which is also a transition zone for soil moisture. Local variation in the July average of SLHF (Figure 6A) reveals a dramatic negative anomaly in the transition zone between the mountains and basin.

Gas concentrations are influenced by SWVL. In a certain range, SWVL will increase the thickness of an impermeable layer that will hinder the exchange of soil gas with the atmosphere and increase the soil gas concentration. However, if SWVL is excessive, soil gas will dissolve or be displaced, reducing the concentration of soil gas (Hinkle, 1994). The study area is an arid/semi-arid environment. In the mountains, bedrock is largely exposed, and vegetation cover is low. As such, the SWVL content is extremely low, and water–heat exchange is weak. In contrast, the thick (~1400 m) Quaternary sediments in the Yinchuan Basin are formed of silty clay and silt; In addition, with flat terrain, the Yinchuan basin is an important area of Yellow River irrigation planted with vegetables, corn and rice; as such, plains have higher soil moisture and a stronger water and heat exchange system. There is a negative correlation between SWVL and concentration of Rn and CO_2 in the Yinchuan Basin. However, there is a positive correlation between SWVL, and Rn and CO_2 concentrations in the mountainous areas around the basin. Accordingly, the long-term process of Yellow River irrigation in the basin has diluted the background value of Rn parent isotopes, resulting in lower Rn concentrations. Moreover, the soil in irrigated areas has a relatively high moisture content, which leads to clay leaching and a sticky soil texture (Yu et al., 2000). The consequent reduction in pores is not conducive to gas migration, blocking the release of deeper gases and contributing to the low values of Rn and CO_2. The shallow soil layer is less affected by irrigation in the transition zone between the basin and mountains, but surface soil moisture is still higher than in the mountains. Local SLHF variation is significantly negative, indicating that the evaporation of surface water is significantly decreased in the transition zone compared with the mountains. In addition, the transition zone is characterized by loosely accumulated alluvial deposits, loose soil, and low shrubs with developed roots. Humus accumulation, rich organic matter, and strong soil microorganism activity have resulted in high CO_2 emissions.

In summary, Rn anomalies in southern Qingtongxia and CO_2 anomalies in the transition area between the basin and mountains are related to underlying rocks and/or shallow soils but not seismic or tectonic activity. In contrast, environmental factors do not contribute to the high-Rn and CO_2 anomalies observed west of Lingwu.

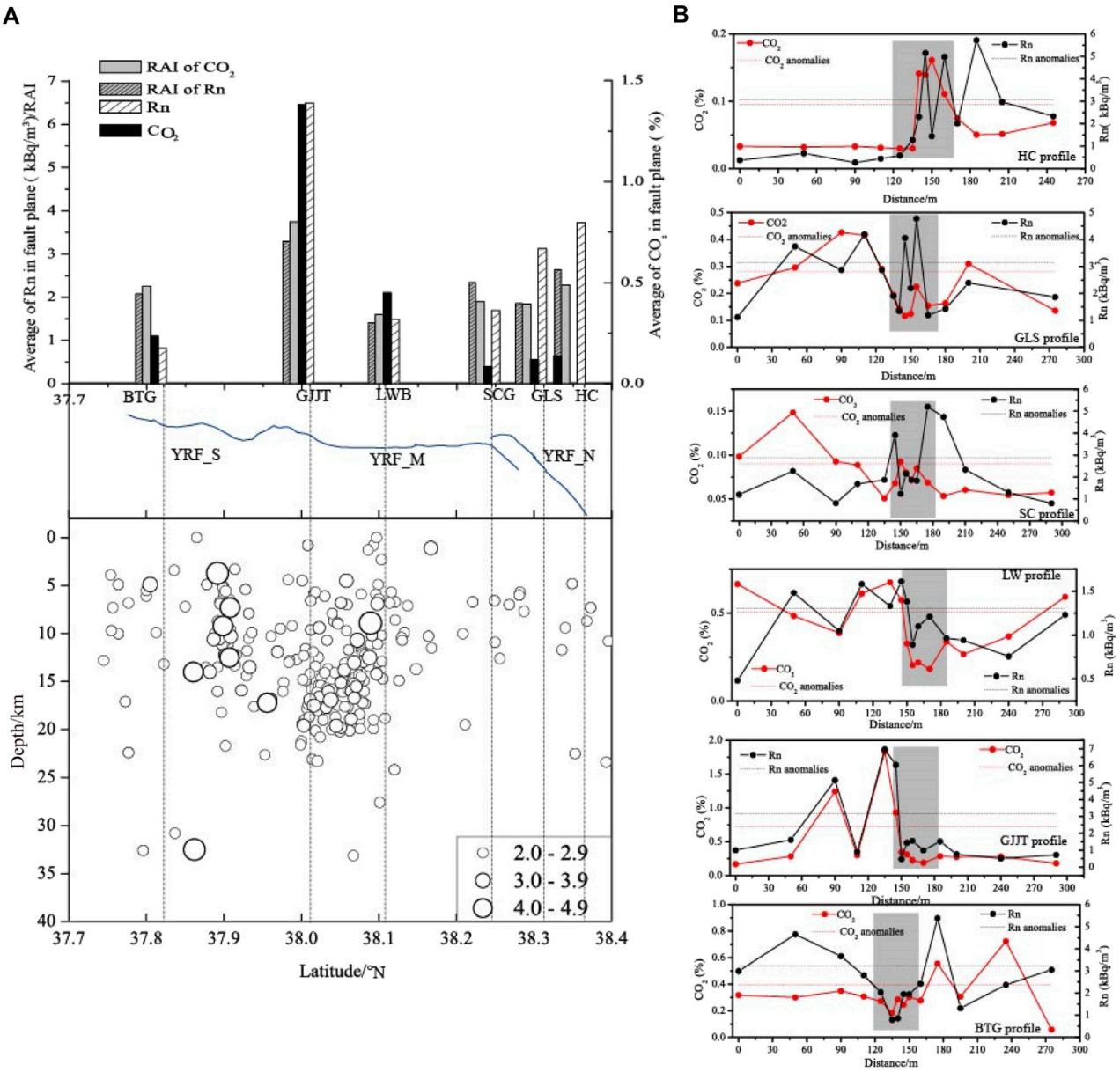

FIGURE 7
Variations in seismic activity and gas concentration along different segments of the Yellow River Fault (gray shading indicates the fault's location, The northern, middle, and southern segments of Yellow River Fault are designated as YRF_N, YRF_M, and YRF_S, respectively).

Soil gas geochemistry in different segments of Yellow River fault

As a deep-cut normal fault on the eastern border of the Yinchuan Basin, the Yellow River Fault controls the seismic activity in Wuzhong-Lingwu (Chai et al., 2001; Fang et al., 2009). According to the soil gas results across faults (Figure 7B), in the HC and GLS profiles of YRF_N, the concentration of Rn and CO_2 has a significant single peak along the fault plane, and the gas concentration differs significantly between the two sides of the fault, reflecting differences in the degree of fragmentation on each side. Moreover, these two profiles exhibit similar concentrations of Rn and CO_2 at their fault planes, being 3.73 kBq/m^3, 0.14% in the HC profile, and 3.25 kBq/m^3, 0.12% in the GLS profile, respectively. There is a significant reduction in the gas concentration in the SC section on the fault plane, and the Rn and CO_2 concentrations are only 1.70 kBq/m^3 and 0.09%. Similarly, the gas concentration on the fault plane of the LWB in YRF_M decreased sharply as well. As in the GJJT profile, the concentration of gas at the fault plane is relatively high, with Rn of 6.50 kBq/m^3 and CO_2 content of 1.38%. The gas concentrations are significantly different between the two walls, with the hanging wall gas concentration being higher and forming two peaks. As seen in the BTG profile of YRF_S, the gas concentration at the fault plane is the lowest, Rn is only 0.8 kBq/m^3, and CO_2 is only 0.24%, which is consistent with the gas emission mode of the normal fault (Annunziatellis et al., 2008), that is, a highly fragmented fault plane results in rapid gas outflow and is susceptible to air dilution and contamination with deep gas, resulting in low measured values. Additionally, most profiles of YRF exhibit the

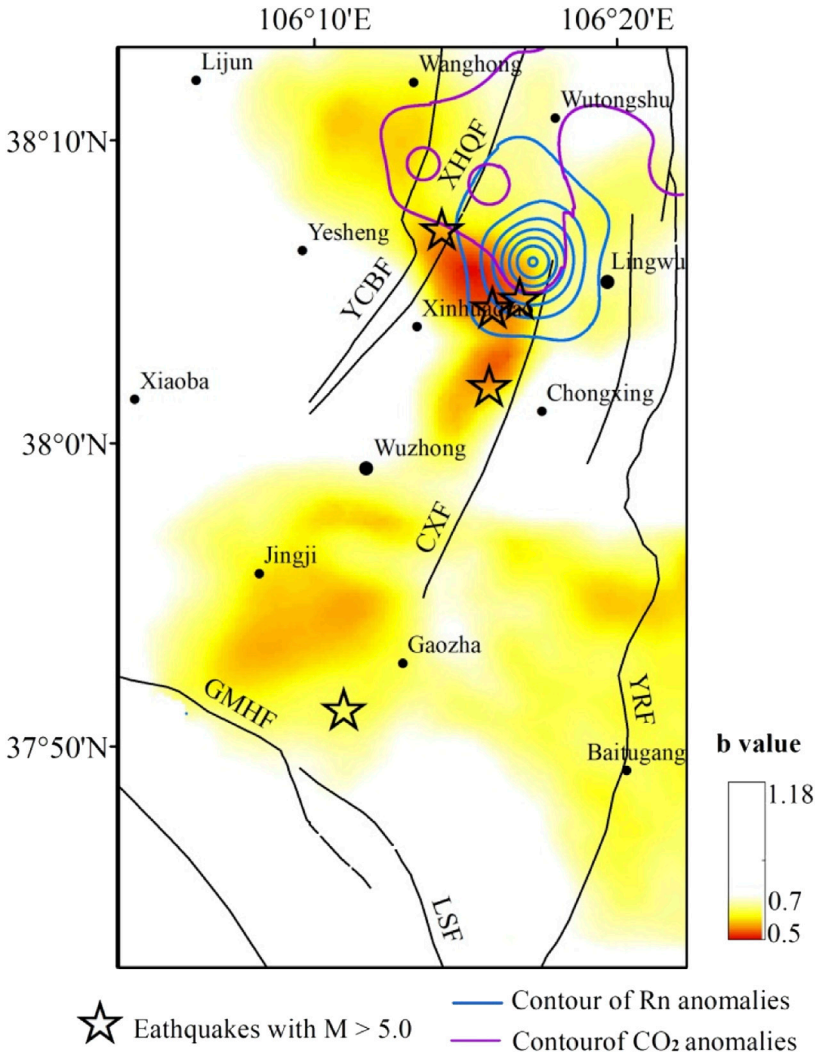

FIGURE 8
Spatial distributions of b-value and anomalies of gas in the Wuzhong–Lingwu area.

characteristics of multi-peak gas emission, which is a characteristic of strike-slip faults (Sun et al., 2017). Therefore, both strike-slip and certain normal fault characteristics have been found in YRF.

Depending on the activity of faults, underground structures, gas sources, geology and human activity within each profile, the concentration of gas released varies (Seminsky & Bobrov, 2009). Considering the distance between the sampling points and the fault plane varied, the degree of fragmentation of the underground rock and the permeability of the formation is also different. This results in variations of the soil gas concentration in the profile. CO_2 and Rn are consistently measured in most points, confirming that CO_2 is one of Rn's carrier gases.

The fault activity in the YRF_N is weak (Lei et al., 2014), and the magnitude of seismic activity in this area is small, primarily magnitude 2, with a shallow depth and low soil gas concentration and weak RAI of Rn and CO_2 were detected (Figure 7A). In the HC to SC profile, Cretaceous sandstone and glutenite are widely distributed and mixed with mudstone, contributing to the high value of Rn. It has been found that the fault in YRF_M is exposed to the surface (Chai et al., 2001), the seismic activity is relatively active, the magnitude and frequency of small earthquakes have both increased significantly, and the focal depth is deeper than what is found in the northern section, with most earthquakes occurring in the range of 5–20 km. Rn and CO_2 concentrations and RAIs were also highest in YRF. Even though the frequency of seismic activity in YRF_S is lower than in YRF_M, the intensity of seismic activity is slightly higher, and there have been numerous earthquakes above magnitude 4. Consequently, with the low concentration of gases at the fault plane, the RAI of Rn and CO_2 is not low. Frequent small earthquake increase underground rock cracks, which can result in gas emissions. At the same time, the deeper the focal depth, the more deep fluids are easier to migrate to the surface during seismic activity, thereby increasing the concentration of gas on the surface. Accordingly, the difference in seismic activity also accounts for the differences in gas concentration and RAI between segments of the YRF.

Gas migration and seismic hazard

Soil gases migrate easily from depth to the surface, making them valuable precursors of crustal transients (Bernard, 2001). The soil gas

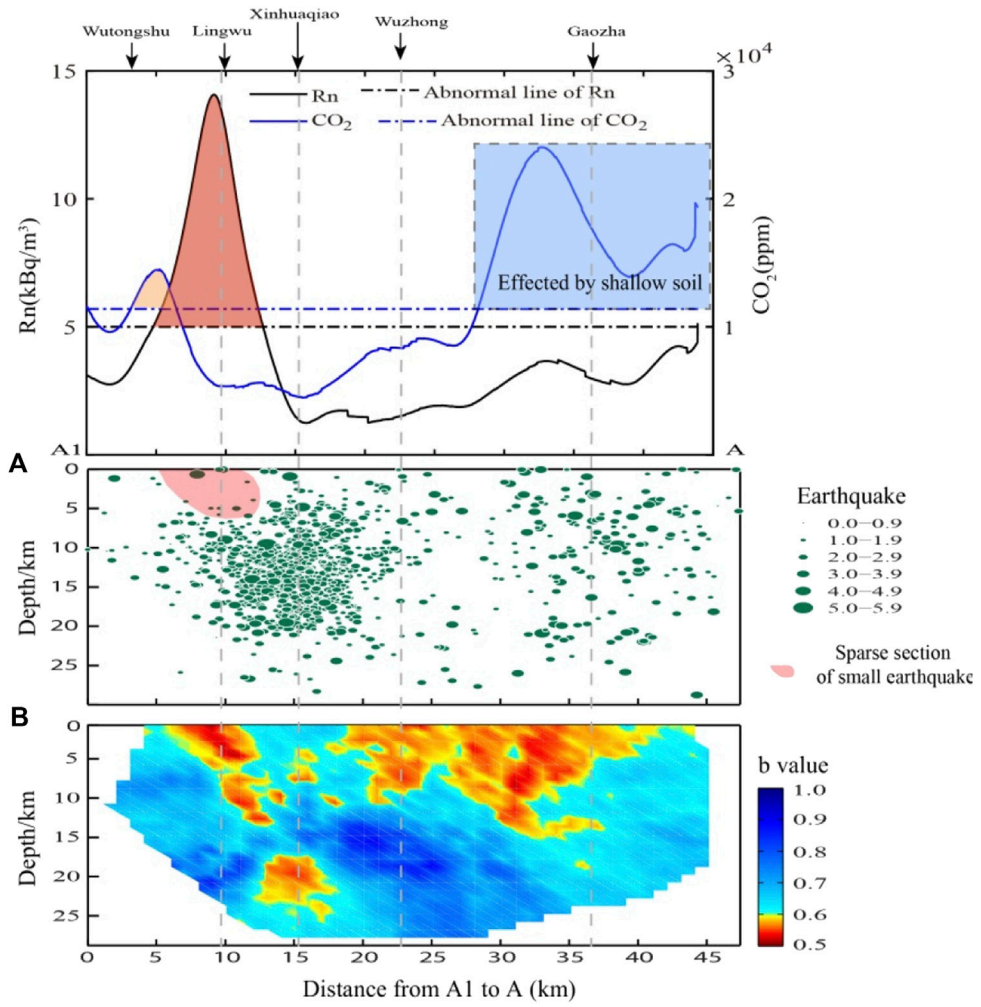

FIGURE 9
Depth profiles of **(A)** gas concentration, **(B)** earthquake scale, and **(C)** b-value in the Wuzhong–Lingwu area. The light pink shadow and dark red shadow represent the anomalies of CO2 and Rn above the threshold.

concentration is directly or indirectly related to subsurface porosity and overburden properties. Moreover, as soil gas concentrations can be related to seismic activity and fault characteristics, they offer insight into crustal stresses and strains (Pizzino et al., 2004; Chen et al., 2022). High soil gas concentrations occur in fault zones with high strain and increased seismicity (Yuce et al., 2017; Sun et al., 2021; Lombardi and Voltattorni., 2020). An inverse relation between seismic b-value and stress can usually be interpreted as a measure of the current stress level of an active fault zone (Wyss et al., 2000; Wiemer, 2001). By finding the position of the asperity structure based on lower b-values, the stress state of different sections of an active fault zone in a specific area can be determined, and the potential risk of strong earthquakes can be assessed (Yi et al., 2004).

We calculated b-values using seismic data collected by the Ningxia Network for the period from 1970 to 2020 (Zeng et al., 2021). Two areas with low b-value anomalies (<0.7) were identified, west of Lingwu and south of Wuzhong (Figure 8), suggesting high-stress levels and higher moderate earthquake risk compared with other parts of the study area. CO_2 anomalies impacted by the shallow soil environment in the transition area between the basin and mountains were removed. Similarly, Rn anomalies in southern Qingtongxia, attributed to overburden lithology, were removed. The relationship between the remaining soil gas anomalies and the b-values was determined. The low b-value in the west of Lingwu was consistent with the region of high-Rn and -CO_2 anomalies. Thus, soil gas emission in the west of Lingwu was considered the contribution to a high-stress state. Similar findings have been found in the different segments of the North-South seismic zone. The distributions of the high soil-gas concentrations in the Xianshuihe-Xiaojiang fault system (XXFS) coincide with the highest stress and maximum strain rates (Sun et al., 2021), indicating that the fault activity enhanced permeability and increased the emission rates of the gases. The relationship between radon concentration and fault activity was investigated on the northern edge of the west Qinling fault, higher radon was detected in a seismically active zone (Li et al., 2016). Furthermore, it has also been observed that the anomalous area of high gas coincides with the area of low b value and strong seismic activity in the generalized Haiyuan fault zone, which is closer to the Lingwu area (Zhou et al., 2016). Owing to the uneven distribution of fluid in crustal fractures and fault zone, variation of stress associated

with earthquakes will cause pore pressure, fluid-rock interaction and fluid migration, leading to changes in the geochemical characteristics of fluid (Lombardi & Voltattorni, 2020). Moreover, considering that the thickness of the crust increases suddenly and high-velocity bodies are widely distributed in this part of the study area (Zeng et al., 2017; Xu et al., 2018), west of Lingwu was identified as a region at risk from strong earthquakes. In fact, three earthquakes of M > 5 have occurred in the west of Lingwu since 1970. Therefore, soil gas Rn and CO_2 anomalies are important indicators for assessing the risk of moderate or strong earthquakes in the west of Lingwu.

The relationship between the b-value of the NNE profile (Figure 9) and the soil gas concentrations were determined. In the profile, western Lingwu is characterized by high-Rn and -CO_2 anomalies and low b-values. The focal depth profile also shows a sparse segment of small earthquakes and low b-values simultaneously distributed at ~5 km depth, confirming the greater risk of moderate earthquakes and that future earthquakes in this region will likely be shallow and destructive. Therefore, the relationship between low b-value and subsurface fluid anomalies also suggests that variation in the crustal state is closely related to the local fluid activity. In addition, small-magnitude seismic activity frequently occurred at a depth of 10–20 km west of Lingwu. Rock fissures opened by seismic activity in the upper crust facilitate deep gas migration, resulting in elevated Rn and CO_2 emissions (Ghosh et al., 2009; Lombardi & Voltattorni, 2010; Zhou et al., 2010).

In the south of Gaozha, low b-values are associated with frequent small earthquakes; However, the lack of credible Rn or CO_2 anomalies associated with seismic activity or high stress further indicates that the seismic risk in this area cannot currently be assessed by geochemical methods.

The frequency of seismic activity has been significantly lower than that in the west of Lingwu since 1970. Studies of low gas anomalies in some active fault zones indicated that the high locking degree of the fault constrains the migration of soil gas, whereas the creeping fault with a low locking degree is more favorable for the discharge of gas from deeper layers up toward the surface (Yang et al., 2018; Zhou et al., 2020; Yang et al., 2021). Although gas concentrations are low in the southern segment of the YRF, according to the slip rate inversed by InSAR, there is ~6.8 km locking in the southern segment of the YRF (Zhang et al., 2020), which the risk of strong earthquakes has increased. Therefore, more gas samples should be collected, and isotope analysis is needed to determine the source of the CO_2. Other deformation observations, such as leveling, Global Navigation Satellite System (GNSS), and interferometric synthetic aperture radar (InSAR), should be employed to monitor seismicity in this region.

Conclusion

This study aimed to investigate the spatial distribution and influencing factors of Rn and CO_2 in the Wuzhong–Lingwu area based on field measurements of 76 measurement points, spatial interpolation and observed results of six crossing-fault profiles along the Yellow River Fault zone (YRF). The following conclusions can be drawn.

1) Observed results of the soil gas Rn and CO_2 in different segments of YRF illustrated that YRF has features of both strike-slip and certain normal fault characteristics. Frequent seismic activity and deeper focal depth could also account for the higher gas concentration and strong RAI in the YRF.
2) The spatial distributions of Rn and CO_2 are distinct. High-Rn values are found in east and south Qingtongxia and are associated with overburden lithology. CO_2 anomalies in the transition area between the basin and mountains are related to the shallow soil environment.
3) Under the influence of irrigation by Yellow River diversion, the soil porosity was reduced, and the parent isotopes of Rn isotopes were diluted. Therefore, low values of Rn and CO_2 were widely distributed in areas with high soil moisture in the basin.
4) After removing Rn and CO_2 anomalies related to shallow soil and rocks, higher gas anomalies are consistent with low b-values in the west of Lingwu. By combining similar studies in the north-south seismic belts, it is believed that high stress and strong seismic activity increased the permeability of rocks and boosted gas emissions. In addition, a crustal thickness variation belt, the distribution of high-velocity bodies, and frequent seismic activity in west of the Lingwu area further reveal a higher seismic hazard.

Data availability statement

The original contributions presented in the study are included in the article/supplementary material, further inquiries can be directed to the corresponding author.

Author contributions

XinL contributed to the sampling, methodology, data analysis and writing. XiaL is the corresponding authors and for the language improvement and methodology. XZ contributed to the calculation of b value and data analysis of seismic activity. Other authors contributed to the sampling.

Funding

This work was supported by the National Natural Science Foundation of China [42071230], Ningxia Natural Science Foundation [2022A1335, 2020AAC03280, 2022AAC03696], Earthquake Science and Technology Spark Plan Project of China Earthquake Administration (XH20064), the Key Research and Development Program of the Ningxia Autonomous Region [2018BEG003004 and 2018BFG02011] and the innovative teams of the Earthquake Agency of Ningxia Hui Autonomous Region [CX 2019–4 9)].

Acknowledgments

The authors thank Du Jianguo for discussion of soil gas origins.

Conflict of interest

The authors declare that the research was conducted in the absence of any commercial or financial relationships that could be construed as a potential conflict of interest.

Publisher's note

References

Al-Hilal, M., and Abdul-Wahed, M. K. (2007). Tectonic and geologic influences on soil gas radon emission along the Western extension of Damascus fault, Syria. *Environ. Earth Sci.* 75 (23), 1–11. doi:10.1007/s12665-016-6292-z

Ando, T., and Ueyama, M. (2017). Surface energy exchange in a dense urban built-up area based on two-year eddy covariance measurements in Sakai, Japan. *Jpn. Urban Clim.* 19, 155–169. doi:10.1016/j.uclim.2017.01.005

Annunziatellis, A., Beaubien, S. E., Bigi, S., Ciotoli, G., Coltella, M., and Lombardi, S. (2008). Gas migration along fault systems and through the vadose zone in the Latera caldera(central Italy): Implications for CO_2 geological storage. *Int. J. Greenh.Gas Con* 2 (3), 353–372. doi:10.1016/j.ijggc.2008.02.003

Baixeras, C., Erlandsson, B., Font, L., and Jonsson, G. (2001). Radon emanation from soil samples. *Radiat. Meas.* 34, 441–443. doi:10.1016/S1350-4487(01)00203-7

Baubron, J. C., Rigo, A., and Toutain, J. P. (2002). Soil gas profiles as a tool to characterise active tectonic areas: The jaut pass example (pyrenees, France). *Earth Planet. Sci. Lett.* 196 (1–2), 69–81. doi:10.1016/s0012-821x(01)00596-9

Beaubien, S. E., Ciotoli, G., and Lombardi, S. (2003). Carbon dioxide and radon gas hazard in the Alban Hills area (central Italy). *J. Volcanol. Geotherm. Res.* 123, 63–80. doi:10.1016/s0377-0273(03)00028-3

Bernard, P. (2001). From the search of 'precursors' to the research on 'crustal transients. *Tectonophysics* 338, 225–232. doi:10.1016/s0040-1951(01)00078-6

Chai, C. Z., Liao, Y. H., Zhang, W. X., Xu, W., Shen, X., and Tian, Q. (2001). Late quaternary paleoearthquakes and their rupture features along the Lingwu fault. *Seismol. Geol.* 23 (1), 15–23. (in Chinese). doi:10.3969/j.issn.0253-4967.2001.01.002

Chen, Z., Li, y., Liu, Z. F., He, H. Y., Martinellib, G., Lu, C., et al. (2022). Geochemical and geophysical effects of tectonic activity in faulted areas of the North China Craton. *Chem. Geol.* 609, 1–11. doi:10.1016/j.chemgeo.2022.121048

Ciotoli, G., Lombardi, S., and Annunziatellis, A. (2007). Geostatistical analysis of soil gas data in a high seismic intermontane basin: Fucino Plain, central Italy. *J. Geophys. Res. Solid Earth* 112, B05407–B05423. doi:10.1029/2005jb004044

Cui, Y., Du, J., Zhang, D., and Sun, Y. (2013). Anomalies of total column CO and O3 associated with great earthquakes in recent years. *Nat. Hazard. Earth Syst. Sci.* 13, 1–7. doi:10.5194/nhess-13-2513-2013

Dogan, T., Mori, T., Tsunomori, F., and Notsu, K. (2007). Soil H_2 and CO_2 surveys at several active faults in Japan. *Pure Appl. Geophys.* 164, 2449–2463. doi:10.1007/s00024-007-0277-5

El-Arabi, A., Abbady, A., Ahmed, N., Michle, R., El-Kamel, A. H., and Abbady, A. G. E. (2006). Assessment of radon-222 concentrations and exhalation rates of rocks and building materials. *Indian. J.Pure Appl. Phys.* 44 (4), 287–291. doi:10.1016/j.apradiso.2004.10.010

Fang, S. M., Zhao, C. B., Chai, Z. Z., Liu, B. J., Feng, S. Y., Liu, M. J., et al. (2009). Seismic evidence of crustal structures in the Yinchuan faulted basin. *Chin. J. Geophys* 52 (7), 1768–1775. doi:10.3969/j.issn.0001-5733.2009.07.010

Fu, C. C., Yang, T. F., Walia, V., and Chen, C. H. (2005). Reconnaissance of soil gas composition over the buried fault and fracture zone in southern Taiwan. *Geochem. J.* 39, 427–439. doi:10.2343/geochemj.39.427

Fu, C. C., Yang, T. F., Du, J., Walia, V., Chen, Y. G., Liu, T. K., et al. (2008). Variations of helium and radon concentrations in soil gases from an active fault zone in southern Taiwan. *Radiat. Meas.* 43, 348–352. doi:10.1016/j.radmeas.2008.03.035

Fu, C. C., Yang, T. F., Tsai, M. C., Lee, L. C., Liu, T. K., Walia, V., et al. (2016). Exploring the relationship between soil degassing and seismic activity by continuous radon monitoring in the Longitudinal Valley of eastern Taiwan. *Chem. Geol.* 469, 1–48. doi:10.1016/j.chemgeo.2016.12.042

Ghosh, D., Deb, A., and Sengupta, R. (2009). Anomalous radon emission as precursor of earthquake. *J. Appl. Geophys.* 69 (2), 67–81. doi:10.1016/j.jappgeo.2009.06.001

Giammanco, S., Gurrieri, S., and Valenza, M. (1998). Anomalous soil CO_2 degassing in relation to faults and eruptive fissures on Mount Etna (Sicily, Italy). *Bull. Volcanol.* 60, 252–259. doi:10.1007/s004450050231

Guerra, M., and Lombardi, S. (2001). Soil-gas method for tracing neotectonic faults in clay basins the Pisticci field (Southern Italy). *Tectonophysics* 339, 511–522. doi:10.1016/s0040-1951(01)00072-5

Han, X. K., Li, Y., Du, J. G., Zhou, X., Xie, C., and Zhang, W. (2014). Rn and CO_2 geochemistry of soil gas across the active fault zones in the capital area of China. *Nat. Hazard. Earth Syst. Sci.* 14, 2803–2815. doi:10.5194/nhess-14-2803-2014

Hinkle, M. E. (1994). Environmental conditions affecting concentrations of He, CO_2, O_2 and N_2 in soil-gases. *Appl. Geochem.* 9, 53–63. doi:10.1016/0883-2927(94)90052-3

Hong, W. L., Yang, T. F., Walia, V., Lin, S. J., Fu, C. C., Chen, Y. G., et al. (2010). Nitrogen as the carrier gas for helium emission along an active fault in NW Taiwan. *Appl. Geochem* 25, 593–601. doi:10.1016/j.apgeochem.2010.01.016

Irwin, W. P., and Barnes, I. (1980). Tectonic relations of carbon dioxide discharges and earthquakes. *Res. Solid Earth* 85, 3115. doi:10.1029/jb085ib06p03115

Jiao, Z. H., Zhao, J., and Shan, X. J. (2018). Pre-seismic anomalies from optical satellite observations: A review. *Nat. Hazard. Earth Syst. Sci.* 18, 1013–1036. doi:10.5194/nhess-18-1013-2018

Khilyuk, L. F., Chilingar, G. V., Robertson, J. O., Jr, and Endres, B. (2000). *Gas migration: Events preceding earthquakes*. Houston, Texas: Gulf Publishing Company.

King, C. Y., King, B. S., Evans, W. C., and Zhang, W. (1996). Spatial radon anomalies on active faults in California. *Appl. Geochem.* 11, 497–510. doi:10.1016/0883-2927(96)00003-0

Kumar, A., Singh, S., Mahajan, S., Bajwa, B. S., Kalia, R., and Dhar, S. (2009). Earthquake precursory studies in Kangra valley of North West Himalayas, India, with special emphasis on radon emission. *Appl. Radiat. Isot.* 67 (10), 1904–1911. doi:10.1016/j.apradiso.2009.05.016

Lei, Q. Y., Chai, C. Z., Zheng, W. J., Peng, D. U., Xie, X. F., Wang, Y., et al. (2014). Activity and slip rate of the northern section of Yellow River fault revealed by drilling. *Seismol. Geol.* 36 (2), 464–477. doi:10.3969/j.issn.0253-4967.2014.02.015

Li, Y., Du, J. G., Wang, F. K., Zhou, X., Pan, X., and Wei, R. (2009). Geochemical characteristics of soil gas in the Yanhuai basin, northern China. *Earthq. Sci.* 22, 93–100. doi:10.1007/s11589-009-0093-3

Li, Y., Du, J. G., Wang, X., Zhou, X., Xie, C., and Cui, Y. (2013). Spatial variations of soil gas geochemistry in the Tangshan area of Northern China. *Terr. Atmos. Ocean. Sci.* 24 (3), 323–333. doi:10.3319/tao.2012.11.26.01(tt)

Li, C. H., Su, H. J., Zhang, H., and Zhou, H. L. (2016). Correlation between the spatial distribution of radon anomalies and fault activity in the northern margin of West Qinling Fault Zone, Central China. *J. Radioanal. Nucl. Chem.* 308, 679–686. doi:10.1007/s10967-015-4504-8

Liao, Y. H., Chai, C. Z., Zhang, W. X., and Xu, W. J. (2000). The active features and slip rate of Lingwu faults in late quaternary. *Earthq. Res. Chin.* 16 (2), 158–165. (in Chinese). doi:10.3969/j.issn.1001-4683.2000.02.008

Liu, Z. F., Li, Y., Chen, Z., Zhao, Z. D., Huangfu, R. L., Zhao, Y. X., et al. (2022). Environmental impacts of ^{222}Rn, Hg and CO_2 emissions from the fault zones in the Western margin of the Ordos block, China. *Environ. Geochem. Health* 08, 1–16. doi:10.1007/s10653-022-01350-5

Lombardi, S., and Voltattorni, N. (2010). Rn, He and CO2 soil gas geochemistry for the study of active and inactive faults. *Appl. Geochem.* 25 (8), 1206–1220. doi:10.1016/j.apgeochem.2010.05.006

Ma, H. Q., Ren, X. M., Jin, C. H., and Shen, J. Q. (2006). 2003~2004 seismicity analysis of the Wuzhong and Lingwu region. *J. Seismol. Res.* 29 (2), 114–117. (in Chinese). doi:10.3969/j.issn.1000-0666.2006.02.002

Neri, M., Giammanco, S., Ferrera, E., Patanè, G., and Zanon, V. (2011). Spatial distribution of soil radon as a tool to recognize active faulting on an active volcano: The example of Mt. Etna (Italy). *J. Environ. Radioact.* 102, 863–870. doi:10.1016/j.jenvrad.2011.05.002

Pizzino, L., Burrato, P., Quattrocchi, F., and Valensise, G. (2004). Geochemical signatures of large active faults: The example of the 5 February 1783, Calabrian earthquake (southern Italy). *J. Seismol.* 8, 363–380. doi:10.1023/b:jose.0000038455.56343.e7

Sciarra, A., Cantucci, B., Sapia, V., De Ritis, R., Ricci, T., Civico, R., et al. (2020). Geochemical and geoelectrical characterization of the Terre Calde di Medolla (Emilia-Romagna, northern Italy) and relations with 2012 seismic sequence. *J. Geochem. Explor.* 221, 106678. doi:10.1016/j.gexplo.2020.106678

Seminsky, K. Z., and Bobrov, A. A. (2009). Radon activity of faults (Western Baikal and southern Angara areas). *Russ. Geol. Geophys.* 50 (8), 682–692. doi:10.1016/j.rgg.2008.12.010

Sun, X. L., Yang, P. T., Xiang, Y., Si, X. Y., and Liu, D. L. (2017). Across-fault distributions of radon concentrations in soil gas for different tectonic environments. *Geosci. J.* 22, 227–239. doi:10.1007/s12303-017-0028-2

Sun, Y., Zhou, X., Yan, Y., Li, J., Fang, W., Wang, W., et al. (2021). Soil degassing from the xianshuihe–xiaojiang fault system at the eastern boundary of the chuan–dian rhombic block, southwest China. *Front. Earth Sci.* 9, 1–12. doi:10.3389/feart.2021.635178

Szabó, K. Z., Jordan, G., Horváth, Á., and Szabó, C. (2014). Mapping the geogenic radon potential: Methodology and spatialanalysis for central Hungary. *J. Environ. Radioact.* 129, 107–120. doi:10.1016/j.jenvrad.2013.12.009

Toutain, J. P., and Baubron, J. C. (1999). Gas geochemistry and seismotectonics: A review. *Tectonophysics* 304, 1–27. doi:10.1016/s0040-1951(98)00295-9

Tramutoli, V., Cuomo, V., Filizzola, C., Pergola, N., and Pietrapertosa, C. (2005). Assessing the potential of thermal infrared satellite surveys for monitoring seismically active areas: The case of Kocaeli (İzmit) earthquake, August 17, 1999. *Remote Sens. Environ.* 96 (3–4), 409–426. doi:10.1016/j.rse.2005.04.006

Tramutoli, V., Aliano, C., Corrado, R., Filizzola, C., Genzano, N., Martinello, G., et al. (2013). On the possible origin of thermal infrared radiation (TIR) anomalies in earthquake-prone areas observed using robust satellite techniques (RST). *Chem. Geol.* 339, 157–168. doi:10.1016/j.chemgeo.2012.10.042

Weinlich, F. H. (2014). Carbon dioxide controlled earthquake distribution pattern in the NW Bohemian swarm earthquake region, Western Eger Rift, Czech Republic–gas migration in the crystalline basement. *Geofluids* 14, 143–159. doi:10.1111/gfl.12058

Wiemer, S. (2001). A software package to analyze seismicity: Zmap. *Seismol. Res. Lett.* 72 (2), 373–382. doi:10.1785/gssrl.72.3.373

Wyss, M., Schorlemmer, D., and Wiemer, S. (2000). Mapping asperities by minima of local recurrence time: San Jacinto-Elsinore fault zones. *J. Geophys. Res.* 105, 7829–7844. doi:10.1029/1999jb900347

Xu, Y. C., Wang, Q., Zeng, X. W., Ma, H. Q., Xu, W. J., and Jin, T. (2018). Moho depth and Poisson's ratio distribution in the Western edge of Ordos block. *Acta Seismol. Sin.* 40 (5), 563–581. doi:10.11939/jass.20170224

Yang, T. F., Chou, C. Y., Chen, C.-H., Chyi, L. L., and Jiang, J. H. (2003). Exhalation of radon and its carrier gases in SW Taiwan. *Radiat. Meas.* 36, 425–429. doi:10.1016/s1350-4487(03)00164-1

Yang, Y., Li, Y., Guan, Z. J., Chen, Z., Zhang, L., Lv, C. J., et al. (2018). Correlations between the radon concentrations in soil gas and the activity of the Anninghe and the Zemuhe faults in Sichuan, southwestern of China. *Appl. Geochem.* 89, 23–33. doi:10.1016/j.apgeochem.2017.11.006

Yang, Y., Li, Y., Li, Y. G., Ji, L. Y., Gong, Y., Du, F., et al. (2021). Present-day activity of the Anninghe fault and Zemuhe fault,southeastern Tibetan Plateau, derived from soil gas CO_2 emissions and locking degree. *Earth. Space. Sci.* 8, 1–21. doi:10.1029/2020EA001607

Yi, G., Wen, X., Xin, H., Qiao, H.-Z., Wang, S.-W., and Gong, Y. (2004). Stress state and major earthquake risk on the southern segment f the Longmen Shan fault zone. Chin. *J. geophys.* 56, 1112–1120. doi:10.6038/cjg20130407

Yu, J. P., Wen, Y. C., Wang, Y. M., and Song, N. P. (2000). Impacts of irrigation on soil environment by lifting up water from the Yellow River in Ningxia. *Prog. Geogr.* 19 (3), 279–284. doi:10.11820/dlkxjz.2000.03.012

Yuce, G., Fu, C. C., Alessandro, W. D., Gulbay, A. H., Lai, C. W., Bellomo, S., et al. (2017). Geochemical characteristics of soil radon and carbon dioxide within the dead sea fault and karasu faultin the amik basin (hatay), Turkey. *Chem. Geol.* 469, 129–146. doi:10.1016/j.chemgeo.2017.01.003

Zeng, X. W., Feng, J. G., Long, F., and Xin, H. L. (2017). Mid-upper crustal velocity tomography of pg wave in western margin of ordos. *J. Seismol. Res.* 40 (02), 176–185. (in Chinese).

Zeng, X. W., Li, W. J., Ma, C. Z., and Cai, X. H. (2021). Strong earthquake risk in Wuzhong–Lingwu region of Ningxia based on b value. *J. Seismol. Res.* 44 (1), 41–48. (in Chinese). doi:10.3969/j.issn.1000-0666.2021.01.006

Zhang, W. T., Ji, L. Y., Zhu, L. Y., Xu, X. X., and Wang, J. S. (2020). Current crustal deformation of Yinchuan Basin based on Sentinel-1 data. *J.Geod. Geodyn.* 40 (9), 902–917. (in Chinese). doi:10.14075/j.jgg.2020.09.005

Zhou, X., Du, J., Chen, Z., Cheng, J., Tang, Y., Yang, L., et al. (2010). Geochemistry of soil gas in the seismic fault zone produced by the Wenchuan Ms 8.0 Earth quake, southwestern China. *Geochem. Trans.* 11 (5), 5–10. doi:10.1186/1467-4866-11-5

Zhou, H. L., Su, H. J., Zhang, H., and Li, C. (2017). Correlations between soil gas and seismic activity in the Generalized Haiyuan Fault Zone, north-central China. *Nat. Hazard.* 85, 763–776. doi:10.1007/s11069-016-2603-7

Zhou, H. L., Su, H. J., Zhang, L., Li, C. H., Ma, D. Z., and Bai, R. L. (2020). Geochemical characteristics of soil gas and strong SeismicHazard potential in the liupanshan Fault Zone (LPSFZ). *Geofluids* 10, 1–14. doi:10.1155/2020/4917924

frontiers | Frontiers in Earth Science

TYPE Original Research
PUBLISHED 09 May 2023
DOI 10.3389/feart.2023.1117862

OPEN ACCESS

EDITED BY
Ziming Yang,
Oakland University, United States

REVIEWED BY
Nunzia Voltattorni,
Istituto Nazionale di Geofisica e Vulcanologia (INGV), Italy
Kan Li,
Woods Hole Oceanographic Institution, United States

*CORRESPONDENCE
Xiaocheng Zhou,
zhouxiaocheng188@163.com
Jinyuan Dong,
dongjinyuan@163.com

RECEIVED 06 December 2022
ACCEPTED 11 April 2023
PUBLISHED 09 May 2023

CITATION
Liu F, Zhou X, Dong J, Yan Y, Tian J, Li J, Ouyang S, He M, Liu K, Yao B, Wang Y, Zeng Z and Zhang Y (2023), Soil gas CO_2 emissions from active faults: a case study from the Anninghe—Zemuhe fault, Southeastern Tibetan Plateau, China. *Front. Earth Sci.* 11:1117862. doi: 10.3389/feart.2023.1117862

Soil gas CO_2 emissions from active faults: a case study from the Anninghe—Zemuhe fault, Southeastern Tibetan Plateau, China

Fengli Liu[1], Xiaocheng Zhou[1,2]*, Jinyuan Dong[1]*, Yucong Yan[2], Jiao Tian[1], Jingchao Li[1], Shupei Ouyang[1], Miao He[1], Kaiyi Liu[3], Bingyu Yao[2], Yuwen Wang[1], Zhaojun Zeng[1] and Yongxian Zhang[1]

[1]CEA Key Laboratory of Earthquake Prediction, Institute of Earthquake Forecasting, China Earthquake Administration, Beijing, China, [2]School of Water Resources and Environment, China University of Geosciences (Beijing), Beijing, China, [3]University of Sydney Business School, Sydney, NSW, Australia

Introduction: Carbon dioxide emissions from non-volcanic areas are undervalued in the carbon cycle.

Methods: First estimates of diffuse CO_2 flux from the Anninghe—Zemuhe fault (AZF), Southeastern Tibetan Plateau, China, which suggests this could equal 15% emissions from all volcanoes in China. Following the accumulation chamber method, CO_2 flux was investigated at 1,483 points, and along 67 profiles crossing the AZF.

Results and discussion: Total CO_2 emissions from the AZF were estimated 1.2 Mt yr^{-1}. The relationship between soil gas CO_2 fluxes, earthquakes, and fault activity was discussed. The intense fault activity in the southern part of the Zemuhe fault (ZMHF) and the northern part of the Anninghe fault (ANH) was inferred, which could have enhanced the porosity of the soil, and accelerated the water-rock interactions and soil gas emission within the fault zone. The chemical and isotopic data indicated that biogenic CO_2 was the primary source of CO_2 from the AZF. Produced by interactions between groundwaters and carbonates, soil gas CO_2 could migrate to the near surface through cracks. Spatial variations of CO_2 flux in soil gas indicate that seismic activity could be responsible for the jumpy variations of CO_2 flux. The diffuse CO_2 from deep faults may contribute considerably to the greenhouse gas cycles.

KEYWORDS

soilgas, carbon dioxide, geochemistry, diffuse degassing, AZF

1 Introduction

Consistently, Global warming is a central focus of climate change and studies have suggested that the growing number of carbon emissions has been considered as an essential factor for global warming (Lee et al., 2016; Isson et al., 2020; Huo et al., 2022). Nowadays, studying the distribution and magnitude of global carbon sources and sinks is an international mainstream for a better understanding of rates and mechanism of carbon cycling in and out of earth (Kämpf et al., 2013; Kang et al., 2020; Hiett et al., 2022; Xu et al.,

2022). In addition to human activities, natural factors (e.g., volcanic eruptions, biological respiration, seismic activity) will also contribute to the increase of greenhouse gas concentration in the atmosphere (Inguaggiato et al., 2012; Muirhead et al., 2020). Therefore, a great interest has been focused on studying of CO_2 Earth degassing. There are many targets for such research, such as the relationships between the CO_2 flux and the tectonic structures (Etiope et al., 1999; Jolie et al., 2015), the researches of volcanic degassing (Inguaggiato et al., 2012; Chen et al., 2019; Fischer and Aiuppa, 2020), and the quantification of deeply derived CO_2 discharging into the atmosphere (Lee et al., 2016; Viveiros et al., 2017; Jacome-Paz et al., 2020; Bekaert et al., 2021; Rahilly and Fischer, 2021).

However, the contribution of CO_2 released from non-volcanic areas, particularly deep and large faults, is also worthy of attention (Fischer et al., 2019; Rahilly and Fischer, 2021; Zhang et al., 2021). Based on a study of ^3He and CO_2 in springs and wells, Kennedy et al. (1997) estimated a mantle-derived CO_2 flux of ~0.02 gm^{-2} d^{-1} for the entire San Andreas Fault system. The relationship between active crustal stress and soil CO_2 flux in southern Italy suggested that crustal stress associated with the seism genic process can effectively modulate the gas release in a seismically active area (Camarda et al., 2016). On the Chaozhou fault in China, significant anomalies in soil gas He and Rn were observed before the earthquake, which may reflect changes in the stress field before the earthquake (Fu et al., 2008); The sudden increase in CO_2 and Rn before the earthquake was observed on a fault in the earthquake cluster area in northwestern Bohemia, Czech Republic, which may indicate an increase in porosity and the opening of transport channels due to stress redistribution (Weinlich et al., 2006). Weinlich and others concluded that underground gas components can objectively and sensitively reflect the stress and tectonic activity changes of the earth's crust, and usually show various anomalies before or after the occurrence of earthquakes.

AZF is a seismic zone with vigorous seismic activity, which has high slip rates and developed fractures providing a channel for fluid migration deep and CO_2 degassing. Therefore, the estimation of CO_2 degassing from the AZF is of great significance to understand the impact of the Earth's natural degassing on the environment. Yang et al. (2028) studied three characteristic points in AZF for soil gas CO_2 concentration measurements. The results showed that the mean and maximum values of soil gas CO_2 concentration in the northern section of the ZMHF were much higher than those in the southern section of the ANHF. The soil gas CO_2 geochemistry produced different anomalous features, which, combined with the degree of occlusion in the AZF, reflect the gas-bearing characteristics of the AZF as well as the seismic hazard. However, there is no research on the characteristics of AZF soil gas CO_2 flux and its causes.

Taken together, the relationship between soil gas CO_2 fluxes and active fault tectonic features is considered a hot topic for discussion in the field of geochemistry. In this paper, measurements of flux of soil gas CO_2 were performed at 1,483 sampling points along 67 profile lines oriented perpendicularly to the AZF. The geochemical characteristics of soil gas CO_2 emissions in study areas and the association between the earthquakes and degassing process were investigated. This investigation aims to evaluate the total output of the CO_2 from the AZF and elucidate the tectonic association between the flux of soil gas CO_2 and the activity of earthquakes.

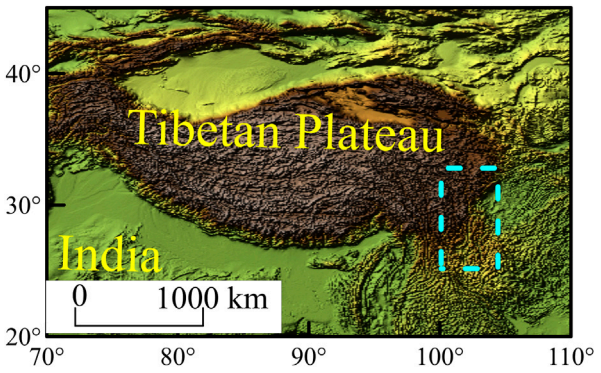

FIGURE 1
Study area location diagram the dotted line is the specific location of the study area on the Tibetan Plateau.

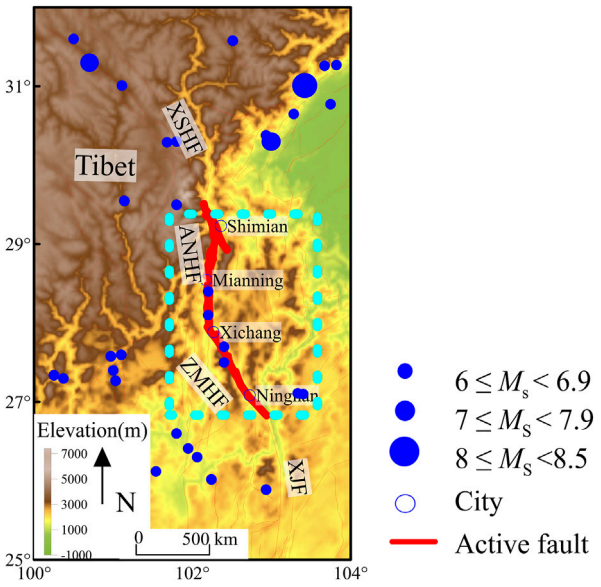

FIGURE 2
Schematic diagram of the Sichuan-Yunnan block structure the earthquakes are the events ($M_S \geq 6.0$) since 1618.

2 Geological setting

The AZF is the main active rift on the eastern boundary of the Sichuan-Yunnan block (Deng et al., 2003; Zhang et al., 2003). Under the combined effect of deep dynamic processes, large shear displacement and deformation zones are formed

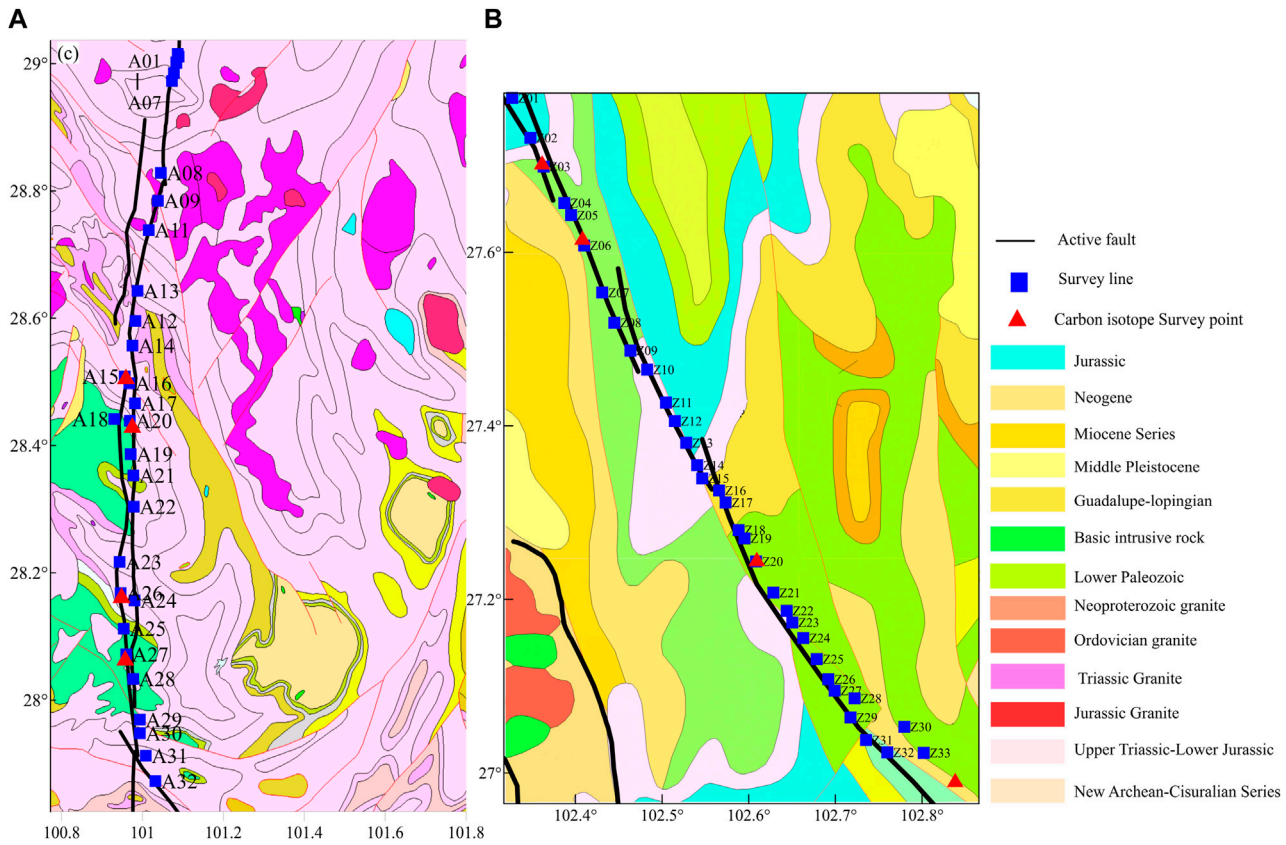

FIGURE 3
AZF measurement line distribution diagram Map showing the CO_2 sampling points along the ANHF **(A)** and the ZMHF **(B)**, together with the geology of the study area.

near the Xianshui fault, the ANHF and the Xiaojiang fault, which control the tectonic pattern of the Sichuan-Yunnan region (Figure 1).

The ANHF starts from Shimian in the north, extending through Xichang to Huili (Figure 2), with an overall northsouth trend. The overall NS trend is dominated by left-slip motion, with a maximum left-slip. The maximum left-slip rate since the Cenozoic is about 6.2 years^{-1} (He and Oguchi, 2008), and the maximum extrusion rate is about 1.4 years^{-1} (Ran et al. 2008; Ren and Lin, 2010). The Shimian-Xichang area in the southern section of the ANHF was the main rupture site of the earthquake with M_S $7^{1/2}$ in 1,536, but no more significant earthquakes have occurred in the ANHF since an M_s 6 earthquake occurred south of Shimian in 1952 (Wen, 2000).

The Zemu River rift zone is connected with the ANHF in the north and the Xiaojiang fault in the south, extending from Xichang to Qiaojia (Figure 2), Yunnan via Puge and Ningnan, with a general strike of 330°. The Zemu River rift zone is dominated by left-slip motion, with a Holocene left-slip rate of about (6.4 ± 0.6) year^{-1} (Wen, 2000). Historically, there were earthquakes of an M_s 7 in Xichang in 1814 and M_s 7 in Dajiaoliangzi in 1850, and the most recent moderately strong earthquake was the Xichang M_s 5.1 earthquake on 31 October 2018.

3 Materials and methods

3.1 Site description

Soil gas flux CO_2 surveys were performed at ANHF and ZMHF (26.8°N-29.2°N, 102°E – 103°E). During the layout of the CO_2 flux measuring line, a large number of field investigations were carried out on the fault zone in the field. First, we found the location of the active fault fracture zone, and then the suitable measuring line was selected. A total of 67 measuring lines were arranged in ANHF and ZMHF, recording the longitude and latitude of the starting point and end point of the measuring line. Finally, the measuring lines designed for the investigation were drawn on the map indoors, according to the line density and feasibility and the final line scheme was obtained. Overall, sampling for soil gas CO_2 flux was conducted at 1,483 sampling points along the 67 profiles that crossed the target faults (Figure 3). The measuring line is perpendicular to the fracture zone of the active fault zone and each line is generally more than 20 measuring points according to the landform. The spacing of measuring points near the active fault fracture zone is generally 10 m. After leaving the fracture zone, the spacing of measuring points was expanded by tens of meters to hundreds of meters according to the terrain (Figure 4).

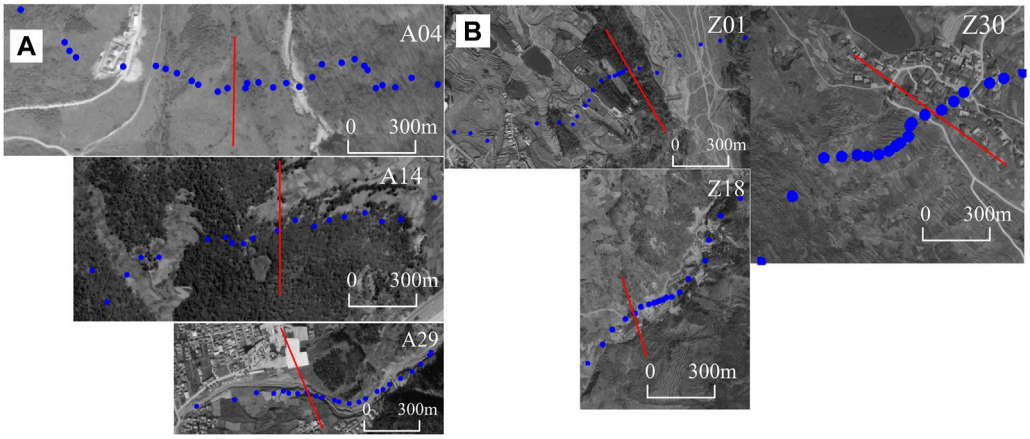

FIGURE 4
AZF sampling point diagram. The figure shows three profile lines for each of ANHF **(A)** and ZMHF **(B)**, the blue points are sampling points and the red is the fault location.

3.2 Measurement methods of soil CO_2 flux

The details and principles of the closed-chamber method were described by Zhou et al. (2016). Analytical error associated with a single measurement was about ±5% and the reproducibility was about ±10% for the range of 100–10,000 gm^{-2} d^{-1}.

Soil temperature at a depth of 10 cm was taken at every site, using a pocket digital thermometer (Henxin AZ8821), which has an accuracy of ±0.1°C. To minimize the inherent variability of gas flux due to soil water and humidity, sampling was performed during dry stable weather. Ambient air temperature and barometric pressure were recorded every 25 samples. Each survey was executed over three consecutive days, and under rain-free conditions, to avoid environmental effects. Both soil temperature and atmospheric pressure, recorded at every measurement, were used for calibrating soil flux values. At each observation site, the wind speed and barometric pressure was measured.

3.3 Measurement methods of carbon isotope

Four samples of CO_2 in soil gas from ANHF and four samples from ZMHF were collected for measurement of values of $\delta^{13}C_{CO2}$(V-PDB). Glass bottles (500 mL) were used to collect soil gas in order to improve the accuracy of carbon isotopes. The gas samples were collected as follows: first, the glass bottle was filled with saturated brine and then inverted into a bucket filled with saturated brine and kept the glass bottle from tipping over. Soil gas is pumped into the glass bottle through a rubber hose. Until the filled saturated brine was replaced by gas in one-half of the bottle, the glass bottles were sealed in water with rubber blocks to avoid air contamination. All gas samples were analyzed at the Key Laboratory of Petroleum Resources Research, Institute of Geology and Geophysics, Chinese Academy of Sciences. Carbon isotope analysis was performed using a Delta Plus XL mass spectrometer. It is manufactured by ThermoFinnigan Inc., consisting of the HP6890 gas chromatograph, combustion/conversion oven, interface and DeltaPlusXP mass spectrometer (Li et al., 2017). The stable carbon isotope composition is generally expressed as $\delta^{13}C$ and has a precision of ±0.2‰.

4 Results

Overall, 734 points along 32 profiles across the ANHF and 728 points along 35 profiles across the ZMHF were sampled for the CO_2 flux analysis (Figure 5). There are two main patterns in the distribution of soil gas CO_2 fluxes on the AZF, one with anomalously high values near the fractures, which are mainly because the fault fractures are well developed at this location, creating many gas escape routes. The other is where the anomaly occurs on both sides of the fault, because the fault is mature and its fractured core is well developed, while the surrounding fragmentation is so high that a peak occurs above the lateral fault. This bimodal distribution is also observed in the San Andreas Fault profile (Kang et al., 2020).

In ANHF, the CO_2 flux in soil gas varied in the range of 0–1996.2 g m^2d^{-1}, and the arithmetic mean values were 73.7 g ±2.36 m^2d^{-1} (Figure 6); In ZMHF, the CO_2 flux in soil gas varied in the range of 0–442.3 gm^2d^{-1}, and the arithmetic mean values were 87.5 g ±4.21 m^2d^{-1}. The $\delta^{13}C_{CO2}$(V-PDB) were in the range of −25.0‰ ~ −19.7‰ (Table 1). The statistics data on the fluxes of CO_2 in soil gas from the AZF are listed in Table 2. The mean fluxes of CO_2 in each soil gas survey line were in the range of 7.23–272.22 gm^{-2} d^{-1} (Figure 7).

5 Discussion

5.1 Sources of CO_2 degassing

The CO_2 in subsurface fluids can be classified into two categories based on the type of parent material formed, organic and inorganic. The organic mainly formed by organic matter decomposition and bacterial activity, and the inorganic mainly from mantle/magmatic activity, thermal decomposition of carbonate rocks and dissolution

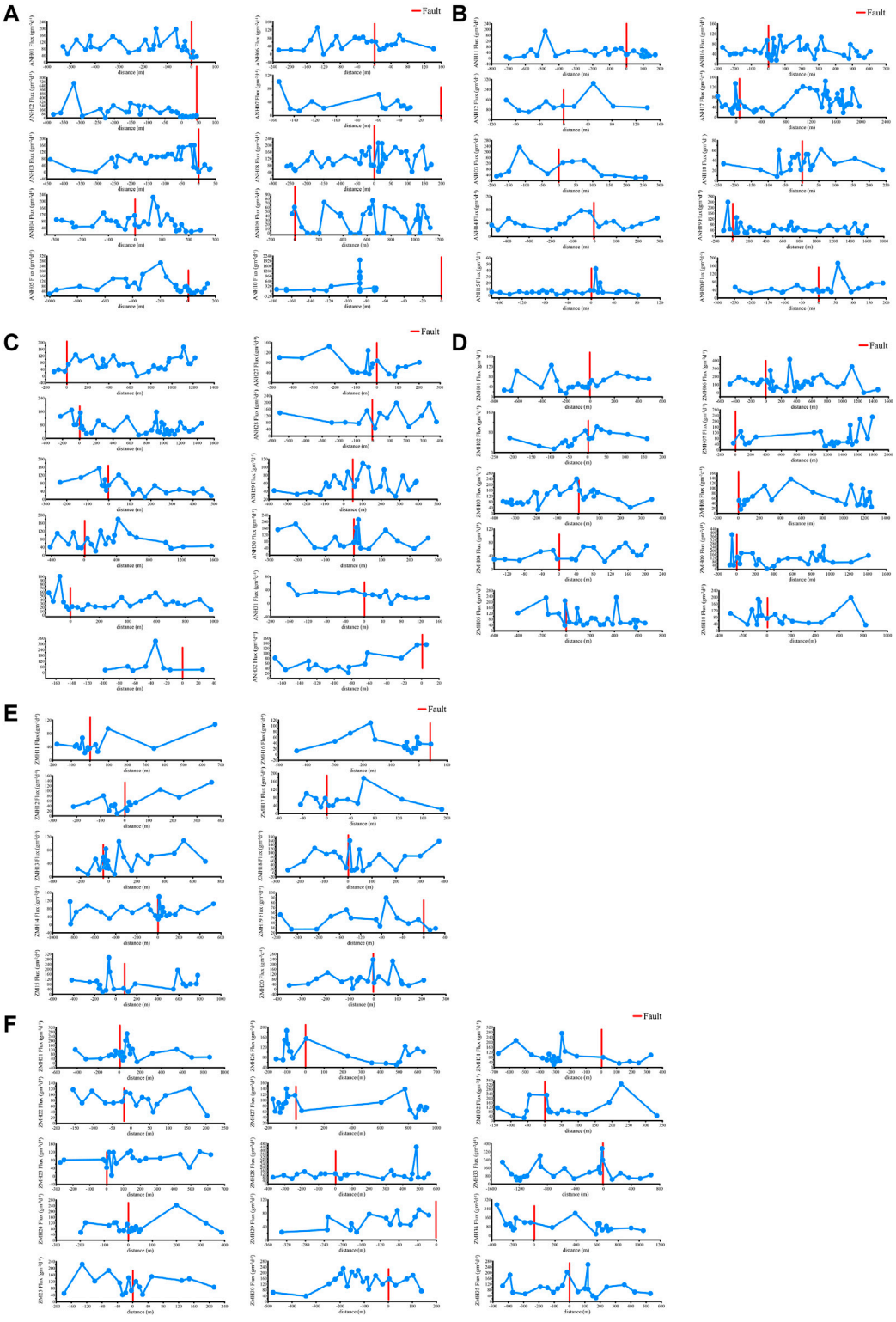

FIGURE 5
Soil gas flux profile. The short red line represents the location of the fault, positive value is the east side of the fault, negative value is the west side of the fault. The order is: **(A)** ANHF 1–10; **(B)** ANHF 11–20; **(C)** ANHF 21–32; **(D)** ZMHF 01–10; **(E)** ZMHF 11–20; **(F)** ZMHF 21–35.

of carbonate rocks (Wycherley et al., 1999). Different types of CO_2 exhibit different carbon isotopic signatures. $\delta^{13}C_{CO2}$ (V-PDB) vs. 1/CO_2 is regarded to be an indicator for gas sources region (Sano and Marty, 1995; Yuce et al., 2017; Chen et al., 2020). The values of end members for $\delta^{13}C_{CO2}$ of mantle and crust are −6.5‰ and 0‰, respectively, while for atmospheric and biogenic end members

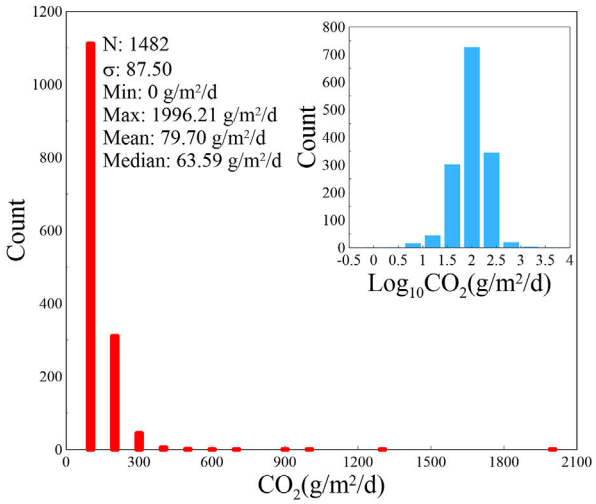

FIGURE 6
Soil gas flux statistics. Statistical histogram of all CO_2 fluxes, showing a normal distribution.

TABLE 1 Values of Soil gas CO_2 carbon isotope.

Name	Line number	Concentration (%)	$\delta^{13}C$-CO_2 (‰)
Soilgas01	ANH15	2.7	−22.3
Soilgas02	ANH20	4.8	−23.9
Soilgas03	ANH26	1.2	−20.8
Soilgas04	ANH27	1.2	−22
Soilgas05	ZMH03	1.7	−25.6
Soilgas06	ZMH06	1.3	−22.8
Soilgas07	ZMH20	0.7	−19.7
Soilgas08	ZMH34	3.1	−25

are −7‰ and −26‰, respectively (Dai, 1995; Sano and Marty, 1995; Dogan et al., 2009).

From Figure 8, it can be seen that the values of $\delta^{13}C_{CO2}$ values of the hot spring gas and soil gas samples are located in the composition mixing range between the mixed end of the crustal mantle and the biological end. The $\delta^{13}C_{CO2}$ values of the soil gas samples are located between the hot spring gas and the end of biological, which indicates that the CO_2 in the surface AZF mainly originates from the biological and the mixed end of the crustal mantle. Compared to the shallow depth of soil air circulation, the circulation of hot spring gas can reach depths of tens of kilometers. The CO_2 in soil gas is closer to the end of biological, which indicates that the oxidation of organic matter during aerobic microbial respiration plays the most important role in the production of CO_2 in soil gas.

Based on the above results, an attempt is made to explain the conceptual model of CO_2 sources and transport in the active fault zone of AZF. Fluids from the crust and mantle that accumulate in the lower crust and upper mantle rise through deep faults with a small amount of crust- and mantle-derived gas diffusing into near-surface soil gas. Although biogenic CO_2 is the primary source of soil gas, crust-derived and mantle-derived CO_2 may be a secondary source. In addition, air can intrude into faulted soil gas due to fluctuations in air pressure (Tamir et al., 2012; Chen et al., 2020).

5.2 Contribution to the atmosphere from CO_2 degassing in the AZHF

Global warming, which has received widespread social attention, is thought to be closely related to the rapid increase in atmospheric CO_2 concentrations over the past 100 years (Joos et al., 1999; solomon et al.,2009; Italiano et al., 2010). However, many scientists currently question the warming caused by increasing atmospheric CO_2 concentrations, and the main debate focuses on what are the main drivers of warming; how accurate predictions of future climate trends based on existing climate models; and what is the magnitude of the impact of climate change (Italiano et al., 2009; Iqbal et al.,2009), all of which are subject to considerable uncertainty. There is a great deal of uncertainty in these issues. Therefore, it is necessary not only to reduce greenhouse gas emissions caused by human activities, but also to study the contribution of natural factors to atmospheric greenhouse gases, so as to distinguish between natural and anthropogenic factors leading to changes in atmospheric greenhouse gas concentrations, and to correctly understand the impact of Earth degassing on the increase of atmospheric greenhouse gas concentrations. In addition, the degassing areas of seismically active fracture zones are also “natural analogue” sites for studying the leakage of CO_2 geological storage, especially the risk of sudden leakage of stored gases to the biosphere (Jing et al., 2019).

The annual contribution of CO_2 degassing from the fault zone to the atmosphere is equal to the amount of the annual average released flux each section of the fault zone multiplied by the area of each section of the fault zone. Based on the AZF and degassing characteristics, the AZF was divided into 5 segments, and the average value of the length and degassing flux of each segment was calculated based on the measurements (Table 3). The width of the fracture zone of the fault is generally tens of meters to hundreds of meters, and the surface avoidance zone of the active fault is more than 50 m (Xu et al., 2002). After the Wenchuan Ms8.0 earthquake, the width of the surface fracture zone of Longmenshan fault is about 200 m (Zhou et al., 2017), Several earthquakes of magnitude 6 or greater have occurred in the history of AZF, with the strongest one occurring north of Xichang with a magnitude of 7.5. The flux data from all sampling points on the AZF were superimposed on a single graph, which could be seen that the outliers with more than double the variance are concentrated within 200 m (Figure 8). High values of soil gas are usually exhibited near the fracture zone (Yuce et al., 2017; Jacome-paz et al., 2020), So the width of AZF was supposed as 200 m in this study.

By calculating the average flux of each survey line of ANHF and ZMHF, the annual contribution of ANHF and ZMHF zone to the atmosphere is 1.2 ±0.4 Mt (Table 3). The total flux of greenhouse gases from typical Cenozoic volcanic areas in Chinese Mainland to the atmosphere is about 8.13 Mt · a^{-1} equivalent to about 6% of the total greenhouse gas emissions caused by global (10^2 ~ 10^3 Mt·y^{-1}) volcanic activities (Guo et al., 2014). The annual emission of AZF is relatively small compared with that of typical volcanoes in China.

TABLE 2 The value of each measurement line on AZF.

Line number	Length of survey lines(m)	Number of measuring points	Mean	Maximum	Minimum
			($gm^{-2}d^{-1}$)	($gm^{-2}d^{-1}$)	($gm^{-2}d^{-1}$)
ANH01	555	28	93.84	201.1	28.83
ANH02	425	29	125.46	688.52	0
ANH03	475	28	74.59	160.54	0
ANH04	539	30	73.68	224.64	18.75
ANH05	1,146	27	79.31	266.41	19.09
ANH06	367	23	54.28	131.93	0
ANH07	125	13	34.75	100.83	13.43
ANH08	428	39	114.6	213.49	43.42
ANH09	1,149	29	32.03	76.18	0
ANH10	106	29	272.22	1996.21	0
ANH11	885	29	37.09	187.28	0
ANH12	235	11	121.74	288.98	60.84
ANH13	441	14	81.89	231.64	19.99
ANH14	756	19	40.46	77.51	20.15
ANH15	255	25	7.23	42.84	0.66
ANH16	878	39	52.05	112.9	14.76
ANH17	2,272	42	62.47	143.65	11.77
ANH18	472	20	35.86	62.45	8.29
ANH19	1,695	32	56.29	239.49	16.9
ANH20	439	21	52.48	173.13	23.6
ANH21	1,339	28	73.23	173.01	0
ANH22	1,677	36	68.98	169.38	20.5
ANH23	718	20	65.25	154.77	12.05
ANH24	1984	21	73.77	179.87	20.61
ANH25	1,130	24	33.5	100.81	13.67
ANH26	123	8	77.34	329.95	22.36
ANH27	663	18	66.63	144.66	26.03
ANH28	928	13	112.51	196.19	45
ANH29	760	23	59.37	109.2	27.75
ANH30	535	18	92.92	212.61	34.27
ANH31	296	14	26.44	57.2	0
ANH32	173	14	66.73	135.01	22.57
ZMH01	1,204	23	53.79	124.74	13.87
ZMH02	367	16	55.42	101.61	14.11
ZMH03	707	27	113.35	241.06	26.62
ZMH04	354	18	46.87	77.92	23.38
ZMH05	1,056	25	88.52	232.36	24.32

(Continued on following page)

TABLE 2 (*Continued*) The value of each measurement line on AZF.

Line number	Length of survey lines(m)	Number of measuring points	Mean	Maximum	Minimum
			($gm^{-2}d^{-1}$)	($gm^{-2}d^{-1}$)	($gm^{-2}d^{-1}$)
ZMH06	1932	35	124.17	414.35	0
ZMH07	1816	24	82.33	229.4	27.45
ZMH08	1,257	22	60.45	136.74	16.11
ZMH09	1,479	26	112.87	378.99	0
ZMH10	1,124	19	87.98	197.56	33.71
ZMH11	844	14	48.32	107.25	22.46
ZMH12	574	16	52.84	133.81	9.98
ZMH13	911	22	46.58	108.37	8.01
ZMH14	1,363	23	69.56	140.15	4.8
ZMH15	1,196	20	92.94	293.41	20.97
ZMH16	478	15	39.38	110.41	6.33
ZMH17	235	13	66.13	176.31	20.68
ZMH18	628	19	68.9	160.53	11.14
ZMH19	295	14	45.51	89.61	25.61
ZMH20	559	20	81.38	236.27	4.78
ZMH21	1,275	27	89.63	264.72	11.11
ZMH22	358	16	82.61	121.76	26.49
ZMH23	894	19	85.71	124.81	4.8
ZMH24	585	20	93.19	244.66	55.09
ZMH25	392	16	109.49	223.55	41.42
ZMH26	787	20	99.74	186.81	50.55
ZMH27	1,093	20	84.78	140.2	39.49
ZMH28	925	24	117.03	442.26	57.96
ZMH29	314	15	55.21	90.2	23.47
ZMH30	616	20	143.79	229.76	37.73
ZMH31	997	22	86.73	271.59	23.28
ZMH32	474	17	111.38	329.66	25.21
ZMH33	2,116	27	114.28	353.48	37.43
ZMH34	1,390	24	92.56	276.18	14.06
ZMH35	965	20	99.29	257.78	24.72

However, there are only 8 active volcanoes in China (Liu., 1999), while there are more than 200 active fault zones in the intraplate area of Chinese Mainland (Deng et al., 2003), among which the Tanlu fault zone, Altun fault zone, Haiyuan fault zone and Xianshuihe fault zone are more than 1000 km long. The total emission of CO_2 from all active fault zones would be huge, which may be higher than that from active volcanoes in China. Only a few of researches were aimed to calculate carbon emissions from faults in the world (Table 4), but it is far from enough. From a public health risk assessment perspective, detailed CO_2 degassing maps should also be performed to evaluate the potential for CO_2 release from fault.

5.3 Diffuse degassing in the ANHF and ZMHF

It is well known that understanding of crustal dynamics and degassing processes can be improved by studying soil gas in fracture zones (Ciotoli et al., 2016). Soil gas CO_2 flux is an important

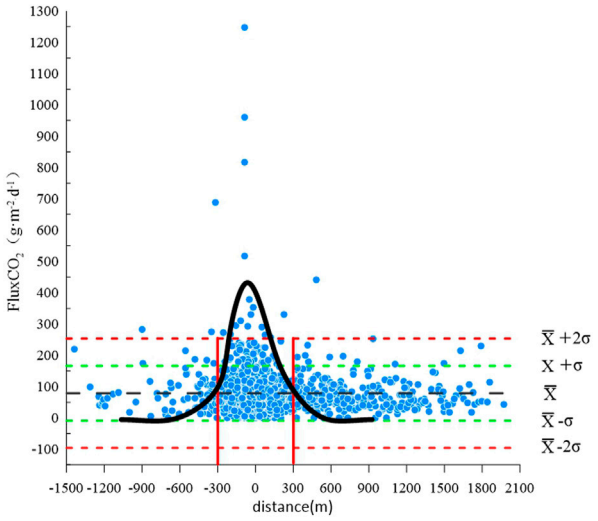

FIGURE 7
CO_2 flux scatter distribution map.

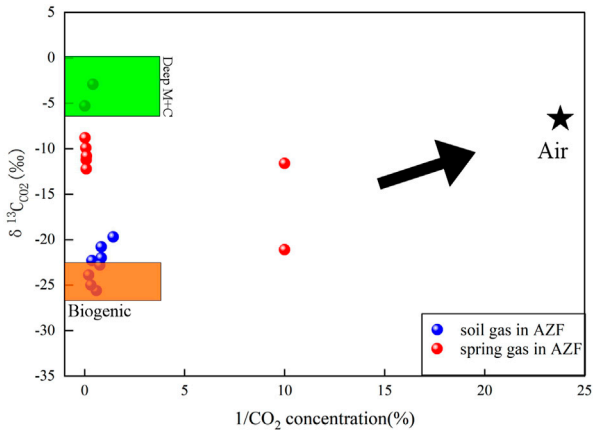

FIGURE 8
Plot showing $\delta^{13}C_{CO2}$ vs.$1/CO_2$ values for gas samples from the soil gas and springs (spring gas data from Tian et al., 2021). Deep (M+C): end-member of mantle and crust sources, biogenic: end-member of biogenic source, Air: end-member of the atmospheric source.

indicator of crustal stress accumulation and fault activity (Irwin and Barnes, 1980; Zhou et al., 2010; Yuce et al., 2017). Changes in tectonic stress leads to expansion or contraction of bedrock, altering the degree of water-rock response and thus affecting CO_2 degassing. The strength of degassing along active faults is related to seismic activity, which can reflect the state of stress accumulation to some extent (Rovira and Vallejo, 2008; Manaker et al.,2008). Hence, there could be some degree of correlation between CO_2 emissions and historical earthquakes and nowadays earthquakes.

According to the location and magnitude of historical strong earthquakes on the fault zone, the seismic gap on the fault zone, and the spatial distribution of current seismic activity, the soil gas flux on the AZF has obvious segmented features (Yu et al., 2014; Yu et al., 2018; Wen, 2000; Zhou et al., 2017; Chen et al., 2019; Walia et al., 2010).

In this paper, our results show that high soil gas CO_2 fluxes are found in the northern section of ANHF, southern section of AMHF and the central section of AZF (Figure 9), which well correlates with the sites that have high seismic activities. Notably, the higher soil gas concentration values in the northern section of the ANHF relative to the southern section of the ANHF, combined with the high flux values at point A (Figure 9), may indicate that the higher degree of fracture fragmentation in the area leads to elevated bedrock permeability, which promotes CO_2 migration from deeper to the surface. B point (Figure 9) is located at the intersection of ANHF and ZMHF. On the one hand, the area has a high stress background value under the interaction of multiple sets of ruptures (Wen, 2000); on the other hand, the study shows that the area is highly occluded and belongs to the seismic gap area for both historical and present-day earthquakes (Deng et al., 2003). Therefore, the fault fragmentation in this area is low, the fracture is not fully developed, and the overall soil gas CO_2 flux values are in the middle. C point (Figure 9) is characterized by the same high seismic activity, but the soil gas CO_2 flux is weaker than point A. This may be due to the "Y" shaped intersection of the ZMHF, Daliangshan fault, and Xiaojiang fault in the southern section, which may not have the tectonic conditions for high stress concentration. Although the frequency of seismic activity is high and the magnitude is large, the stress drop value of the earthquake source is generally in the middle. Therefore, the degree of fault fragmentation in this area is weak, resulting in relatively low bedrock permeability and fewer soil gas CO_2 migration channels.

The higher degree of active fault fragmentation and the increased permeability of bedrock and soil, provide an upward

TABLE 3 CO_2 emissions by segment.

Number	Number of survey lines	Name	length (km)	Size (10^6m^2)	Mean flux ($gm^{-2}d^{-1}$)	emission ($t{\cdot}y^{-1}$)
1	16	ANHF Northern Section	60	12	80.95	354,561
2	16	ANHF Southern Section	65	13	63.99	303,632.6
3	13	ZMHF Northern Section	48	9.6	73.29	256,808.1
4	12	ZMHF Middle Section	26.5	5.3	77.04	149,033.9
5	10	ZMHF Southern Section	22.5	4.5	100.48	165,038.4
Total	67		222	44.4	395.75	1,229,074

TABLE 4 Study on soil gas CO_2 fluxes in fracture zones in the world.

Location	Country	Average CO_2 flux ($gm^{-2}d^{-1}$)	Max CO_2 flux ($gm^{-2}d^{-1}$)	References
ANHF	China	72.47	1996.21	This study
ZMHF	China	82.93	442.26	This study
Dead Sea Fault	Turkey	26.7	55.4	Yuce et al. (2017)
San Andreas Fault	United States	19	631.40	Lee et al. (2016)
Calaveras Fault	United States	56	428	Lee et al. (2016)
Arbia Fault	Italy	78	204.98	Etiope (1999)
Chukuo Fault	China	17	29	Chen et al. (2019)

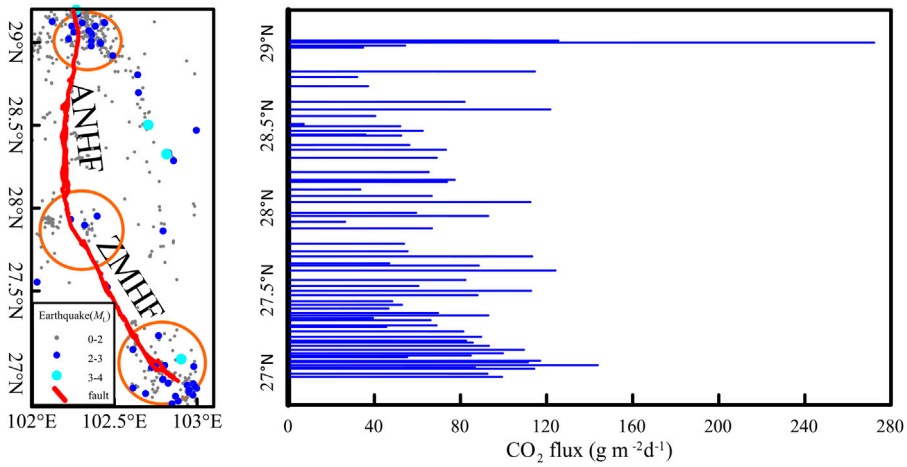

FIGURE 9
Spatial distribution of soil gas CO_2 fluxes and seismicity in AZF.

channel for gas transport (Ciotoli et al., 2016). However, under the action of tectonic stress, the degree of water-rock response varies at different stages of deformation evolution, and the permeability within the fault changes temporally and spatially (Dai et al., 1996; King, 1986; Pei et al., 1998; Neri et al., 2006; Annunziatellis et al., 2008). It is well known that faults can be both an upward pathway for transporting gases and can also block deep gas leaks (Caine et al., 1996; Dai et al., 1996; Sizova et al., 2019). Moreover, fault permeability is subject to self-sealing processes that might limit or inhibit fluid gas motion (Pei et al., 1998). The pore pressure of faulted soils usually depends on the crustal stresses associated with tectonic activity, which promotes the development of fractures and the formation of microfractures, resulting in the migration and redistribution of gases within the pore space (Holub and Brady, 1981; Zhang et al., 2003). CO_2 transport to the surface along well-developed fractures driven by pressure, which explains the higher soil gas CO_2 fluxes are often found near faults.

6 Conceptual model of soil gas in the AZF

The cross-cutting and interaction of fracture zones of different scales on the AZF, with some strongly extruded passages forming blockages, leads to stress concentration, earthquake nucleation and breeding (Shen et al., 2005). The geometric structure and activity habits of different sections of the fault zone is also controlled by the general dynamical background of the east boundary of the Sichuan-Yunnan active block (Chiodini et al., 1998; Toda et al., 2008). This is reflected in the uncoordinated deformation movement of the tectonic units. This incoordination is probably the main reason for the type and size of earthquakes and the local stress distribution pattern. In discussing the seismic activity and stress distribution in this multi-crossing fault zone, it is necessary to consider the characteristics of the cross-faults (Brune et al., 1970; Jiang et al., 2015). The interaction of

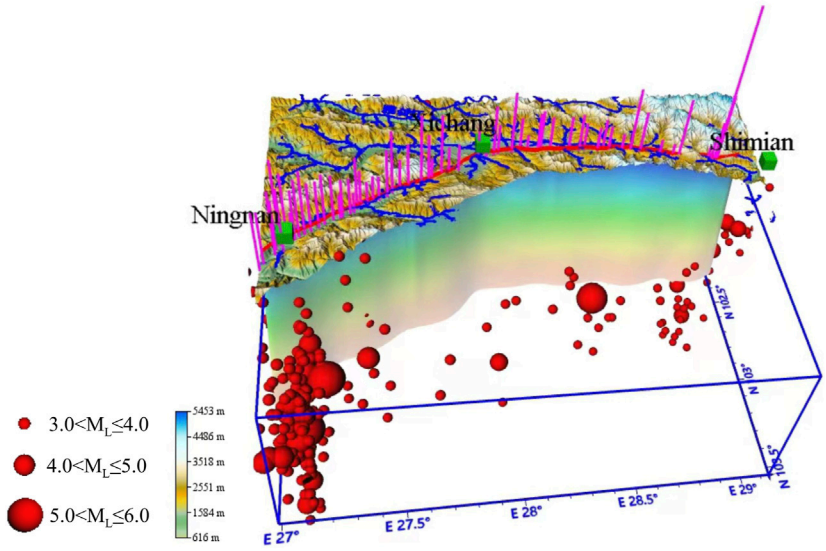

FIGURE 10
Coupling model of soil gas CO_2 flux and seismic activity in AZF.

cross-faults on the local stress field and seismic hazard needs to be considered when discussing the seismic activity and stress distribution characteristics in this multi-cross-fault region.

The northern section of the ANHF meets the Xianshuihe fault and the Daliangshan fault at an acute angle, which has local conditions of high stress concentration, high seismic activity, large magnitude, and high source stress, so the soil gas CO_2 flux is the highest (Figure 10) (Wang et al., 1998; Toda et al., 2008); the ANHF and ZMHF meet at an obtuse angle, which has weak seismic activity and low source stress in general, so the soil gas CO_2 flux is the lowest; the southern section of the AZF, ZMHF meets the Xiaojiang fault and the Daliangshan fault at an obtuse angle, which may not have high source stress (Xu et al., 2022) (Figure 10). The southern section of AZF, ZMHF and Xiaojiang fault and Daliangshan fault meet at an obtuse angle, so they may not have the tectonic condition of high stress concentration, and although the seismic activity is frequent, the source stress is relatively not high (Wu, 2020). Therefore, the overall performance of soil gas CO_2 flux is at medium level.

It has been suggested that degassing features similar to the AZF can be found in worldwide geologic extensional contexts (Apollaro et al., 2012), and spatial variations in CO_2 emissions from deep sources may be attributed to tectonic activity (Irwin and Barnes, 1980). In addition, it has also been demonstrated that areas with enhanced crustal permeability may show precursors of CO_2 degassing activity. Therefore, the geochemical exploration method proposed in this paper for AZF would be applied to other CO_2 degassing areas on Earth (Martinelli and Dadomo, 2017). Meanwhile, tectonic activity in possible future earthquakes can be monitored by implementing soil gas CO_2 flux and concentration measurements on active faults.

7 Conclusion

In this study, geochemical characteristics and causes of the fluids released from the AZF were systematically analyzed, and the seismic activity of various segments of the AZF was discussed. The main conclusions are as follows:

(1) The investigation of carbon isotopic of underground fluid in AZF highlighted that: there are multiple sources of underground fluids in AZF; Soil gas CO_2 was demonstrated to be mainly biogenesis in AZF, while the spring gas is mainly of crustal and mantle origin.
(2) Soil gas CO_2 emissions surveys in this study and previous studies reveal a substantial range of average soil CO_2 fluxes (1996.2 gm^{-2} d^{-1}) for the AZF, which may have close affnities with the influence of regional fault systems and the seismic activity. Total soil CO_2 output of the AZF is about 1.2 Mt a^{-1}, suggesting high CO_2 outgassing flux of the eastern boundary of the Chuan–Dian rhombic block. There are many longer fracture zones than AZF in the worldwide, so more attention should be given to CO_2 emissions from faults.
(3) The variation of CO_2 emissions in the study area is consistent with the strength of regional seismicity, and CO_2 fluxes are also relatively low in areas with weaker tectonic stresses. These results indicate that seismicity and regional stress are the major triggering mechanism for CO_2 emissions from the AZF.

Data availability statement

The original contributions presented in the study are included in the article/Supplementary Material, further inquiries can be directed to the corresponding authors.

Author contributions

XZ, YL, and JD conceived the study. FL performed the literature review with support from YY, JT, JL, MH, OY, and SZ. KL, BY, ZZ, and YW participated in data processing. All authors contributed to interpretation and writing of the manuscript.

Funding

The work was funded by the National Key Research and Development Project (2018YFE0109700 and 2019YFC1509203), Central Public-interest Scientific Institution Basal Research Fund (CEAIEF2022030205, CEAIEF20220213, CEAIEF2022030200, and CEAIEF20220507), and the National Natural Science Foundation of China (41673106, 42073063, 4193000170, and U2039207), IGCP Project 724.

Acknowledgments

Special thanks are addressed to Chang Lu and Zhaofei Liu for the support during the fieldwork.

Conflict of interest

The authors declare that the research was conducted in the absence of any commercial or financial relationships that could be construed as a potential conflict of interest.

Publisher's note

Supplementary material

The Supplementary Material for this article can be found online at: https://www.frontiersin.org/articles/10.3389/feart.2023.1117862/full#supplementary-material

References

Annunziatellis, A., Beaubien, S. E., Bigi, S., Ciotoli, G., Coltella, M., and Lombardi, S. (2008). Gas migration along fault systems and through the vadose zone in the Latera caldera (central Italy): Implications for CO_2 geological storage[J]. *Inter. J. Greenhouse Gas Cont.* 2 (3), 353–372.

Apollaro, C., Dotsika, E., Marini, L., Barca, D., Bloise, A., De Rosa, R., et al. (2012). Chemical and isotopic characterization of the thermo mineral water of Terme Sibarite springs (Northern Calabria, Italy). *Geochem. J.* 46, 117–129. doi:10.2343/geochemj.1.0166

Bekaert, D. V., Turner, S. J., Broadley, M. W., Barnes, J., Halldórsson, S., Labidi, J., et al. (2021). Subduction-driven volatile recycling: A global mass balance. *Annu. Rev. Earth Planet. Sci.* 49, 37–70. doi:10.1146/annurev-earth-071620-055024

Brune, J. N. (1970). Tectonic stress and the spectra of seismic shear waves from earthquakes[J]. *J. Geophys. Res.* 75 (6), 4997–5009.

Camarda, M., De Gregorio, S., Di Martino, R. M. R., and Favara, R. (2016). Temporal and spatial correlations between soil CO_2 flux and crustal stress[J]. *J. Geophys. Res. Solid Earth* 121 (10), 7071–7085. doi:10.1002/2016jb013297

Caine, J. S, Evans, J. P., and Forster, C. B. (1996). Fault zone architecture and permeability structure[J]. *Geology* 24(11), 1025–1028.

Chen, Z., Li, Y., Liu, Z., Zheng, G., Xu, W., Yan, W., et al. (2019). CH_4 and CO_2 emissions from mud volcanoes on the southern margin of the Junggar basin, NW China: Origin, output, and relation to regional tectonics[J]. *J. Geophys. Res. Solid Earth* 124 (5), 5030–5044. doi:10.1029/2018jb016822

Chen, Z., Li, Y., Martinelli, G., Liu, Z., Lu, C., and Zhao, Y. (2020). Spatial and temporal variations of CO_2 emissions from the active fault zones in the capital area of China[J]. *Appl. Geochem.* 112, 104489. doi:10.1016/j.apgeochem.2019.104489

Chiodini, G., Cioni, R., Guidi, M., Raco, B., and Marini, L. (1998). Soil CO_2 flux measurements in volcanic and geothermal areas[J]. *Appl. Geochem.* 13 (5), 543–552. doi:10.1016/s0883-2927(97)00076-0

Ciotoli, G., Sciarra, A., Ruggiero, L., Annunziatellis, A., and Bigi, S. (2016). Soil gas geochemical behaviour across buried and exposed faults during the 24 August 2016 central Italy earthquake. *Ann. Geophys.* 59 (5), 1. doi:10.4401/ag-7242

Dai, J., Song, Y., Dai, C., Yan, S., Chun-sen, D., Da-rui, W., et al. (1996). Geochemistry and accumulation of carbon dioxide gases in China[J]. *AAPG Bull.* 80 (10), 1615–1625. doi:10.1306/64EDA0D2-1724-11D7-8645000102C1865D

Dai, J. X. (1995). Abiogenic gas in oil-gas bearing basins in China and its reservoirs. *Nat. Gas. Ind.* 15 (3), 22–27.

Deng, Q., Zhang, P., Ran, Y., Xiaoping, Y., Weie, M., Quanzhi, C., et al. (2003). Basic characteristics of active tectonics of China[J]. *Sci. China Ser. D Earth Sci.* 46 (4), 356–372. doi:10.1360/03yd9032

Doğan, T., Sumino, H., Nagao, K., Notsu, K., Tuncer, M. K., and Çelik, C. (2009). Adjacent releases of mantle helium and soil CO_2 from active faults: Observations from the Marmara region of the North Anatolian Fault zone, Turkey[J]. *Geochem. Geophys. Geosystems* 10 (11). doi:10.1029/2009gc002745

Etiope, G., Beneduce, P., Calcara, M., Favali, P., Frugoni, F., Schiattarella, M., et al. (1999). Structural pattern and CO_2–CH_4 degassing of Ustica Island, Southern Tyrrhenian basin[J]. *J. Volcanol. Geotherm. Res.* 88 (4), 291–304. doi:10.1016/s0377-0273(99)00010-4

Fischer, T. P., and Aiuppa, A. (2020). AGU centennial grand challenge: volcanoes and deep carbon global CO_2 emissions from subaerial volcanism—recent progress and future challenges[J]. *Geochem. Geophys. Geosystems* 21 (3), e2019GC008690. doi:10.1029/2019GC008690

Fischer, T. P., Arellano, S., and Carn, S. (2019). The emissions of CO_2 and other volatiles from the world's subaerial volcanoes[J]. *Sci. Rep.* 9 (1), 1–11.

Fu, C. C., Yang, T. F., Du, J., Walia, V., Chen, Y. G., Liu, T. K., et al. (2008). Variations of helium and radon concentrations in soil gases from an active fault zone in southern Taiwan. *Radiat. Meas.* 43, S348–S352. doi:10.1016/j.radmeas.2008.03.035

Guo, Z., Zhang, M., Cheng, Z., Zhang, L., and Liu, J. (2014). Fluxes and Genesis of greenhouse gases emissions from typical volcanic fields in China. *Acta Petrol. Sin.* 30 (11), 346–3480. (in Chinese).

He, H., and Oguchi, T. (2008). Late Quaternary activity of the Zemuhe and Xiaojiang faults in southwest China from geomorphological mapping. *Geomorphology* 96 (1-2), 62–85. doi:10.1016/j.geomorph.2007.07.009

Hiett, C. D., Newell, D. L., Jessup, M. J., Grambling, T. A., Scott, B. E., and Upin, H. E. (2022). Deep CO_2 and N_2 emissions from Peruvian hot springs: Stable isotopic constraints on volatile cycling in a flat-slab subduction zone[J]. *Chem. Geol.* 595, 120787. doi:10.1016/j.chemgeo.2022.120787

Holub, R. F., and Brady, B. T. (1981). The effect of stress on radon emanation from rock. *J. Geophys. Res.* 86, 1776–1784. doi:10.1029/jb086ib03p01776

Huo, C., Hameed, J., Sharif, A., Ohoud, A., Nouf, A., Noor ul-ain, B., et al. (2022). Recent scenario and nexus of globalization to CO2 emissions: Evidence from wavelet and Quantile on Quantile Regression approach. *Environ. Res.*, 113067. doi:10.1016/j.envres.2022.113067

Inguaggiato, S., Mazot, A., Diliberto, I. S., Inguaggiato, C., Madonia, P., Rouwet, D., et al. (2012). Total CO_2 output from Vulcano island (Aeolian Islands, Italy)[J]. *Geochem. Geophys. Geosystems* 13 (2). doi:10.1029/2011gc003920

Iqbal, J., Lin, S., Hu, R., and Feng, M. (2009). Temporal variability of soil-atmospheric CO_2 and CH_4 fluxes from different land uses in mid-subtropical China[J]. *Atmosph. Environ.* 43(37), 5865–5875.

Irwin, W. P., and Barnes, I. (1980). Tectonic relations of carbon dioxide discharges and earthquakes. *J. Geophys. Res.* 85, 3115–3121. doi:10.1029/JB085iB06p03115

Isson, T. T., Planavsky, N. J., Coogan, L. A., et al. (2020). Evolution of the global carbon cycle and climate regulation on Earth[J]. *Glob. Biogeochem. Cycles* 34 (2), 1–28. doi:10.1029/2018GB006061

Italiano, F., Bonfanti, P., Ditta, M., Petrini, R., and Slejko, F., Helium and carbon isotopes in the dissolved gases of Friuli Region (NE Italy): Geochemical evidence of CO_2 production and degassing over a seismically active area, *Chem. Geol.*,266,Issues 76–85, 2009, Pages 76–85. ISSN 0009-2541, doi:10.1016/j.chemgeo.2009.05.022

Italiano, F., Bonfanti, P., Pizzino, L., and Quattrocchi, F. (2010). Geochemistry of fluids discharged over the seismic area of the Southern Apennines (Calabria region, Southern Italy): Implications for Fluid-Fault relationshipsfluids discharged over the seismic area of the southern apennines (Calabria region,southern Italy): Implications for fluid-fault relationships. *Appl. Geochem.* 25, 540–554. doi:10.1016/j.apgeochem.2010.01.011

Jacome-Paz, M. P., Gonzalez-Romo, I. A., Prol-Ledesma, R. M., Torres Vera, M., Pérez-Zárate, D., Rodríguez-Díaz, A., et al. (2020). Multivariate analysis of CO_2, H_2S and CH_4 diffuse degassing and correlation with fault systems in Agua Caliente-Tzitzio, Michoacan, Mexico[J]. *J. Volcanol. Geotherm. Res.* 394, 106808. doi:10.1016/j.jvolgeores.2020.106808

Jiang, G. Y., Xu, X. W., Chen, Y. H., Liu, Y. J., Fukahata, Y., Wang, H., et al. (2015). Geodetic imaging of potential seismogenic asperities on the Xianshuihe-Anninghe-Zemuhe fault system, southwest China, with a new 3-D viscoelastic interseismic coupling model. *J. Geophys. Res.* 120, 1855–1873. doi:10.1002/2014JB011492

Jing, J., Tang, Z., Yang, Y., and Ma, L. (2019). Impact of formation slope and fault on CO_2 storage efficiency and containment at the Shenhua CO2 geological storage site in the Ordos Basin, China[J]. *Int. J. Greenh. Gas Control* 88, 209–225. doi:10.1016/j.ijggc.2019.06.013

Jolie, E., Moeck, I., and Faulds, J. E. (2015). Quantitative structural–geological exploration of fault-controlled geothermal systems—A case study from the Basin-and-Range Province, Nevada (USA). *Geothermics* 54, 54–67. doi:10.1016/j.geothermics.2014.10.003

Joos, F., Plattner, G. K., Stocker, T. F., Marchal, O., and Schmittner, A. (1999). Global warming and marine carbon cycle feedbacks on future atmospheric CO_2[J]. *Sci.* 284 (5413), 464–467.

Kämpf, H., Bräuer, K., Schumann, J., Hahne, K., and Strauch, G. (2013). CO_2 discharge in an active, non-volcanic continental rift area (Czech Republic): characterisation (δ13C, 3He/4He) and quantification of diffuse and vent CO_2 emissions[J]. *Chem. Geol.* 339, 71–83. doi:10.1016/j.chemgeo.2012.08.005

Kang, Y. J., Yun, S. T., Yu, S., Do, H. K., and Chae, G. (2020). Quantitative assessment of deep-seated CO_2 leakage around CO_2-rich springs with low soil CO_2 efflux using end-member mixing analysis and carbon isotopes[J]. *J. Environ. Manag.* 276, 111333. doi:10.1016/j.jenvman.2020.111333

Kennedy, B. M., Kharaka, Y. K., Evans, W. C., Ellwood, A., DePaolo, D. J., Thordsen, J., et al. (1997). Mantle Fluids in the San Andreas Fault System, California. *Science* 278 (5341), 1278–1281. doi:10.1126/science.278.5341.1278

King, C. Y. (1986). Gas geochemistry applied to earthquake prediction: An overview [J]. *J. Geophys. Research: Solid Earth* 91 (B12), 12269–12281. doi:10.1038/ngeo2622

Lee, H., Muirhead, J. D., Fischer, T. P., Ebinger, C. J., Kattenhorn, S. A., Sharp, Z. D., et al. (2016). Massive and prolonged deep carbon emissions associated with continental rifting. *Nat. Geosci.* 9 (2), 145–149. doi:10.1038/ngeo2622

Li, Y. C., Shan, X. J., Qu, C. Y., Zhang, Y. F., Song, X. G., Jiang, Y., et al. (2017). Elastic block and strain modeling of GPS data around the Haiyuan-Liupanshan fault, northeastern Tibetan Plateau. *J. Asian Earth Sci.* 150, 87–97. doi:10.1016/j.jseaes.2017.10.010

Liu, J. (1999). Volcanoes hazards and montoring[J]. *Quadrangular Res.* (05), 414–422. (in Chinese abstract).

Manaker, D. M., Calais, E., Freed, A. M., Ali, S. T., Przybylski, P., Mattioli, G., et al. (2008). Interseismic plate coupling and strain partitioning in the northeastern Caribbean[J]. *Chem. Geol.* 469, 176–184. doi:10.1016/j.chemgeo.2017.01.006

Martinelli, G., and Dadomo, A. (2017). Factors constraining the geographic distribution of earthquake geochemical and fluid-related precursors. *Chem. Geol.* 469, 176–184. doi:10.1016/j.chemgeo.2017.01.006

Muirhead, J. D., Fischer, T. P., Oliva, S. J., Laizer, A., van Wijk, J., Currie, C. A., et al. (2020). Displaced cratonic mantle concentrates deep carbon during continental rifting. *Nature* 582 (7810), 67–72. doi:10.1038/s41586-020-2328-3

Neri, G., Barberi, G., Oliva, G., Orecchio, B., and Presti, D. (2006). A Possible Seismic Gap within a Highly Seismogenic Belt Crossing Calabria and Eastern Sicily, Italy. *Italy. Bull. Seismol. Soc. Am.* 96, 1321–1331. doi:10.1785/0120050170

Pei, X. Y., Wang, X. M., and Zhang, C. G. (1998). Basic character of segmentation of the Quaternary movement on the Anninghe fault[J]. *Earthq. Res. Sichuan* 4, 52–61.

Rahilly, K. E., and Fischer, T. P. (2021). Total diffuse CO_2 flux from Yellowstone caldera incorporating high CO_2 emissions from cold degassing sites[J]. *J. Volcanol. Geotherm. Res.* 419, 107383. doi:10.1016/j.jvolgeores.2021.107383

Ran, Y. K., Cheng, J. W., Gong, H. L., and Chen, L. (2008). Late Quaternary geomorphic deformation and displacement rates of the Anninghe fault around Zimakua[J]. *Seismology and Geology* 30 (1), 86–98.

Ren, Z., and Lin, A. (2010). Deformation characteristics of co-seismic surface ruptures produced by the 1850 M 7.5 Xichang earthquake on the eastern margin of the Tibetan Plateau. *J. Asian Earth Sci.* 38 (1-2), 1–13. doi:10.1016/j.jseaes.2009.12.008

Rovira, P., and Vallejo, V. (2008). Changes in δ13C composition of soil carbonates driven by organic matter decomposition in a Mediterranean climate: a field incubation experiment. *Geoderma* 144 (3), 517–534. doi:10.1016/j.geoderma.2008.01.006

Sano, Y., and Marty, B. (1995). Origin of carbon in fumarolic gas from island arcs. *Chem. Geol.* 119 (1–4), 265–274. doi:10.1016/0009-2541(94)00097-r

Shen, Z. K., Lü, J., Wang, M., and Bürgmann, R. (2005). Contemporary crustal deformation around the southeast borderland of the Tibetan Plateau. *J. Geophys. Res. Solid Earth* 110. doi:10.1029/2004JB003421

Sizova, E., Hauzenberger, C., Fritz, H., Faryad, S. W., and Gerya, T. (2019). Late orogenic heating of (ultra)high pressure rocks: Slab rollback vs. slab breakoff. *Geosciences* 9, 499. doi:10.3390/geosciences9120499

Solomon, S., Plattner, G. K., Knutti, R., and Friedlingstein, P. (2009). Irreversible climate change due to carbon dioxide emissions[J]. *Proc. Natl. Acad. Sci.* 106 (6), 1704–1709.

Tamir, G., Shenker, M., Heller, H., Bloom, P. R., Fine, P., and Bartal, A. (2012). Dissolution and recrystallization processes of active calcium carbonate in soil developed on tufa. *Soil. Sci. Soc. Am. J.* 76 (5), 1606–1613. doi:10.2136/sssaj2012.0041

Toda, S., Lin, J., Meghraoui, M., and Stein, R. S. (2008). May 2008 M = 7.9 Wenchuan, China, earthquake calculated to increase failure stress and seismicity rate on three major fault systems[J]. *Geophy. Res. Let.* 35 (17).

Viveiros, F., Marcos, M., Faria, C., João, L. G., Catarina, S., Teresa, F., et al. (2017). Soil CO_2 degassing path along volcano-tectonic structures in the Pico-Faial-São Jorge islands (Azores archipelago, Portugal)[J]. *Front. Earth Sci.* 5, 50. doi:10.3389/feart.2017.00050

Walia, V., Lin, J., Fu, C., Yang, F., Hong, W., Wen, L., et al. 2010. Soil-gas monitoring: a tool for fault delineation studies along Hsinhua Fault (Tainan),Southern Taiwan. *Appl. Geochem.* 25 (4), 602–607. doi:10.1016/j.apgeochem.2010.01.017

Wang, Q. L., Wang, W. P., Liang, W. F., and Chen, B. (1998). Stress-dissipative heat geotemperature precursor mechanism of earthquakes[J]. *Acta Seismologica Sinica* 11, 615–621.

Weinlich, F. H., Faber, E., Boušková, A., Horálek, J., Teschner, M., and Poggenburg, J. (2006). Seismically induced variations in Mariánské Lázně fault gas composition in the NW Bohemian swarm quake region, Czech Republic — A continuous gas monitoring. *Tectonophysics* 421 (1-2), 89–110. doi:10.1016/j.tecto.2006.04.012

Wen, X. Z. (2000). Character of rupture segmentation of the Xianshuihe-Anninghe-Zemuhe fault zone, Western Sichuan. *Seismol. Geol.* 22 (3), 239–249. doi:10.3969/j.issn.0253-4967.2000.03.005

Wycherley, H., Fleet, A., and Shaw, H. (1999). Some observations on the origins of large volumes of carbon dioxide accumulations in sedimentary basins. *Mar. Petroleum Geol.* 16 (6), 489–494. doi:10.1016/s0264-8172(99)00047-1

Xu, S., Guan, L., Zhang, M., Zhong, J., Liu, W., Xie, X., et al. (2022). Degassing of deep-sourced CO_2 from Xianshuihe-Anninghe fault zones in the eastern Tibetan Plateau[J]. *Sci. China Earth Sci.* 65 (1), 139–155. doi:10.1007/s11430-021-9810-x

Xu, X., Yu, G., Ma, W., Yongkang, R., You, H.-C., Zhang, L.-F., et al. (2002). Evidence and methods for determining the safety distance from the potential earthquake surface rupture on active fault[J]. *Seismol. EGOLOGY* 24 (4), 470.

Yang, Y., Li, Y., Guan, Z., Chen, Z., Zhang, L., Lv, C. J., et al. (2018). Correlations between the radon concentrations in soil gas and the activity of the Anninghe and the Zemuhe faults in Sichuan, southwestern of China. *Appl. Geochem.* 89, 23–33. doi:10.1016/j.apgeochem.2017.11.006

Yu, X., Yang, C., Dong, G., and Zhan, D. (2014). Drilling and completion technology in the first geothermal well construction in Jixian system in Tangshan. *Explor. Eng. Media* 41 (2), 41–44.

Yuce, G., Fu, C., D'Alessandro, W., Gulbay, A., Walia, V., Bellomo, S., et al. (2017). Geochemical characteristics of soil radon and carbon dioxide within the Dead Sea fault and Karasu fault in the Amik basin (Hatay), Turkey. *Chem. Geol.* 469, 129–146. doi:10.1016/j.chemgeo.2017.01.003

Zhang, M., Xu, S., Zhou, X., Caracausi, A., Sano, Y., Guo, Z., et al. (2021). Deciphering a mantle degassing transect related with India-Asia continental convergence from the perspective of volatile origin and outgassing. *Geochimica Cosmochimica Acta* 310, 61–78. doi:10.1016/j.gca.2021.07.010

Zhang, P., Deng, Q., and Zhang, G. (2003). Active tectonic blocks and strong earthquakes in the continent of China. *Sci. China Ser. D Earth Sci.* 46 (2), 13–24. doi:10.1360/03dz0002

Zhou, X., Sun, F., and Chen, Z. (2017). Degassing of CO2, CH4, Rn and Hg in the rupture zones produced by Wenchuan Ms 8.0 earthquake. *Acta Petrol. Sin.* 33 (1), 291–303. (in Chinese with English abstract). Web of Science Id WOS: 000393257900023 .

Zhou, X. C., Du, J. G., Chen, Z., Cheng, J. W., Tang, Y., Yang, L. M., et al. (2010). Geochemistry of soil gas in the seismic fault zone produced by the Wenchuan *Ms* 8.0 earthquake, southwestern China. *Geochem. Trans.* 11, 5. doi:10.1186/1467-4866-11-5

Zhou, X., Chen, Z., and Cui, Y. (2016). Environmental impact of CO2, Rn, Hg degassing from the rupture zones produced by Wenchuan Ms 8.0 earthquake in Western Sichuan,China. *Environ. Geochem. Health* 38 (5), 1067–1082. doi:10.1007/s10653-015-9773-1

frontiers | Frontiers in Earth Science

TYPE Original Research
PUBLISHED 24 May 2023
DOI 10.3389/feart.2023.1174315

OPEN ACCESS

EDITED BY
Maoliang Zhang,
Tianjin University, China

REVIEWED BY
Wenbin Zhao,
Chinese Academy of Sciences, China
Zhi Chen,
China Earthquake Administration, China

*CORRESPONDENCE
Guohui Gu,
15943085753@163.com

RECEIVED 26 February 2023
ACCEPTED 10 May 2023
PUBLISHED 24 May 2023

CITATION
Pan X, Gu G, Han D, Bao B, Guan S and Song Y (2023), Investigation of hot spring gas components and soil gas fluxes in Arxan Holocene volcanic field, Inner Mongolia, NE China.
Front. Earth Sci. 11:1174315.
doi: 10.3389/feart.2023.1174315

Investigation of hot spring gas components and soil gas fluxes in Arxan Holocene volcanic field, Inner Mongolia, NE China

Xiaodong Pan[1,2], Guohui Gu[1,2]*, Di Han[1,2], Baoxiao Bao[3], Sheng Guan[1,2] and Yujia Song[1,2]

[1]Jilin Earthquake Agency, Jilin Changbaishan Volcano National Observation and Research Station, Changchun, China, [2]Institute of Volcanology, China Earthquake Administration, Changchun, China, [3]Ulanhot Earthquake Monitoring Center Station, Ulanhot, China

The latest research results show that there is a unified magma system and heating channel beneath the Arxan volcanic field, indicating a potential risk of eruption. The Arxan volcanic field features multiple gas emission sites (e.g., Jinjianggou hot springs and Yinjianggou hot springs) and exhibits strong hydrothermal activity. In this study, measurements of the hot spring gas composition and soil CO_2 flux in the Arxan Holocene volcanic field were conducted, and the results were combined with previous research results to analyze the degassing characteristics of this region. The results show that the volcanic gases in the Arxan volcanic field are composed of 0.07%–1.09% CO_2, 0.33–12 ppm CH_4, 1.57–53 ppm H_2, 800–30,241 ppm He, and 1.14%–1.86% Ar. The He content in this area is notably higher than that in other dormant volcanoes in China. This difference is possibly caused by U–Th decay in the Mesozoic granodiorite and acidic volcanic rocks in the study area, which can produce substantial radiogenic He. The soil gas concentrations near the Jinjianggou and Yinjianggou hot springs are higher than those of two Holocene volcanoes. The peak CO_2 concentration in the soil near the Jinjianggou hot spring can reach 35,161 ppm. The single-site soil microseepage CO_2 flux in the Arxan volcanic field is 4.66–107.18 g m^{-2} d^{-1}, and the estimated annual CO_2 emission flux from the volcanic field to the atmosphere is 0.63 × 10^5 t, which also demonstrates that soil CO_2 flux of Arxan volcano is comparable to the soil CO_2 emission level of the Iwojima volcano.

KEYWORDS

dormant volcano monitoring, volcanic gas emissions, soil gas fluxes, hot spring gas components, Arxan volcanic field

1 Introduction

Due to the existence of underground high-temperature magma chambers in active volcanic fields, a variety of geothermal fluids quickly escape to the surface along volcanic channels or faults, where they are emitted through hot springs, vents and soils. During the volcanic eruption intervals, large amounts of volcanic gases are emitted to the atmosphere because of the continuous heating of the country rock caused by the high-temperature chambers (Guo et al., 2015; Aiuppa et al., 2015; Tassi et al., 2016; Liu et al., 2021). It has been demonstrated that 14 volcanoes in mainland China erupted during the Holocene (wei et al., 1998; Wei et al., 2003; Pan et al., 2021) and are currently in a dormant state. Among the current dormant volcanoes in China, the Changbaishan, Tengchong, and Wudalianchi

volcanoes have been investigated by numerous studies to determine their fluid backgrounds (Du et al., 1999; Shangguan et al., 2008; Zhang et al., 2011; 2015 ; 2016 ; 2018 ; Liu et al., 2011; Guo et al., 2015; Li, 2015; Zhao, 2012; Wei et al., 2021; Zhao et al., 2019). Some studies on the geothermal fluids in the Arxan volcano have been conducted, but studies focusing on the volcanic greenhouse gas emissions in this area are scarce. Therefore, to ascertain the components and emission levels of hot spring gases, this study investigates the CO_2 emissions in the Arxan volcanic field and analyzes the emission characteristics of greenhouse gases in dormant volcanoes. This study provides significant information for deep magmatism investigations and volcano monitoring in the future.

A vast majority of previous investigations on the Arxan volcano focus on the volcanic geology, geophysical exploration, and geothermal heat in the peripheral area of the volcanic field (Liu, 1987; Bai et al., 2005; Tang, 2005; Zhao and Fan, 2010; Han et al., 2018; Gu, 2018; Cui et al., 2022; Li et al., 2023). The latest research illustrates that the Arxan volcanic cluster consists of 46 volcanoes ranging from Pliocene to Holocene in age, including four active volcanoes that have erupted during the Holocene, namely, the Gaoshan volcanoes, Yanshan volcanoes, Shihaogou basin volcanoes, and Xiaodonggou volcanoes. Among them, Gaoshan and Yanshan volcanoes are considered to be active volcanoes that erupted approximately 2,000 years ago (Bai et al., 2005). In recent years, some magnetotelluric sounding observations have shown that the region 10–12 km below the active volcanoes retains a high thermal state, and a mantle upwelling channel conducting heat may exist in the region at a depth of 30–50 km (Tang et al., 2005). Han et al. (2018) reports that the Arxan magma system is uniformly composed of arch bridge-shaped magma transportation channels and basaltic magma from the asthenosphere. In addition, two high-conductivity anomalies have been discovered, with burial depths from 40 to 90 km. Recent studies on fluid geochemistry in Arxan show that the excess N_2, Ar, He and CO_2 in hot springs are mainly from the crust and upper mantle, and approximately 3%–23% of the He in crater lake water and bubble gas in hot springs comes from the mantle (Cui et al., 2022).

The purpose of this study is to analyze the degassing characteristics and emission mechanisms of greenhouse gases in the Arxan volcano through the investigation of the relevant gas components, the concentrations of volcanic gas, and the emissions of soil gases. Moreover, this study aims to explore the emission characteristics of volcanic greenhouse gases during the dormant period and compare the results to those of other dormant volcanoes.

2 Geological setting

The Arxan volcanic cluster is located in the eastern section of the China–Mongolia border. The geographical coordinates are 120°14′–121°20′E, 47°15′–47°45′N. The volcanoes in this cluster

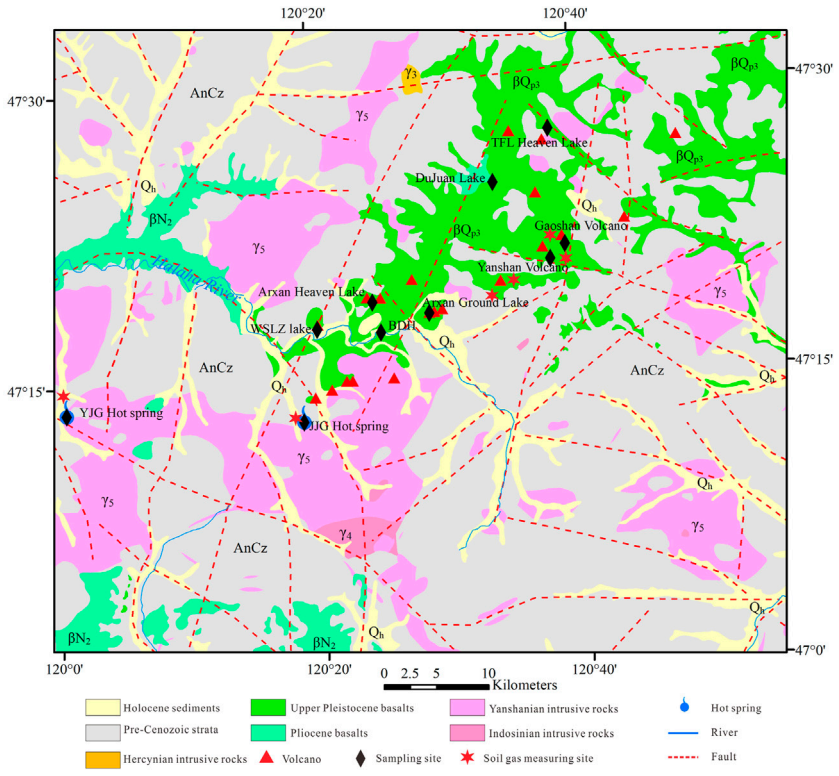

FIGURE 1
Geological map and sampling site locations in the Arxan active volcanic field (modified from 1:250000 geological structure map of Chaihe sheet).

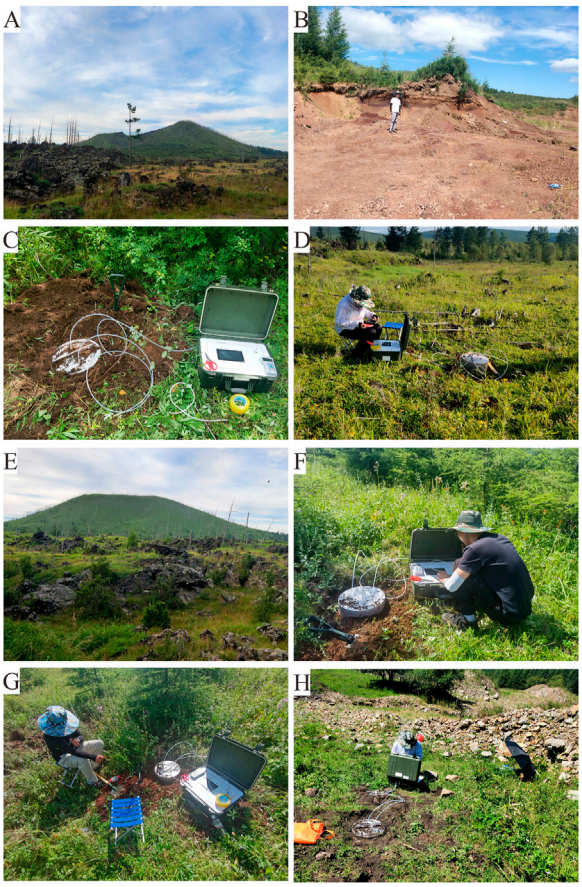

FIGURE 2
Soil gas observation in the field [**(A)** Gaoshan volcanic landscape; **(B)** Gaoshan volcanic pyroclastic flow; **(C)** Gaoshan volcanic cone measurement site; **(D)** Gaoshan volcanic periphery measurement site; **(E)** Yanshan volcanic landscape; **(F)** Yanshan volcanic cone measurement site; **(G)** Yanshan volcanic periphery measurement site; **(H)** Jinjianggou hot spring measurement site].

are distributed in the upper reaches of the Halaha River in the southwest of the Greater Khingan Mountains situated in the back-arc region of the subducting western Pacific plate. Since the early Jurassic, affected by the subduction of the Pacific plate and the blocking of the Eurasian plate, a series of NE-oriented faults and volcanic rock belts with different scales have developed. Since the start of the Cenozoic, extensive basaltic magma has violently erupted (Liu, 1987; Liu et al., 2001; Pan et al., 2021). The volcanism in this region is multi-episodic and can be divided into the Pliocene, Pleistocene and Holocene eruption stages. The volcanic products overlie the Jurassic volcanic–intrusive rocks, with an overall NE trending distribution and an exposed area of approximately 1,300 km^2. The Pliocene series is composed of tholeiite, and the Quaternary rocks are mainly alkaline olivine basalt.

Faults with different directions are developed in the study area (Figure 1). The NE trending Halaha River fault cuts the lithosphere and has a length of approximately 500 km. Furthermore, it provides two channels transporting Quaternary magma from the mantle: one features a high-temperature and fluid-rich mass at a depth of 10–12 km, and the other features a low-temperature mass at a depth of 30 km (Tang et al., 2005). According to previous research (Cui et al., 2022), the hot springs exhibiting fluid derived from a deep mantle source include the Jinjianggou hot spring, Yinjianggou hot spring, Budonghe River, and the two volcanoes active in the Holocene.

3 Sampling and analytical techniques

The hot spring gas samples were collected by the drainage method. At the beginning of our research, the gas-collecting hood was placed in a bubble-free area of hot spring water, and water was filled into a 100 ml syringe to discharge the air inside. Then, the funnel was moved underwater to the bubbling area, and the water in the gas path was drained by the pressure of the hot spring gas itself and the syringe. The collected hot spring gases were subsequently injected into a vacuumized aluminum foil gas sample bag and an inverted water-sealed glass bottle. The gas components were analyzed using a gas chromatograph in the Key Laboratory of Earthquake Prediction, Institute of Earthquake Forecasting, China Earthquake Administration. A total of 11 gas samples were collected from the Jinjianggou hot spring(JJG), Yinjianggou hot spring(YJG), Budonghe river(BDH) and Arxan Tianchi Lake(TC). The locations of the sampling sites are shown in Figure 1.

Soil gas observation in the volcanic field was conducted using an EDK6900-X-type portable greenhouse gas analyzer, which can measure the concentrations of CO_2 and CH_4 with a range of 0–100,000 ppm and a measurement accuracy of less than ±1%. The instrument completes an air inflow observation every 3 min. Before the measurements, a pit with a depth of approximately 50 cm and a diameter of approximately 40 cm was dug in the surface soil layer. Then, the aluminum gas collector with a diameter of 35 cm and a height of 50 cm was buried in the pit, and the soil was backfilled to seal the gas collector (Figure 2). Then, the air inlet of the instrument was connected with the air inlet and outlet of the gas collecting hood, forming a closed loop. The instrument software can display the test results in real-time. After the real-time test data stabilized, the soil gas at this site was considered to have reached equilibrium. This study observed the soil gas of Gaoshan volcano, Yanshan volcano, and the Jinjianggou and Yinjianggou hot springs. The sample collection and field observations were conducted in August 2022.

The field work of this study mainly includes soil CO_2 and CH_4 gas observations (measured with a EDK6900-X portable greenhouse gas analyzer) in Gaoshan volcano, Yanshan volcano, and the Jinjianggou and Yinjianggou hot springs in the Arxan volcanic field. CO_2 is one of the primary components of volcanic gases, and the results are easy to compare with those of other volcanoes. The field work of this study was carried out during sunny days in July and August. During the observations, the atmospheric temperature was approximately 29°C, the atmospheric pressure was approximately 88 kPa, and the soil moisture content was 5%. For the soil gas observations in the hot spring areas, we selected regions with loose soil and soil thicknesses greater than 80 cm. For the volcanic soil gas observations, the volcanic cone and the pyroclastic-covered peripheral area were selected. This field work

TABLE 1 Gas compositions of the Arxan volcanic field.

Location	T	Sampling date	N_2	O_2	Ar	CO_2	N*	Ar*	CH_4	H_2	He	$^3He/^4He$	$^3He/^4He^*$	$\delta^{13}C_{CO2}$	$\delta^{15}N$	$^{20}Ne/^{22}Ne$	$^{21}Ne/^{22}Ne$	$^4He/^{20}Ne$
	°C		%						$\times10^{-6}$			R/R_A		‰ PDB	‰ Air			
Dichi[a]	19.20	08.2010	95.55	2.15	1.86	0.34	91.65	1.76			6.00	1.41	1.02			9.96	0.028	0.44
TFL TC[a]	18.60	08.2010									7.00	1.64	1.53			11.50	0.028	0.36
Tianchi[a]	21.80	08.2010									4.00	1.12	0.27	−15.9		9.77	0.025	0.34
BDH[a]	7.50	08.2010									9.00	0.92	0.44			10.06	0.027	0.62
JJG HS[a]	37.50	08.2010									8212	0.29	0.21	−18.4		9.72	0.026	385.30
JJG HS[a]	19.90	08.2010	97.19	0.56	1.73	0.41	96.17	1.70	12.00		7338	0.30	0.22	−21.0		10.05	0.023	293.45
HSM No. 34[a]	27.40	08.2010									6469	0.23	0.16	−18.2		10.54	0.026	257.79
HSM No. 0[a]	3.50	08.2010									1.00	0.27	0.16	−22.3		9.80	0.025	7.03
JJG HS[b]	36.60	09.2018	96.70	1.45	1.45	0.18	94.07	1.38			3191	0.24	0.17	−6.2	1.9			334
JJG HS[b]	36.60	09.2018	95.83	1.83	1.14	0.26	92.51	1.05			2840	0.20	0.14	−8.7	1.3			152
JJG HS[b]	24.80	09.2018	96.60	1.93	1.19	0.14	93.10	1.10			1457	0.25	0.18	−10.7	1.6			306
JJG HS[b]	24.80	09.2018	96.53	2.01	1.18	0.12	92.88	1.08			1585	0.22	0.16	−13.7	1.7			384
JJG HS[b]	24.80	09.2018	96.56	1.97	1.19	0.13	92.99	1.09										
JJG river	10.00	31.07.2022	74.62	22.00		0.07	34.71		0.60	53.00	19.64							
JJG-1	38.40	01.08.2022	77.58	17.80		0.37	45.29		0.52	34.76	899.86							
JJG-2	38.40	01.08.2022	75.13	19.70		0.19	39.39		0.33	11.67	800.60							
JJG-3	38.40	01.08.2022	89.36	5.25		0.29	79.84		0.64	7.85	9254.40							
JJG-4	38.40	01.08.2022	89.18	5.57		0.28	79.08		0.56	8.11	9261.70							
YJG-1	37.70	04.08.2022	84.35	2.38		0.93	80.03		0.62	7.60	18996							
YJG-2	37.70	04.08.2022	86.49	2.11		1.09	82.66		0.66	1.57	30241							
YJG-3	37.70	04.08.2022	77.91	16.3		0.39	48.34		0.67	9.80	5736.70							
YJG-4	37.70	04.08.2022	86.18	2.48		0.92	81.68		0.58	2.75	20718							

(Continued on following page)

10.3389/feart.2023.1174315

TABLE 1 (*Continued*) Gas compositions of the Arxan volcanic field.

Location	T	Sampling date	%						×10^{-6}			R/R_A		$\delta^{13}C_{CO2}$	$\delta^{15}N$	$^{20}Ne/^{22}Ne$	$^{21}Ne/^{22}Ne$	$^{4}He/^{20}Ne$
	°C		N_2	O_2	Ar	CO_2	N*	Ar*	CH_4	H_2	He	$^{3}He/^{4}He$	$^{3}He/^{4}He^{*}$	‰ PDB	‰ Air			
BDH	10.60	02.08.2022	75.26	21.7		0.10	35.90		0.59	10.04	18.59							
TC	29.70	02.08.2022	75.66	22.0		0.10	35.75		0.49	2.99	4.67							

[a]After Cui et al., 2022.

[b]After Zhao et al., 2021.

An empty cell indicates no data.

N*: excess N_2 corrected by the N_2/O_2 ratio of ASW at 3°C, N* = N_2-1.814 O_2.

Ar*: excess Ar corrected by the O_2/Ar ratio of ASW at 3°C, Ar* = Ar-O_2/20.5.

$^{3}He/^{4}He^{*}$: ASW-corrected $^{3}He/^{4}He$ ratio; Atm: percentage of atmospheric He in the total He of the hot spring gases (Cui et al., 2022).

was conducted based on previous studies and geological surveys. In the measurement process, we selected areas far from ponds, rivers, and regions with dense vegetation and human activities. Faults are highly developed in the study area, and the formation of hot springs is the result of the interaction between groundwater and faults. Some appropriate soil gas observation sites near the Jinjianggou and Yinjianggou hot springs were selected to determine the soil gas emission characteristics in the fault zone. Additionally, two sites on the cone and peripheral area of the two Holocene volcanoes (i.e., the Gaoshan and Yanshan volcanoes) were selected to show the level of soil gas emission in the volcanic field.

4 Results

4.1 Volcanic gas composition and content

The upward migration of magmatic gases is one of the most significant observable factors preceding volcanic eruptions. Due to the early and rapid upward gas migration, eruptions can be predicted earlier. Therefore, most volcanic monitoring studies focus on the gas geochemistry in dormant volcanic fields. In this study, we tested the gas components in Jinjianggou and Yinjianggou hot springs, Budonghe river and Tianchi volcanic field. The gas composition of the Arxan volcanic field is shown in Table 1, and previous observation data were also collected.

We analyzed the O_2/N_2 ratio (air = 0.268, Holland, 1987) of the hot spring gas components in the Arxan volcanic field. It can be found that the O_2/N_2 ratios of the samples JJG-1 and JJG-2 are close to that of the air. The Jinjianggou river, Budong river, and Arxan Tianchi lake samples are all surface water, which may be seriously contaminated by the atmosphere. The hot spring gases (Jinjianggou and Yinjianggou hot springs and Budonghe river) in the Arxan volcanic field are mainly composed of N_2 (Figures 3, 4), accounting for 86.2%–97.2%. For volcanic gases, the CO_2 content is low (0.07%–1.09%), while the He (800×10^{-6}–30241×10^{-6}) and Ar (1.14%–1.86%) contents are relatively high (Table 1). The ratios of He–CO_2–N_2 (Figure 3) in the triangular diagram show that the hot spring and surface water gases feature different components and that the hot spring gases are mainly enriched in N_2. Specifically, the CO_2/N_2 ratio of the Jinjianggou hot spring gases is 0.001–0.004, while that of the Yinjianggou hot spring gases is 0.005–0.01. The Yinjianggou hot spring gases are more enriched in CO_2 than the Jinjianggou hot spring gases. In addition, the hot spring gases in the volcanic field are generally enriched in N_2, similar to the surface water in the Jinjianggou River, Arxan Tianchi and Dichi (DC) (Figure 5). The N_2/Ar ratio (67–84) of the volcanic gases is close to that of the air (83.6, Hilton, 1996), but the O_2 content (1.45%–5.57%) is low, and the $^{4}He/^{20}Ne$ ratio (152–384) is much higher than that of the air (0.32, Magro et al., 2013). The surface water in the Arxan volcanic field is characterized by high N_2 contents (95.55%), low CO_2 contents (0.34%) and low He contents (6%–9%), which is different from the hot spring samples.

Previous investigations into the isotopic compositions of hot spring gases in the Arxan volcanic field have demonstrated that the $^{3}He/^{4}He$ ratio of the Arxan volcanic gas is low, ranging from 0.20 to 0.92 R_A (Table 1). This value is higher than that of the crustal source (0.02 R_A, Ballentine et al., 2002) but significantly lower than that of

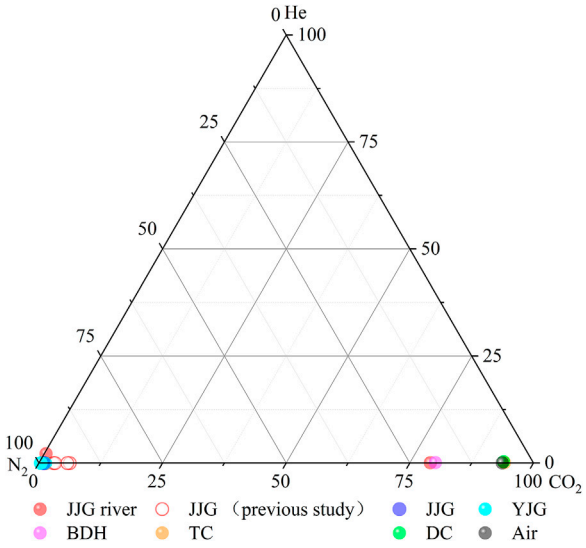

FIGURE 3
CO_2–N_2–He diagram comparing the hot spring and surface water gas compositions. Data sources are shown in Table 1. Filled and open symbols represent data from this study and published data, respectively.

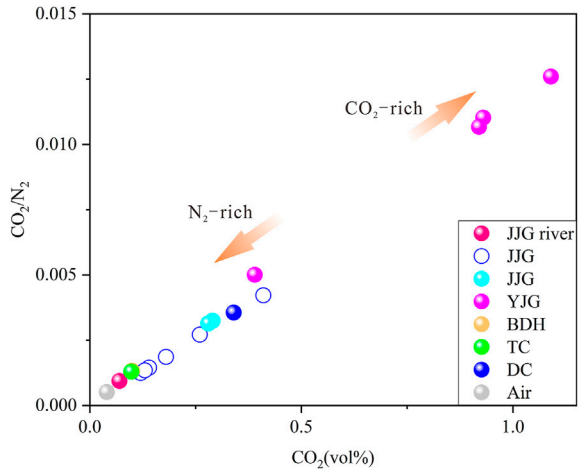

FIGURE 4
CO_2/N_2 vs. CO_2 (vol%) for air, hot spring gases, and surface water gases in the Arxan volcanic field. Data sources are shown in Table 1. Filled and open symbols represent data from this study and published data, respectively.

gas from the upper mantle or lithospheric mantle. This pattern suggests that the crustal source is the major contributor (Zhao et al., 2021). The $^4He/^{20}Ne$ ratio of surface water in the Arxan volcanic field is close to the atmospheric value (0.32, Ozima and Podosek, 2002), while the $^4He/^{20}Ne$ ratio of hot spring water is much higher than the atmospheric value. The $\delta^{13}C$ ranges from −22.3‰ to −6.2‰, indicating that the CO_2 in the hot springs may come from the mantle or be associated with biogenic and metamorphic gases in the crust (Cui et al., 2022). The excess N_2, Ar, He, and CO_2 in hot springs in the study area are mainly from the crust and upper mantle, and approximately 12%–63% of the He in the hot spring gas comes from the mantle (Cui et al., 2022). The CO_2 content of the Arxan volcanic field is lower than that of the Changbaishan, Wudalianchi, and Tengchong volcanoes in China, where the CO_2 contents are higher than 90%. The CH_4 concentration of the Arxan volcanic field is slightly higher than that of the Changbaishan volcano (1,900–4,300 ppm) but lower than that of the Tengchong volcano (300–16,900 ppm); the H_2 concentration is close to that of the Changbaishan volcano (1.1–29.2 ppm). However, the He concentrations in the gas from the Jinjianggou and Yinjianggou hot springs are prominently higher than those of the Changbaishan (7.6–53 ppm), Wudalianchi (10–330 ppm) (Gao and Li, 1999), and Tengchong (10–380 ppm) volcanoes (Wei et al., 2016).

4.2 Gas flux measurement

The curve of soil gas concentration measured in the field is shown in Figure 5. The accumulation chamber methodology (Figure 2) was employed in the gas flux observation to measure the diffusive emission of CO_2 in the soil (Chiodini et al., 1998; Mazot et al., 2009; Mazot et al., 2011; Pérez et al., 2011). According to the methods described in Mazot et al. (2009) and Mazot et al. (2015), the soil temperature, atmospheric pressure and water temperature were measured during the field work. Moreover, we calibrated the instrument based on the atmospheric concentration before measurement. The gas diffusing through the soil accumulates and circulates in the closed-circuit system, migrating from the soil to the observation instrument and then returning to the collecting hood through the connecting tube. The soil CO_2 flux was calculated using the following formula (Sun et al., 2018):

$$F_{(CO_2)} = \rho \cdot H \cdot (T_0/T_S) \cdot \left(\frac{P_S}{P_0}\right) \cdot \left(\frac{d_c}{d_t}\right), \quad (1)$$

where T_0 and P_0 are the temperature and atmospheric pressure under standard temperature and pressure, respectively. *Ts* and *Ps* denote the soil temperature (°C) and atmospheric pressure (kPa) of each measurement site, respectively. *dc/dt* represents the concentration change rate for each measurement site.

The single-site soil microseepage CO_2 fluxes in the Arxan volcanic field range from 4.66 to 107.18 g m^{-2} d^{-1}, as shown in Table 2. Previous studies have shown that soil microseepage CO_2 flux data in the range of 0.2–10,000 g m^{-2} d^{-1} are credible when adopting the closed-chamber method (Chiodini et al., 1998; Guo et al., 2014). Thus, the observed data in this study conform to the CO_2 emission level of soil microseepage in most quiescent volcanoes. The CO_2 fluxes in the Jinjianggou and Yinjianggou hot springs are high, whereas the soil CO_2 fluxes in the two Holocene active volcanic non-volcanic fields are 4–13 times lower than those of the hot springs. Figure 1 shows that the faults of the entire Arxan volcanic field are highly developed, and the hot springs and active volcanic non-volcanic fields are all dissected or partially dissected by faults, providing channel for the release of deeply sourced gases.

Vegetation may have an effect on soil CO_2 emissions, and the soil gas measurement sites of Gaoshan and Yanshan volcanoes had more vegetation cover, such as weeds and shrubs. We reviewed some

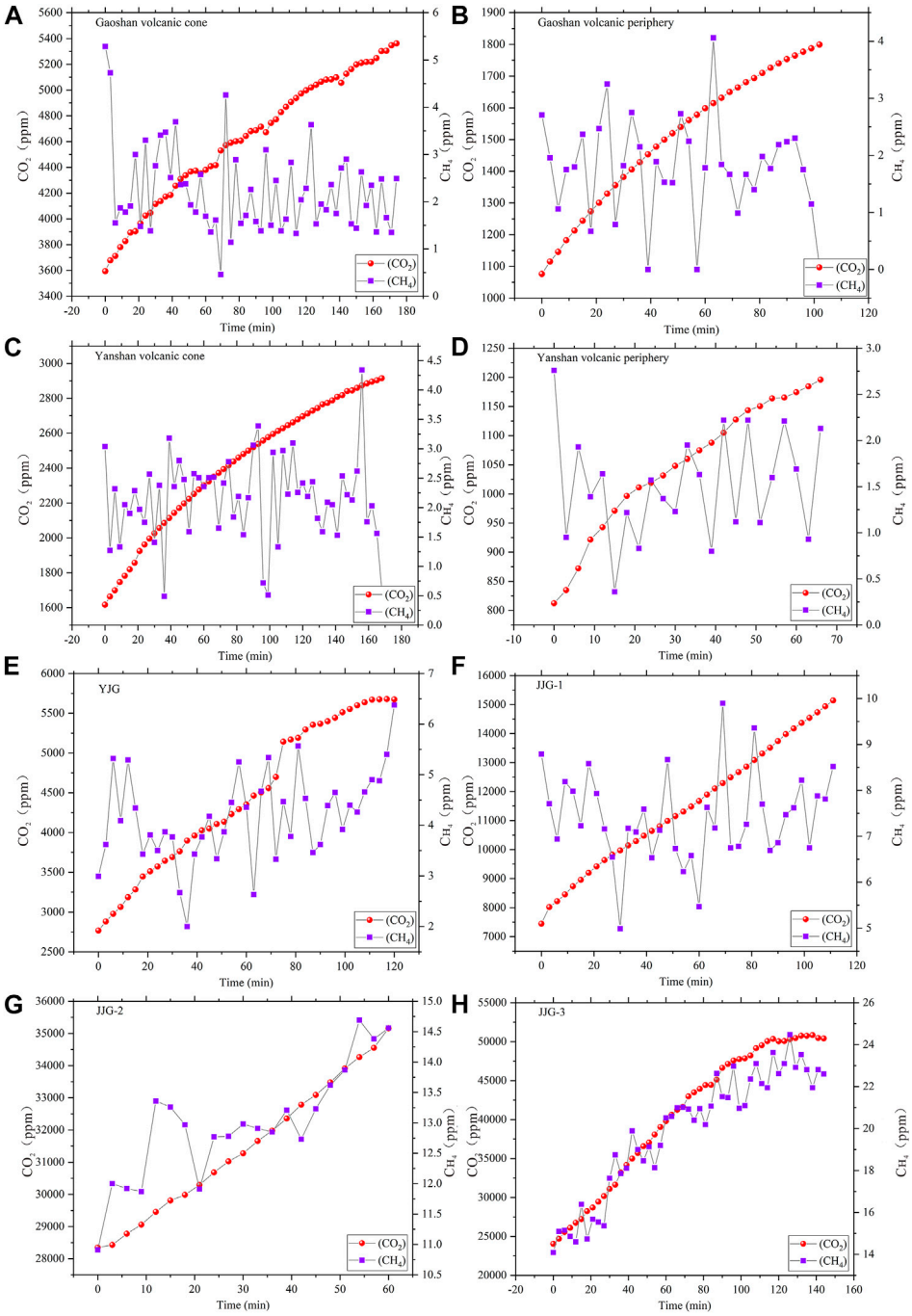

FIGURE 5
The measured curve of soil gas concentration in the volcanic field [**(A)** Gaoshan volcanic cone, **(B)** Gaoshan volcanic periphery, **(C)** Yanshan volcanic cone, **(D)** Yanshan volcanic periphery, **(E)** Yinjianggou hot spring, **(F)** Jinjianggou hot spring-1, **(G)** Jinjianggou hot spring-2, **(H)** Jinjianggou hot spring-3].

relevant studies on CO_2 fluxes emitted from non-volcanic soil vegetation. Norman et al. (1992) measured CO_2 fluxes from a large number of vegetated soils in Wisconsin and obtained an average CO_2 flux of 0.6 g m^{-2} d^{-1} (Norman et al., 1992). Mäki et al. (2019) conducted a soil CO_2 flux study in a coniferous forest at Hyytiälä (Juupajoki, Finland) and observed fluxes of 0.72–5.04 μg m^{-2} d^{-1} (Mäki et al., 2019). Other scholars have performed a study on CO_2 fluxes from natural vegetation in the Xilin River basin in the grasslands of Inner Mongolia, China, which has a similar geological background and climatic environment to the study area. Thus, our data can be compared to the CO_2 emissions from natural vegetation in non-volcanic fields. That study found that the natural vegetation in the grasslands of the Xilin River basin in Inner Mongolia is associated with a CO_2 flux of 2.4–12 g m^{-2} d^{-1}

TABLE 2 Results of soil CO_2 flux in the Arxan volcanic field.

Measurement site	Atmospheric pressure/kPa	Temperature/°C	CO_2 flux/g m^{-2} d^{-1}	Area/m^2	CO_2 output/t·a^{-1}
Gaoshan volcanic cone	85.80	29.3	8.73	4.195×10^6	13367.16
Gaoshan volcanic periphery	85.83	31.9	4.66		
Yanshan volcanic cone	85.98	31.6	6.30	3.892×10^6	8949.65
Yanshan volcanic periphery	86.01	34.3	5.32		
YJG	89.06	23.4	31.82	233445	2706.13
JJG-1	88.13	26.0	42.32	981537	38338.30
JJG-2	88.13	26.0	45.11		
JJG-3	88.36	29.4	107.18		

TABLE 3 Comparison of CO_2 emission fluxes between the Arxan volcano and similar volcanoes.

Volcano	Region	Type	CO_2 soil flux/ $\times 10^5$ t·a^{-1}	Area/ km^{-2}	CO_2 soil flux/Area ($\times 10^5$ t $km^{-2}a^{-1}$)	Measurement time	References
Arxan	China	Intraplate	0.63	9.3	0.068	2022	
Changbaishan	China	Intraplate	9.4	110	0.085	2010, 2011, 2016	Zhang et al. (2011), Guo et al. (2014), Sun et al. (2018), Zhao et al. (2021)
Wudalianchi	China	Intraplate	12	215	0.056	2010, 2011, 2017	Guo et al. (2014), Zhao et al. (2021)
Tengchong	China	subduction-related	70	790	0.089	2012, 2013	Cheng et al. (2014)
St. Helens	United States	subduction-related	115	90	1.27	1980	Harris et al. (1996)
Yellowstone	United States	mantle plume-related	1.5	1	1.5	2006	Werner et al. (2008)
White Island	New Zealand	subduction-related	0.032	0.2	0.16	1998	Wardell et al. (2001)
Iwojima	Japan	Island arc	1.64	22	0.07	2000	Notsu et al. (2005)

(Ma, 2006). We can see that the CO_2 fluxes of natural vegetation in non-volcanic fields are all relatively low, and the CO_2 fluxes near the Jinjianggou and Yinjianggou hot springs are markedly higher than those released by vegetation in the above non-volcanic fields. However, the CO_2 fluxes in the Arxan and Yanshan volcanic fields are close to the levels released by natural vegetation in the grasslands of the Xilin River basin in Inner Mongolia. For the above reasons, it is likely that the surface faults of Gaoshan and Yanshan volcanoes are not well developed, and deep gases do not easily pass through the volcanic cones to reach the surface directly.

5 Discussion

We identified some unique characteristics of the hot spring gases in our study area during the sampling and observation process. The hot spring gas in the Arxan volcanic field is characterized by abnormally high He concentrations. The faults in the study area are highly developed, especially the NNE and NE oriented ones. Tang et al. (2005) observed two deep faults that acted as channels for the upward migration of magma from the mantle. One fault shows high temperatures and fluid enrichment at a depth of 10–12 km, and the other shows low temperatures at a depth of 30 km. The He content in the study area is significantly higher than that in other dormant volcanoes in China. According to previous studies on the petrological and geochemical characteristics of the volcanic rocks in the Yinjianggou of the Arxan volcanic field, the most remarkable feature is the anomalously strong enrichment of U in the regional volcanic rocks (the U content reaches 4.27–7.82 ug/g), which may be associated with the evolution of crust-derived magma (Wu et al., 2010). Thus, we speculate that the high He content is likely caused by the decay of U and Th in the Mesozoic granodiorite and acidic volcanic rocks.

Furthermore, the soil CO_2 concentrations near the Jinjianggou and Yinjianggou hot springs are much higher than those in the Holocene volcanic field. The results of previous magnetotelluric and seismic surveys (Han et al., 2018; Li et al., 2023) have shown that NE and NNE trending faults are located in the vicinity of the two hot springs and may act as underlying magma channels. Therefore, the soil CO_2

and the gases present in the two springs are remarkably higher in concentration than those in other regions. In contrast, the soil CO_2 and CH_4 concentrations in the Holocene Gaoshan and Yanshan volcanoes are lower than those in the Jinjianggou and Yinjianggou hot springs. These lower concentrations of volcanic gases at the surface may be due to the seal formed by lava flows generated by the eruption 2,000 years ago. The geological surveys of the volcanic cone and adjacent areas have not observed any obvious fault exposure.

Compared with the monitoring of erupting volcanoes, it is equally important to investigate the characteristics of gas release from dormant ones. The volcanic degassing trend is related to the type of volcanic gases. Previous studies have proposed that in response to the rise of magma, volcanic gases preferentially exsolve in the order of CO_2, S, H_2, HCl and HF (Werner et al., 2013). The analysis of the Arxan volcanic hot springs shows that the gas composition of the volcanic non-volcanic field is characterized by high N_2, He, and Ar contents and low CO_2 contents. In the hot spring gases, the $\delta^{15}N$ value ranges from 1.3‰–1.9‰, and the N_2/He ratio ranges from 303 to 663. The results suggest the existence of a high proportion of N_2-rich organic matter (Zhao et al., 2021). Additionally, both the $^3He/^4He$ and $CO_2/^3He$ ratios of the hot spring gas samples in the study area are low and differ from the patterns of the mantle endmember (high $^3He/^4He$, low $CO_2/^3He$) and subduction recycling endmember (low $^3He/^4He$, high $CO_2/^3He$). Furthermore, these values are far lower than the values of the volcanic and geothermal gases in volcanic arcs and mid-ocean ridges (Sano and Marty, 1995). The He concentrations in hot spring gases in the Arxan volcanic field ($1{,}457 \times 10^{-6} \sim 30{,}241 \times 10^{-6}$) are much higher than the atmospheric value (5.24×10^{-6}), indicating a deep origin, i.e., a crustal and/or mantle source.

Several active volcanoes with the same tectonic background are compared to the Arxan volcanic field. Arxan, Changbaishan and Wudalianchi are all intraplate volcanoes, whereas Tengchong, Mount St. Helens and White Island are all subduction-related volcanoes. Additionally, Arxan, Changbaishan, Mount St. Helens, and Yellowstone are all currently dormant, while the White Island volcano has been in a slightly active state (2019 eruption, VEI = 2). Due to the large difference in the area of each volcanic field, it is not reasonable to directly compare the annual total flux of volcanic CO_2. Therefore, the annual CO_2 flux of each volcanic field was divided by the corresponding area in this study. According to Table 3, it can be seen that the soil CO_2 flux of the Arxan volcano is approximately 20 times lower than that of the Mount St. Helens and Yellowstone volcanoes and approximately 2 times lower than that of the White Island volcano in New Zealand during the eruption stage. Iwo Jima volcano has erupted intermittently since 1922, with the most recent eruption occurring in July–August 2022. The historical eruption VEI maximum of one also indicates that soil CO_2 fluxes from Alsan volcano are comparable to soil CO_2 emission levels from Iwo Jima volcano, which is active and has erupted frequently in recent years (e.g., 2001, 2020, 2021 and 2022).

6 Conclusion

Based on the observation of soil gases and the composition of the gases escaping from hot springs, we analyzed the degassing characteristics of the Arxan volcanic field. The major conclusions include the following:

(1) In the studied hot springs in the Arxan volcanic field, the concentrations of CO_2, CH_4, H_2, He, and Ar are 0.07%–1.09%, 0.33–12 ppm, 1.57–53 ppm, 800–30,241 ppm, and 1.14%–1.86%, respectively. The notably high He content is likely due to U–Th decay in the Mesozoic granodiorite and acidic volcanic rocks in the study area.

(2) The soil gas concentrations near the Jinjianggou and Yinjianggou hot springs are higher than those near two Holocene volcanoes. The peak CO_2 concentration in the soil near the Jinjianggou hot spring can reach 35,161 ppm. The single-site soil microseepage CO_2 flux in the Arxan volcanic field is 4.66–107.18 gm^{-2} d^{-1}, and the estimated annual CO_2 emission flux from the volcanic non-volcanic field to the atmosphere is 0.63×10^5 t, which also demonstrates that soil CO_2 flux of Arxan volcano is comparable to the soil CO_2 emission level of the Iwojima volcano.

Data availability statement

The original contributions presented in the study are included in the article/Supplementary Material, further inquiries can be directed to the corresponding author.

Author contributions

XP, GG, DH, BB, and SG conducted the field survey. XP and YS processed the data and prepared the first draft. All authors contributed to the article and approved the submitted version.

Funding

This work was supported by the Science for Earthquake Resilience (XH23013B), Jilin Scientific and Technological Development Program-Key technologies for early warning of volcanic eruption in Changbaishan Tianchi based on multi-source volcano monitoring (20230203132SF), Chinese Academy of Engineering and Local Cooperation Strategic Consulting Project (JL2021-03-01), and the National Observation and Research Station, Institute of Geology, China Earthquake Administration (NORSCBS21-04, NORSCBS21-07, and NORSCBS22-07).

Acknowledgments

We are grateful to Baojin Jia from the Arxan Volcano Monitoring Station for his support during the field investigation and to Jianguo Du and Yueju Cui from the Institute of Earthquake Forecasting, China Earthquake Administration, for their helpful suggestions.

Conflict of interest

The authors declare that the research was conducted in the absence of any commercial or financial relationships that could be construed as a potential conflict of interest.

Publisher's note

References

Aiuppa, A., Bani, P., Moussallam, Y., Napoli, R. D., Allard, P., Gunawan, H., et al. (2015). First determination of magma-derived gas emissions from bromo volcano, eastern java (Indonesia). *J. Volcanol. Geotherm. Res.* 304 (OCT.1), 206–213. doi:10.1016/j.jvolgeores.2015.09.008

Bai, Z., Tian, M., Wu, F., Xu, D., and Li, T. (2005). Yanshan, gaoshan-two active volcanos of the volcanic cluster in arshan, inner Mongolia. *Earthq. Res. China* 21 (1), 5. (In Chinese with English abstract).

Ballentine, C. J., Burgess, R., and Marty, B. (2002). Tracing fluid origin, transport and interaction in the crust. *Rev. Mineral. Geochem.* 47, 539–614. doi:10.2138/rmg.2002.47.13

Cheng, Z., Guo, Z., Zhang, M., and Zhang, L. (2014). Carbon dioxide emissions from Tengchong cenozoic volcanic field.Yunnan province,SW China. *Acta Petrol. Sin.* 30 (12), 3657–3670. (In Chinese with English abstract).

Chiodini, G., Cioni, R., Guidi, M., Raco, B., and Marini, L. (1998). Soil CO2 flux measurements in volcanic and geothermal areas. *Appl. Geochem.* 13 (5), 543–552. doi:10.1016/S0883-2927(97)00076-0

Cui, Y., Sun, F., Liu, L., Xie, C., Li, J., Chen, Z., et al. (2023). Contribution of deep-earth fluids to the geothermal system: A case study in the arxan volcanic region, northeastern China. *Front. Earth Sci.* 10, 996583. doi:10.3389/feart.2022.996583

Du, J., Li, S., Zhao, Y., Ren, J., Sun, R., and Duanmu, H. (1999). Geochemicalcharacteristics of gases from the volcanic area Wudalianchi, Northeastern China. *Acta Geol. Sin.* 73 (2), 103–107. doi:10.1111/j.1755-6724.1999.tb00830.x

Gao, Q., and Li, N. (1999). A discussion on fluid geochemistry and origin of the Tengchong and Wudalianchi volcanic areas. *Geol. Rev.* (04), 345–351. (In Chinese with English abstract).

Gu, X. (2018). *Geochemical characteristics and evolution mechanism of thermal and mineral springs in Arxan*. north eastern Beijing China: China University of Geosciences. (In Chinese with English abstract).dissertation

Guo, Z., Zhang, M., Cheng, Z., Zhang, L., and Lu, J. (2014). Fluxes and Genesis of greenhouse gases emissions fromtypical volcanic fields in China. *Acta Petrol. Sin.* 30 (11), 3467–3480. (In Chinese with English abstract).

Guo, Z., Zhang, M., Sun, Y., Cheng, Z., Zhang, L., and Liu, J. (2015). Research advances in greenhouse gases degassingfrom cenozoic volcanic active fields. *J.Bulletin Mineralogy, Petrology Geochem.* 34 (4), 690–700. (In Chinese with English abstract). doi:10.3969/i.issn.1007-2802.2015.04.003

Han, J., Wang, T., Liu, W., Liu, G., Han, S., and Liu, L. (2018). Deep"arch-bridge"magmatic system of the Aershan volcanic group and its stability analysis. *J. Seismol. And Egology.* 40 (3), 21. (In Chinese with English abstract). doi:10.3969/jissn.0253-4967.2018.03.007

Harris, D. M., and Rose, W. I. (1996). Dynamics of carbon dioxide emissions, crystallization, and magma ascent: Hypotheses, theory, and applications to volcano monitoring at Mount St. Helens. *Bull. Volcanol.* 58, 163–174. doi:10.1007/s004450050133

Hilton, D. R. (1996). The helium and carbon isotope systematics of a continental geothermal system: Results from monitoring studies at long valley caldera (California, USA). *Chem. Geol.* 127 (4), 269–295. doi:10.1016/0009-2541(95)00134-4

Holland, P. W., and Emerson, D. E. (1987). A determination of the helium 4 content of near-surface atmospheric air within the continental United States. *J. Geophys. Res. Solid Earth* 92 (B12), 12557–12566. doi:10.1029/jb092ib12p12557

Li, J., Tian, Y., Zhao, D., Yan, D., Li, Z., and Li, H. (2023). Magmatic system and seismicity of the Arxan volcanic group in Northeast China. *Geophys. Res. Lett.* 50 (6), e2022GL101105. doi:10.1029/2022GL101105

Li, T., Liu, J., Wang, X., Guo, Z., Guo, W., Cheng, Z., et al. (2015). Geochemical characteristics and genesis of gases from Tianchi volcanic Springs,Changbai Mountains, Jilin, China. *J4* 34 (6), 1192–1202. (In Chinese with English abstract).

Liu, E. J., Wood, K., Aiuppa, A., Giudice, G., Bitetto, M., Fischer, T. P., et al. (2021). Volcanic activity and gas emissions along the south sandwich arc. *Bull. Volcanol.* 83, 3–23. doi:10.1007/s00445-020-01415-2

Liu, G., Sun, Y., and Guo, Z. (2011). The newest monitoring information of Changbaishan volcano, NE China. *J.Acta Petrol. Sin.* 27 (10), 2905–2911. (In Chinese with English abstract). doi:10.1016/j.pgeola.2011.03.006

Liu, J., Han, J., and Fyfe, W. S. (2001). Cenozoic episodic volcanism and continental rifting in northeast China and possible link to Japan Sea development as revealed from K–Ar geochronology. *Tectonophysics* 339 (3-4), 385–401. doi:10.1016/S0040-1951(01)00132-9

Liu, J. (1987). Study on geochronology of the Cenozoic volcanic rocks in Northeast China. *J.Acta Petrol. Sin.* (04), 23–33. (In Chinese with English abstract).

Ma, X. (2006). *Dissertation. The Institute of botany, Chinese Academy of Sciences. Effects of cultivation and grazing on SoilCarbon pool and GreenhouseGasesFluxes in the inner Mongolia steppes*. Institute of Botany, The Chinese Academy of Science Beijing, Beijing China

Magro, G., Gherardi, F., and Bayon, F. E. B. (2013). Noble and reactive gases of Palinpinon geothermal field (Philippines): Origin, reservoir processes and geodynamic implications. *Chem. Geol.* 339, 4–15. doi:10.1016/j.chemgeo.2012.09.036

Mäki, M., Aaltonen, H., Heinonsalo, J., Hellén, H., Pumpanen, J., and Bäck, J. (2019). Boreal forest soil is a significant and diverse source of volatile organic compounds. *Plant Soil* 441, 89–110. doi:10.1007/s11104-019-04092-z

Mazot, A., and Bernard, A. (2015). "CO2 degassing from volcanic lakes," in *Volcanic lakes. Advances in volcanology*. Editors D. Rouwet, B. Christenson, F. Tassi, and J. Vandemeulebrouck (Berlin, Heidelberg: Springer). doi:10.1007/978-3-642-36833-2_15

Mazot, A., Rouwet, D., Taran, Y., Inguaggiato, S., and Varley, N. (2011). CO2 and He degassing at el chichón volcano, chiapas, Mexico: Gas flux, origin and relationship with local and regional tectonics. *Bull. Volcanol.* 73, 423–441. doi:10.1007/s00445-010-0443-y

Mazot, A., and Taran, Y. (2009). CO2 flux from the volcanic lake of El Chichón (Mexico). *Geofísica Int.* 48 (1), 73–83. doi:10.22201/igeof.00167169p.2009.48.1.100

Norman, J. M., Garcia, R., and Verma, S. B. (1992). Soil surface CO2 fluxes and the carbon budget of a grassland. *J. Geophys. Res. Atmos.* 97 (D17), 18845–18853. doi:10.1029/92JD01348

Notsu, K., Sugiyama, K., Hosoe, M., Uemura, A., Shimoike, Y., Tsunomori, F., et al. (2005). Diffuse CO2 efflux from Iwojima volcano, Izu-Ogasawara arc, Japan. *J. Volcanol. Geotherm. Res.* 139 (3-4), 147–161. doi:10.1016/j.jvolgeores.2004.08.003

Ozima, M., and Podosek, F. A. (2002). *Noble gas geochemistry*. Cambridge University Press. Cambridge, United Kingdom.

Padrón, E., Pérez, N. M., Hernández, P. A., Sumino, H., Melián, G. V., Barrancos, J., et al. (2013). Diffusive helium emissions as a precursory sign of volcanic unrest. *Geology* 41 (5), 539–542. doi:10.1130/G34027.1

Pan, B., Liu, G., Cheng, T., Zhang, J., Sun, Z., Ma, B., et al. (2021). Development and status of active volcano monitoring in China. *Geol. Soc. Lond. Spec. Publ.* 510 (1), 227–252. doi:10.1144/SP510-2020-62

Sano, Y., and Marty, B. (1995). Origin of carbon in fumarolic gas from island arcs. *Chem. Geol.* 119 (1-4), 265–274. doi:10.1016/0009-2541(94)00097-R

Shangguan, Z., and Wu, C. (2008). Geochemical features of magmatic gases in the regions of dormant volcanoes in China. *J.Acta Petrol. Sin.* 24 (11), 2638–2646. (In Chinese with English abstract).

Sun, Y., Guo, Z., Liu, J., and Du, J. (2018). CO_2 diffuse emission from maar lake: An example in Changbai volcanic field, NE China. *J. Volcanol. Geotherm. Res.* 349, 146–162. doi:10.1016/j.jvolgeores.2017.10.012

Tang, J., Wang, J., Chen, X., Zhao, G., and Zhan, Y. (2005). A PreliminaryInvestigation on electric structure of the crust and upper mantle in ArxanVolcanic area. *Chin.*J. Geophys. 48 (1), 214–221. doi:10.1002/cjg2.642

Tassi, F., Cabassi, J., Calabrese, S., Nisi, B., Venturi, S., Capecchiacci, F., et al. (2016). Diffuse soil gas emissions of gaseous elemental mercury (GEM) from hydrothermal-volcanic systems: An innovative approach by using the static closed-chamber method. *Appl. Geochem.* 66, 234–241. doi:10.1016/j.apgeochem.2016.01.002

Wardell, L. J., Kyle, P. R., Dunbar, N., and Christenson, B. (2001). White Island volcano, New Zealand: Carbon dioxide and sulfur dioxide emission rates and melt inclusion studies. *Chem. Geol.* 177 (1-2), 187–200. doi:10.1016/S0009-2541(00)00391-0

Wei, F., Xu, J., Kong, Q., Liu, S., Xu, D., and Pan, B. (2021). Sources of CH4 with variable carbon isotopes from Changbaishan volcano in NE China: Implications for the feeding system. *J. Volcanol. Geotherm. Res.* 419, 107355. doi:10.1016/j.jvolgeores.2021.107355

Wei, F., Xu, J., Shangguan, Z., Pan, B., Yu, H., Wei, W., et al. (2016). Heliumand carbon isotopes in the hot springs of Changbaishan volcano, northeasternChina: A material connection between Changbaishan volcano and the westPacifc plate? J. *Volcanol. Geotherm. Res.* 327, 398–406. doi:10.1016/jjvolgeores.2016.09.005

Wei, H., Liu, R., Fan, Q., and Li, N. (1998). Active volcanoes in China and their relavant hazards. *Chin. J. Nat.* 20 (4), 5. (In Chinese with English abstract)

Wei, H., Sparks, R. S. J., Liu, R., Fan, Q., Wang, Y., Hong, H., et al. (2003). Three active volcanoes in China and their hazards. *J. Asian Earth Sci.* 21 (5), 515–526. doi:10.1016/S1367-9120(02)00081-0

Werner, C., Hurwitz, S., Evans, W. C., Lowenstern, J. B., Bergfeld, D., Heasler, H., et al. (2008). Volatile emissions and gas geochemistry of hot spring basin, Yellowstone national park, USA. *J. Volcanol. Geotherm. Res.* 178 (4), 751–762. doi:10.1016/j.jvolgeores.2008.09.016

Werner, C., Kelly, P. J., Doukas, M., Lopez, T., Pfeffer, M., McGimsey, R., et al. (2013). Degassing of CO2, SO2, and H2S associated with the 2009 eruption of redoubt volcano, Alaska. *J. Volcanol. Geotherm. Res.* 259, 270–284. doi:10.1016/j.jvolgeores.2012.04.012

Wu, C., Yin, H., Shen, K., Zhu, Y., Xie, H., Cao, T., et al. (2010). Characteristics of petrology and geochenistry of volcanic rocks in the Yin jianggou Aershan area. *Geol. Explor.* 46 (3), 0515–0524. (In Chinese with English abstract).

Zhang, M., Guo, Z., Liu, J., Liu, G., Zhang, L., Lei, M., et al. (2018). The intraplate changbaishan volcanic field (China/north Korea): A review on eruptive history, magma Genesis, geodynamic significance, recent dynamics and potential hazards. *Earth Sci. Rev.* 187, 19–52. doi:10.1016/j.earscirev.2018.07.011

Zhang, M., Guo, Z., Sano, Y., Cheng, Z., and Zhang, L. (2015). Stagnant subducted Pacific slab-derived CO2 emissions: Insights into magma degassing at Changbaishan volcano, NE China. *J. Asian Earth Sci.* 106, 49–63. doi:10.1016/j.jseaes.2015.01.029

Zhang, M., Guo, Z., Sano, Y., Zhang, L., Sun, Y., Cheng, Z., et al. (2016). Magma-derived CO2 emissions in the Tengchong volcanic field, SE Tibet: Implications for deep carbon cycle at intra-continent subduction zone. *J. Asian Earth Sci.* 127, 76–90. doi:10.1016/j.jseaes.2016.06.009

Zhang, M. L., Guo, Z. F., Cheng, Z. H., Zhang, L. H., and Wen, X. Y. (2011). Greenhouse gases flux estimation of hot springs in changbaishan volcanic field, ne China. *Acta Petrol. Sin.* 27 (10), 2898–2904. (In Chinese with English abstract). doi:10.1016/j.pgeola.2011.03.006

Zhao, C., Ran, H., and Wang, Y. (2012). Present-day mantle-derived helium release in the Tengchong volcanic field, Southwest China: Implications for tectonics and magmatism. *J. Acta Petrol. Sin.* 28 (4), 1189–1204.

Zhao, W., Guo, Z., Lei, M., Zhang, M., Zheng, G., Fortin, D., et al. (2019). Volcanogenic CO2 degassing in the songliao continental rift system, ne China. *Geofluids* 2019 (6), 1–14. doi:10.1155/2019/8053579

Zhao, W., Guo, Z., Liu, J., Zhang, M., Sun, Y., Lei, M., et al. (2021). Fluxes and Genesis of carbon dioxide emissions from Cenozoic volcanic fields in NE China. *Acta Petrol. Sin.* 37 (4), 1255–1269. (in Chinese with English abstract). doi:10.18654/1000-0569/2021.04.17

Zhao, Y., and Fan, Q. (2010). Yanshan and Gao Shan Volcanoes in the Daxinganmounta in range - a new eruption style. *Seismol. And Egology* 32 (1), 28–37. (In Chinese with English abstract). doi:10.3969/jissn.0253-4967.2010.01.003

frontiers | Frontiers in Earth Science

TYPE Brief Research Report
PUBLISHED 17 July 2023
DOI 10.3389/feart.2023.1128949

OPEN ACCESS

EDITED BY
Daniele L. Pinti,
Université du Québec à Montréal, Canada

REVIEWED BY
Giovanni Martinelli,
National Institute of Geophysics and Volcanology, Section of Palermo, Italy
Milos Briestensky,
Institute of Rock Structure and Mechanics (ASCR), Czechia

*CORRESPONDENCE
F. Gherardi,
f.gherardi@igg.cnr.it

RECEIVED 21 December 2022
ACCEPTED 06 July 2023
PUBLISHED 17 July 2023

CITATION
Fidani C, Gherardi F, Facca G and Pierotti L (2023), Correlation between small earthquakes and CO_2 anomalies in spring waters: a statistical experiment on the probability of seismic occurrence. *Front. Earth Sci.* 11:1128949. doi: 10.3389/feart.2023.1128949

Correlation between small earthquakes and CO_2 anomalies in spring waters: a statistical experiment on the probability of seismic occurrence

C. Fidani[1,2], F. Gherardi[3]*, G. Facca[3] and L. Pierotti[3]

[1]Istituto Nazionale di Geofisica e Vulcanologia, Roma, Italy, [2]Central Italy Electromagnetic Network, Fermo, Italy, [3]Istituto di Geoscienze e Georisorse CNR, Pisa, Italy

We correlated carbon dioxide (CO_2) time series detected at the Gallicano site in Tuscany, Italy, with low-magnitude earthquakes occurred in the surrounding area between 2017 and 2021. The CO_2 irregular component distribution was analyzed by a Pearson type VII fit, and its cumulate probability by the Gauss's hypergeometric function, to statistically evidence anomalous fluctuations. We calculated the Matthews correlation between gas concentrations and low-magnitude earthquakes by defining a binary occurrence of CO_2 anomalies and seismic events. A positive correlation was highlighted by a time lag between the digital series, which resulted in CO_2 anomaly detections ahead of the earthquake time of two days. The correlated earthquakes were mainshocks of local magnitude 1.2 to 3.6, with epicenters within 40 *km* from the Gallicano site. Correlations among rainfalls, CO_2 concentrations and earthquakes were also considered, showing that only few rainfall events were followed by a CO_2 anomaly, mostly a day late.

KEYWORDS

statistical correlations, conditional probability, small earthquakes, hydrogeochemical continuous monitoring, CO_2 time series

1 Introduction

The circulation of crustal fluids affects not only the transport of heat and chemical constituents, but also the mechanical processes that control rock deformation, and possibly generate earthquakes. Abnormal pressures in tectonically active areas were first reported by Anderson (1927), and overpressurized fluids were later identified as a primary agent of tectonic deformation by Hubbert and Rubey (1959). The observation of anomalous soil CO_2 concentrations in correspondence with major faults/fractured areas (Caucasus region; Netreba et al., 1971), and of CO_2 degassing episodes after major seismic events (Gold, 1979; Gold and Soter, 1979; Gold and Soter, 1981) dates back to early 1970s'. Based on a worldwide compilation of data, it has been later established that crustal CO_2 predominantly discharges in tectonically active regions, and along major seismic zones (Barnes et al., 1978; Irwin and Barnes, 1980; Gold and Soter, 1985; Gold, 1999). The occurrence of CO_2 emissions in correspondence with principal zones of seismicity was recently observed whether during the preparation stages of major earthquakes (e.g., among many others, Kingsley, 2001; Bräuer et al., 2003), or during aftershock evolutions (Ventura et al., 2007; Massin et al., 2013; Miller, 2013; Fischer et al., 2017; Yoshida and Hasegawa, 2018; Chiodini et al., 2020), or in

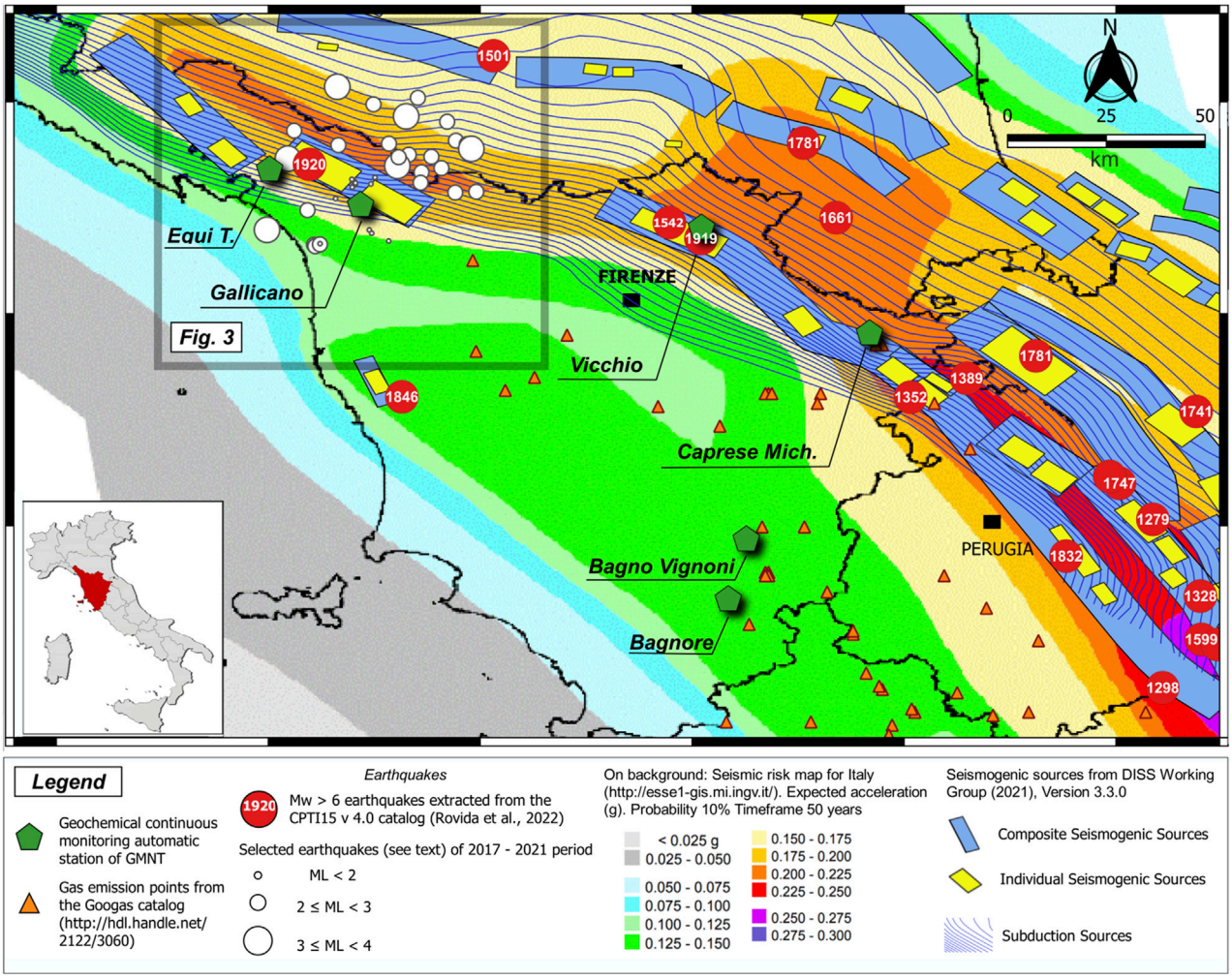

FIGURE 1
Location of the Gallicano monitoring station and other sites of the GMNT. The tectonic background and the epicenters of relevant seismic events are also shown.

concomitance with small seismic events (Heinicke et al., 1995). CO_2 excesses are predominantly observed in extensional domains (Tamburello et al., 2018), whereas compressional tectonic structures are suspected to create geological traps where crustal CO_2 may accumulate, possibly creating overpressurized reservoirs that may have the potential to trigger earthquakes (Chiodini et al., 2004). Overall, a strong connection between CO_2 discharge, seismic activity, and the existence of major faults has been identified in a number of different geodynamic contexts (Lee et al., 2016; Hunt et al., 2017).

In Central Italy, due to intense crustal deformation processes driven by the relative motion of the African and the Eurasian plates, two major areas affected by different tectonic and CO_2 degassing regimes have been identified (Chiodini et al., 2004): 1) the Tyrrhenian hinterland, characterized by extensional tectonic, crustal thinning, high heat flux and active volcanism near the Tyrrhenian Sea, where CO_2 is directly released into the atmosphere by the Tuscan-Roman and Campanian degassing structures; 2) the Adriatic foreland, characterized by compressional tectonics, where CO_2 is predominantly dissolved into groundwaters circulating through major carbonate aquifers hosted along the Apennine fold-and-thrust belt.

The central-southern part of Apennines is a highly active seismic area, and some authors (e.g., Chiodini et al., 2004; 2020) have speculated that the existence of high-pressure, CO_2-rich fluid pockets at depth may play a major role in the generation of Apennine earthquakes.

Since early 1990s', a large amount of information on the possible correlation between CO_2 degassing and seismic activity has been obtained in Italy using manual samplings techniques (Dall'Aglio et al., 1990; Di Bello et al., 1998; Italiano et al., 2001; Italiano et al., 2004; Cardellini et al., 2017; Giudicepietro et al., 2019; Chiodini et al., 2020; Martinelli et al., 2020). The collection of continuous time series by means of automatic ground-based stations has started more recently (Cioni et al., 2007; Heinicke et al., 2012; Di Martino et al., 2013; Pering et al., 2014; Pierotti et al., 2015; Camarda et al., 2016; Camarda et al., 2018; Pierotti et al., 2017; Gherardi and Pierotti, 2018), and since early 2003 a network of six automatic monitoring

stations is operating in Tuscany, Central Italy (Geochemical Monitoring Network of Tuscany, GMNT; Figure 1).

Here we report on CO_2 time series collected during the 2017–2021 period from one of the stations of the GMNT (Gallicano station, NW Tuscany), advancing a new statistical interpretative approach borrowed from satellite data processing procedures (Fidani, 2021). So far, in fact, Gallicano time series have been processed with the aim to identify possible anomalies merely related to most energetic seismic events ($M_w > 4$; e.g., Pierotti et al., 2015). Now, instead, the focus is on the possible correlation between low to moderate seismic events, which are inherently more numerous, and geochemical anomalies identified in the residuals of the CO_2 continually recorded signal. The proposed statistical approach allows for identifying CO_2 anomalies by cumulative probability, and for correlating them with earthquakes, without explicitly addressing the cause-effect mechanisms between the two classes of observable events. Finally, a conditional probability of earthquake occurrence is defined for possible short-term forecasting. At this stage, for ease of interpretation of the correlations, we focused solely on the geochemical signal of the Gallicano monitoring station, which has proven to be sensitive to crustal deformations (Pierotti et al., 2015). Future work will improve on this by extending the approach to the analysis of multiple geochemical time series collected from different monitoring stations, insofar as they are geologically linked to the same seismogenic structures.

2 Description of the study area

2.1 The Gallicano site

By discharging high-salinity Na-Ca-Cl waters (2.4 to 4.2 g/L), with a temperature of 23.4°C–25.2°C, and an average flow rate of about 1.5 L/s, the Gallicano thermomineral spring (209 m a.s.l., Garfagnana Valley, northern Tuscany, Italy), is considered a suitable site to investigate possible correlations between seismic events and anomalies in CO_2 dissolved concentrations (Cioni et al., 2007; Pierotti et al., 2015). Garfagnana Valley is one of the areas with the highest seismic risks in Tuscany. The region was struck by a M_w 6.5 earthquake in 1920 (Garfagnana earthquake; Rovida et al., 2022), and is characterized by an expected horizontal peak ground acceleration (PGA) higher than 0.175 g, with a 10% probability of exceedance in 50 years (national reference seismic hazard model; Stucchi et al., 2011). The Gallicano thermomineral spring is fed by a major, fractured carbonate aquifer. After long underground circulation paths, thermal waters emerge in correspondence with neotectonic structures (Molli et al., 2021) belonging to one of the seismogenic boxes identified by the DISS Working group (2021). Chemical and isotopic data indicate that during their underground circulation path, Gallicano waters interact with evaporitic rocks of Triassic age, and experience the inflow of deep-seated CO_2 (Pierotti et al., 2015). These conditions reflect the essential criteria required for the successful monitoring of preseismic gas-geochemical signals (Martinelli and Albarello, 1997; King et al., 2006; Weinlich et al., 2006; Martinelli and Dadomo, 2017). Since April 2003, the spring is continuously monitored for a number of parameters, which include water temperature, pH, electrical conductivity, redox potential, and dissolved concentration of CO_2 and CH_4. Full details on the setup, operating mode, sensor technology, and performance of the automatic station are given by Pierotti et al. (2015).

2.2 Meteorological data

Operative since 2000, the automatic meteorological station of Gallicano (179 m.a.s.l., 44.064° Latitude North, and 10.443° Longitude East) is part of a regional network of about 440 manual and 133 automatic stations (Agro-Metereological Network) managed by the Regional Hydrological Service (SIR) of Tuscany. The station is located in the municipality of Gallicano, some 800 m ENE of the monitored spring, and acquires meteorological data every 5 min. Rainfall data for the period April 2017 to March 2021 are characterized by an average annual value of 1732 mm/yr, consistent with the average annual value of about 1880 mm/yr estimated for the preceding period without data loss 2011–2016 (https://www.sir.toscana.it/pluviometria-pub). The two most abundant events recorded during the period of interest occurred on 2 February 2019 (134.8 mm) and 23 January 2021 (106.6 mm).

3 Methods

3.1 CO_2 monitoring

CO_2 concentrations are measured with a specifically designed cell built in the Pisa laboratories of CNR-IGG (Cioni et al., 2007). The apparatus relies on the measurement of variations in P_{CO2} within the cell, with P_{CO2} values expressed as percent of the total pressure. The measure is done with an IR spectrophotomer operating over the analytical range 0%–10%, with an accuracy better than ± 2% of the range. Chemical speciation calculations and salting out corrections are used to periodically verify the response of the apparatus, by exploiting Henry's law to relate carbon dioxide partial pressure (P_{CO2}) values measured in the cell to aqueous concentration ($CO_{2(aq)}$) measured in water samples. In this contribution, we focus on CO_2 time series acquired during the 2017–2021 period. We processed raw data with appropriate moving median smoothing procedures (Box and Jenkins, 1976; Velleman and Hoaglin, 1981) to filter out a number of outliers recorded during monthly maintenance operations. The moving-median smoothing approach was preferred to the moving-average smoothing because of its superior ability to reduce the impact of the outliers present in the smoothing window. Our protocol considers a standard maintenance activity that includes monthly inspection of the whole apparatus, with an interruption of about one hour of the spring water supply to the measurement equipment. Therefore, in order to eliminate the outliers due to maintenance operations without affecting the signal, we applied a moving median smoothing window of $2N + 1 = 25$ points. Following Pierotti et al. (2015), CO_2 time series have been decomposed according to Census I method (Makridakis et al., 1998) to detrend the CO_2 signal for external influences. In particular, according to Census technique, we polished the original time series for seasonal and cyclical components (combined with the additive

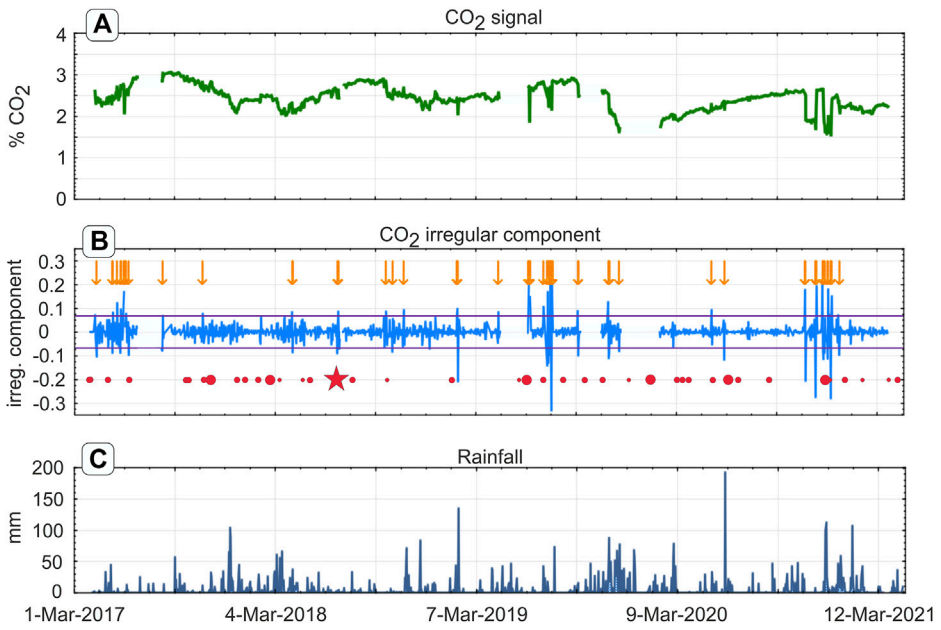

FIGURE 2
(A) CO_2 signal in vol.% of the headspace of the measurement cell; Cioni et al., 2007; Pierotti et al., 2015) acquired during the period April 2017–March 2021. **(B)** Irregular component of CO_2 time series, obtained by application of the Census I method. Purple lines represent the threshold for anomalous values (values outside this range have 99% probability of not belonging to a Pearson distribution). Orange arrows and red dots mark sixty-one (61) selected CO_2 anomalies and forty-two (42) selected seismic events (see text), respectively. Dots dimensions progressively increase with local magnitude (M_L). Seismic events are ranked into three classes of magnitude: low- (M_L <2), intermediate- (2≤ M_L <3), and high-energy events (M_L ≥3). The most energetic event of 7 January 2018 (M_L 3.6) is indicated by a red star. **(C)** rainfall at the Gallicano pluviometric station (data from https://www.sir.toscana.it/pluviometria-pub).

model) to separate a residual component called "irregular component" (Figure 2). The decomposition was performed following a step-by-step procedure that considered a reference frame of 12 months (Makridakis et al., 1998). By definition, the irregular component of the CO_2 time series is the residual CO_2 time series resulting from non-systematic, short-term fluctuations, and corresponds to the high-frequency fluctuations of the series.

3.2 Earthquake declustering

We downloaded earthquake data from the catalog of the ISIDe Working Group (Italian Seismological Instrumental and parametric database; http://iside.rm.ingv.it) to obtain a subset of "significant events" with magnitude greater or equal to 1.0. The set was declustered using the Reasemberg (1985); Gardner and Knopoff (1974) methods, as implemented in the zmap suite of Matlab tools (Wiemer, 2001). The focus was on the low seismicity period between 19 March 2017, to 18 April 2021. During this period, we identified 785 seismic events within a radius of 50 km from the Gallicano site, and a maximum hypocentral depth of 50 km. The estimated magnitude of completeness was 1.4 (Figures 3A, B), and the greatest observed local magnitude $M_L = 3.6$ (1 July 2018; epicenter near Pievepelago, about 700 m elevation, Modena Province). The areal distribution of seismicity is shown in Figure 3A, along with the traces of the main faults around the Gallicano site, whereas the distribution of hypocentral depths is shown in Figure 3C. Meteorological data were retrieved from the web archive of the Gallicano pluviometric station (https://www.sir.toscana.it/pluviometria-pub).

3.3 Statistical treatment

The identification of CO_2 anomalies from the irregular dataset was realized with a standard step-by-step method. First, we fitted the CO_2 irregular component to the shape of the input dataset. Then, we calculated the probability density value from any given test input, to evaluate the probability of each of these test input to be an anomaly. The lower the probability, the higher the likelihood of being an anomaly. Therefore, the challenge to identify anomalies was converted into the problem of setting an anomaly threshold. We considered as anomaly "1" any datum beyond this threshold, and the remaining data as anomalies "0". This approach transformed the data series into binary series, given a certain time step, where the probability of the anomaly was given by the anomaly frequency

$$P = \frac{N(1)}{N_{tot}}, \quad (1)$$

with N_{tot} being the total number of steps for any chosen time interval.

We calculated the Pearson cross-correlation coefficient R to compare pairs of data series. The Pearson correlation measures the strength of the linear relationship between two variables. It may take values between −1 and 1, with a $R = -1$ meaning total negative linear correlation, $R = 0$ no correlation, and $R = +1$ total positive

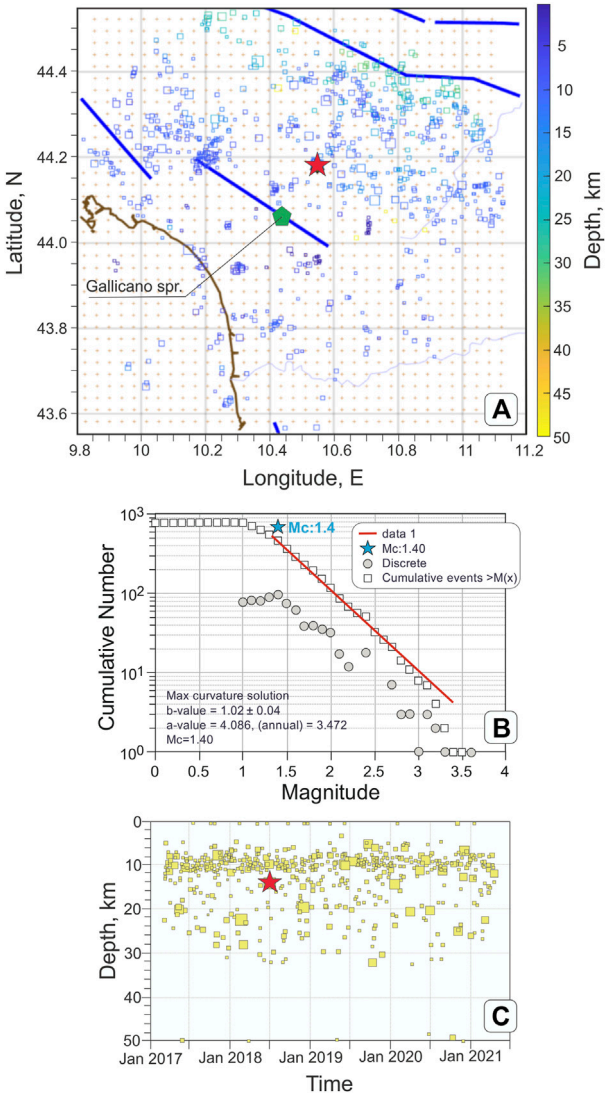

FIGURE 3
(A) Declustered earthquake dataset (785 declustered events of 3402 seismic events registered during the period), before further reduction for correlation analysis (42 seismic events after reduction). Brown line: Tyrrhenian coastline; blue line: main local faults; green pentagon: location of the Gallicano monitoring station. Dimensions and colors of square symbols indicate earthquakes magnitudes and depths, respectively, while the red star marks the most energetic seismic event occurred in the period of interest. **(B)** frequency-magnitude distribution. **(C)** earthquakes depth distribution (overall dataset, before processing).

correlation. In this study, we considered three time series, and we compared them two-by-two: CO_2 anomalies, earthquakes in the surroundings of the Gallicano site, and rainfall amounts registered at the Gallicano pluviometric station. Three Pearson correlation coefficients were then calculated, one for each of the three possible pairs. After having defined a threshold for both CO_2 anomalies and "significant earthquakes", each of these series was transformed into a binary series of events, separated by the same time step of the others series: variations in CO_2 concentration = (EC), earthquake occurrences = (EQ). The correlation coefficient between binary series is the Matthews correlation (Matthews, 1975), and possesses specific properties (Fidani, 2020):

$$corr(EQ;EC) = \frac{(\sum EQ \times EC)/N_{tot} - P(EQ)\,P(EC)}{\sqrt{P(EQ)\,[1-P(EQ)]\,P(EC)\,[1-P(EC)]}}, \quad (2)$$

where $\sum EQ \times EC$ is the number of coincidences between the two types of events that runs over the same time steps, and both $P(EQ)$ and $P(EC)$ were defined by (1). By introducing a time shift Δt, the possible time lag between the different type of events taken into consideration was evaluated by creating a correlation histogram for each pair of time series

$$corr(EQ;EC(\Delta t)) = \frac{(\sum EQ \times EC(\Delta t))/N_{tot} - P(EQ)\,P(EC)}{\sqrt{P(EQ)\,[1-P(EQ)]\,P(EC)\,[1-P(EC)]}}. \quad (3)$$

In Eq. 3, the presence of Δt indicates that the time step of the considered EC event is given by the sum $t_{EQ} + \Delta t$, where t_{EQ} is the time step of the event EQ. $P(EC)$ is defined by the EC frequency and not depends on Δt, $P(EC) = N(EC = 1)/N_{tot}$, where $N(EC)$ is the number of $EC = 1$, that is the number of CO_2 anomalies.

It was demonstrated (Fidani, 2018) that the conditional probability between two sets of digital events can be defined starting from the Matthews correlation. For negative values of the time shift ($\Delta t < 0$), the conditional probability becomes a forecasting probability. Given two EC and EQ events, with EC occurred earlier by a time $|\Delta t|$, the conditional probability of the EQ event is given by

$$P(EQ|EC(\Delta t)) = P(EQ) + corr(EQ, EC(\Delta t))\sqrt{P(EQ)[1-P(EQ)]\,[1/P(EC)-1]}. \quad (4)$$

The forecasting relation (4) means that if a correlation exists between EQ and EC values, and a CO_2 anomaly is observed, then an EQ of magnitude above the threshold is expected to occur with a probability increased by a term proportional to the correlation at a time following the CO_2 anomaly observation by $|\Delta t|$. The ratio $P(EQ|EC(\Delta t))/P(EQ)$ defines the increase in earthquake probability due to the CO_2 anomaly observation, and is called probability gain $G(\Delta t)$.

4 Results and discussion

4.1 CO_2 anomalies

The CO_2 irregular component obtained by application of the Census method was distributed on 29 amplitude intervals, and analyzed. The irregular component showed a very peaked, although symmetric distribution. We obtained adequate confidence levels of the fit distribution by means of a type VII Pearson distribution (Pearson, 1916). The four-parameter function was:

$$P(x) = \frac{A\,\Gamma[m]}{\Gamma[m-1/2]}\,[\pi\,(2m-1)]^{-1/2}\left\{1 + \frac{(x-\mu)^2}{\sigma^2\,(2m-1)}\right\}^{-m}, \quad (5)$$

where Γ is the Gamma function, μ the average, σ^2 the variance, and A a generic fitting parameter. After having selected appropriate m values to get a well-defined variance (e.g., $m = 1.51 > 3/2$), we got the

following best fitting values: $\mu = 4.8 \times 10^{-4}$, $\sigma^2 = 1.6 \times 10^{-3}$, $A = 37.246$. Due to the combination of 29 intervals and 4 parameters, the statistical system had 25 degrees of freedom. The Chi-square test gave a χ^2 value of 9.1, equivalent to a goodness of approximation >99%.

CO_2 anomalies were statistically defined by comparison with a reference threshold. Fluctuations of the CO_2 irregular component above this threshold had a 99% of probability of not occurring by chance. The cumulative probability of every fluctuation was calculated by the cumulate of the relation (5), which was demonstrated to correspond to the Gauss's hypergeometric function (Johnson et al., 1995):

$$\Pr(x) = 1/2 + \frac{(x-\mu)}{\sigma[\pi(2m-1)]^{1/2}} \frac{\Gamma[m]}{\Gamma[m-1/2]} \, {}_2F_1\left[m; 1/2; 3/2; -\frac{(x-\mu)^2}{\sigma^2(2m-1)}\right]. \quad (6)$$

Given the symmetry around the averages, positive and negative thresholds were defined as $x_+ = 0.07243$, $x_- = -0.07147$. Finally, sixty-one (61) CO_2 anomalies were selected from the CO_2 irregular component over the 1,458 days-long time interval between April 2017 and April 2021, and tagged with the number "1" in the series of daily anomalies. This analysis revealed that a CO_2 anomaly preceded by 3 days the most energetic event (M_L 3.6) of the period. Further inspection of our time series also allowed excluding any hypothetical correlation between CO_2 anomalies and major earthquakes occurred worldwide during the same period (passage of Rayleigh seismic waves; e.g., Manga and Wang, 2015), as observed elsewhere for groundwater level variations (e.g., Cooper et al., 1965; Brodsky et al., 2003; Sil and Freymueller, 2006; Shi and Wang, 2014; Zhang et al., 2015; Barberio et al., 2020; He and Singh, 2020). This assessment was based on the lack of correlation with Italian, Mediterranean, and global earthquakes with magnitude greater than or equal to 4.5, 5.5, and 6.5, respectively (see Supplementary Material S1).

4.2 Correlations

The purpose of the statistical treatment presented in this work was to explore possible correlations between declustered small earthquakes and CO_2 anomalies obtained by a Pearson type VII fit. The applicability of this approach strictly relies on the availability of a large number of data. Accordingly, we have leveraged a long-term record of CO_2 data to evaluate the characteristics of the geochemical signal, along with a relatively large number of seismic events occurred within a hypocentral radius of 50 *km* from the Gallicano station. The distance between the hypocenters of relevant earthquakes to the Gallicano spring was the basis for estimating the statistical significance of the correlations. Different theoretical and empirical models exist in the literature to correlate epicentral distance and magnitude of seismic events (e.g., Dobrovolsky et al., 1979; Ohnaka, 1992; Rikitake, 1994; Bowman et al., 1998), but their applicability is still under debate (e.g., Rebetsky and Lermontova, 2018; Woith et al., 2018), in particular for low magnitude phenomena. We considered all these models, along with an empirical correlation recently proposed for Italy (e.g., Martinelli et al., 2021, and references therein), to approximate the largest region where a physical connection could be expected between earthquake occurrences and variations in CO_2 concentration. None of these models resulted in a database of seismic events sufficiently large to be considered statistically relevant for our application (three events at most, selected over the period of interest). We thus iteratively enlarged the area of physical connection until obtaining a comparable number of selected seismic events per number of selected geochemical anomalies. This allowed to identify a maximum radius of about 47 *km*, equivalent to considering seismic events with hypocenter distances below three (3) Dobrovolsky radii ($< 3D$) from Gallicano station. Under these conditions, forty-two (42) earthquakes of M_L 1.2 to 3.6, with epicentral distances $< 40\,km$, were tagged as relevant ($EQ = 1$). This was equivalent to assuming a physical link between CO_2 anomalies and seismic events around the magnitude of completeness in the epicentral region, and in a larger area, likely beyond the borders of Tuscany region, for seismic events of moderate magnitude.

The time lag correlation was obtained by filling a histogram with each CO_2 anomaly, $\sum_{\{EQ;EC\}}(EQ \times EC)$, occurred within a temporal interval (Δt lag) of ±20 days, with respect to the date of occurrence of each selected seismic event. Moreover, a correlation histogram was also created between rain events (ER) and CO_2 anomalies, to assess any possible influence of rainfall amounts on CO_2 concentrations in spring waters. Rain events were considered to be significant ($ER = 1$) above the arbitrary rainfall threshold of $10\,mm/day$. So, another histogram based on the coincidence of one rainfall significant event with one CO_2 anomaly, $\sum_{\{ER;EC\}}(ER \times EC)$, was filled. Finally, for sake of completeness, an additional correlation histogram between rain events and seismic events was created, $\sum_{\{ER;EQ\}}(ER \times EQ)$, to possibly exclude any direct link between rainfalls and seismicity. A time difference Δt of 1 day was used for all correlation diagrams of Figure 4.

The correlation plots were drawn for time differences Δt of ± 20 days (i.e., $\Delta t = +20\,days$ and $\Delta t = -20\,days$ indicate an advance and a delay of 20 days, respectively, of the first type of event with respect to the second one). The correlation between rain and earthquake events is shown in Figure 4 (top diagram). We did not observe any significant correlation between meteorological and seismic phenomena. The middle plot of Figure 4 reports a significant peak of correlation between seismic and CO_2 events associated with a time difference Δt of −2 days. Being Δt the time difference $T_{CO_2} - T_{EQ}$, this is equivalent to say that on a statistical basis CO_2 anomalies tend to anticipate seismic events by 2 days. The cross-correlation peak corresponding to −2 days is 0.0947. We evaluated the uncertainty of the procedure by repeating the correlation calculus for 100 additional randomly generated earthquakes datasets. By obtaining correlation histograms with correlation peaks greater than 0.1 in only three cases (equivalent to 3%), we can discard the hypothesis that the correlation peak is due to chance. In an entirely equivalent way, by applying the Statistica® software (Statsoft Inc., 2013), we also obtained a p-value <5%, which further confirms that the null hypothesis can be discarded. Noteworthy, the statistical procedure has highlighted the same cross-correlation peak corresponding to −2 days also when we considered a larger temporal interval (Δt lag) of ±30 days, or a smaller earthquake dataset devoid of

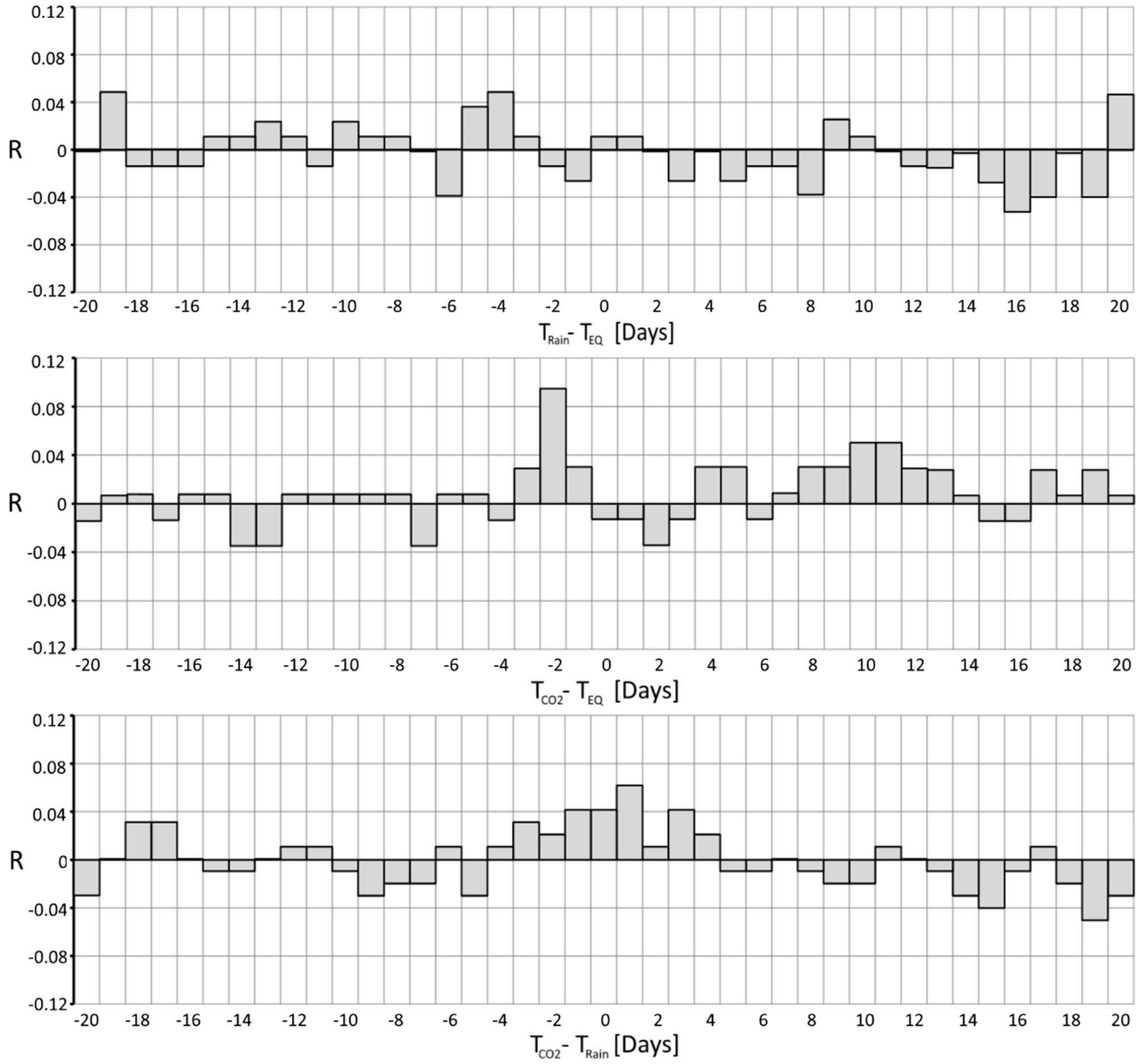

FIGURE 4
Matthews correlation coefficients in the range Δt from −20 to +20 days of the time difference between earthquake and rain events (top), CO_2 anomalies and earthquake events (middle), and CO_2 anomalies and rain events (down).

$M_L < 2$ seismic events, as shown in the Supplementary Material S1.

Based on Eq. 4, the correlation peak defines the conditional probability that a seismic event may occur 2 days after a CO_2 anomaly $P(EQ|EC)$. This probability can be significantly greater than the normal frequency of earthquakes $P(EQ) = 0.0277$ of a given magnitude, within a distance of $3\,D$ from the Gallicano station. It was calculated that $P(EQ|EC) = 3.63\,P(EQ)$, which corresponds to a probability gain of $G \approx 3.6$. The plot at the bottom of Figure 4 represents the correlation between rainfalls and CO_2 anomalies. Here, a mild correlation aroused for a time difference $\Delta t = T_{CO_2} - T_{Rain} = +1\,day$, indicating that rainfalls tend to anticipate CO_2 anomalies by 1 day.

5 Conclusion

We propose a first comprehensive statistical analysis of CO_2 time series registered at the Gallicano test site, Italy, where a continuous automatic station is operating since 2003 to investigate the geochemical response to local seismic activity of a deep aquifer feeding a thermomineral spring. The availability of continuous time series emerged as an essential prerequisite to evolve towards the calculus of the conditional property of the seismic events. The focus is on CO_2 concentration values measured in spring water during the period April 2017 to April 2021. We modeled the irregular component of the CO_2 time series by a suitable fit based on the Pearson type VII distribution, and we used the Gauss's

hypergeometric function to retrieve the cumulate probability. Based on this value, we defined the threshold for 99% probability of fluctuations not occurring by chance. We calculated the cross-correlation between the binary series of CO_2 anomalies and low to moderate magnitude seismic events, disclosing a positive correlation for CO_2 anomalies occurring 2 days before the earthquakes. We extended the procedure to rainfalls vs. earthquakes, and CO_2 vs. rainfalls time series. In both cases, we estimated negligible correlations, compared to the CO_2 vs. earthquakes case. In particular, rainfall and earthquakes appeared completely uncorrelated, and just a mild correlation was observed for rains occurring 1 day before CO_2 anomalies.

A key aspect of this analysis is that the observed positive correlation between CO_2 anomalies and seismic events concerned small earthquakes with hypocenters within relevant distances from the Gallicano spring, and that this assessment is independent from the mechanisms possibly suggested to explain the cause-effect relationship between CO_2 anomalies and small seismic events. This allows us to advance the hypothesis that CO_2 variations registered in Gallicano spring water can be considered a "short-term candidate precursor" (Molchanov and Hayakawa, 2008) for low seismic activity, regardless of whether the natural mechanisms behind this correlation inherently remain poorly constrained. From this perspective, we calculated a conditional probability based on the observation of a CO_2 anomaly, which resulted in 3.6 times the unconditioned earthquake probability. The knowledge of the conditional probability of the seismic events is, in perspective, a fundamental step to switch from the mere recognition of anomalous signals to the possible forecasting of seismic events. Future work will focus on the analysis of longer time series that also includes moderate to strong seismic activity, to augment the applicability of the method in terms of seismic hazard mitigation. Moreover, it is expected that the statistical analysis of the correlation between CO_2 anomalies and seismic events can be further refined through a more in-depth examination of the possible relations between CO_2 anomalies and rainfalls.

Data availability statement

The raw data supporting the conclusion of this article will be made available by the authors, without undue reservation.

Author contributions

CF: Conceptualization, statistical method and interpretation, Writing the original draft, review and editing FG: conceptualization, hydrogeological and geochemical framework, writing the original draft, review and editing GF: instrument implementation and maintenance, acquisition of data series, writing the original draft, review and editing LP: conceptualization, hydrogeological and geochemical framework, writing the original draft, review and editing. All authors contributed to the article and approved the submitted version.

Acknowledgments

We warmly acknowledge the reviewers for their constructive criticisms, and L. Pinti for his editorial supervision.

Conflict of interest

The authors declare that the research was conducted in the absence of any commercial or financial relationships that could be construed as a potential conflict of interest.

Publisher's note

Supplementary material

The Supplementary Material for this article can be found online at: https://www.frontiersin.org/articles/10.3389/feart.2023.1128949/full#supplementary-material

References

Anderson, R. V. V. (1927). Tertiary stratigraphy and orogeny of the Northern Punjab. *Geol. Soc. Am. Bull.* 38, 665–720. doi:10.1130/gsab-38-665

Barberio, M. D., Gori, F., Barbieri, M., Billi, A., Caracausi, A., De Luca, G., et al. (2020). New observations in Central Italy of groundwater responses to the worldwide seismicity. *Sci. Rep.* 10, 17850. doi:10.1038/s41598-020-74991-0

Barnes, I., Irwin, P. W., and White, D. E. (1978). "Global distribution of carbon dioxide discharges, and major zones of seismicity," in *Water resources investigation WRI 78-39* Editors I. Barnes, W. P. Irwin, and D. E. White (Washington: U.S. Geological Survey), 1–17.

Bowman, D. D., Ouillon, G., Sammis, C. G., Sornette, A., and Sornette, D. (1998). An observational test of the critical earthquake concept. *J. Geophys. Res.* 103, 24359–24372. doi:10.1029/98JB00792

Box, G. E. P., and Jenkins, G. M. (1976). *Time series analysis: Forecasting and control.* San Francisco: Holden Day.

Bräuer, K., Kämpf, H., Strauch, G., and Weise, S. M. (2003). Isotopic evidence (^{3}He/^{4}He, δ^{13}C-CO_2) of fluid-triggered intraplate seismicity. *J. Geophys. Res.* 108 (B2), 2070. doi:10.1029/2002JB002077

Brodsky, E. E., Roeloffs, E., Woodcock, D., Gall, I., and Manga, M. (2003). A mechanism for sustained groundwater pressure changes induced by distant earthquakes. *J. Geophys. Res.* 108, 88. doi:10.1029/2002JB002321

Camarda, M., Caracausi, A., Chiaraluce, L., De Gregorio, S., and Favara, R., (2018). Two years of geochemical monitoring along the Alto Tiberina Fault (Italy): New inferences on fluids and seismicity in central Apennines. In Proceedings of the 20th EGU General Assembly, Vienna, Austria, 4–13 April 2018.

Camarda, M., De Gregorio, S., Di Martino, R. M. R., and Favara, R. (2016). Temporal and spatial correlations between soil CO_2 flux and crustal stress. *J. Geophys. Res.* 121, 7071–7085. doi:10.1002/2016JB013297

Cardellini, C., Chiodini, G., Frondini, F., Avino, R., Bagnato, E., Caliro, S., et al. (2017). Monitoring diffuse volcanic degassing during volcanic unrests: The case of campi flegrei (Italy). *Sci. Rep.* 7 (1), 6757–6815. doi:10.1038/s41598-017-06941-2

Chiodini, G., Cardellini, C., Amato, A., Boschi, E., Caliro, S., Frondini, F., et al. (2004). Carbon dioxide Earth degassing and seismogenesis in central and southern Italy. *Geophys. Res. Lett.* 31 (7). doi:10.1029/2004GL019480

Chiodini, G., Cardellini, C., Di Luccio, F., Selva, J., Frondini, F., Caliro, S., et al. (2020). Correlation between tectonic CO_2 Earth degassing and seismicity is revealed by a 10-year record in the Apennines, Italy. *Sci. Adv.* 6 (35), eabc2938. eabc 2938. doi:10.1126/sciadv.abc2938

Cioni, R., Guidi, M., Pierotti, L., and Scozzari, A. (2007). An automatic monitoring network installed in Tuscany (Italy) for studying possible geochemical precursory phenomena. *Nat. Hazards Earth Syst. Sci.* 7, 405–416. doi:10.5194/nhess-7-405-2007

Cooper, H. H., Jr, Bredehoeft, J. D., Papadopulos, I. S., and Bennett, R. R. (1965). The response of well-aquifer systems to seismic waves. *J. Geophys. Res.* 70, 3915–3926. doi:10.1029/JZ070i016p03915

Dall'Aglio, M., Quattrocchi, F., and Venanzi, G. (1990). La stazione automatica per lo studio dei precursori geochimici nei colli albani: Il prototipo del sottosistema geochimico della rete sismica nazionale dell'ING. *Proc. IX Convegno GNGTS 1990, CNR-Roma* 1990, 95–100. (*in Italian*).

Di Bello, G., Heinicke, J., Koch, U., Lapenna, V., Macchiato, M., Martinelli, G., et al. (1998). Geophysical and geochemical parameters jointly monitored in a seismic area of Southern Apennines (Italy). *Phys. Chem. Earth* 23, 909–914. doi:10.1016/S0079-1946(98)00118-9

Di Martino, R. M., Camarda, M., Gurrieri, S., and Valenza, M. (2013). Continuous monitoring of hydrogen and carbon dioxide at Mt Etna. *Chem. Geol.* 357, 41–51. doi:10.1016/j.chemgeo.2013.08.023

DISS Working Group (2021). *Database of individual seismogenic sources (DISS), version 3.3.0: A compilation of potential sources for earthquakes larger than M 5.5 in Italy and surrounding areas*. United States: Istituto Nazionale di Geofisica e Vulcanologia. doi:10.13127/diss3.3.0

Dobrovolsky, I. P., Zubkov, S. I., and Miachkin, V. I. (1979). Estimation of the size of earthquake preparation zones. *Pure Appl. Geophys. Pageoph* 117, 1025–1044. doi:10.1007/bf00876083

Fidani, C. (2018). Improving earthquake forecasting by correlations between strong earthquakes and NOAA electron bursts. *Terr. Atmos. Ocean. Sci.* 29 (2), 117–130. doi:10.3319/tao.2017.10.06.01

Fidani, C. (2020). Probability, causality and false alarms using correlations between strong earthquakes and NOAA high energy electron bursts. *Ann. Geophys.* 63 (5), 543. doi:10.4401/ag-7957

Fidani, C. (2021). West pacific earthquake forecasting using NOAA electron bursts with independent L-shells and ground-based magnetic correlations. *Front. Earth Sci.* 9, 673105. doi:10.3389/feart.2021.673105

Fischer, T., Matyska, C., and Heinicke, J. (2017). Earthquake-enhanced permeability – evidence from carbon dioxide release following the ML 3.5 earthquake in West Bohemia. *Earth Planet. Sci. Lett.* 460, 60–67. doi:10.1016/j.epsl.2016.12.001

Gardner, J. K., and Knopoff, L. (1974). Is the sequence of earthquakes in Southern California, with aftershocks removed, Poissonian? *Bull. Seismol. Soc. Am.* 64, 1363–1367. doi:10.1785/bssa0640051363

Gherardi, F., and Pierotti, L. (2018). The suitability of the Pieve Fosciana hydrothermal system (Italy) as a detection site for geochemical seismic precursors. *Appl. Geochem.* 92, 166–179. doi:10.1016/j.apgeochem.2018.03.009

Giudicepietro, F., Chiodini, G., Caliro, S., De Cesare, W., Esposito, A. M., Galluzzo, D., et al. (2019). Insight into Campi Flegrei caldera unrest through seismic tremor measurements at Pisciarelli fumarolic field. *Geochem. Geophys. Geosystems* 20 (11), 5544–5555. doi:10.1029/2019gc008610

Gold, T., and Soter, S. (1979). Brontides: Natural explosive noises. *Science* 204, 371–375. doi:10.1126/science.204.4391.371

Gold, T., and Soter, S. (1985). Fluid ascent through the solid lithosphere and its relation to earthquakes. *Pure Appl. Geophys.* 122 (2), 492–530. doi:10.1007/bf00874614

Gold, T., and Soter, S. (1981). *Response*: Natural explosive noises. *Science* 212, 1297–1298. doi:10.1126/science.212.4500.1297

Gold, T. (1979). Terrestrial sources of carbon and earthquake outgassing. *J. Petroleum Geol.* 1 (3), 3–19. doi:10.1111/j.1747-5457.1979.tb00616.x

Gold, T. (1999). *The deep hot biosphere*. New York: Springer, 235.

He, A., and Singh, R. P. (2020). Coseismic groundwater temperature response associated with the Wenchuan earthquake. *Pure Appl. Geophys.* 177, 109–120. doi:10.1007/s00024-019-02097-4

Heinicke, J., Koch, U., and Martinelli, G. (1995). CO_2 and Radon measurements in the Vogtland area (Germany) - a contribute to earthquake prediction research. *Geoph. Res. Lett.* 22 (7), 771–774. doi:10.1029/94gl03074

Heinicke, J., Martinelli, G., and Telesca, L. (2012). Geodynamically induced variations in the emission of CO_2 gas at san faustino (central Apennines, Italy). *Geofluids* 12, 123–132. doi:10.1111/j.1468-8123.2011.00345.x

Hubbert, M. K., and Rubey, W. W. (1959). Role of fluid pressure in mechanics of overthrust faulting: I. Mechanics of fluid-filled porous solids and its application to overthrust faulting. *GSA Bull.* 70 (2), 115–166.

Hunt, J. A., Zafu, A., Mather, T. A., Pyle, D. M., and Barry, P. H. (2017). Spatially variable CO_2 degassing in the main Ethiopian rift: Implications for magma storage, volatile transport, and rift-related emissions. *Geochem. Geophys. Geosyst.* 18, 3714–3737. doi:10.1002/2017gc006975

Irwin, W. P., and Barnes, I. (1980). Tectonic relations of carbon dioxide discharges and earthquakes. *J. Geophys. Res.* 85 (B6), 3115–3121. doi:10.1029/jb085ib06p03115

Italiano, F., Martelli, M., Martinelli, G., Nuccio, P. M., and Paternoster, M. (2001). Significance of earthquake-related anomalies in fluids of Val D'Agri (southern Italy). *Terra nova.* 13 (4), 249–257. doi:10.1046/j.1365-3121.2001.00346.x

Italiano, F., Martinelli, G., and Rizzo, A. (2004). Geochemical evidence of seismogenic-induced anomalies in the dissolved gases of thermal waters: A case study of umbria (central Apennines, Italy) both during and after the 1997–1998 seismic swarm. *Geochem. Geophys. Geosystems* 5 (11), Q11001. doi:10.1029/2004GC000720

Johnson, N. L., Kotz, S., and Balakrishnan, N. (1995). "Chapter 28," in *Continuous univariate distributions*. 2nd ed. (United States: Wiley).

King, C. Y., Zhang, W., and Zhang, Z. (2006). Earthquake-induced groundwater and gas changes. *Pure Appl. Geophys.* 163 (4), 633–645. doi:10.1007/s00024-006-0049-7

KingsleyBiagi, P., Piccolo, R., Capozzi, V., Ermini, A., Khatkevich, Y., et al. (2001). Hydrogeochemical precursors of strong earthquakes: A realistic possibility in kamchatka. *Phys. Chem. Earth C* 26 (10-12), 769–774. doi:10.1016/s1464-1917(01)95023-8

Lee, H., Muirhead, J. D., Fischer, T. P., Ebinger, C. J., Kattenhorn, S. A., Sharp, Z. D., et al. (2016). Massive and prolonged deep carbon emissions associated with continental rifting. *Nat. Geosci.* 9, 145–149. doi:10.1038/ngeo2622

Makridakis, S., Wheelwright, S. C., and Hyndman, R. J. (1998). *Forecasting methods and applications*. 3rd ed. New York: John Wiley and Sons, 642.

Manga, M., and Wang, C. Y. (2015). Earthquake hydrology. *Treatise Geophys.* 2015, 305–328. doi:10.1016/b978-0-444-53802-4.00082-8

Martinelli, G., and Albarello, D. (1997). Main constraints for siting monitoring networks devoted to the study of earthquake related phenomena in Italy. *Ann. Geophys.* 40, 1505–1522.

Martinelli, G., Ciolini, R., Facca, G., Fazio, F., Gherardi, F., Heinicke, J., et al. (2021). Tectonic-related geochemical and hydrological anomalies in Italy during the last fifty years. *Minerals* 11, 107. doi:10.3390/min11020107

Martinelli, G., and Dadomo, A. (2017). Factors constraining the geographic distribution of earthquake geochemical and fluid-related precursors. *Chem. Geol.* 469, 176–184. doi:10.1016/j.chemgeo.2017.01.006

Martinelli, G., Facca, G., Genzano, N., Gherardi, F., Lisi, M., Pierotti, L., et al. (2020). Earthquake-related signals in Central Italy detected by hydrogeochemical and satellite techniques. *Front. Earth Sci.* 8, 584716. doi:10.3389/feart.2020.584716

Massin, F., Farrell, J., and Smith, R. B. (2013). Repeating earthquakes in the yellowstone volcanic field: Implications for rupture dynamics, ground deformation, and migration in earthquake swarms. *J. Volcanol. Geotherm. Res.* 257, 159–173. doi:10.1016/j.jvolgeores.2013.03.022

Matthews, B. W. (1975). Comparison of the predicted and observed secondary structure of T4 phage lysozyme. *Biochimica Biophysica Acta (BBA) - Protein Struct.* 405 (2), 442–451. doi:10.1016/0005-2795(75)90109-9

Miller, S. A. (2013). *Advances in Geophysics*, R. Dmowska, Ed. (Amsterdam: Elsevier). 1–46.

Molchanov, O. A., and Hayakawa, M. (2008). *Seismo-electromagnetics and related phenomena*. Tokyo: Terrapub.

Molli, G., Manighetti, I., Bennett, R., Malavieille, J., Serpelloni, E., Storti, F., et al. (2021). Active fault systems in the inner northwest Apennines, Italy: A reappraisal one century after the 1920 Mw~6.5 fivizzano earthquake. *Geosciences* 11 (3), 139. doi:10.3390/geosciences11030139

Netreba, A. V., Fridman, A. I., Plotnikov, I. A., and Khurin, M. I. (1971). On the large-scale mapping of closed ore-bearing areas in the north Caucasus with the uses of gas surveying as a geochemical method. *Geokhimia* 8, 1016–1021. (*in Russian*).

Ohnaka, M. (1992). Earthquake source nucleation: A physical model for short term precursors. *Tectonophysics* 211, 149–178. doi:10.1016/0040-1951(92)90057-D

Pearson, K. (1916). Mathematical contributions to the theory of evolution, XIX: Second supplement to a memoir on skew variation. *Philosophical Trans. R. Soc. A* 216 (538–548), 429–457.

Pering, T. D., Tamburello, G., McGonigle, A. J. S., Aiuppa, A., Cannata, A., Giudice, G., et al. (2014). High time resolution fluctuations in volcanic carbon dioxide degassing from Mount Etna. *J. Volcanol. Geotherm. Res.* 270, 115–121. doi:10.1016/j.jvolgeores.2013.11.014

Pierotti, L., Botti, F., D'Intinosante, V., Facca, G., and Gherardi, F. (2015). Anomalous CO_2 content in the Gallicano thermo-mineral spring (serchio valley, Italy) before the 21 june 2013, alpi apuane earthquake (M= 5.2). *Phys. Chem. Earth, Parts A/B/C* 85, 131–140. doi:10.1016/j.pce.2015.02.007

Pierotti, L., Gherardi, F., Facca, G., Piccardi, L., and Moratti, G. (2017). Detecting CO_2 anomalies in a spring on Mt. Amiata volcano (Italy). *Phys. Chem. Earth, Parts A/B/C* 98, 161–172. doi:10.1016/j.pce.2017.01.008

Reasenberg, P. (1985). Second-order moment of central California seismicity, 1969-1982. *J. Geophys. Res.* 90, 5479–5495. doi:10.1029/jb090ib07p05479

Rebetsky, Y. L., and Lermontova, A. S. (2018). On the long-range influence of earthquake rupture zones. *J. Volcanol. Seismol.* 12, 341–352. doi:10.1134/S0742046318050068

Rikitake, T. (1994). Nature of macro-anomaly precursory to an earthquake. *J. Phys. Earth* 42, 149–163. doi:10.4294/jpe1952.42.149

Rovida, A., Locati, M., Camassi, R., Lolli, B., Gasperini, P., and Antonucci, A. (2022). *Catalogo Parametrico dei Terremoti Italiani (CPTI15)*. versione 4.0. Italy: Istituto Nazionale di Geofisica e Vulcanologia. doi:10.13127/CPTI/CPTI15.4

Shi, Z., and Wang, G. (2014). Hydrological response to multiple large distant earthquakes in the Mile well, China. *J. Geophys. Res.* 119, 2448–2459. doi:10.1002/2014JF003184

Sil, S., and Freymueller, J. T. (2006). Well water level changes in Fairbanks, Alaska, due to the great Sumatra-Andaman earthquake. *Earth Planets Space* 58, 181–184. doi:10.1186/BF03353376

Statsoft Inc. (2013). *STATISTICA (data analysis software system) version 12 for windows: Statistics*. Tulsa, OK.: STATSOFT Inc.

Stucchi, M., Meletti, C., Montaldo, V., Crowley, H., Calvi, G. M., and Boschi, E. (2011). Seismic hazard assessment (2003–2009) for the Italian building code. *Bull. Seismol. Soc. Am.* 101 (4), 1885–1911. doi:10.1785/0120100130

Tamburello, G., Pondrelli, S., Chiodini, G., and Rouwet, D. (2018). Global-scale control of extensional tectonics on CO_2 Earth degassing. *Nat. Commun.* 9, 4608. doi:10.1038/s41467-018-07087-z

Velleman, P. F., and Hoaglin, D. C. (1981). *Applications, basics, and computing of exploratory data analysis*. Boston, MA: Duxbury Press.

Ventura, G., Cinti, F. R., Di Luccio, F., and Pino, N. A. (2007). Mantle wedge dynamics versus crustal seismicity in the Apennines (Italy). *Geochem. Geophys. Geosys.* 8, Q02013. doi:10.1029/2006gc001421

Weinlich, F. H., Faber, E., Boušková, A., Horálek, J., Teschner, M., and Poggenburg, J. (2006). Seismically induced variations in mariánské lázně fault gas composition in the NW bohemian swarm quake region, Czech republic—a continuous gas monitoring. *Tectonophysics* 421 (1-2), 89–110. doi:10.1016/j.tecto.2006.04.012

Wiemer, S. (2001). A software package to analyze seismicity: ZMAP. *Seismol. Res. Lett.* 72 (3), 373–382. doi:10.1785/gssrl.72.3.373

Woith, H., Petersen, G. M., Hainzl, S., and Dahm, T. (2018). Review: Can animals predict earthquakes? *Bull. Seismol. Soc. Am.* 108, 1031–1045. doi:10.1785/0120170313

Yoshida, K., and Hasegawa, A. (2018). Hypocenter migration and seismicity pattern change in the yamagata-fukushima border, NE Japan, caused by fluid movement and pore pressure variation. *J. Geophys. Res. Solid Earth* 123 (6), 5000–5017. doi:10.1029/2018jb015468

Zhang, Y., Fu, L. Y., Huang, F., and Chen, X. (2015). Coseismic water-level changes in a well induced by teleseismic waves from three large earthquakes. *Tectonophysics* 651, 232–241. doi:10.1016/j.tecto.2015.02.027

frontiers | Frontiers in Earth Science

TYPE Original Research
PUBLISHED 20 July 2023
DOI 10.3389/feart.2023.1172643

OPEN ACCESS

EDITED BY
Soumendra Nath Bhanja,
Oak Ridge National Laboratory (DOE),
United States

REVIEWED BY
Josef Vlcek,
Charles University, Czechia
Ching-Chou Fu,
Institute of Earth Sciences, Academia Sinica, Taiwan

*CORRESPONDENCE
Sofia De Gregorio,
sofia.degregorio@ingv.it

RECEIVED 23 February 2023
ACCEPTED 10 July 2023
PUBLISHED 20 July 2023

CITATION
Caracausi A, Camarda M, Chiaraluce L, De Gregorio S, Favara R and Pisciotta A (2023), A novel infrastructure for the continuous monitoring of soil CO_2 emissions: a case study at the alto Tiberina near fault observatory in Italy. *Front. Earth Sci.* 11:1172643. doi: 10.3389/feart.2023.1172643

A novel infrastructure for the continuous monitoring of soil CO_2 emissions: a case study at the alto Tiberina near fault observatory in Italy

Antonio Caracausi[1], Marco Camarda[1], Lauro Chiaraluce[2], Sofia De Gregorio[1]*, Rocco Favara[1] and Antonino Pisciotta[1]

[1]Istituto Nazionale di Geofisica e Vulcanologia, Sezione di Palermo, Palermo, Sicily, Italy, [2]National Institute of Geophysics and Volcanology (INGV), Roma, Lazio, Italy

Static and dynamic stress, along with earthquakes, can trigger the emission and migration of crustal fluids, as frequently observed on the surface and within the upper crust of tectonically active areas such as the northern Apennines of Italy. To investigate the origin of these fluids and their interconnection with the seismogenic process, we complemented The Alto Tiberina Near Fault Observatory (TABOO-NFO), a multidisciplinary monitoring infrastructure composed of a dense array of seismic, geodetic, strain, and radon sensors, with a proper geochemical network grounded on four soil CO_2 flux monitoring stations and weather sensors, placed near the main vents of the superficial manifestations. The TABOO-NFO is a state-of-the-art monitoring infrastructure, which allows for studying various geophysical parameters connected to the deformation processes active along a crustal fault system dominated by the Alto Tiberina fault (ATF), which is a 60 km long normal fault dipping at a low angle (<15°–20°). The region is favourable for conducting geochemical studies, as it is characterised by the presence of over-pressurised fluids trapped at certain depths and superficial manifestations associated with the emission of large quantities of fluids. After describing the theoretical framework and the technological aspects based on which we developed the geochemical monitoring network, we described the data recorded in the first months. Over the studied period, the results showed that soil CO_2 flux was primarily influenced by environmental parameters, and that the selected sites received a regular supply of deep-origin CO_2.

KEYWORDS

soil CO_2 emissions, Tiberina fault, tectonic stress and strain, TABOO-NFO, seismogenic processes

1 Introduction

Crustal faults are complex natural systems whose mechanical properties change over time. Hence, understanding multi-scale chemical-physical processes, which control rock deformation, faulting, and seismicity, requires the examination of processes at the boundaries between different research fields, and the availability of multidisciplinary long-term series of data. To fulfil this aim, the Italian National Institute of Geophysics

and Vulcanology created The Alto Tiberina Near Fault Observatory (TABOO-NFO) (Chiaraluce et al., 2014) located in the upper Tiber Valley within the inner sector of the northern Apennines (Italy). TABOO continuously monitors at a high rate and resolution a relatively small and actively deforming area (120 km × 120 km) using state-of-the-art geophysical networks comprising multidisciplinary instruments (Chiaraluce et al., 2014). Specifically, TABOO focuses on investigating preparatory processes, slow and fast deformations along a fault system, dominated by a 60 km long low-angle normal fault (Alto Tiberina fault, ATF), active since the Quaternary. The region is characterised by high-pressure fluids (mainly CO_2) at a certain depth (Chiodini and Cioni, 1989; Chiodini et al., 2004) and very high flux of CO_2 emissions (up to 5,800 t/yr) on the surface in the absence of any evidence of active volcanism (Italiano et al., 2009; Burton et al., 2013). The ATF strongly influences the redistribution of CO_2-rich emissions and represents a key pathway for gas transfers from regions deep below the surface to the surface (e.g., Chiodini et al., 2000; 2004; Collettini et al., 2008). Indeed, the ATF crosscuts the entire upper crust, showing continuous microseismic events from 15 km to 4 km below the surface (Chiaraluce et al., 2007; Valoroso et al., 2017). Regarding this aspect, several studies have shown that tectonic stress can influence the circulation of crustal fluid, generating detectable changes in the superficial fluid discharge (Horálek and Fischer, 2008; Wang and Manga, 2010; De Gregorio et al., 2012; Carapezza et al., 2018; Martinelli et al., 2021; Liu et al., 2022). Several studies have extensively investigated the relationships between fluid circulation and tectonic stress in the West Bohemia-Vogtland district, a natural laboratory that displays frequent earthquake swarms and anomalous fluid emissions (Weinlich et al., 2006; Bräuer et al., 2008; Bräuer et al., 2009; Faber et al., 2009; Weinlich et al., 2013; Fischer et al., 2014; Fischer et al., 2017; Fischer et al., 2020). Also, in Central Italy, the relationships between fluid circulation and tectonic stress were comprehensively examined in the last decade by conducting dedicated geochemical investigations at the regional and local scales, searching for the key elements describing fluid circulation processes and variations in the chemical composition of gases and solids dissolved in cold and thermal groundwater (Heinicke et al., 2000; Italiano et al., 2004; Caracausi et al., 2005; Heinicke et al., 2006; Italiano et al., 2009; Bonfanti et al., 2012; Chiodini et al., 2020; Martinelli et al., 2020; Di Luccio et al., 2022). The relationship between tectonic stress and fluid circulation is not completely constrained. According to Sibson (1994) and Miller et al. (2004), tectonic stress can modify the properties of rocks, such as porosity, permeability, and pore fluid pressure. Buttitta et al. (2020) showed that micro-fracturation due to the stress field generated by the local seismicity can increase the release of volatiles stored in the rocky matrix. The flow of fluids into fault zones can trigger two main types of weakening mechanisms that operate over different timescales and facilitate the movement of faults by reducing the shear stress or frictional resistance to slip. Crustal fluids can be trapped by low-permeability mature fault zone seals or stratigraphic barriers (Yang et al., 2021). Doglioni et al. (2014) inferred that crustal fluids flow can be controlled by the formation of dilated or over-compressed bands along active fault zones and that tectonic-related fluids anomalies recorded at surface depend on the tectonic style and the stage of the seismic cycle (interseismic, pre-seismic, co-seismic, and post-seismic). Besides undergoing the influence of tectonic stress acting in the crust, fluids can play an active role in seismogenic processes since an increase in fluid pore pressure can induce seismicity via a decrease in the shear strength of the faults (Sibson, 1994; Hickman et al., 1995; Miller et al., 2004). Specifically for Apennine earthquakes, fluid over-pressure is a key triggering mechanism (Chiodini et al., 2004; Miller et al., 2004; Antonioli et al., 2005; Collettini et al., 2008; Di Luccio et al., 2022). In this framework, the area of the ATF represents a natural laboratory to investigate the relationship between soil CO_2 flux variations and tectonic crustal stress. To realise this aim, within TABOO-NFO, we established a network of four stations to continuously monitor the soil CO_2 flux at the sites of CO_2-rich gas emissions. In this study, we described the characteristics of monitoring stations, the criteria, and the investigations conducted to select the monitoring sites, and finally, we discussed the data acquired during the first 5 months of monitoring.

2 General frameworks and rationales

The northern Apennines consist of a complex pattern of thrusts, folds, and normal faults, which reflect the superposition of several tectonic phases. The last two phases consist of a compressional phase during upper Miocene-lower Pleistocene, generating N-NE verging thrusts and folds, and a Quaternary extensional phase, forming intermountain basins bounded by NW-SE trending normal faults and offsetting earlier structures (Barchi et al., 1998; Boncio et al., 2000; Collettini and Barchi, 2002; Pauselli et al., 2006). The ATF is found in this region and represents the youngest and eastern expression of crustal extension in the northern Apennines. It is located in the inner sector of the Umbria-Marche Apennines, where an extensional stress field is currently active (Barchi et al., 1998; Boncio et al., 2000; Collettini and Barchi, 2002; Pauselli et al., 2006). The ATF is a 60 km long NNW-trending low-angle normal fault (LANF) dipping toward the ENE (Chiaraluce et al., 2007) (Figure 1). It has accumulated a minimum time-averaged long-term slip rate of about 1–3 mm/year in the last two million years without large historical events unambiguously associated with this fault (Chiaraluce et al., 2007; Mirabella et al., 2011; Latorre et al., 2016). More seismic reflection profiles provided by the CROP03-NVR data (Crosta Profonda Project Near Vertical Reflection) showed that in the northern Apennines, the extension is mainly accommodated by a system of east-dipping LANF with associated high-angle antithetic structures (Figure 2A) (Pialli et al., 1998). From a seismological perspective, the ATF is characterised by an active hanging wall block and an aseismic footwall. In the hanging wall block, seismic reflection profiles and seismological data showed that moderately to steeply synthetic and antithetic structures were present (Chiaraluce et al., 2007; De Luca et al., 2009; Valoroso et al., 2017). Micro-earthquakes (ML < 2.5) continuously nucleate along the ATF plane, whereas the higher angle synthetic and antithetic structures located within the hanging wall block usually generate seismic sequences led by events of relatively larger (ML < 3.7) magnitudes (Chiaraluce et al., 2007). Vuan et al. (2020) systematically investigated the seismicity patterns and concluded that a source of overpressurised fluids was present in the fault footwall. This inference matched with those of previous studies on

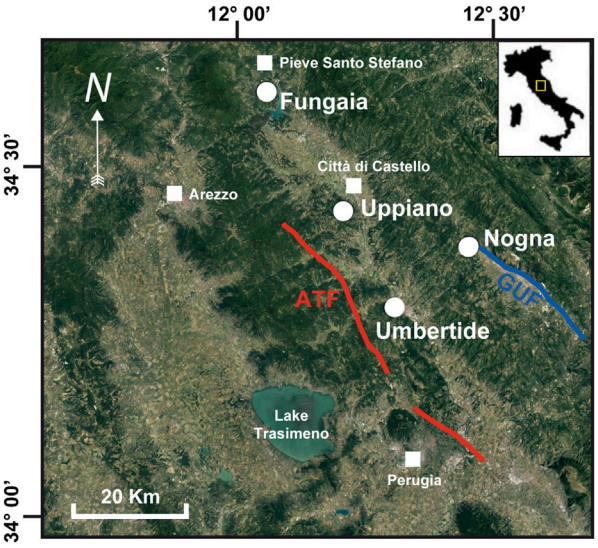

FIGURE 1
A Google Earth satellite image of the investigated area is shown with the Alto Tiberina Fault (ATF), GUF (Gubbio Fault) and the four monitoring sites at Fungaia, Uppiano, Umbertide, and Nogna.

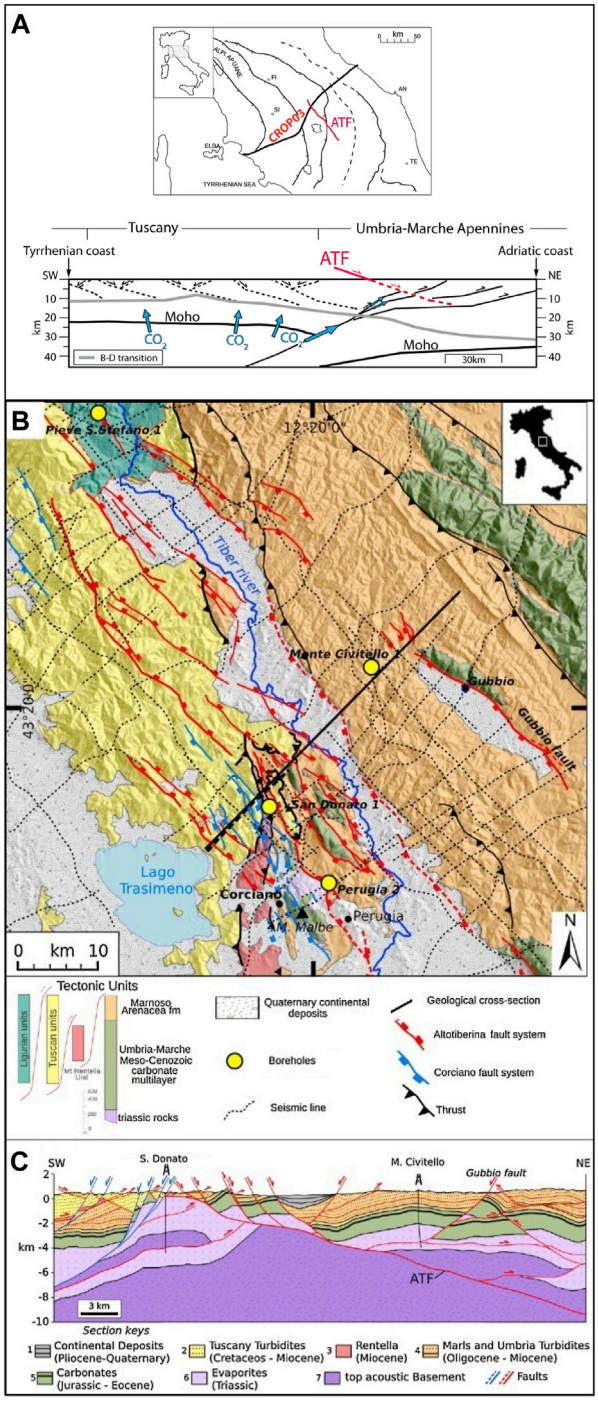

FIGURE 2
(A) Cross-section, based on the CROP03 deep seismic reflection profile (after Barchi et al., 1998), modified from Trippetta et al. (2013) and Collettini and Barchi, (2002) and conceptual model of deep CO_2 degassing from Chiodini et al. (2004; 2011). **(B)** Geological sketch of the study area and **(C)** geological section showing the depth geometries of the structures (modified from Trippetta et al. (2013) and Mirabella et al. (2011).

seismicity patterns characterizing the main seismic sequences that occurred in this sector of the Apennines that found that fluid overpressure can promote the generation of prolonged aftershock sequences (Miller et al., 2004; Antonioli et al., 2005; Collettini et al., 2008; Chiarabba et al., 2009). The presence of deep-seated CO_2 reservoirs along the ATF is confirmed by the data on two deep boreholes drilled in the area (Figure 2B). Specifically, the S. Donato borehole placed about 20 km NW of the town of Perugia encountered an overpressure of 99 MPa at depths of 4,700 m and the Pieve S. Stefano borehole encountered CO_2 overpressure of about 67 MPa at depths of 3,700 m (Chiodini and Cioni, 1989). This area has deep CO_2-rich fluids and a complex structural arrangement of faults (Figure 2C). In this scenario, the fluids along the pathway that rise to the surface can be entrapped when encountering stratigraphic or structural seals (Collettini and Barchi, 2002; Chiodini et al., 2004). In geological traps, the continuous input of CO_2 leads to the formation of CO_2 reservoirs. The gases tend to escape from the overpressurised reservoirs via low-permeability zones mainly placed along tectonic discontinuities present in the upper crust, generating numerous surface manifestations consisting of cold CO_2-rich gas seepages (Minissale et al., 2000; Chiodini et al., 2000; Rogie et al., 2000; Chiodini et al., 2004; Minissale, 2004; Italiano et al., 2009; Trippetta et al., 2013). Though, CO_2-rich seepage sites and CO_2 trapped at depth were placed only on the western side of the Tiber River (e.g., S. Donato and Pieve Santo Stefano wells), whereas no CO_2-rich seepage sites were found on the eastern side. Furthermore, in a deep borehole drilled on the eastern side of the Tiber River, Montecivitello (Figure 2B), no CO_2 trapped at depth was encountered (Trippetta et al., 2013). According to Trippetta et al. (2013) the key parameters driving CO_2 trapping are: the distance from the deep CO_2 source and the structural setting. In particular, the western side of the Tiber River is closer to the deep CO_2-degassing area outlined by Chiodini et al. (2004). Further, on the western side the formation trapping the CO_2, i.e., the Triassic Evaporites of the Burano Fm.(TE) is placed in the footwall of the ATF (Figure 2C) and the maximum fault displacement, on the order

of 10 km is observed (Mirabella et al., 2011). Conversely, on the eastern side, the TE is located in the hanging wall of both the ATF and its major antithetic (i.e., Gubbio fault, Figure 2C) (Trippetta et al., 2013).

The origin of fluids emitted in the seepage sites of the northern Apennines is a widely debated topic due to the lack of the presence of unique and consistent isotopic markers. The isotopic composition of CO_2 emitted in seepage sites displays a wide range of $\delta^{13}C$ values ranging from 1.5 to −6.1‰ (Chiodini et al., 2004; Collettini et al., 2008), and helium isotopic compositions range from 0.019 R/Ra to 1.5 R/Ra (where R is the $^3He/^4H$ ratio in the sample and Ra is the air $^3He/^4H$ ratio). These values do not correspond to a pure mantellic marker, but point out also a crustal contribution. Many of the superficial manifestations linked to fluid emission (seepage sites) are located along the Tiber Valley, which runs parallel to the east (e.g., hanging wall) of the ATF breakaway zone. Thus, both the periodic monitoring of the variations in chemical and isotopic composition of fluids emitted from main vents of seepage sites and the high-frequency acquisition of the soil CO_2 flux emitted around them, are important issues that need further investigation. Through the periodic monitoring of the chemical and isotopic composition of gases emitted in main vents of seepage sites the origin of the emitted fluids can be evaluated. Whereas, using contemporaneous high-frequency (hourly) monitoring of soil CO_2 flux emitted around the main vents the acquired data can be compared with high-frequency geophysical data (e.g., seismic, geodetic) to investigate possible relationships. Thus, the contemporary record of high-frequency geophysical and geochemical parameters, along with the periodic acquisition of more detailed geochemical data in the seismogenic area, is the key to building conceptual models that can describe the relationship between fluid emission seismicity patterns and faulting. These relationships might help to better understand the preparatory processes of earthquakes, including the identification of seismic precursors (e.g., transient signals detected almost regularly before the occurrence of relatively larger seismic events).

3 Seepage sites description and geochemical features

The seepage sites along the Tiber Valley generally consist of areas of high fluid discharge with dry vents and muddy water pools with bubbling gas (Minissale et al., 2000; Chiodini et al., 2004; Minissale, 2004; Heinicke et al., 2006) (Supplementary Video S1). The site selection process within the TABOO area starts with the accurate geochemical characterisation of fluids emitted by the main vents of seepage sites. It is the fundamental requirement for any study that aims to investigate the relationships between fluid variations and crustal stress changes. We selected fluid seepage sites along the ATF (Figure 1), which we sampled periodically to collect the emitted fluids for analysing the chemical and isotopic composition. Among the selected sites, we identified four sites where the fluids were released not only through the main vents but also via the surrounding soil. Depending on the superficial geological, morphological, and lithological features, deep-seated CO_2 might be released through the soil near the main vents. We adopted this strategy because, in case of an increase in fluid pressure at a certain depth, the disposal of gases can increase not only in the main vents but also along the soil. In this framework, monitoring the soil CO_2 flux is a valid proxy to detect changes in the rate of fluid emissions. However, the variations recorded in soil CO_2 flux must always be compared to the chemical and isotopic variation of fluids emitted by the main vents to better frame and understand the ongoing processes. The four sites are located far from each other and covered a distance of 50 km, almost covering the whole ATF (Figure 1). The northernmost site (Fungaia) is located 4 km southwest of the Pieve Santo Stefano village on the northern flank of Mt. Fungaia. The anomalous emission area covers a surface of about 1 km^2, and the main vent is a muddy pool with vigorous bubbling gas (Figure 3A; Supplementary Video S1). About 1.5 km westward to Fungaia, a group of CO_2-rich vents is located, known as Caprese Michelangelo (Vaselli et al., 1997; Minissale, 2004). Heinicke et al. (2006) reported anomalous fluid expulsion triggered by fluid redistribution and induced by local seismic activity in Caprese Michelangelo. For this area, detailed studies on structural control on seepage sites distributions pointed out as the main venting centers are located along a transverse system of steep faults associated with the Arbia-Val Marecchia Line (AVML) (Supplementary Figure S1) (Bonini, 2009). In addition, Bicocchi et al. (2013) suggested that Caprese Antiform acted as the main structural control on the main fluid reservoir of Caprese Michelangelo, and steep transverse faults pertaining to AVML are pathways connecting the Caprese Reservoir with the Mt. Fungaia gas seepage sites. The second site (Uppiano) is located north of Citta di Castello near the small town of Uppiano. The site consists of ferruginous bubbling pools generated by the outpouring of several springs with different chemical characteristics (Figure 3B) with a mean water temperature of 22°C. The third site (Umbertide) is located near the town of Umbertide. Unlike the other two sites, this is a man-made manifestation, indeed the seepage site was created during drilling for hydrocarbon exploration up to a depth of about 4,800 m. The site includes a semi-circular depression about 6 m deep and 15 m in diameter. A muddy water pool with vigorous bubbling gases is found at the bottom of the depression (Figure 3C). The water temperature is around 13°C, and the venting gas had a flow rate of about 16 t d^{-1} (Rogie et al., 2000). The last site (Nogna) is located 10 km northeast of Gubbio and consists of an artesian well with bubbling gases.

The chemical and isotopic composition of the collected gases is reported in Table 1. Carbon dioxide was the main component in the three sites (Table 1), whereas methane dominated the emission in Nogna. The sites in Fungaia and Umbertide had a similar chemical composition with the highest CO_2 concentration (>90%) and very low concentrations of CH_4 (<0.3%), N_2 (5%), and He (<40 ppm). Uppiano had a slightly lower CO_2 concentration (82%) along with higher concentrations of CH_4 (5%), N_2 (21%), and He (>300 ppm). Enrichment in less soluble gases relative to CO_2 was partially due to the scrubbing processes during the rise of fluids toward the surface. The emission of fluids in Uppiano was characterised by a significantly lower emission rate relative to that in Fungaia and Umbertide. A lower emission rate allows wider water-gas interactions, which promotes the scrubbing of more soluble gases. However, the carbon isotopic composition of CO_2 in the three sites was slightly variable and had a $\delta^{13}C$ range between −3.4‰ and −4.8‰. Similarly, the helium isotopic composition had a narrow range of 0.026–0.019 R/Ra. Finally, in Nogna, the CH_4

FIGURE 3
The main vents of three high CO_2 discharging sites are: **(A)** Fungaia; **(B)** Uppiano; **(C)** Umbertide. The stations were located around the main vents.

TABLE 1 Chemical and isotopic composition of bubbling gases emitted in the selected sites. CO_2, CH_4, N_2 and O_2 concentrations expressed in vol%,: He, Ne, Ar in ppm. Carbon isotope ratios ($\delta^{13}C$-CO_2) are expressed as δ‰ units vs. V-PDB. All the measured $^3He/^4He$ ratios are expressed as Rc/Ra units and normalized to the atmospheric ratio [Ra= 1.38 10^{-6} (*Ozima and Podosek, 2002*)]. Rc/Ra is the R/Ra value corrected for air component.

Site	Date	CO_2	CH_4	N_2	O_2	He	Ne	Ar	$\delta^{13}C$-CO_2	Rc/Ra
Fungaia	19/07/2017	94.1	0.2	5.0	0.03	33	0.054	28.6	−4.8	0.026
Umbertide	19/07/2017	91.0	0.2	7.0	0.7	40	0.050	34.6	−3.8	0.022
Uppiano	19/07/2017	82.4	4.4	20.9	0.05	336	0.183	208.8	−3.4	0.019
Nogna	18/07/2017	0.5	93.4	7.2	0.02	63	0.389	760.1	−12.1	0.013

concentration was >90%, and the CO_2 concentration and $\delta^{13}C$ values were the lowest (0.5% and −12.1‰, respectively). The R/Ra value of Nogna, although slightly lower, was similar to that of other sites (R/Ra =0.013). The chemical and isotopic composition of bubbling gases supported the deep origin of fluids emitted in the selected sites. Additionally, the low O_2 concentrations and the high $^4He/^{20}Ne$ ratios in all the analysed gas samples indicated that these gases had low air contamination.

4 Methods

4.1 The stations

The monitoring stations (Figure 4A) were designed and developed by the INGV staff following the methodology proposed by Camarda et al. (2016). Each station (Figure 4B) had a data logger with an on-board programmable real-time clock, an electronic circuit board for signal and power supply input (input module), a GSM modem for telemetry, a CO_2 Infrared Gas Analyser (IRGA; NG Gascard, manufactured by Edinburgh Gas Sensors, accuracy 2% full scale 0%–10% vol. or 0%–100% vol., depending on the site), and a pneumatic module consisting of a pump, an electrovalve, and a fluxmeter. The power supply was provided by a solar panel, a charge controller, and a battery. The stations acquired hourly data on the soil CO_2 flux and main environmental parameters and transmitted the recorded data to the INGV acquisition centre daily.

4.2 Soil CO_2 flux measurement

The soil CO_2 flux was measured by using the dynamic concentration method (Camarda et al., 2006). Using this method,

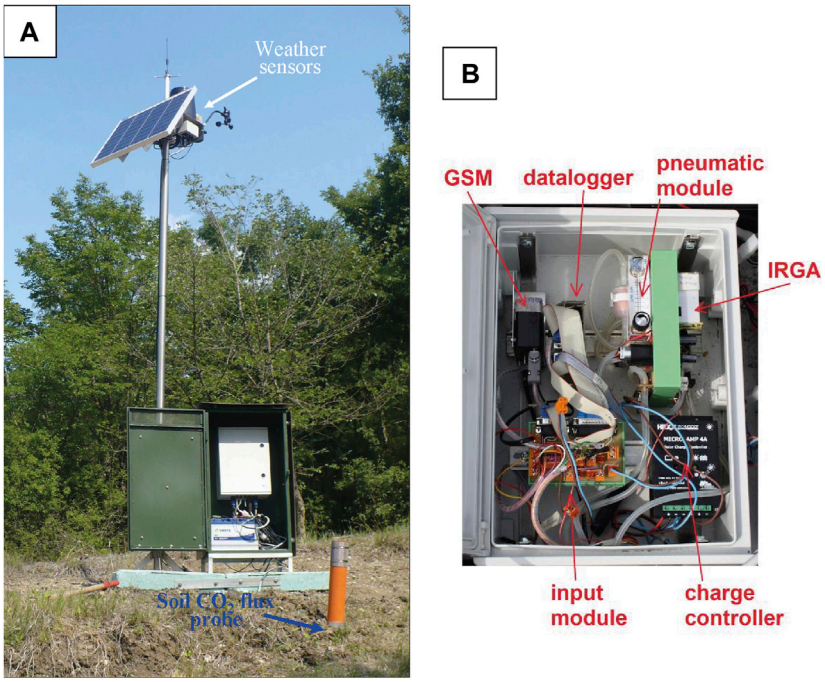

FIGURE 4
Monitoring station. **(A)** The arrangement of the monitoring station: the orange tube is the upper part of the soil CO_2 measurement probe, and the lower part of the probe was inserted 50 cm into the soil. The green case had a watertight box carrying the electronic devices and the battery. The weather sensors and solar panels were installed on top of the steel pool. **(B)** The details of the inner part of the station with the layout of the main components.

the CO_2 concentration was measured in a mixture of air and soil gas generated in a specially designed probe, which was inserted 50 cm below the soil surface. The gas mixture was obtained by producing a very small negative pressure in the probe using a pump at constant flux. The concentration of CO_2 in the mixture was determined by using the IRGA. After keeping the pump on for a certain time (generally less than 1 min), the gas mixture reached a constant CO_2 concentration, known as the dynamic concentration, which is proportional to the soil CO_2 flux. The relationship used to calculate the CO_2 flux from dynamic concentration values was determined in the laboratory by measuring the dynamic concentration several times in a soil layer that had known and constant values of CO_2 flux (Camarda et al., 2006). Four soil samples with air permeability ranging from 0.36 to 123 μm^2 were examined; such a wide range adequately represented the range of permeability values normally found in the soil.

4.3 Environmental parameters

The emission of gases from the soil is strongly influenced by environmental parameters, such as atmospheric pressure, air temperature, and precipitation (Granieri et al., 2003; Viveiros et al., 2009; De Gregorio et al., 2013; Laiolo et al., 2016; Camarda et al., 2019). These factors can directly modulate the CO_2 emission generating forced flux and also modulate indirectly by inducing changes in the physical characteristics of the soil such as diffusion coefficient, permeability, and soil volumetric water content (VWC). Information on these parameters is hence required to adequately filter the signal of soil CO_2 flux. Thus, the soil CO_2 flux stations were equipped with sensors for measuring the atmospheric parameters and soil characteristics. Weather sensors were placed at the top of a steel pool close to the station to measure the air temperature, atmospheric pressure, and precipitation (Figure 4A). To directly measure soil proprieties, a sensor for measuring the soil VWC was inserted 50 cm below the soil surface.

4.4 Soil gas sampling and isotope measurements

Soil gases were sampled at a depth of 50 cm using a Teflon tube (5 mm in diameter) connected to a syringe. Then, the gas was stored in glass flasks equipped with vacuum stopcocks. The isotopic composition of carbon in the collected CO_2 was measured using a Finnigan Mat Delta Plus Mass Spectrometer. The isotopic values were expressed as $\delta^{13}C$ in per mill relative to the Vienna Pee Dee Belemnite (V-PDB) standard; the uncertainty was ±0.2‰.

4.5 Feature checks

Whether each monitoring station was working properly was checked by analysing daily data; any errors were noted to arrange maintenance interventions in advance. Field maintenance campaigns were periodically performed to repair the detected faults. Maintenance included specific tests to verify the functionality of all the pneumatic components and the IRGA. To

test whether the IRGA was working properly, an independent measurement of the soil CO_2 flux was performed each time using a portable IRGA. Then, the value of CO_2 flux was compared with the flux value acquired by the station.

5 Selection of soil CO_2 monitoring sites

In the selected seepage sites, CO_2 was released not only through the main vents but also via the surrounding soil. The selection of the soil CO_2 flux monitoring site is important for recording variations linked to changes in the crustal stress and the associated deformations. A basic requirement is that the site must receive a deep supply of CO_2. Generally, in the soil, CO_2 is produced by superficial organic processes, such as microbial decomposition of soil organic matter and root respiration. A deep supply of CO_2 is recorded in soils located in areas undergoing tectonic and volcanic activity (Burton et al., 2013; Camarda et al., 2019; Di Martino et al., 2020). Deep-origin CO_2 can derive directly from the mantle, by the exsolution from a magmatic rising body, via the decarbonation of crustal limestone and from deep-seated sediments rich in organic matter (Chiodini et al., 2004; Lee et al., 2016; Camarda et al., 2020). The deep-origin gases, such as CO_2 and He, migrate to the surface preferentially through faults and high permeability zones (McCaig, 1989; Rowland and Sibson, 2004; Caracausi et al., 2013; Cui et al., 2019; Yang et al., 2021). Thus, they are particularly sensitive to crustal stress changes and also to processes acting within the crust, in general.

The soil CO_2 flux values ascribable to the CO_2 of organic origin are known, and several studies reported values, ranging from 0.2 to 21 g m^{-2} d^{-1}, for various ecosystems (Raich and Schlesinger, 1992; Raich and Tufekcioglu, 2000). Hence, to detect a deep supply component, it is usually used a threshold value that exceeded the value generally recorded in various ecosystems, i.e., 21 g m^{-2} d^{-1} (Raich and Schlesinger, 1992; Raich and Tufekcioglu, 2000).

In certain situations, however, sites with typical CO_2 values of biogenic origin might also receive a deep CO_2 supply during the anomalous release of fluid linked to crustal transients (Camarda et al., 2019). Hence, these sites are the most sensitive ones for recording deep-origin soil CO_2 flux variations. However, these sites are quite difficult to identify because the process requires conducting several soil CO_2 surveys over time, and at least one survey must be performed during an anomaly emission (Camarda et al., 2019). However, since such data were unavailable for the selected areas, we started selecting sites by identifying those with soil CO_2 flux values above the organic origin threshold. For selecting the monitoring site, besides a minimum threshold value, it is important to be careful with very high values of soil CO_2 flux. A high value of the soil CO_2 flux implies a stronger influence of atmospheric and soil parameters (e.g., permeability and VWC) (De Gregorio et al., 2013; Camarda et al., 2019). Therefore, in sites with high soil CO_2 flux, temporal records showed large variations associated with environmental parameters. However, although such variations can be removed through a careful data filtering process, the variation linked to the crustal transient can be easily masked and, therefore, might be more difficult to detect. Thus, regarding the usage of soil CO_2 flux values for selecting the best monitoring site, we followed the saying "*medio stat virtus*" since, as explained above, the more suitable values of soil CO_2 flux should neither be too high nor too low.

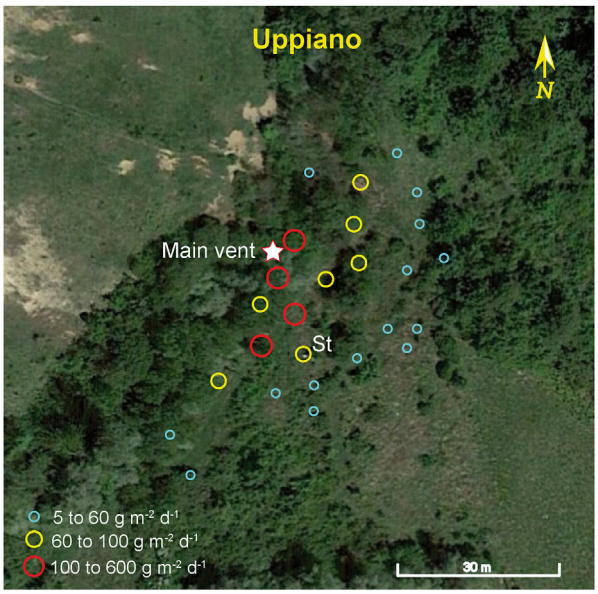

FIGURE 5
A Google Earth satellite image of the site at Uppiano. The location in which the measurements were performed to select the monitoring site with the relative soil CO_2 flux values (circles); "St" indicates the site selected for installing the monitoring station. The location of the main vent is shown by the star.

Another marker for detecting deep CO_2 supply is the isotopic composition of the carbon in soil CO_2. The CO_2 of different origins have a well-defined isotopic signature: CO_2 of atmospheric origin has values of $\delta^{13}C$ (CO_2) of −8‰ (Di Martino and Capasso, 2021); CO_2 of organic origin has values of $\delta^{13}C$ (CO_2) in the range of −30‰ to −24‰ (Hoefs, 1980; O'Leary, 1988); CO_2 of deep origin derived directly from the mantle or by the exsolution from the rising magmatic body generally have values between −4‰ and −8‰ (Pineau and Javoy, 1983; Javoy et al., 1986; Taylor, 1986). However, for volcanoes in the Mediterranean region, fewer negative values were reported (Chiodini et al., 2011). CO_2 generated via the decarbonation of crustal limestone has the same value as that of the carbonatic basement, and hence, is around or above 0‰.

Another key requirement for the monitoring site is a morphological position, avoiding stagnation or a massive flux of water. While measuring the soil CO_2 flux, water might be aspired by a pump and might enter the IRGA, permanently damaging the measuring system.

Based on the above-mentioned considerations, a fundamental step in site selection has to include at least one soil CO_2 flux survey in the surrounding location of the main emission vent coupled with isotopic determinations. Accordingly, we conducted several measurements of soil CO_2 flux and isotopic determinations in the surrounding area of each manifestation. The maps with the placements of soil CO_2 flux measurements, the main vents, and the monitoring stations are shown in Figures 5–7. In every site, the measurement points were asymmetrically distributed relative to the

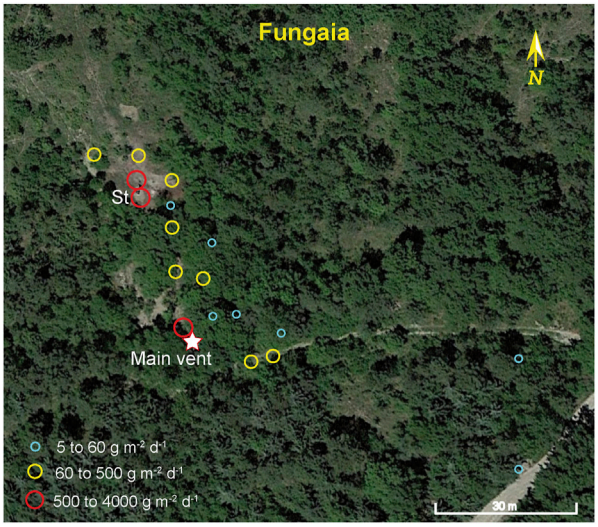

FIGURE 6
A Google Earth satellite image of the site at Fungaia. The location in which the measurements were performed to select the monitoring site with the relative soil CO_2 flux values (circles); "St" indicates the site selected for installing the monitoring station. The location of the main vent is shown by the star.

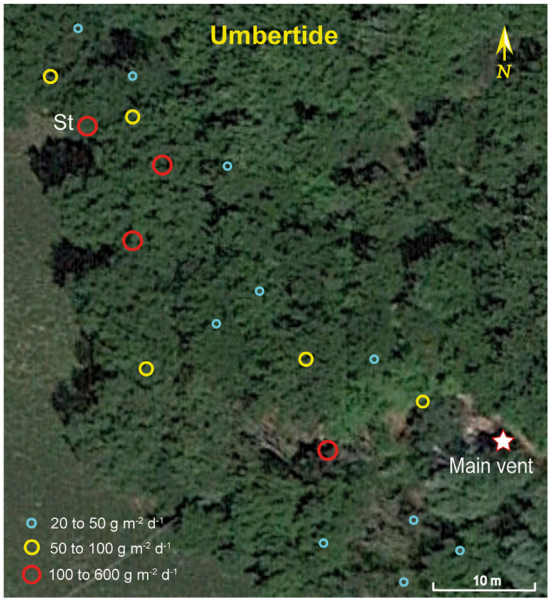

FIGURE 7
A Google Earth satellite image of the site at Umbertide. The location in which the measurements were performed to select the monitoring site with the relative soil CO_2 flux values (circles); "St" indicates the site selected for installing the monitoring station. The location of the main vent is shown by the star.

main vents, covering only one side most of the time. We were forced to operate in this way because not all areas around the main vents were accessible for technical and practical reasons.

In Uppiano (Figure 5), we performed 28 measurements over an area of about 1 km^2. The soil CO_2 flux varied from 5 to 570 g m^{-2} d^{-1}. The sites with the highest values (red dots in Figure 5) were placed closer to the main flow line, i.e., the preferential drainage area of the water. As discussed above, an area with such features is unsuitable for continuous monitoring purposes. Hence, we selected a site with a lower soil CO_2 flux value, but above the selected organic threshold value (21 g m^{-2} d^{-1}), located at the highest position. We selected the site for the suitability of its position and because it was the nearest to the highest emission zone. The $\delta^{13}C$ value of the carbon of CO_2 measured in the selected site was −2.5‰, which indicated a prevalent deep intake of CO_2.

In Fungaia, we performed 18 measurements over an area of about 600 m^2 (Figure 6) with values between 5 and 4,300 g m^{-2} d^{-1}. The site with higher flux also had an optimal morphology position since it was located on the apical part of the impluvium, which ensured good drainage of the measuring site (Figure 6). In addition, the selected site is located in a zone away from the treetops, this last feature ensured optimal exposure of the solar panel and efficient recharge of the battery. The value of $\delta^{13}C$ was −6.3‰, indicating that this site also had a high deep CO_2 component. In Umbertide, the main vent was placed in a wide almost semi-circular depression. Thus, we decided to perform the measurements outside it. The soil CO_2 flux values recorded here were lower than those recorded in Fungaia and Uppiano, and they varied between 20 and 180 g m^{-2} d^{-1}. The highest emission points were located 50 m northwest of the main vent (Figure 7). We selected the site closest to the forest border because, among other reasons, it offered the best sun exposure conditions for the solar panel. For this site, we obtained a $\delta^{13}C$ CO_2 value equal to −14.4‰. This value was between those of deep-origin CO_2 (ranging from 1.5‰ to −6‰) for the area (Chiodini et al., 2004) and those of organic origin CO_2 (−24‰), which reflected a mix between these two-end members. Thus, we inferred that this site might be suitable for recording variations in deep CO_2 supply.

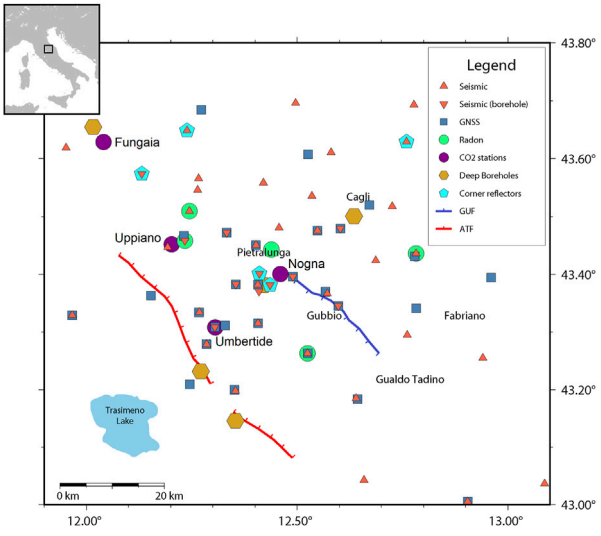

FIGURE 8
The TABOO network stations.

Finally, in Nogna, we performed a few measurements near the well. The soil CO_2 flux values were between 10 and 280 g m^{-2} d^{-1}.

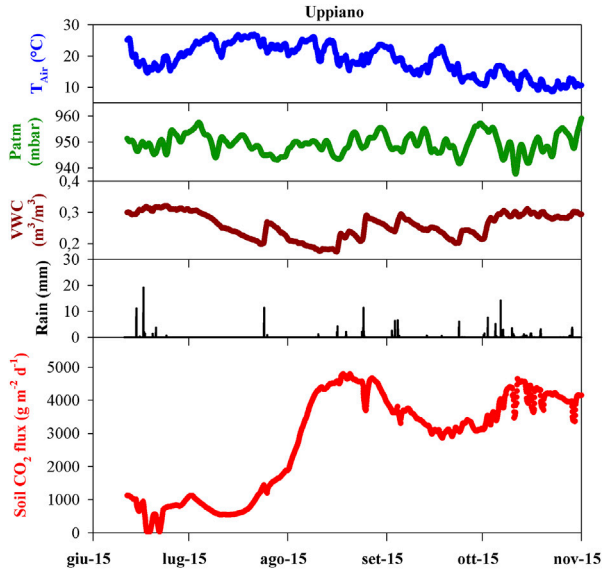

FIGURE 9
Daily running average time series of the air temperature, atmospheric pressure, VWC, precipitation, and soil CO_2 flux acquired at Uppiano.

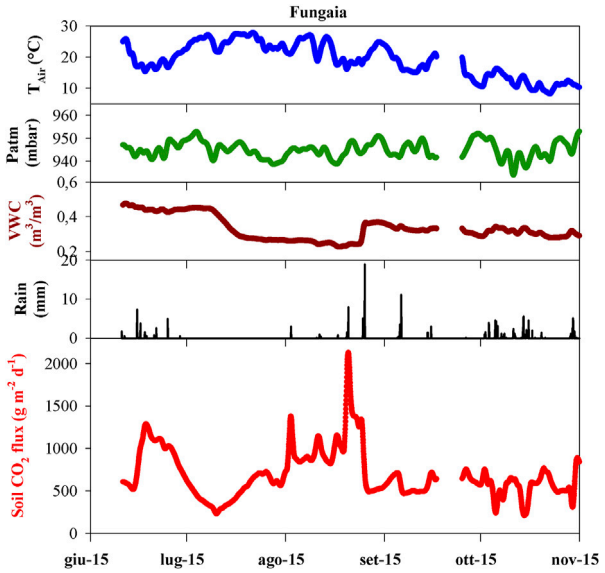

FIGURE 10
Daily running average time series of the air temperature, atmospheric pressure, VWC, precipitation, and soil CO_2 flux acquired at Fungaia.

We selected a point with a soil CO_2 flux of 200 g m^{-2} d^{-1} located between the monitoring station and the well. For this site, we obtained the lowest value of $\delta^{13}C$ CO_2 equal to −20‰. The deep CO_2 supply at this site was lower than that in other sites because the main component of the bubbling gas in the well water at this site was methane.

6 Results and discussion

After identifying the most suitable sites, we installed the stations; the stations at Fungaia and Uppiano were installed in June 2015, the station at Umbertide was installed in November 2015, and finally, the station at Nogna was installed in October 2016. As shown in Figure 8, the four soil CO_2 flux monitoring stations were well-integrated within the NFO-TABOO infrastructure.

A preparatory step for investigating the relationship between the soil CO_2 flux and tectonic stress was to identify all the processes related to the exogenous factors that affected the emission of soil CO_2. The primary exogenous factors that can influence soil CO_2 emissions were found to be environmental parameters, such as air temperature, atmospheric pressure, VWC, and precipitation (Granieri et al., 2003; Viveiros et al., 2008; Camarda et al., 2019). Besides directly modulating the soil CO_2, these parameters can also change the soil properties (Camarda et al., 2019). Thus, for investigating the relationship between soil CO_2 flux and atmospheric parameters we compared the time series of the soil CO_2 flux with the time series of the air temperature, atmospheric pressure, VWC, and precipitation. To minimise the stress-induced perturbations in the signals of the soil CO_2 flux, whenever possible, we used the data preceding the earthquake (ML = 6.0) that occurred on 24 August 2016, which affected a large part of the central

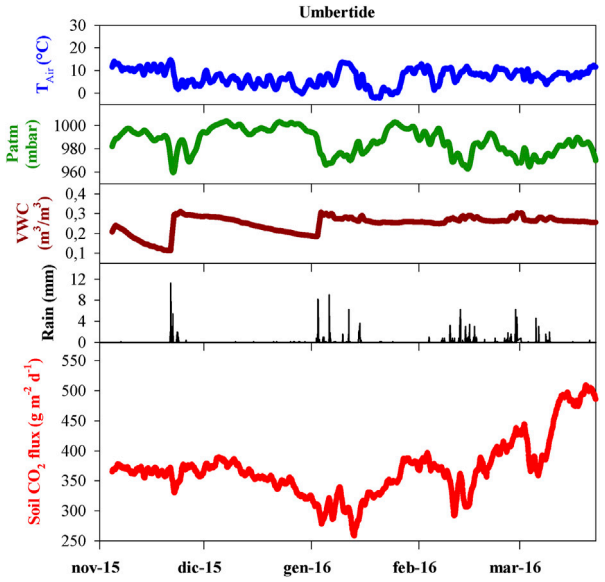

FIGURE 11
Daily running average time series of the air temperature, atmospheric pressure, VWC, precipitation, and soil CO_2 flux acquired at Umbertide.

Apennine. For consistency, we used the same time length of 5 months for all sites. The daily running average of air temperature, atmospheric pressure, the VWC, precipitation, and the soil CO_2 flux at Fungaia, Uppiano, and Umbertide are reported in Figures 9–11. The data from Nogna was not considered because the station was installed after August 2016.

TABLE 2 Basic statistical parameters for Uppiano, Fungaia e Umbartide sites.

Site	Mean soil CO_2 flux (g m^{-2} d^{-1})	Standard deviation (g m^{-2} d^{-1})	Coefficient of variation (%)	Min. (g m^{-2} d^{-1})	Max. (g m^{-2} d^{-1})
Uppiano	2,800	1,500	54	36	4,793
Fungaia	690	300	43	186	2,333
Umbertide	370	48	13	258	508

The soil CO_2 flux series are characterised by mean values that are different, ranging from 370 g m^{-2} d^{-1} at Umbertide to 2,800 g m^{-2} d^{-1} at Uppiano (Table 2). At each site, the soil CO_2 flux showed a highly uneven trend with different coefficients of variation (CV). The CV is obtained from the ratio of the standard deviation to the average and shows the extent of variability concerning the mean of the population. They varied from the lowest value of 13% at Umbertide to the highest value of 54% at Uppiano. The CV was positively correlated with the mean soil CO_2 flux, which suggested that over 5 months of observation, the variability in soil CO_2 flux was mainly induced by environmental parameters, given that the higher the flux, the heavier the influence of environmental parameters, and hence, the greater the variability.

Regarding environmental parameters, the air temperature changed with the seasonal cycle, with a maximum value of 28°C recorded in late July 2015 at Fungaia and a minimum value of −2°C recorded in mid-January at Umbertide. The time-dependent evolution of VWC was more variable because it was influenced by air temperature and precipitation. The VWC decreases when depletion caused by evapotranspiration losses exceeds input from precipitation. The VWC dynamic depends on soil moisture conditions: under dry soil conditions, precipitation sharply increases the VWC, whereas under wet soil conditions, only small fluctuations are recorded in response to the precipitation.

At Uppiano (Figure 9), during the first 2 months of monitoring, the values were low, with a mean value of 1,000 g $m^{-2}d^{-1}$. In early August, the soil CO_2 flux increased and reached an average value of 4,000 g $m^{-2}d^{-1}$ and remained around this value until the end of November 2015.

At Fungaia (Figure 10), the average value of soil CO_2 flux showed narrow long-term variability, but in the short-term, the signal displayed wide and frequent oscillations, especially from August to September 2015. In this last period, particularly intense precipitation was recorded.

At Umbertide (Figure 11), the soil CO_2 flux mean value was slightly variable and remained around a mean value of 350 g $m^{-2}d^{-1}$. From late December 2015 until the middle of January 2016, the soil CO_2 flux decreased to about 250 g $m^{-2}d^{-1}$. Then, the values increased, with episodes of small and brief decreases, reaching the maximum value at the end of March 2016. Even in this case, the period of higher variability coincided with the main rainy events.

To more comprehensively evaluate the relationship between the soil CO_2 flux and the environmental and soil parameters, we applied two different approaches: frequency analyses and multivariate regression analyses (MRA). We used frequency analysis to identify correlation on a short time scale by searching equivalent high-frequency signals among the data series of CO_2 flux and environmental parameters. The frequency analysis was performed by using the Fast Fourier Transform (FFT) method that transforms a function of time into a function of frequency. The results of FFT analysis of air temperature, atmospheric pressure, and VWC are very similar (Figure 12) displaying dominant peaks at the diurnal frequency and smaller peaks at the semidiurnal frequency. The FFT of soil CO_2 flux gives a very similar picture to that shown by atmospheric parameters and VWC. The similarity demonstrates that the soil CO_2 flux is strongly influenced by external parameters on the short time scale. The high-frequency oscillations are clearly visible in hourly data signals, for example, in Supplementary Figure S2 we reported the first period of monitoring at Fungaia site, with hourly data recording and daily running average.

To investigate the mid time scale correlations, we applied, to daily running average signals, the multiple regression analyses (MRA). The MRA is a statistical tool for the investigation of the relationships between two or more variables. In this analysis the values of one parameter are compared with one or more parameters by means of scatter plots. The degree of correlation between parameters is obtained by the value of the correlation coefficient (R) of best-fitting straight lines.

We performed the MRA among the datasets of the soil CO_2 flux, the air temperature, the atmospheric pressure, and the VWC, the results are reported in Table 3. For the air temperature and the atmospheric pressure series, to avoid perturbations induced by rainy events, we performed the MRA without considering rainy periods. In the sites, Umbertide and Uppiano, the air temperature exerts a moderate influence with positive R values of 0.41 and 0.37, respectively. The positive correlation between soil CO_2 flux is a behavior commonly observed in other environments, such as geothermal and volcanic areas (e.g., Viveiros et al., 2008). Indeed, the variation of the air temperature can modify the parameters affecting the gas transport through the soils (e.g., bulk diffusion coefficient). Then a moderate negative correlation was observed with the atmospheric pressure in the sites Umbertide and Fungaia, with R values of −0.41 and −0.34, respectively. The atmospheric pressure changes induce the subsurface motion of gases in porous media and specifically concern transport by advection driven by a pressure gradient. The phenomenon is reported in the literature as "barometric pumping" (Auer et al., 1996) and was described particularly for soil CO_2 emissions on the Island of Vulcano (Camarda et al., 2019). In detail, a decrease in atmospheric pressure enhances the pressure gradient between the gas source and the atmospheric one, leading to an increase in the soil CO_2 flux; as a result a negative correlation is observed. Lastly, the VWC has a slight negative influence on the soil CO_2 emissions, with R absolute values lower than 0.3.

Over the period under consideration, the results show the soil CO_2 flux was primarily influenced by environmental parameters, especially

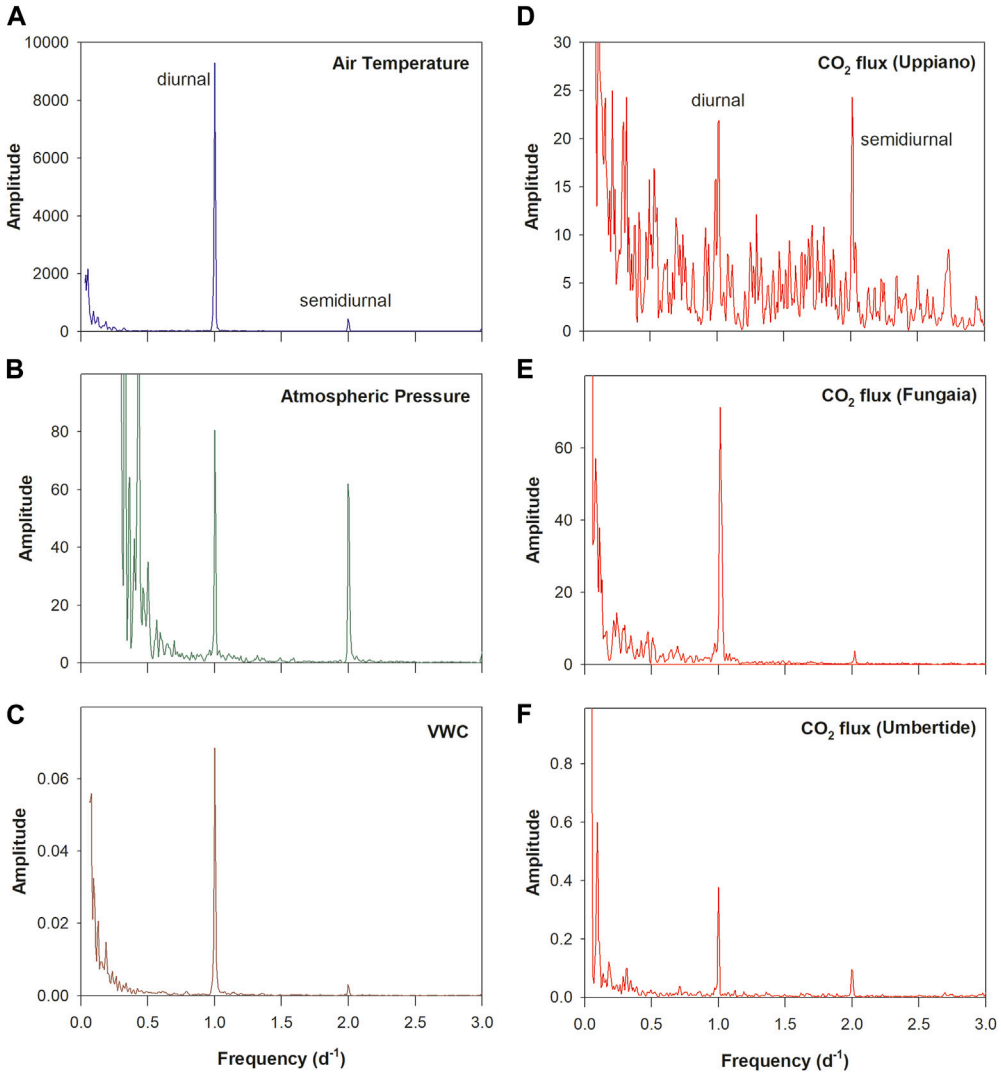

FIGURE 12
Result of Fast Fourier Trasformer analysys: **(A)** Air temperature, **(B)** Atmospheric pressure; **(C)** VWC; **(D)** Soil CO_2 flux in Uppiano site; **(E)** Soil CO_2 flux in Fungaia site; **(F)** Soil CO_2 flux in Umbertide site. Low frequencies (<0.5 d^{-1}) include noise because of relatively short duration of measurement.

TABLE 3 Correlation Matrix between soil CO_2 flux and environmental parameters.

Site	$R^a(CO_2$ flux/$T)$	$R^a(CO_2$ flux/$P_{atm})$	$R(CO_2$ flux/VWC)
Uppiano	0.37	−0.26	−0.22
Fungaia	−0.03	−0.34	−0.25
Umbertide	0.41	−0.41	0.04

[a]Correlation coefficients computed without rainy periods.

on the short time scale. On the mid time scale, only air temperature and atmospheric pressure displayed moderate influences in some sites. Overall, the soil CO_2 flux values are differently affected by the environmental parameters in each site concerning the peculiar characteristics of each. However, is noteworthy that, the soil CO_2 flux values, albeit with fluctuations, remain well above the typical values for organic-derived CO_2 (21 g $m^{-2}d^{-1}$), indicating a regular supply of deep-origin CO_2 for the selected sites.

These findings are promising for future studies on the possible links between soil CO_2 flux and stress and seismic rate variations.

The data acquired by the four stations are available in the Data Portal of the *European Plate Observing System* (EPOS) at the following web address: http://fridge.ingv.it/nfoineurope.php, along with the data from six European NFOs.

Data availability statement

The datasets presented in this study can be found in online repositories. The names of the repository/repositories and accession number(s) can be found below: Data are available inside on EPOS Data Portal—the European Plate Observing System at the following web address: http://fridge.ingv.it/nfoineurope.php.

Author contributions

AC, MC, and SD install the stations; MC and SD analysed and interpreted the data; LC and SD wrote the original draft of the manuscript; MC, LC, and SD drafted the figures. All authors contributed to the article and approved the submitted version.

Funding

Part of this work has been financially supported by the EPOS Research Infrastructure through the contribution of the Italian Ministry of University and Research (MUR).

Acknowledgments

The authors would to thank Giuseppe Messina and Ivano Carluccio for database management, Fabio Di Gangi for field work support for the installation of the stations, Santo Cappuzzo for technical support.

Conflict of interest

The authors declare that the research was conducted in the absence of any commercial or financial relationships that could be construed as a potential conflict of interest.

Publisher's note

Supplementary material

The Supplementary Material for this article can be found online at: https://www.frontiersin.org/articles/10.3389/feart.2023.1172643/full#supplementary-material

References

Antonioli, A., Piccinini, D., Chiaraluce, L., and Cocco, M. (2005). Fluid flow and seismicity pattern: Evidence from the 1997 Umbria-Marche (central Italy) seismic sequence. *Geophys. Res. Lett.* 32, L10311. doi:10.1029/2004GL022256

Auer, L. H., Rosenberg, N. D., Birdsell, K. H., and Whitney, E. M. (1996). The effects of barometric pumping on contaminant transport. *J. Contam. Hydrol.* 24, 145–166. doi:10.1016/s0169-7722(96)00010-1

Barchi, M., Minelli, R., and Pialli, G. (1998). The crop 03 profile: A synthesis of results on deep structures of the northern apennines. *Mem. Soc. Geol. Ital.* 52, 383–400.

Bicocchi, G., Tassi, F., Bonini, M., Capecchiacci, F., Ruggieri, G., Antonella Buccianti, A., et al. (2013). The high pCO2 Caprese Reservoir (Northern Apennines, Italy): Relationships between present- and paleo-fluid geochemistry and structural setting. *Chem. Geol.* 351, 40–56. doi:10.1016/j.chemgeo.2013.05.001

Boncio, P., Brozzetti, F., and Lavecchia, G. (2000). Architecture and seismotectonics of a regional low-angle normal fault zone in central Italy. *Tectonics* 19, 1038–1055. doi:10.1029/2000tc900023

Bonfanti, P., Genzano, N., Heinicke, J., Italiano, F., Martinelli, G., Pergola, N., et al. (2012). Evidence of CO_2-gas emission variations in the central Apennines (Italy) during the L'Aquila seismic sequence (March-April 2009). *B. Geofis. Teor. Appl.* 53, 147–168. doi:10.4430/bgta0043

Bonini, M. (2009). Structural controls on a carbon dioxide-driven mud volcano field in the northern apennines (Pieve Santo Stefano, Italy): Relations with pre-existing steep discontinuities and seismicity. *J. Struct. Geol.* 31, 44–54. doi:10.1016/j.jsg.2008.10.003

Bräuer, K., Kämpf, H., Niedermann, S., Strauch, G., and Tesař, J. (2008). Natural laboratory NW bohemia: Comprehensive fluid studies between 1992 and 2005 used to trace geodynamic processes. *Geochem. Geophys. Geosyst.* 9 (Q04018). doi:10.1029/2007GC001921

Bräuer, K., Kämpf, H., and Strauch, G. (2009). Earthquake swarms in non-volcanic regions: What fluids have to say. *Geophys. Res. Lett.* 36, L17309. doi:10.1029/2009GL039615

Burton, M. R., Sawyer, G. M., and Granieri, D. (2013). Deep carbon emissions from volcanoes. *Rev. Mineral. Geochem.* 75, 323–354. doi:10.2138/rmg.2013.75.11

Buttitta, D., Caracausi, A., Chiaraluce, L., Favara, R., Morticelli, M. G., and Sulli, A. (2020). Continental degassing of helium in an active tectonic setting (northern Italy): The role of seismicity. *Sci. Rep.* 10, 162. doi:10.1038/s41598-019-55678-7

Camarda, M., Gurrieri, S., and Valenza, M. (2006). CO_2 flux measurements in volcanic areas using the dynamic concentration method: Influence of soil permeability. *J. Geophys. Res.* 111, B05202. doi:10.1029/2005JB003898

Camarda, M., De Gregorio, S., Di Martino, R. M. R., and Favara, R. (2016). Temporal and spatial correlations between soil CO_2 flux and crustal stress. *J. Geophys. Res. Solid Earth* 121, 7071–7085. doi:10.1002/2016JB013297

Camarda, M., De Gregorio, S., Capasso, G., Di Martino, R. M. R., Gurrieri, S., and Prano, V. (2019). The monitoring of natural soil CO_2 emissions: Issues and perspectives. *Earth-Sci. Rev.* 198, 102928. doi:10.1016/j.earscirev.2019.102928

Camarda, M., De Gregorio, S., Di Martino, R. M. R., Favara, R., and Prano, V. (2020). Relationship between soil CO_2 flux and tectonic structures in SW Sicily. *Ann. Geophys.* 63 (1). doi:10.4401/ag-8264

Caracausi, A., Italiano, F., Martinelli, G., Paonita, A., and Rizzo, A. (2005). Long-term geochemical monitoring and extensive/compressive phenomena: Case study of the Umbria region (central apennines, Italy). *Ann. Geophys.* 48 (1), 43–53. doi:10.4401/ag-3178

Caracausi, A., Martelli, M., Nuccio, P. M., Paternoster, M., and Stuart, F. M. (2013). Active degassing of mantle-derived fluid: A geochemical study along the vulture line, southern apennines (Italy). *J. Volc. Geother. Res.* 253, 65–74. doi:10.1016/j.jvolgeores.2012.12.005

Carapezza, M. L., Barberi, F., Ranaldi, M., Tarchini, L., and Pagliuca, N. M. (2018). Faulting and gas discharge in the Rome area (Central Italy) and associated hazards. *Tectonics* 38 (3), 941–959. doi:10.1029/2018tc005247

Chiarabba, C., Amato, A., Anselmi, M., Baccheschi, P., Bianchi, I., Cattaneo, M., et al. (2009). The 2009 L'Aquila (central Italy) MW6.3 earthquake: Main shock and aftershocks. *Geophys. Res. Lett.* 36, L18308. doi:10.1029/2009GL039627

Chiaraluce, L., Chiarabba, C., Collettini, C., Piccinini, D., and Cocco, M. (2007). Architecture and mechanics of an active low-angle normal fault: Alto Tiberina Fault, northern Apennines, Italy. *J. Geophys. Res.* 112, B10310. doi:10.1029/2007JB005015

Chiaraluce, L., Amato, A., Carannante, S., Castelli, V., Cattaneo, M., Cocco, M., et al. (2014). The Alto Tiberina Near Fault Observatory (northern apennines, Italy). *Ann. Geophys.* 57 (3). doi:10.4401/ag-6426

Chiodini, G., and Cioni, R. (1989). Gas geobarometry for hydrothermal systems and its application to some Italian geothermal areas. *Appl. Geochem.* 4, 465–472. doi:10.1016/0883-2927(89)90004-8

Chiodini, G., Frondini, F., Cardellini, C., Parello, F., and Peruzzi, L. (2000). Rate of diffuse carbon dioxide Earth degassing estimated from carbon balance of regional aquifers: The case of central Apennines, Italy. *J. Geophys. Res.* 105 (B4), 8423–8434.

Chiodini, G., Cardellini, C., Amato, A., Boschi, E., Caliro, S., Frondini, F., et al. (2004). Carbon dioxide Earth degassing and seismogenesis in Central and southern Italy. *Geophys. Res. Lett.* 31, L07615. doi:10.1029/2004gl019480

Chiodini, G., Caliro, S., Cardellini, C., Frondini, F., Inguaggiato, S., and Matteucci, F. (2011). Geochemical evidences for and characterization of CO_2 rich gas sources in the epicentral area of the Abruzzo 2009 earthquakes. *Earth Planet. Sci. Lett.* 304, 389–398. doi:10.1016/j.epsl.2011.02.016

Chiodini, G., Cardellini, C., Di Luccio, F., Selva, J., Frondini, F., Caliro, S., et al. (2020). Correlation between tectonic CO_2 Earth degassing and seismicity is revealed by a 10-year record in the Apennines. *Italy.* Sci. Adv. 6 (35), eabc2938. doi:10.1126/sciadv.abc2938

Collettini, C., and Barchi, M. R. (2002). A low angle normal fault in the Umbria region (central Italy): A mechanical model for the related microseismicity. *Tectonophysics* 359, 97–115. doi:10.1016/s0040-1951(02)00441-9

Collettini, C., Cardellini, C., Chiodini, G., De Paola, N., Holdsworth, R. E., and Smith, S. A. F. (2008). Fault weakening due to CO_2 degassing in the northern apennines: Short- and long-term processes. *Geol. Soc. Lond. Spec. Publ.* 299, 175–194. doi:10.1144/SP299.11

Cui, Y. J., Li, Y., Si, X. Y., Yang, L. X., Liu, Z. F., Sun, F. X., et al. (2019). Tectonic controls on near-surface variations in CH_4 and CO_2 concentrations along the northwestern margin of the ordos block, China. *Geofluids* 2019, 1–10. doi:10.1155/2019/7909483

De Gregorio, S., Federico, C., Cappuzzo, S., Favara, R., Giudice, G., Gurrieri, S., et al. (2012). Stress-induced temperature variations in groundwater of the Monferrato area (north-western Italy). *Geofluids* 12, 142–149. doi:10.1111/j.1468-8123.2011.00348.x

De Gregorio, S., Camarda, M., Cappuzzo, S., and Gurrieri, S. (2013). An innovative method for continuous measurement of soil CO_2 flux. *Chem. Geol.* 341, 102–109. doi:10.1016/j.chemgeo.2013.01.011

De Luca, G., Cattaneo, M., Monachesi, G., and Amato, A. (2009). Seismicity in central and northern Apennines integrating the Italian national and regional networks. *Tectonophysics* 476, 121–135. doi:10.1016/j.tecto.2008.11.032

Di Luccio, F., Palano, M., Chiodini, G., Cucci, L., Piromallo, C., Sparacino, F., et al. (2022). Geodynamics, geophysical and geochemical observations, and the role of CO_2 degassing in the Apennines. *Earth-Sci. Rev.* 234, 104236. doi:10.1016/j.earscirev.2022.104236

Di Martino, R. M. R., and Capasso, G. (2021). On the complexity of anthropogenic and geological sources of carbon dioxide: Onsite differentiation using isotope surveying. *Atmos. Environ.* 256, 118446. doi:10.1016/j.atmosenv.2021.118446

Di Martino, R. M. R., Capasso, G., Camarda, M., De Gregorio, S., and Prano, V. (2020). Deep CO2 release revealed by stable isotope and diffuse degassing surveys at Vulcano (Aeolian Islands) in 2015–2018. *J. Volc. Geother. Res.* 401, 106972. doi:10.1016/j.jvolgeores.2020.106972

Doglioni, C., Barba, S., Carminati, E., and Riguzzi, F. (2014). Fault on-off versus coseismic fluids reaction. *Geosci. Front.* 5, 767–780. doi:10.1016/j.gsf.2013.08.004

Faber, E., Horálek, J., Boušková, A., Teschner, M., Koch, U., and Poggenburg, J. (2009). Continuous gas monitoring in the West bohemian earthquake area, Czech republic: First results. *Stud. Geophys. Geod.* 53, 315–328. doi:10.1007/s11200-009-0020-z

Fischer, T., Horálek, J., Hrubcová, P., Vavryčuk, V., Bräuer, K., and Kämpf, H. (2014). Intra-continental earthquake swarms in west-bohemia and vogtland: A review. *Tectonophysics* 611, 1–27. doi:10.1016/j.tecto.2013.11.001

Fischer, T., Matyska, C., and Heinicke, J. (2017). Earthquake-enhanced permeability – evidence from carbon dioxide release following the ML 3.5 earthquake in West Bohemia. *Earth Planet. Sci. Lett.* 460, 60–67. doi:10.1016/j.epsl.2016.12.001

Fischer, T., Vlček, J., and Lanzendörfer, M. (2020). Monitoring crustal CO_2 flow: Methods and their applications to the mofettes in West Bohemia. *Solid Earth.* 11 (3), 983–998. doi:10.5194/se-11-983-2020

Granieri, D., Chiodini, G., Marzocchi, W., and Avino, R. (2003). Continuous monitoring of CO_2 soil diffuse degassing at phlegraean fields (Italy): Influence of environmental and volcanic parameters. *Earth Planet. Sci. Lett.* 212, 167–179. doi:10.1016/S0012-821X(03)00232-2

Heinicke, J., Italiano, F., La Penna, V., Martinelli, G., and Nuccio, P. M. (2000). Coseismic geochemical variations in some gas emissions of Umbria region (Central Italy). *Phys. Chem. Earth* 25, 289–293. doi:10.1016/s1464-1895(00)00046-6

Heinicke, J., Braun, T., Burgassi, P., Italiano, F., and Martinelli, G. (2006). Gas flow anomalies in seismogenic zones in the upper Tiber Valley, central Italy. *Geophys. J. Int.* 167, 794–806. doi:10.1111/j.1365-246x.2006.03134.x

Hickman, S., Sibson, R., and Bruhn, R. (1995). Introduction to special section: Mechanical involvement of fluids in faulting. *J. Geophys. Res.* 100 (B7), 12831–12840. doi:10.1029/95JB01121

Hoefs, J. (1980). *Stable Isotope Geochemistry*. Berlin: Springer, 12831

Horálek, J., and Fischer, T. (2008). Role of crustal fluids in triggering the West Bohemia/vogtland earthquake swarms: Just what we know (a review). *Stud. Geophys. Geod.* 52, 455–478. doi:10.1007/s11200-008-0032-0

Italiano, F., Martinelli, G., and Rizzo, A. (2004). Geochemical evidence of seismogenic-induced anomalies in the dissolved gases of thermal waters: A case study of Umbria (central apennines, Italy) both during and after the 1997-1998 seismic swarm: 1997-1998 SEISMIC SWARM, UMBRIA. *Geochem. Geophys. Geosyst.* 5 (11). doi:10.1029/2004GC000720

Italiano, F., Martinelli, G., Bonfanti, P., and Caracausi, A. (2009). Long-term (1997-2007) geochemical monitoring of gases from the Umbria-Marche region. *Tectonophysics* 476, 282–296. doi:10.1016/j.tecto.2009.02.040

Javoy, M., Pineau, F., and Delorme, H. (1986). Carbon and nitrogen isotopes in the mantle. *Chem. Geol.* 57, 41–62. doi:10.1016/0009-2541(86)90093-8

Laiolo, M., Ranaldi, M., Tarchini, L., Carapezza, M. L., Coppola, D., Ricci, T., et al. (2016). The effects of environmental parameters on diffuse degassing at Stromboli volcano: Insights from joint monitoring of soil CO_2 flux and radon activity. *J. Volc. Geother. Res.* 315, 65–78. doi:10.1016/j.jvolgeores.2016.02.004

Latorre, D., Mirabella, F., Chiaraluce, L., Trippetta, F., and Lomax, A. (2016). Assessment of earthquake locations in 3-D deterministic velocity models: A case study from the altotiberina Near Fault Observatory (Italy). *J. Geophys. Res. Solid Earth* 121 (11), 8113–8135. doi:10.1002/2016jb013170

Lee, H., Muirhead, J. D., Fischer, T. P., Ebinger, C. J., Kattenhorn, S. A., Sharp, Z. D., et al. (2016). Massive and prolonged deep carbon emissions associated with continentalrifting. *Nat. Geosci.* 9, 145–149. doi:10.1038/ngeo2622

Liu, W., Guan, L., Liu, Y., Xie, X., Zhang, M., Chen, B., et al. (2022). Fluid geochemistry and geothermal anomaly along the Yushu-Ganzi-Xianshuihe fault system, eastern Tibetan Plateau: Implications for regional seismic activity. *J. Hydrol.* 607, 127554. doi:10.1016/j.jhydrol.2022.127554

Martinelli, G., Facca, G., Genzano, N., Gherardi, F., Lisi, M., Pierotti, L., et al. (2020). Earthquake-related signals in Central Italy detected by hydrogeochemical and satellite techniques. *Front. Earth Sci.* 8, 584716. doi:10.3389/feart.2020.584716

Martinelli, G., Ciolini, R., Facca, G., Fazio, F., Gherardi, F., Heinicke, J., et al. (2021). Tectonic-related geochemical and hydrological anomalies in Italy during the last fifty years. *Minerals* 11 (2), 107. doi:10.3390/min11020107

McCaig, A. M. (1989). Fluid flow through fault zones. *Nature* 340, 600. doi:10.1038/340600a0

Miller, S. A., Collettini, C., Chiaraluce, L., Cocco, M., Barchi, M., and Kaus, J. P. K. (2004). Aftershocks driven by a high-pressure CO_2 source at depth. *Nature* 427 (6976), 724–727. doi:10.1038/nature02251

Minissale, A., Magro, G., Martinelli, G., Vaselli, O., and Tassi, G. F. (2000). Fluid geochemical transect in the northern apennines (central-northern Italy): Fluid Genesis and migration and tectonic implications. *Tectonophysics* 319 (3), 199–222. doi:10.1016/S0040-1951(00)00031-7

Minissale, A. (2004) Origin, transport and discharge of CO_2 in central Italy. *Earth-Sci. Rev.* 66 (1-2), 89–141. doi:10.1016/j.earscirev.2003.09.001

Mirabella, F., Brozzetti, F., Lupatelli, A., and Barchi, M. R. (2011). Tectonic Evolution of a low angle extensional fault system from restored cross-sections in the Northern Apennines (Italy). *Tectonics* 30, TC6002. doi:10.1029/2011TC002890

O'Leary, M. H. (1988). Carbon isotopes in photosynthesis. *Bioscience* 38, 328–336. doi:10.2307/1310735

Ozima, M., and Podosek, F. A. (2002). *Noble gas Geochemistry*. 2nd ed. Cambridge, New York, Melbourne: Cambridge University Press. xiv + 286.

Pauselli, C., Barchi, M. R., Federico, C., Magnani, M. B., and Minelli, G. (2006). The crustal structure of the northern apennines (Central Italy): An insight by the crop03 seismic line. *Am. J. Sci.* 306, 428–450. doi:10.2475/06.2006.02

Pialli, G., Barchi, M., and Minelli, G. (1998). Results of the CROP 03 deep seismic reflection profile. *Mem. Soc. Geol. It.* 52, 1–647.

Pineau, F., and Javoy, M. (1983). Carbon isotopes and concentrations in mid-oceanic ridge basalts. *Earth Planet. Sci. Lett.* 62, 239–257. doi:10.1016/0012-821x(83)90087-0

Raich, J. W., and Schlesinger, W. H. (1992). The global carbon dioxide flux in soil respiration and its relationship to vegetation and climate. *Tellus* 44B, 81–99. doi:10.1034/j.1600-0889.1992.t01-1-00001.x

Raich, J. W., and Tufekcioglu, A. (2000). Vegetation and soil respiration: Correlations and controls. *Biogeochemistry* 48, 71–90. doi:10.1023/a:1006112000616

Rogie, J. D., Kerrick, D. M., Chiodini, G., and Frondini, F. (2000). Flux measurements of nonvolcanic CO_2 emission from some vents in central Italy. *J. Geophys. Res. Solid Earth* 105, 8435–8445. doi:10.1029/1999jb900430

Rowland, J. V., and Sibson, R. H. (2004). Structural controls on hydrothermal flow in a segmented rift system, Taupo Volcanic Zone, New Zealand. *Geofluids* 4, 259–283. doi:10.1111/j.1468-8123.2004.00091.x

Sibson, R. H. (1994). "Crustal stress, faulting and fluid flow," in *Geofluids: Origin, migration and evolution of fluids in sedimentary basins*. Editor J. Parnell (Geological Society, London, Special Publication), 78, 69–84.

Taylor, B. E. (1986). Magmatic volatiles: Isotopic variation of C, H and S. Rev. *Mineral* 16, 185–225.

Trippetta, F., Collettini, C., Barchi, M. R., Lupattelli, A., and Mirabella, F. (2013). A multidisciplinary study of a natural example of a CO_2 geological reservoir in central Italy. *Int. J. Greenh. Gas. Control* 12, 72–83. doi:10.1016/j.ijggc.2012.11.010

Valoroso, L., Chiaraluce, L., Di Stefano, R., and Monachesi, G. (2017). Mixed-mode slip behavior of the Altotiberina low-angle normal fault system (Northern Apennines, Italy) through high-resolution earthquake locations and repeating events. *J. Geophys. Res. Solid Earth* 122, 10,220. 10,240. doi:10.1002/2017JB014607

Vaselli, O., Tassi, F., Minissale, A., Capaccioni, B., Magro, G., and Evans, W. C. (1997). Geochemistry of natural gas manifestations from the upper Tiber Valley (central Italy). *Mineral. Petrog. Acta* 40, 201–212.

Viveiros, F., Ferreira, T., Cabral Vieira, J., Silva, C., and Gaspar, J. L. (2008). Environmental influences on soil CO_2 degassing at furnas and fogo volcanoes (são miguel Island, azores archipelago). *J. Volcanol. Geotherm. Res.* 177, 883–893. doi:10.1016/j.jvolgeores.2008.07.005

Viveiros, F., Ferreira, T., Silva, C., and Gaspar, J. L. (2009). Meteorological factors controlling soil gases and indoor CO_2 concentration: A permanent risk in degassing areas. *Sci. Total Environ.* 407, 1362–1372. doi:10.1016/j.scitotenv.2008.10.009

Vuan, A., Brondi, P., Sugan, M., Chiaraluce, L., Di Stefano, R., and Michele, M. (2020). Intermittent slip along the Alto Tiberina low-angle normal fault in central Italy. *geophys. Res. Lett.* 47, e2020GL089039. doi:10.1029/2020GL089039

Wang, C. Y., and Manga, M. (2010). Hydrologic responses to earthquakes and a general metric. *Geofluids* 10, 206–216. doi:10.1111/j.1468-8123.2009.00270.x

Weinlich, F. H., Faber, E., Boušková, A., Horálek, J., Teschner, M., and Poggenburg. J. (2006). Seismically induced variations in MariánskéLázně fault gas composition in the NW Bohemian swarm quake region, Czech Republic – a continuous gas monitoring. *Tectonophysics* 421, 89–110. doi:10.1016/j.tecto.2006.04.012

Weinlich, F. H., Stejskal, V., Teschner, M., and Poggenburg, J. (2013). Geodynamic processes in the NW Bohemian swarm earthquake region, Czech Republic, identified by continuous gas monitoring. *Geofluids* 13, 305–330. doi:10.1111/gfl.12027

Yang, Y., Li, Y., Li, Y., Ji, L., Gong, Y., Du, F., et al. (2021). Present-day activity of the Anninghe fault and Zemuhe fault, southeastern Tibetan Plateau, derived from soil gas CO_2 emissions and locking degree. *Earth Space Sci.* 8, e2020EA001607. doi:10.1029/2020EA001607

Frontiers in Earth Science

Investigates the processes operating within the major spheres of our planet

Advances our understanding across the earth sciences, providing a theoretical background for better use of our planet's resources and equipping us to face major environmental challenges.

Discover the latest Research Topics

See more →

Frontiers

Avenue du Tribunal-Fédéral 34
1005 Lausanne, Switzerland
frontiersin.org

Contact us

+41 (0)21 510 17 00
frontiersin.org/about/contact